U.S. DEPARTMENT OF COMMERCE/ National Oceanic and Atmospheric Administration

OFCM

OFFICE OF THE FEDERAL COORDINATOR FOR
METEOROLOGICAL SERVICES AND SUPPORTING RESEARCH

FEDERAL METEOROLOGICAL HANDBOOK NO. 11

DOPPLER RADAR METEOROLOGICAL OBSERVATIONS

PART B
DOPPLER RADAR THEORY AND METEOROLOGY

FCM-H11B-2005

Washington, DC
December 2005

THE FEDERAL COMMITTEE FOR
METEOROLOGICAL SERVICES AND SUPPORTING RESEARCH (FCMSSR)

VADM CONRAD C. LAUTENBACHER, JR., USN (RET.)
Chairman, Department of Commerce

DR. SHARON HAYS (Acting)
Office of Science and Technology Policy

DR. RAYMOND MOTHA
Department of Agriculture

BRIG GEN DAVID L. JOHNSON, USAF (RET.)
Department of Commerce

MR. ALAN SHAFFER
Department of Defense

DR. ARISTIDES PATRINOS
Department of Energy

DR. MAUREEN MCCARTHY
Science and Technology Directorate
Department of Homeland Security

DR. MICHAEL SOUKUP
Department of the Interior

MR. RALPH BRAIBANTI
Department of State

MR. RANDOLPH LYON
Office of Management and Budget

MR. CHARLES E. KEEGAN
Department of Transportation

MR. DAVID MAURSTAD (Acting)
Federal Emergency Management Agency
Department of Homeland Security

DR. MARY L. CLEAVE
National Aeronautics and Space
Administration

DR. MARGARET S. LEINEN
National Science Foundation

MR. PAUL MISENCIK
National Transportation Safety Board

MR. JAMES WIGGINS
U.S. Nuclear Regulatory Commission

DR. LAWRENCE REITER
Environmental Protection Agency

MR. SAMUEL P. WILLIAMSON
Federal Coordinator

MR. JAMES B. HARRISON, Executive Secretary
Office of the Federal Coordinator for
Meteorological Services and Supporting Research

THE INTERDEPARTMENTAL COMMITTEE FOR
METEOROLOGICAL SERVICES AND SUPPORTING RESEARCH (ICMSSR)

MR. SAMUEL P. WILLIAMSON, Chairman
Federal Coordinator

MR. THOMAS PUTERBAUGH
Department of Agriculture

MR. JOHN E. JONES, JR.
Department of Commerce

MR. ROBERT WINOKUR, USN (Acting)
United States Navy
Department of Defense

BRIG GEN THOMAS E. STICKFORD, USAF
United States Air Force
Department of Defense

MR. RICKEY PETTY
Department of Energy

MR. CHRISTOPHER DOYLE
Science and Technology Directorate
Department of Homeland Security

MR. JOHN VIMONT
Department of the Interior

MS. REGINA MCELROY
Federal Highway Administration
Department of Transportation

MS. LISA BEE
Federal Aviation Administration
Department of Transportation

DR. JONATHAN M. BERKSON
United States Coast Guard
Department of Homeland Security

MR. JEFFREY MACLURE
Department of State

DR. S. T. RAO
Environmental Protection Agency

MR. JOHN GAMBEL
Federal Emergency Management Agency
Department of Homeland Security

DR. RAMESH KAKAR
National Aeronautics and Space
Administration

DR. JARVIS MOYERS
National Science Foundation

MR. DONALD E. EICK
National Transportation Safety Board

MS. LETA A. BROWN
U.S. Nuclear Regulatory Commission

MS. ANDREA PETRO
Office of Management and Budget

MR. JAMES B. HARRISON, Executive Secretary
Office of the Federal Coordinator for
Meteorological Services and Supporting Research

FEDERAL COORDINATOR FOR
METEOROLOGICAL SERVICES AND SUPPORTING RESEARCH

DOPPLER RADAR
METEOROLOGICAL OBSERVATIONS

FEDERAL
METEOROLOGICAL
HANDBOOK NO. 11
DECEMBER 2005

PART B
DOPPLER RADAR THEORY
AND METEOROLOGY

FCM-H11B-2005

Washington, DC

PREFACE

The Federal Coordinator for Meteorological Services and Supporting Research has the responsibility to maintain and publish Federal Meteorological Handbooks. This series of documents provides standards and procedures to facilitate the efficient collection, sharing, and use of meteorological information by agencies of the federal government and private industry.

The original Federal Meteorological Handbook, Number 11 (FMH-11), DOPPLER RADAR METEOROLOGICAL OBSERVATIONS, was prepared and published under the auspices of the Office of the Federal Coordinator for Meteorological Services and Supporting Research (OFCM) at the request of the Next Generation Weather Radar (NEXRAD) Program Council and in coordination with the federal agencies that are represented on the Interdepartmental Committee for Meteorological Services and Supporting Research. The purpose of FMH-11 is to standardize, insofar as practical, the operation of the Weather Surveillance Radar-1988, Doppler (WSR-88D) systems and the procedures used by personnel of the Departments of Commerce, Defense, and Transportation. By approving publication of this handbook, those agencies have agreed to operate their WSR-88D systems accordingly. Some flexibility under certain meteorological, siting, or mission circumstances is permitted to enhance the quality and utility of some WSR-88D products.

The revision process is dependent on the evolution of WSR-88D subsystems software and products. Part A has been revised to ensure it provides users current operations guidance. Parts B, C, and D are being revised in a separate effort principally through the guidance of the Radar Operations Center (ROC). All revisions are coordinated among the NEXRAD triagencies (Department of Commerce (DoC), Department of Defense (DoD), and Department of Transportation (DoT)); thus, they possess the same authority as the initial edition of FMH-11.

The agencies shall review the documents at least annually. The goal is to review and update (as necessary) the handbooks as part of every WSR-88D software build release. Suggestions for modifications and additions shall be forwarded through the appropriate channels in each agency for consideration, and issuance, if appropriate. Changes will be issued as a total update of each chapter of the handbook. The handbook updates will be issued in electronic format and made available on the OFCM home page (http://www.ofcm.gov). Readers can make copies of the handbook without a request for approval from the OFCM. A summary of changes made during updates will be annotated in the preface of each part.

Each major part of the FMH-11 is designed to stand alone, except where cross references avoid voluminous redundancy. In all, FMH-11 has four parts:

Part A - System Concepts, Responsibilities, and Procedures (December 2005)

Part B - Doppler Radar Theory and Meteorology (December 2005)

Part C - WSR-88D Products and Algorithms (February 1991)

Part D - WSR-88D Unit Description and Operational Applications (April 1992)

Part B brings together in one document most of the theory required to understand how the WSR-88D acquires and processes the Doppler radar signal. It presents mathematical formulations of the physical processes and laws, explains how the Doppler technology "sees" various meteorological and hydrological events, and explores the strengths and problems in data acquisition with a Doppler radar. It then addresses aspects of radar meteorology regarding recognition of velocity patterns and applications of Doppler radar to storm events.

Summary of Changes:
This version of Part B updates and replaces the original document, published in June, 1990. This version updates the document as of Radar Product Generator Build 6 (released in September 2004) and provides updated information related to large-scale precipitation weather systems and individual thunderstorms and attendant phenomena. The section related to hurricanes has been deleted, but may be updated and included in a future version.

Samuel P. Williamson
Federal Coordinator for Meteorological
Services and Supporting Research

FEDERAL METEOROLOGICAL HANDBOOK NO. 11
DOPPLER RADAR METEOROLOGICAL OBSERVATIONS
PART B
DOPPLER RADAR THEORY AND METEOROLOGY

TABLE OF CONTENTS

CHAPTER 6. INTERPRETATION OF DOPPLER VELOCITY PATTERNS

CHAPTER 7. MORPHOLOGY OF LARGE-SCALE PRECIPITATING WEATHER SYSTEMS

CHAPTER 8. MORPHOLOGY OF INDIVIDUAL THUNDERSTORMS AND ATTENDANT PHENOMENA

APPENDIX A: PHYSICS OF METEOROLOGICAL RADARS

LIST OF FIGURES

LIST OF TABLES

LIST OF SYMBOLS

a	Radius
A	Signal Amplitude
A_e	Effective Aperture Area of the Antenna
b	Gain Constant
c	Speed of Light = 3×10^8 m s^{-1}
dB	Decibel
D	Drop Size
D_e	Diameter of an Equivalent Volume Spherical Raindrop
f	Frequency
f_d	Doppler Frequency
f_n	Nyquist Frequency
f_s	Sampling Frequency
G	Gain
h	Height
h_s	Surface Height
I	Inphase Component of the Complex Signal
k	Multiplicative Factor Determined by Refraction Index Profile
$k \cdot a$	Equivalent Earth's Radius
K	Complex Index of Refraction
K_p	Two-Way Attenuation
L	Loss Factor
M	Modified Index of Refraction; Mass Liquid Water Content
n	Index of Refraction
N	Refractivity = $(n - 1) \times 10^6$
N_o	Number Density (Number of Particles Per Unit Volume)
P	Pressure
P_i	Incident Power Density
P_r	Echo (Return) Power
P_t	Peak Transmitted Power
Q	Quadrature Phase Component of the Complex Signal

r	Range to Target
r_a	Unambiguous Range
r_c	Core Radius
R	Rainfall Rate
S	Signal Power
t	Time
T	Air Temperature, ° Kelvin
U	Gating Function
v	Velocity
v_a	Unambiguous Velocity
v_d	Doppler Velocity
v_h	Average Horizontal Wind Velocity Around the Scanning Circle at Height h
v_m	Measured Velocity
v_r	Radial Component of Velocity
v_t	Terminal Fall Velocity for Precipitation Particles
v_T	True Velocity
v_x	Maximum Velocity
V	Voltage
W	Spectrum Width
Z	Reflectivity
Z_e	Equivalent (Effective) Radar Reflectivity Factor
α	Antenna Rotation Rate
β	Azimuth Angle Measured from the Upwind Direction
Δ_θ	Angular Sampling Interval
Δ_ϕ	Angular Increment
ε	Partial Pressure of Water Vapor, Millibars; Dielectric Constant
η	Target Backscattering Cross Section Per Unit Volume
θ	Angular Distance from Beam Axis
θ_e	Equivalent Angular Distance from Beam Axis
θ_m	Measured Angular Distance from Beam Axis
θ_T	True Angular Distance from Beam Axis

θ_2	Two-way Antenna 3dB Beam Width
θ_{3dB}	Antenna Horizontal Half-Power Beam Width
λ	Radar Wavelength
ρ	Vapor Pressure
σ_b	Target Backscattering Cross Section
σ_d^2	Variance Due to Drop Size Distribution
σ_{do}	Standard Deviation of Drop Terminal Velocities
σ_f	Frequency Standard Deviation
σ_r^2	Variance Due to Antenna Motion
σ_s^2	Variance Due to Wind Shear
σ_t	Time Standard Deviation
σ_t^2	Variance Due to Turbulence
σ_v	Standard Deviation of the Velocity Spectrum
τ	Pulse Width (Duration)
ϕ	Vertical Distance from Beam Axis
ϕ_e	Elevation Angle
ϕ_{3dB}	Antenna Vertical Half-Power Beam Signal
ψ	Initial Phase of Transmitter Signal
ω	Angular Velocity

CHAPTER 1

INTRODUCTION

1.1 Background. Material presented in this Part B, Doppler Radar Theory and Meteorology, of the Federal Meteorological Handbook No. 11 (FMH-11) was provided from a number of sources. The basic material for chapters dealing with Doppler meteorological radar and those that treat meteorological and hydrological phenomena detectable by the radar was provided by the staff of the National Oceanic and Atmospheric and Oceanographic Administration (NOAA), Environmental Research Laboratories (ERL), National Severe Storms Laboratory (NSSL); and the National Weather Service (NWS) Hydrologic Research Laboratory (now the Office of Hydrologic Development). Most of this material remains unchanged since the original 1990 version of Part B which this version replaces. The updates were primarily provided by the National Weather Service's Warning Decision Training Branch, Radar Operations Center (ROC) subject matter experts, and a support services contractor. The updates included in this version update the material to the last software of the legacy Radar Data Acquisition (RDA) (Build 10.2) and Radar Product Generator (RPG) (Build 6). In addition, updated meteorological applications have been added in the later chapters.

1.2 Purpose and Scope. Part B of this Federal Meteorological Handbook is intended to provide the professional meteorologist with the background in radar meteorology necessary to make effective use of the WSR-88D in an operational forecast and warning environment. The information in this Handbook should help the increasing number of users of WSR-88D product data and Level II data apply these data to their responsibilities. Recommended changes/corrections to this manuscript are welcome and should be sent to: **http://www.roc.noaa.gov/Feedback/**.

1.3 Organization and Content. Part B is organized into eight chapters and four appendices that present the Handbook material for two general areas dealing with Doppler weather radar fundamentals and radar meteorology. This chapter, Chapter 1, provides background information and an overall summary of contents.

1.3.1 Doppler Meteorological Radar Fundamentals. Chapter 2 introduces the reader to the Weather Surveillance Radar-1988, Doppler (WSR-88D) unit and presents fundamental concepts of Doppler weather radar. It is provided as background for those users who desire an in-depth understanding of the WSR-88D. (Knowledge of physics and graduate-level statistics will be helpful.)

Chapter 3 continues the in-depth presentation of Chapter 2 with a detailed explanation of the physics of radar data acquisition. Data sampling is discussed along with the propagation of electromagnetic waves in the atmosphere. (Knowledge of physics and graduate-level statistics will be helpful.)

Chapter 4 summarizes the fundamental concepts presented in Chapters 2 and 3 for the reader without a background in physics and graduate-level statistics. Doppler radar principles are addressed, as are inherent data sampling problems.

1.3.2 Radar Meteorology. Chapter 5 reviews the theory and application of physical principles of the measurement process of particle size distribution and the reflectivity-rainfall relationship. Chapter 6 presents an introduction to the interpretation of Doppler velocity patterns. It is intended to familiarize the reader with the use of base Doppler velocity products to analyze significant meteorological events by exhibiting the differences that result from changes in an idealized wind field. It displays patterns resulting from vertical and horizontal variations in the wind field and discusses a technique to quantitatively derive a vertical profile of the horizontal wind. (The reader is assumed to understand solid geometry.)

Chapter 7 distinguishes between stratiform and convective precipitation. It describes the development and organization of mesoscale convective systems. (The presentation is non-mathematical, presuming a familiarity with the concepts and terminology of radar meteorology.)

Chapter 8 describes the evolutions and life cycles of various types of convective precipitation cells. It distinguishes between thunderstorm complexes composed of single and multiple cells. Storm motion and organization are related to the environmental wind profile. Reflectivity structure and Doppler velocity patterns are related to different types and evolutionary stages of severe thunderstorms. In addition, hail and turbulence are related to base data fields. (Although non-mathematical, the presentation level presumes a working knowledge of thunderstorm meteorology and attendant phenomena.)

The WSR-88D images used in Part B are from the many diverse NEXRAD agency user display systems available. The list of the primary user display systems is in the Definition of Terms section in Part A of this Handbook. In addition, figures from the proof-of-concept National Severe Storms Laboratory Warning Decision Support System (WDSS) and the National Climatic Data Center (NCDC) Level III/product archives via the NCDC NEXRAD Viewer are used. These diverse displays are used to ensure the best representative examples of the phenomena being depicted are presented.

1.3.3 Appendices. Appendices A and B provide amplification to Chapters 2, 3, and 5. Appendix C contains a listing of acronyms and abbreviations while Appendix D is a glossary of terms.

CHAPTER 2

INTRODUCTION TO THE WSR-88D

2.1 General. The WSR-88D is the second-generation, operational meteorological radar replacing the non-Doppler meteorological radars of the National Weather Service and the Air Force.

The WSR-88D represents a quantum leap from the earlier meteorological radars both in engineering technology and in meteorological measurements. As a fully coherent "Doppler" radar, it provides not only accurate reflectivity measurement and its attendant information on spatial location, distribution, etc., but also measurement of the radial component of motion (mean Doppler velocity along the axis of the radar beam) of the scatterers and the dispersion of velocities in the radar sample volume (spectrum width). The information flow rate from the WSR-88D is an order of magnitude larger than the earlier incoherent radars and requires high-speed data processing for signal analysis and information extraction for effective utilization and man-machine interface.

2.2 Basic Unit Description. For descriptive purposes the WSR-88D unit can be divided into three parts.

- Radar - composed of transmitter, receiver, antenna and the associated support circuitry.
- Dedicated Signal Processors - composed of reflectivity, velocity, and spectrum width estimators; ground clutter cancellers; and data formatting, quality checking, and radar control processors.
- Data Analysis and Display - composed of the meteorological analysis processor, product generator, associated color displays, and communications ports.

The radar is a coherent "chain-transmitter" design. Coherence, or phase information, in this type of design is maintained by very stable oscillators or signal sources that operate continuously. These sources are used as the reference in extracting the Doppler shift of the return signal, which is proportional to the radial motion of the target from which the transmitter signal is backscattered. A chain transmitter is one in which the transmitter signal is initially generated at a low power level, in this case a few hundred milliwatts, and increased to a high power, 750 kilowatts (kw), by an amplifier chain. Intermediate amplification is by solid-state devices and the final high-power amplifier is a klystron. The klystron is a vacuum tube device capable of high gain amplification (~60 dB) with negligible signal distortion or spurious emission. The antenna is a center-feed, parabolic reflector having a diameter of approximately 28 ft (8.5 m). The antenna has a main lobe one-way 3 dB beam width of 0.93° at 2850 MHz (measured average), a first sidelobe level of 29 dB below the main lobe, a sidelobe taper greater than 1 dB per degree between 2° and 10° from the main lobe axis, and a far out sidelobe level more than 40 dB below the main lobe. The receiver uses two frequency mixers to down convert the received signal to zero frequency carrier (video signal). The first conversion generates an intermediate signal carrier at which most amplification, bandpass filtering, and automatic gain control (AGC) are done. The second frequency conversion is a synchronous detection (a detection that retains received signal amplitude and phase shift difference between received and transmitted signal phases but which removes the intermediate frequency carrier). At this point, the signal has an amplitude proportional to echo radar reflectivity and contains a frequency component equal to the Doppler shift. This is a "complex" signal; complex meaning that it contains both amplitude and phase information and, for convenience of handling and analysis, is decomposed into its vector components, i.e., two signals, inphase and quadrature, having a phase difference of 90° that, when added vectorally, form the complex signal.

The signal processors extract three meteorological quantities from the returned signal. These are: volume reflectivity, expressed in terms of equivalent radar reflectivity, Z_e; the radial velocity, i.e., the component of motion of the reflecting particles toward or away from the radar; and spectrum width, which is a measure of dispersion of velocities within the radar sample volume. Reflectivity, Z, is calculated from the returned signal power and the known characteristics of the radar (Appendix A.4.1). Estimation is by a linear average of several return pulses, usually about 25, from each range cell. Velocity, v, is also estimated from several pulses (usually 40 to 50) pulses. The mathematical quantity computed is the return signal complex covariance argument using a technique called "pulse-pair processing" since the computation requires two pulses (two consecutive signal returns from the same target; Appendix A.4.2). Physically, the covariance argument provides a measurement of rotation rate of the complex vector representing the returned signal that is directly related to the Doppler frequency, Spectrum width, W, or velocity dispersion within the radar sample volume, is estimated indirectly. The computation performed is the returned signal autocorrelation which is related to the velocity spectrum standard deviation. It uses the same pulses as radial velocity (Appendix A.4.3). These quantities are calculated by dedicated digital processors, i.e., processors designed and configured to perform a specific operation with only limited changes in parametric values.

Physically the WSR-88D is divided into three functional components: RDA, RPG, and display systems. These components are described in Part D of this Handbook.

2.3 WSR-88D Radar Characteristics. A tabulation of some of the fundamental engineering characteristics of the radar is given in Table 2-1. The implications of these values in the meteorological measurements are discussed in Chapter 3. These system parameters, when substituted into the general radar equation (Eq. 5-3 and Appendix A), result in the detection capability shown in Figure 2-1.

Table 2-1
WSR-88D Radar Characteristics

Antenna Subsystem		
Radome	Rigid fiberglass	
Diameter	39 ft (12 meters)	
RF loss - two way	0.24 dB at 2850 MHz	
Pedestal	Elevation Over Azimuth	
	Azimuth	Elevation
Steerability	360°	+0.5 to +19.5
Rotational rate - maximum	$30° s^{-1}$	$30° s^{-1}$
Acceleration - maximum	$15° s^{-2}$	$15° s^{-2}$
Mechanical limits		-1° to +60°
Antenna	Paraboloid of Revolution	
Polarization	Linear Horizontal	
Reflector diameter	28 ft (8.5 meters)	
Gain (at 2800 MHz)	45 dB	
Beam Width	0.93° (at 2850 MHz, Measured Average)	
First sidelobe level	-29 dB	
Transmitter and Receiver Subsystem Coherent - Chain Design		
Transmitter		
Frequency range	2700 MHz to 3000 MHz	
Peak power	750 kw	
Pulse widths (nominal)	1.57 μs and 4.5 μs	
rf duty cycle	0.002 maximum	
PRFs	Short pulse: 318 Hz to 1304 Hz	
	Long pulse: 318 Hz to 452 Hz	
Receiver		
Dynamic range	93 dB	
Noise temperature	450° K	
Intermediate frequency	57.6 MHz	
Band width, 3 dB	0.63 MHz	

Table 2-1 WSR-88D Radar Characteristics (Concluded)	
Signal Processor Subsystem	
Clutter Canceller	Infinite Impulse Response Design
Suppression	30 dB to 50 dB
Notch half widths	0 to 4 ms^{-1} (0 to 8 kts)
Intensity bias	0 to 1 dB
Minimum usable velocity	0 to 4 ms^{-1} (0 to 8 kts)
Range increment	0.25 km (0.13 nm)
Azimuth increment	1°
Velocity Calculation	Complex Covariance Argument
Algorithm	Pulse-pair processing
Estimate accuracy (nominal)	1 ms^{-1} (2 kts)
Number of pulses averaged	40 to 280
Range increment	0.25 km (0.13 nm)
Azimuth increment	1°
Spectrum Width Calculation	Autocorrelation
Algorithm	Single lag correlation
Estimate accuracy (nominal)	1 ms^{-1} (2 kts)
Number of pulses averaged	40 to 280
Range increment	0.25 km (0.13 nm)
Azimuth increment	
Intensity Calculation	Return Power Average
Algorithm	Linear average
Estimate accuracy (nominal)	1 dB
Number of pulses averaged	6 to 64
Range increment	1 km (0.54 nm)
Azimuth increment	1°

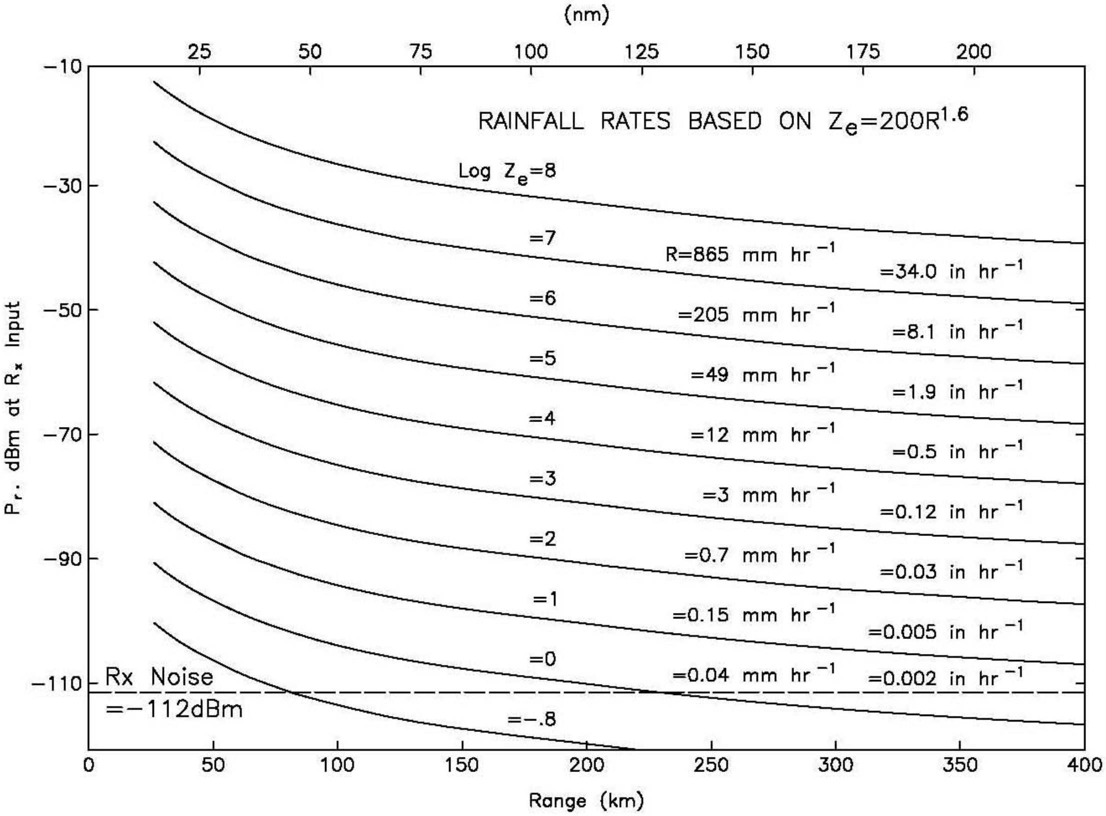

Figure 2-1
Reflectivity Detection Capability of the WSR-88D

The equivalent reflectivity, Z_e, rainfall rate relationship of $Z_e = 200R^{1.6}$ is a good general relationship, but is not optimum for all types of liquid precipitation and is not valid for snow.

2.4 Fundamental Concepts of Doppler Radar. A pulse Doppler radar, in its simplest form, is one providing a signal reference by which changes in the radio frequency (rf) phase of successively received pulses may be recognized. Such a radar is termed "coherent," i.e., it maintains rf waves with a continuous relationship among phases. The known phase of the transmitted signal enables measurement of the phase of the received signal. The Doppler shift associated with the echo from which the return originated is calculated from the time rate of change of phase.

2.4.1 Doppler Frequency. The relationship between phase time rate of change and Doppler frequency can be visualized by considering the returned signal from a single target. The complex signal, i.e., inphase, I, and quadrature, Q, returned from a single target at a radial range, *r*, is of the form:

$$\mathrm{I} = A\cos\left[\frac{4\pi r}{\lambda} - \psi\right]$$

$$\mathrm{Q} = A\sin\left[\frac{4\pi r}{\lambda} - \psi\right]$$

where:

A = signal amplitude (proportional to target cross-sectional area)

λ = radar wavelength

$\frac{4\pi}{\lambda}$ = phase due to range propagation of 2r (to the target and back)

Ψ = initial phase of the transmitter signal

If the range, *r*, changes with time (target moving relative to the radar), the argument, $4\pi r / \lambda - \Psi$, becomes a function of time. Time rate of change of phase is the angular velocity, ω, expressed as:

$$\frac{d}{dt}\left[\frac{4\pi r(t)}{\lambda} - \Psi\right] = \frac{4\pi}{\lambda}\frac{d[r(t)]}{dt} = \frac{4\pi}{\lambda} v_r = \omega$$

since time rate of change of range d[r(t)]/dt is radial velocity, v_r, by definition. Since angular velocity, ω, is related to frequency, *f*, by $\omega = 2\pi f$:

$$2\pi\frac{2v_r}{\lambda} = 2\pi f_d$$

and the Doppler frequency, f_d, is given by:

$$f_d = \frac{2v_r}{\lambda}$$

The angular rate of change is equal to 20 Hz per meter per second of radial velocity for a radar wavelength of 10 cm.

In summary, the fundamental transformations of meteorological characteristics to radar signal characteristics are: target cross-sectional area becomes proportional to signal power, target radial range becomes proportional to signal phase, and target radial velocity becomes proportional to time rate of phase change.

Thus, estimates of these electrical signal properties provide estimates of the corresponding meteorological properties.

2.4.2 Range-Velocity Ambiguity. Pulse radar is intrinsically a "sampled data system" since the measurement is time and space discrete. Time corresponds to the pulse repetition time (PRT) and space to the sample volume depth of the radar. The discrete time sampling results in a coupling between the maximum unambiguous range and the maximum unambiguous velocity associated with the radar and the discrete spatial sampling limits the scale that can be resolved by the radar (Section 3.2).

The maximum unambiguous range, r_a, i.e., the maximum range to which a transmitted pulse wave can travel and return to the radar before the next pulse is transmitted, is simply:

$$r_a = \frac{\mathrm{c}\,PRT}{2}$$

where c is the wave propagation constant (speed of light); $c = 3(10^8)\ \mathrm{ms}^{-1}$. For example, a PRT of 1 millisecond (PRF = 1000 Hz) results in an unambiguous range of 150 km (81 nm).

Discrete time sampling, i.e., sampling at the radar PRT interval, also limits the maximum frequency that can be resolved. The rigor for this is given by the Nyquist Sampling Theorem and is somewhat involved, but the mechanisms and implications can be understood by the following considerations.

The Nyquist frequency, f_n, is the highest frequency that can be resolved by Δt spaced samples. It is given by $f_n = 1/(2\Delta t)$ and corresponds to two samples per cycle on a sinusoid of f_n.

Sampling of frequencies higher than f_n results in an "aliasing" by which frequencies higher than f_n appear in the range from zero to f_n. Sampling of frequencies less than and greater than f_n is illustrated in Figure 2-2.

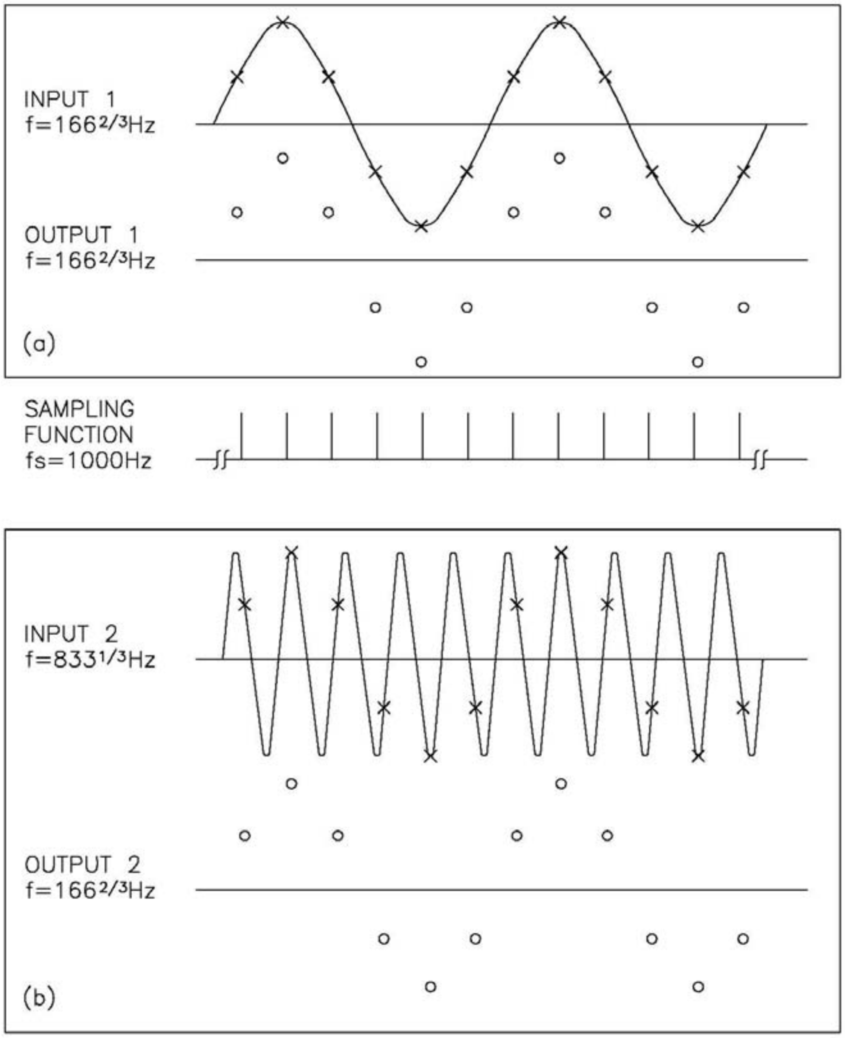

Figure 2-2
Example of Sampling a Signal

Input frequency (a) below the Nyquist frequency and (b) above the Nyquist frequency.

Consider the case shown in Figure 2-2a where a frequency of 166 2/3 Hz is sampled every one thousandth of a second (a 1000 Hz rate) and the extrapolated output is a frequency of 166 2/3 Hz, i.e., same frequency as the input. Consider now the case shown in Figure 2-2b where a frequency of 833 1/3 Hz (above the Nyquist frequency) is sampled at a 1000 Hz rate. The extrapolated output frequency is equal to the sampling frequency, 1000 Hz, minus the input frequency of 833 1/3 Hz, which yields a frequency of 166 2/3 Hz.

The limitations on maximum unambiguous frequency, f_n, imposed by the sampling rate $f_s = 1/PRT$ results in "coupling" between unambiguous frequency (velocity) and unambiguous range since both are functions of radar PRT. Since:

$$\frac{2v_a}{\lambda} = f_n = \frac{1}{2}\,\frac{1}{PRT} \quad \text{and} \quad r_a = \frac{c\,PRT}{2}$$

thus,

$$r_a v_a = \frac{c\lambda}{8}$$

where: v_a = unambiguous velocity
r_a = unambiguous range

Thus, the product of unambiguous range and unambiguous velocity is a constant determined by the wavelength of the radar. This relationship is shown in Figure 2-3 for the WSR-88D operating near mid-band. (A detailed discussion is given in Appendix A).

The range-velocity coupling is probably the most important operational constraint of the WSR-88D since it results in the operational problems of range folding and velocity aliasing.

2.4.3 Velocity Measurement. The velocity measurement technique used in the WSR-88D is essentially a method of Doppler angular frequency measurement, i.e., measurement of $\omega = 2\pi f$ in a time-varying function of the form $y = \cos \omega t$. This is equivalent to a measure of velocity since frequency is linearly related to velocity by the Doppler equation.

The actual computation is a minimum-variance, unbiased estimation of the complex covariance of the Doppler signal represented by the inphase, I, and quadrature, Q, video signals (a complex signal is needed to measure the sign of the Doppler frequency, i.e., whether the frequency shift is above or below the transmitted signal corresponding to velocities toward or away from the radar).

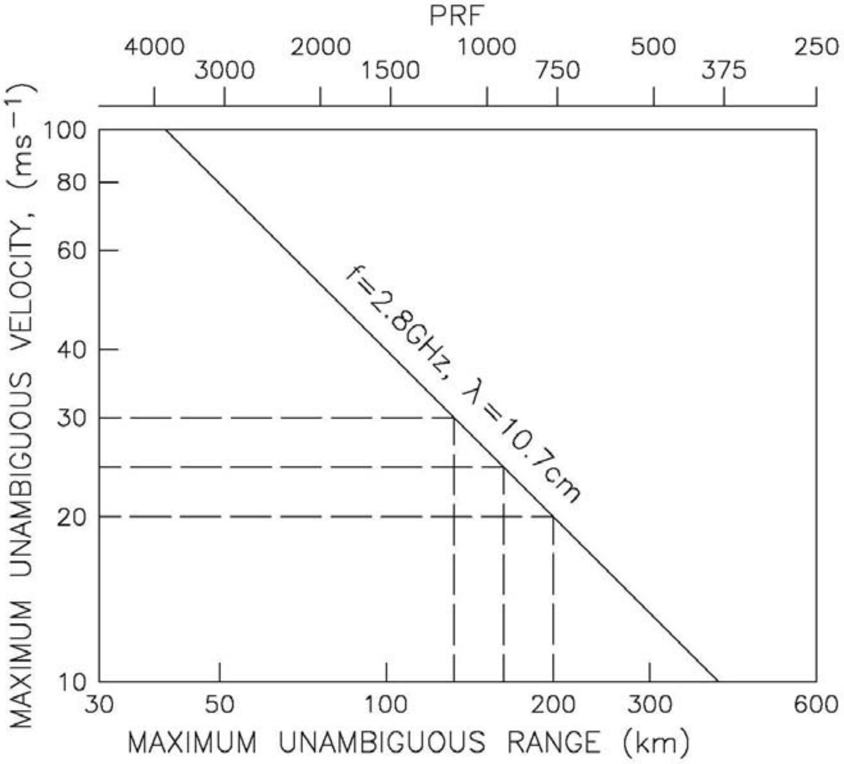

Figure 2-3
Unambiguous Range-Velocity Relationship for the WSR-88D

Dashed lines are for unambiguous velocities of 30, 25, and 20 ms^{-1} with associated unambiguous ranges of 134, 160, and 200 km.

The estimate of velocity (v) is:

$$\hat{v} = k \, Arg \sum_{n=1}^{N-1} [Z_{n+1} Z^*_n]$$

where:

k = a constant specified by X and PRT

Arg [] = the argument or angle of the quantity

Z = a complex signal of the form Z = I + jQ

Z* = complex conjugate of Z, Z* = I - jQ

n = sample sequence index

N = total number of samples

Due to the discrete nature of the sampling, the angular velocity of the vector represented by Z is measured as a differential. For example, given the vector $Z_n = 3 + j3$ in the first quadrant as shown in Figure 2-4a, assume that, by one PRT later, the next sample, $Z_{n+1} = -4 + j2$, appears in the second quadrant corresponding to a displacement between samples of 108 degrees. The complex multiplication of the second sample, Z_{n+1}, and the conjugate of the first Z^*_n produces a vector (Z_{n+l} Z^*_n) magnitude equal to the product of magnitudes of Z_n and Z_{n+l} with an angle equal to the difference in angles of Z_n and Z_{n+1} or the displacement of the vector over the radar PRT as shown in Figure 2-4b. Angular velocity is thus $\omega = (\theta_{n-1} - \theta_n)/PRT$.

The summation, as shown in Figure 2-4c, produces a mean displacement in which the individual displacements are weighted by the product of the two vector lengths (power of the signal) and the mean velocity is estimated from the power-weighted, average vector displacement.

Using the linear relationship between phase displacement and velocity, Figure 2-4d illustrates what occurs when the input velocity v_T, corresponding to θ_T, exceeds the unambiguous velocity, $\pm v_a$, corresponding to $\pm \pi$. When the true displacement is greater than $\pm \pi$, but less than $\pm 2\pi$ principal angle detection, θ_m corresponds to a measured velocity, v_m, having a magnitude $|v_m| = 2v_a - |v_T|$ and with a sign opposite that of v_T.

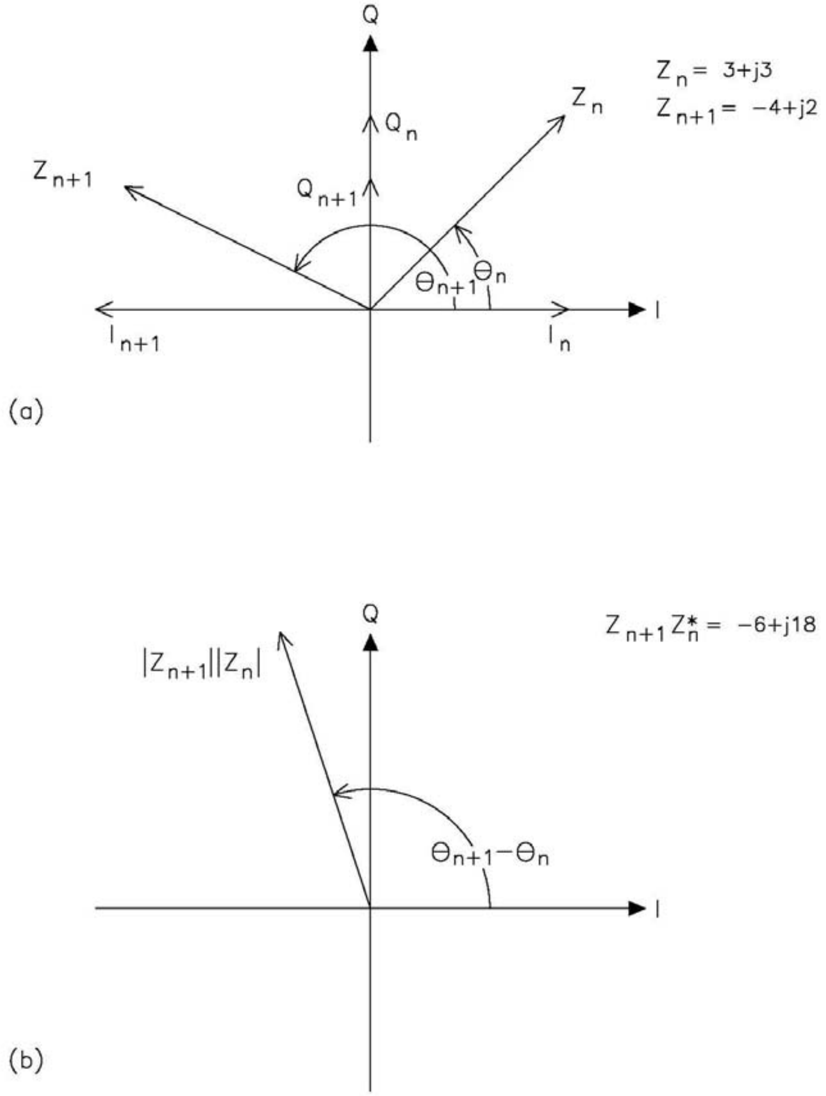

Figure 2-4
Velocity Sampling

(a) Vector representation of two consecutive complex video samples (I, Q).

(b) Result of the complex multiplication $Z_{n+l}\, Z^{*}_{n}$

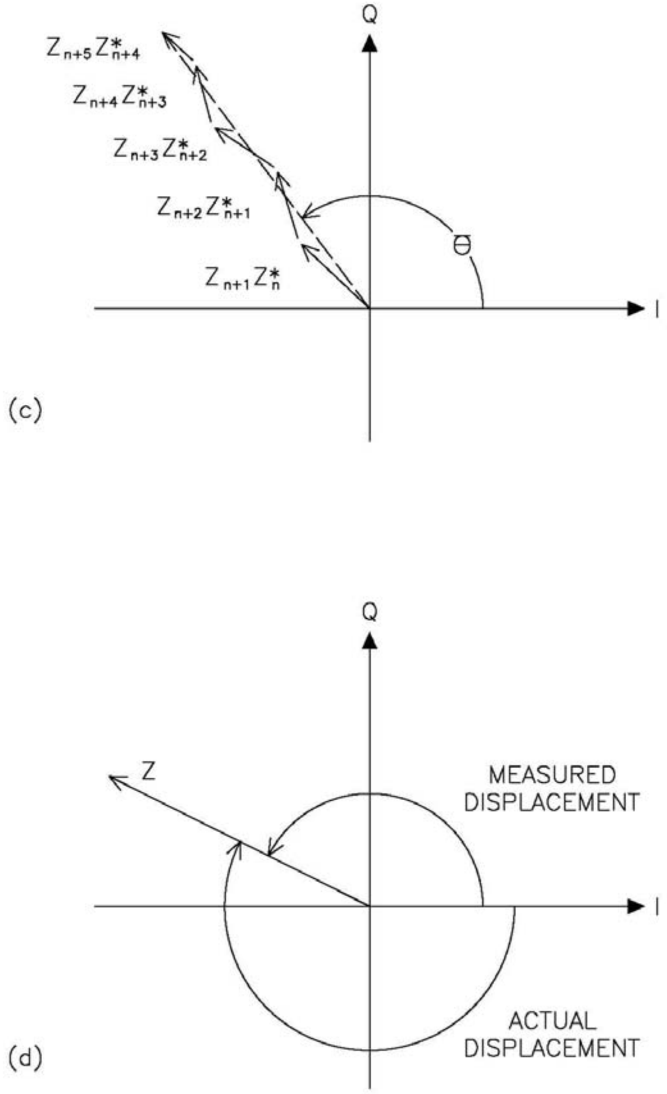

Figure 2-4
(Concluded)

(c) Schematic of vector summation.

(d) Frequency aliasing in the complex plane.

The uncertainty of the velocity estimate, i.e., how well the estimate represents the true mean velocity values, is dependent on input spectrum width--the larger the width the larger the uncertainty. Estimate accuracy can be improved or uncertainty reduced by increasing the number of samples in the estimate. Figure 2-5 gives the estimate accuracy or standard deviation, SD[v], (the measured velocity will be within $\pm$ one standard deviation of the true velocity 63% of the time) as a function of spectrum width with signal-to-noise ratio as the parameter of variation for unambiguous velocities representative of the WSR-88D.

It is seen from Figure 2-5 that the estimate of the standard deviation is dependent on unambiguous velocity, v_a, input spectrum width, W, signal-to-noise ratio (SNR), and the square root of the number of samples in the estimate ($N^{1/2}$).

For example, the WSR-88D with wavelength of 10 cm and a pulse repetition frequency (PRF) of 1 kHz [$v_a = 25$ m s^{-1} (49 kts)], operating at an antenna speed of 3 rpm, delivering estimates on a 1° polar grid (55 samples per estimate), and viewing a meteorological target having spectrum width of 5 m s^{-1} (10 kts) at a signal-to-noise ratio of 10 dB delivers a standard error of mean Doppler velocity estimate of 1 m s^{-1} (2 kts).

In summary, the mean Doppler velocity estimation technique used on the WSR-88D is a vector calculation of the time rate of change of signal phase that is converted to velocity through radar system constants (λ, PRT). The calculation operates in the continuum of vector space from 0 to $\pm \pi$ that provides a smooth transition through the Nyquist frequency or maximum unambiguous velocity. Measured velocities, v_m that are aliased, appear as the difference between the Nyquist co-interval, $+2v_a$, and the true velocity, v_T, i.e. $v_m = 2v_a - v_T$. Examination of Figure 2-5 reveals that meteorological parameters influencing estimate standard deviation for a given radar setup are spectrum width and SNR. For a given signal-to-noise ratio, the standard deviation of the velocity estimate increases as the square root of input spectrum width up to widths of about $0.4v_a$. At larger spectrum widths, the standard deviation of estimate increases very rapidly (loss of signal coherency) and becomes unacceptable for widths greater than about $0.5v_a$. Noise influence on estimate accuracy is negligible for SNR>10 dB. However, the increase in standard deviation increases very rapidly for SNR<10 dB and becomes unacceptable in most cases for SNR<0 dB.

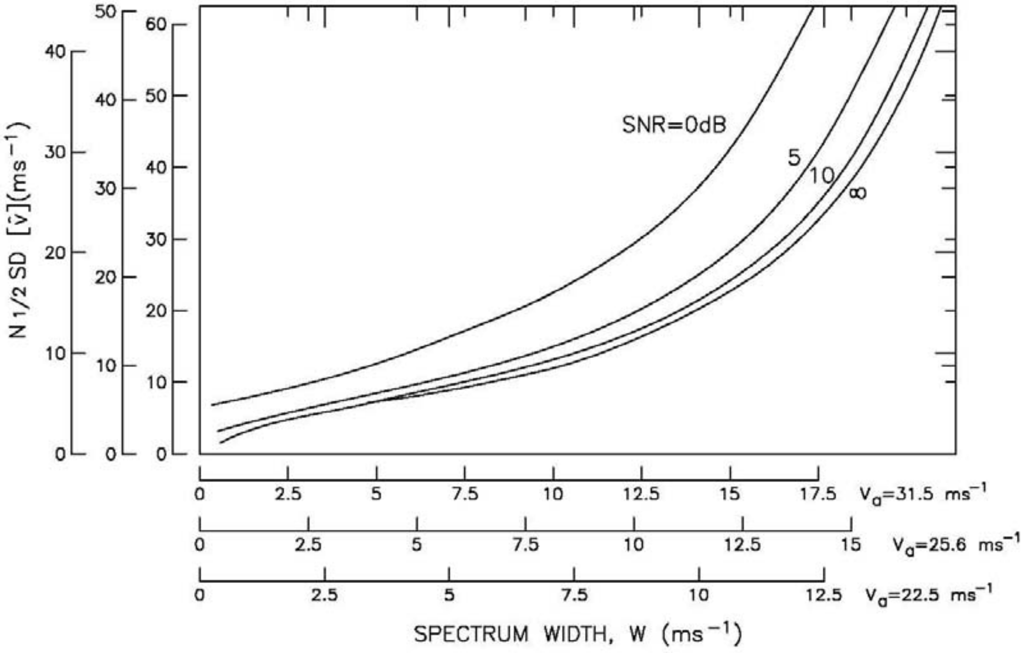

Figure 2-5
Standard Deviation of the Mean Velocity Estimate

This figure depicts the normalized standard deviation of the mean velocity estimate as a function of spectrum width for three unambiguous velocities and four levels of signal-to-noise ratio (SNR). Note the ordinate value must be divided by $N^{1/2}$, the square root of the number of samples in the estimate.

REFERENCES

Miller, K. S., and M. M. Rochwarger, 1972: A covariance approach to spectral moment estimation. *IEEE Transactions on Information Theory*, **IT- 18,** No. 5.

Sirmans D., 1975: Estimation of spectral density mean and variance by covariance argument techniques. Preprints, *16th Conference on Radar Meteorology*, Houston, TX, Amer. Meteor. Soc., 6-13.

Sirmans, D., and R. J. Doviak, 1973: Meteorological Radar Signal Intensity Estimation. NOAA Technical Memoranda, ERL, NSSL-64, 80 pp.

Sirmans, D., and B. Bumgamer, 1975: A numerical comparison of five mean frequency estimations. *J. Appl. Meteor.*, **14**, 991-1003.

CHAPTER 3

DATA ACQUISITION CONSIDERATIONS

3.1 Introduction. The WSR-88D has a number of user-selectable and site-specific data acquisition parameters enabling the user to optimize the acquisition and signal analysis to the particular meteorological situation. Acquisition optimization requirements often present conflicting demands on the system such as where estimate accuracy improvements require longer dwell times but the lifetime of meteorological features requires fast temporal sampling and thus short dwell times. Usually, the actual acquisition scheme will be a compromise between several conflicting requirements so as to satisfy the critical meteorological requirements such as temporal sampling and spatial resolution.

3.2 Temporal and Spatial Sampling. The temporal sampling time, i.e., the volume throughput rate, is driven by two general considerations: 1) the rate of change with time of the general information content of the meteorological characteristics being examined and 2) the lifetime of the weather event to be detected.

One of the more descriptive measures of general information change in the meteorology is correlation, as either a function of time or space, since this provides a measure of how much the process is changing. Values of correlation close to unity imply small changes from sample to sample with little new information. Values of correlation close to zero imply large changes from sample to sample with new information. For example, for purposes of estimate variance reduction with Gaussian statistics, a correlation of 0.15 means that about 25 percent of the information is redundant, a correlation of 0.5 means that about 50 percent is redundant, and a correlation of 0.9 means that about 80 percent is redundant. Measured values of the correlation of reflectivity and mean velocity are shown in Figure 3-1. Two general conclusions that can be drawn from the given behavior are: the mean velocity field is more persistent in time than the reflectivity field, and both reflectivity and mean velocity are significantly correlated (>0.3) with sampling intervals less than about 9 minutes. For the approximately Gaussian behavior exhibited by the correlation, this implies a significant information redundancy. Thus, temporal sampling intervals less than about 9 minutes will enable recovery of most information concerning total precipitation, storm type, mean motion, and other general characteristics of the system.

In most cases, the more stringent temporal sampling requirement will be imposed by detection of a weather event. Some representative events and approximate life times are tabulated in Table 3-1. It is seen that detection of the shorter life phenomena requires temporal sampling at about 5-minute intervals.

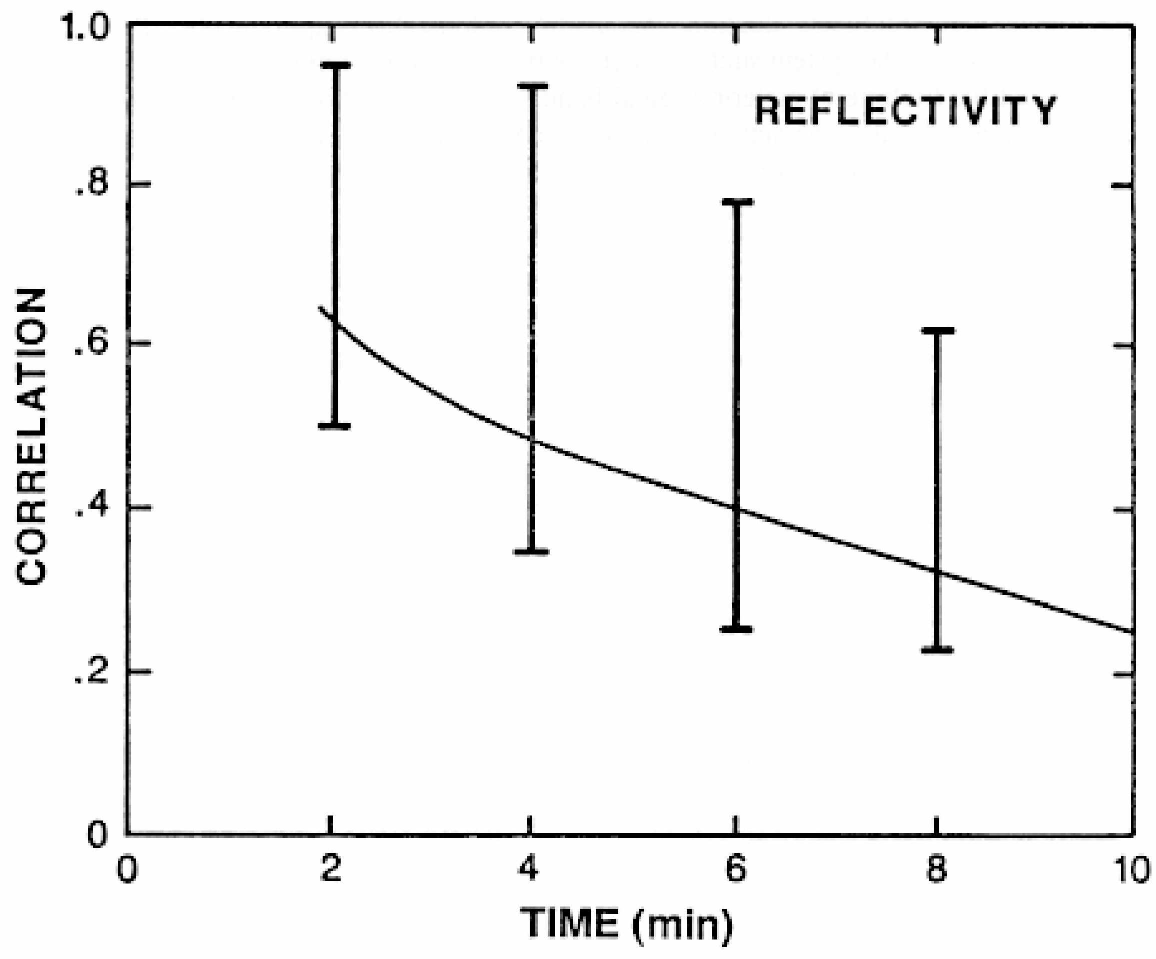

Figure 3-1a
Autocorrelation of Reflectivity with Time

Autocorrelation provides a measure of time rate of change of the measured parameter, i.e., how much new information is available as a function of the sampling rate. Vertical bars bracket the range of values reported for a variety of meteorological situations.

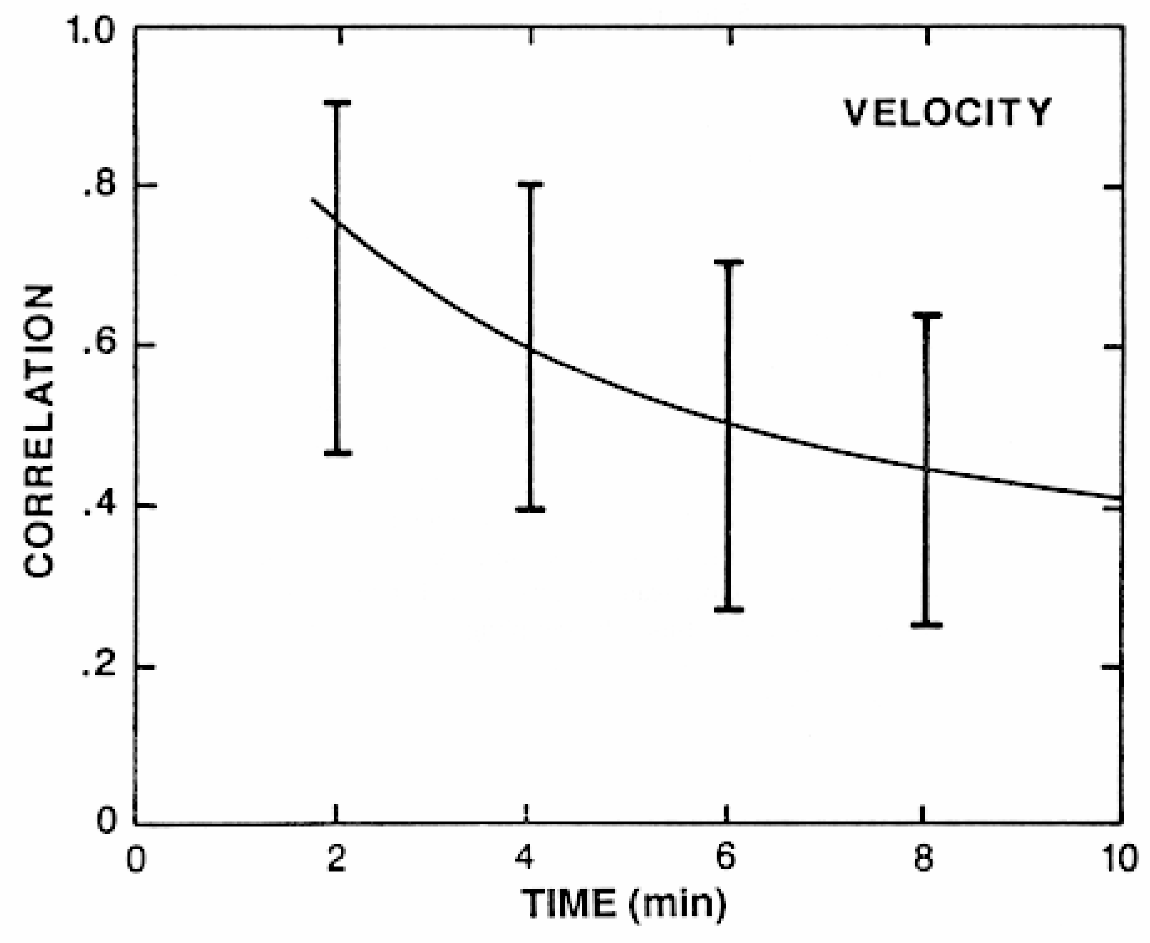

Figure 3-1b
Autocorrelation of Mean Radial Velocity with Time

Autocorrelation of mean radial velocity for a given lag is higher than reflectivity implying more redundancy for a given sampling rate. Vertical bars bracket the range of values reported for a variety of meteorological situations.

Spatial sampling requirements can also be described in terms of the general field correlation and spatial scale of weather events. The general behavior of the correlation with distance is similar to Figure 3-1 with correlation lengths (i.e., ~0.3) of about 600 m (1969 ft) for both reflectivity and velocity. However, as in the case for temporal sampling, the driving criterion is usually detection of weather events. Some common events and associated scales are also given in Table 3-1. Obviously, resolution scales of a few km must be maintained to detect the smaller events.

Table 3-1
Temporal and Spatial Sampling

Weather Event	Temporal Scale (mins)	Spatial Scale (km/nm)
Heavy Rain	5 to 60	~10/5.4
Hail	5 to 10	~5/2.7
Wind Features		
Gust Front	5 to 30	~1 x 30/0.54 x 16.2
Shear Zone	10 to 30	~1 x 10/0.54 x 5.4
Mesocyclone	15 to 60	~4/2.2 (Signature)
Convergence/ Divergence	10 to 60	~5 x 20/2.7 x 10.8 (Signature)

The resolution maintained by the polar grid associated with the basic radar data acquisition is proportional to the sampling interval (but is not, by the conventional definition, numerically equal to the sampling interval). Acquiring data by averaging over a finite interval (in either time or space or both) and outputting the average as representative of the value over the acquisition interval has the spatial transfer associated with the “zero order hold,” i.e., each cell has a data value equal to the average over the range and angle equal to the cell dimensions and zero otherwise. The signal amplitude transfer (ordinate) as a function of the radial periodicity (abscissa) of the field is shown in Figure 3-2. The half power cutoff scale, i.e., the scale that has an amplitude reduction to 70% of the large-scale value, is about 2.27 times the sampling or averaging interval. Note also the sharp cutoff of the transfer function for scales less than the half-power value. Features having a scale less than the cutoff will not be retained in the data. For the WSR-88D, this means that meteorological parameters less than 2.27 times the range averaging interval will not be retained in the data. The range averaging interval for reflectivity is 1 km (0.54 nm) out to 230 km (124 nm) and is 2 km (1.1 nm) beyond 230 km (124 nm). The range averaging interval for velocity and spectrum width is 0.25 km (0.13 nm) out to 230 km (124 nm).

A similar derivation can be made for resolution in the azmuthal direction of the polar grid. The half power cutoff is again 2.27 times the angular sampling interval, $\Delta\theta$, with a spatial cutoff length given by $r \sin \Delta\theta$. The cutoff scale in the azmuthal direction is shown in Figure 3-3.

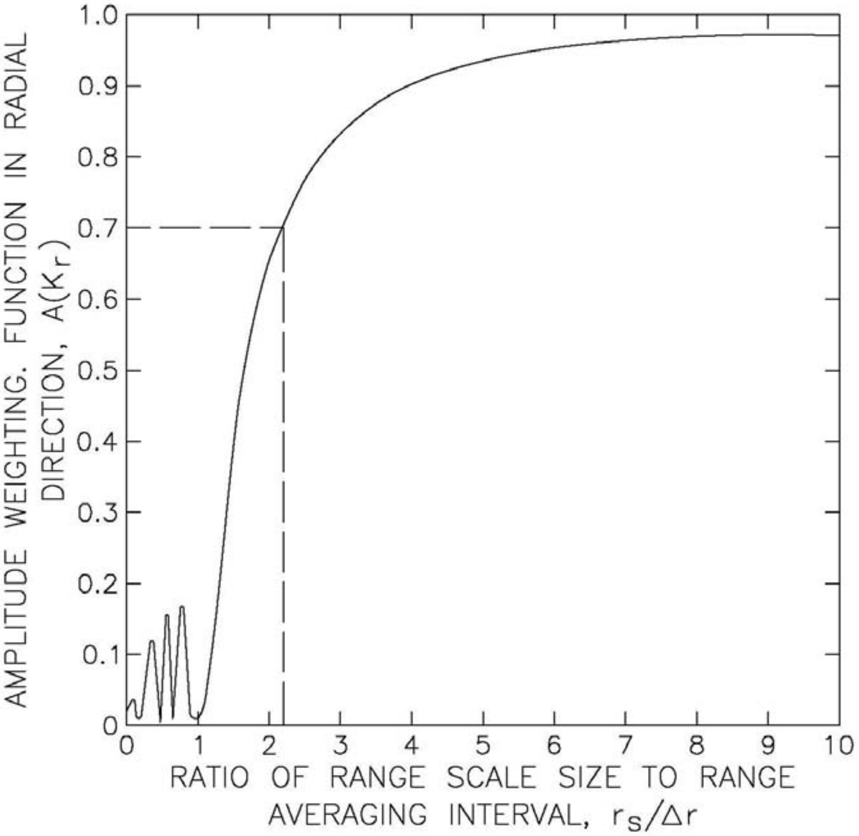

Figure 3-2
Meteorological Field Spatial Scale Amplitude Weighting Function

Transfer for sinusoidal variations with period, r_s, due to averaging over an interval, Δr. Note that variations having a period less than twice the averaging interval are not retained in the average.

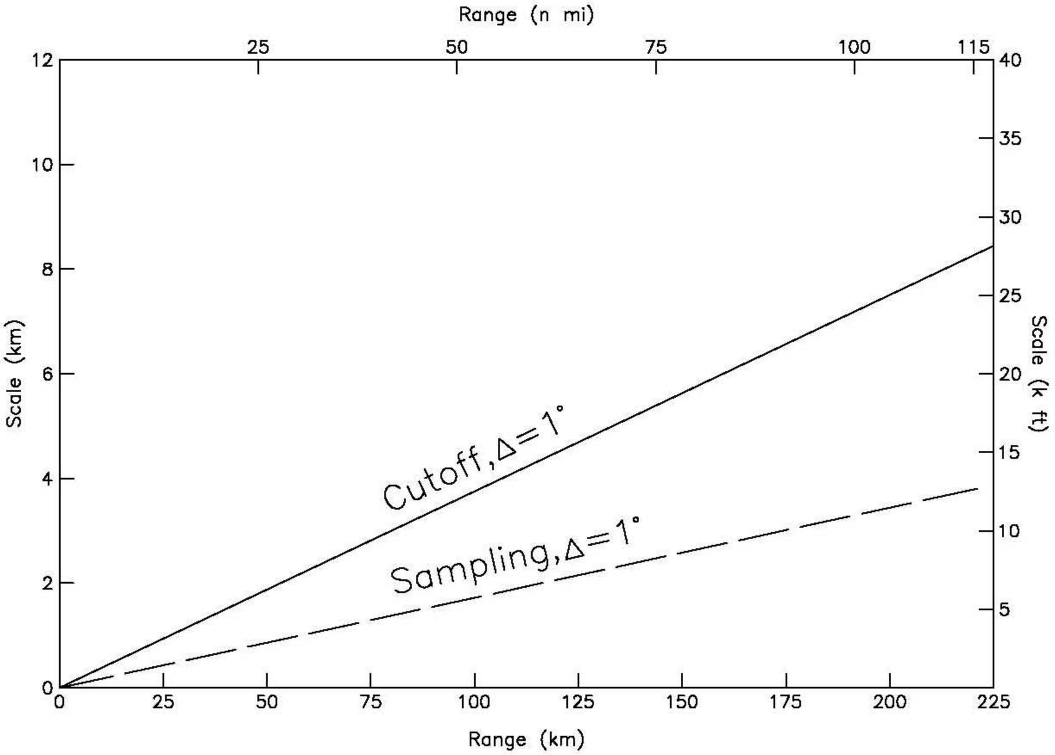

Figure 3-3
Sampling and Cutoff Scale Length

Cutoff scale for radar resolution in the azmuthal direction of the polar grid.

In summary, the sampling density limits the meteorological scale that can be resolved by the radar in that dimension. The cutoff scales are: 2.27 Δr (Δr is the range sampling interval) in the radial direction and sin (2.27 $\Delta\theta$) in the angular direction. For the WSR-88D base data, the range cutoff scale is 500 m (1640 ft) for radial velocity and spectrum width [sampled at a 250 m (820 ft) interval] and 2.27 km (1.2 nm) for reflectivity [sampled at 1 km (0.54 nm)]. Cutoff scales in the azimuth and elevation directions are range dependent and equal to r sin (2.27 $\Delta\phi$), where $\Delta\phi$ is angular increment. For 1° samples this reduces to about $4(10^{-2})$r.

Polar grid density and data throughput rate (i.e., antenna rotation rate), by determining the number of radar samples available for processing, determine the performance of the radar system in areas such as accuracy of the estimates and magnitude of the clutter suppression.

Signal coherency merely requires that the radar Nyquist co-interval, $\pm 2v_a$, be "large" compared to input signal spectrum width. This is interpreted as being such as to maintain the majority of input widths in the linear region of mean velocity estimates of performance, i.e., below the inflection point of the performance curve shown in Figure A-6.

From the cumulative distribution of spectrum widths given in Figure 3-4, it is seen that the 95-percentile spectrum width in convective storm systems (generally a worst case) is about 10 ms^{-1} (19 kts). From Figure A-6 it is seen that signal coherency and, thus, estimate accuracy deteriorate rapidly for input spectrum greater than 14 ms^{-1} (27 kts) for a Nyquist velocity of 31.5 ms^{-1} (62 kts), 11 ms^{-1} (22 kts) for v_a=25.6 ms^{-1} (50 kts), and 10 ms^{-1} (19 kts) for $v_{\mathbf{a}}$ = 22.5 ms^{-1} (44 kts). Thus, spectrum coherency is maintained for most signals at all PRTs of the WSR-88D and the variation of estimator accuracy and suppression is nominal (less than 10% of any parameter). A more important aspect of PRT selection is to minimize range folding and velocity aliasing.

Range folding and velocity aliasing are other examples of conflicting operational criteria. Minimizing velocity aliasing requires a high Nyquist velocity (high PRF) while minimizing range folding requires a low Nyquist velocity (low PRF). The automatic PRF selection of the WSR-88D is based on minimizing range folding, i.e., the system selects that PRF (from the choices available) that will minimize the area obscured by overlaid echoes. This provides maximum data recovery but has two drawbacks.

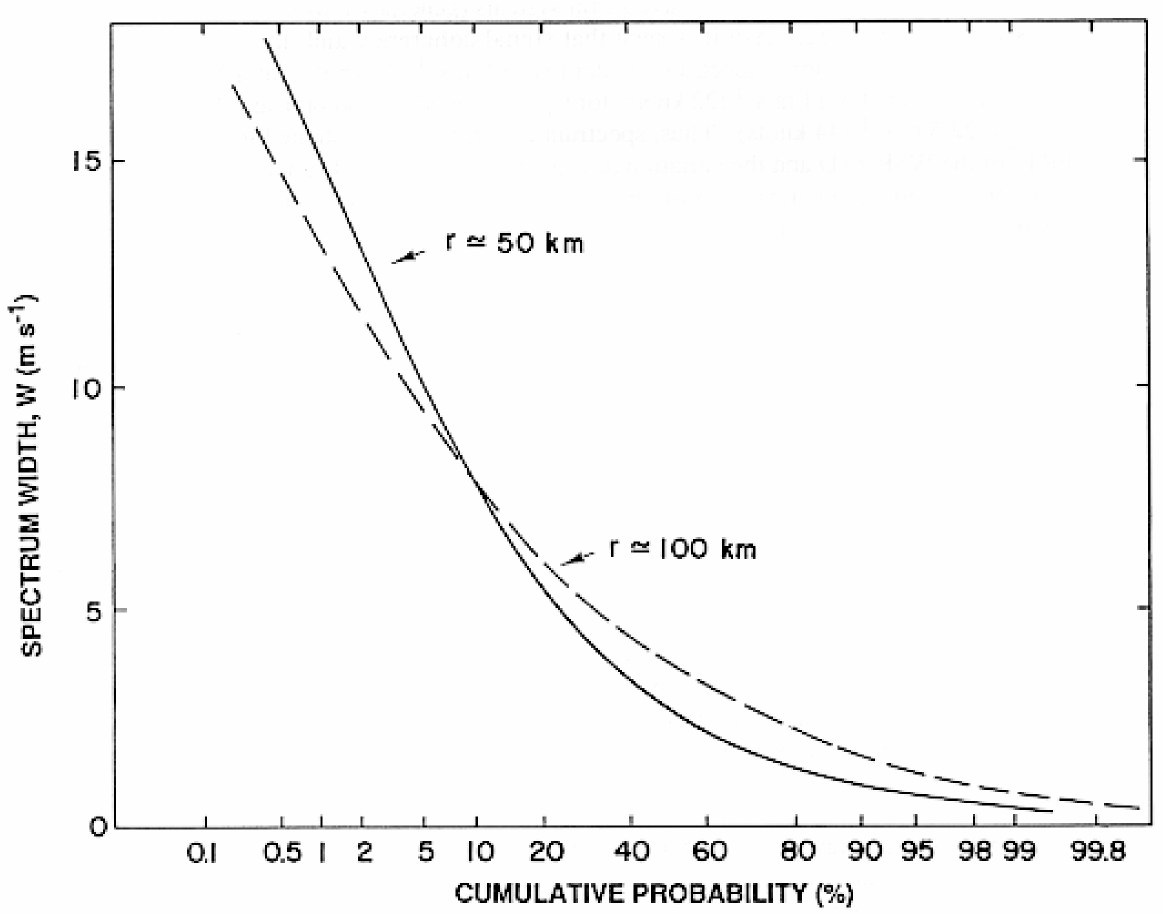

Figure 3-4
Cumulative Probability for Convective Storms

The probability that the spectrum width is larger than the ordinate value, for convective storms at 50 km and 100 km. The median value, that value for which half of the widths are larger and half the widths are smaller, is about 4 ms^{-1}.

Minimizing the area obscured by overlaid echoes will tend to utilize the maximum system PRT and thus the minimum Nyquist velocity that, in turn, will increase the velocity aliasing for a given situation. From the velocity magnitude percent of occurrence shown in Figure 3-5 it is seen that some aliasing will occur at any of the PRTs available (without using Volume Coverage Pattern (VCP) 121 and the Multiple PRF Dealiasing Algorithm, MPDA). It is also evident from the steep slopes of the velocity distribution that velocity aliasing will change rapidly with a change in Nyquist co-interval. For the Nyquist co-intervals available and without reliance on an alternate VCP such as VCP 121, the percent aliasing will increase about an order of magnitude as the Nyquist co-interval is decreased from ± 31 ms^{-1} to ± 22.5 ms^{-1} (± 60 to ± 44 kts). Without using VCP 121 (and the MPDA), there will be situations where the user must assume manual control of the PRT in order to achieve optimum data recovery. On the other hand, the user can opt to use VCP 121 to minimize range overlaid echo while at the same time minimizing velocity aliasing. In fact, this is the preferred solution. Another occasional drawback of minimizing the area obscured is loss of high-interest data due to the minimal residual obscuration. In this case the user will again need to assume manual control and select the PRT such as to clear the region of interest. But even this occurrence will be greatly minimized through use of VCP 121.

In summary, the WSR-88D estimate accuracy and clutter suppression performance, as a function of antenna speed for a 1° azimuth sampling, is shown in Figure 3-6. Accuracy of the estimates and suppression is also dependent on the transmitter PRT through its influence on signal coherency.

3.3 Data Recovery by Ground Clutter Suppression. Prior to calculation of reflectivity, R, velocity, v, or spectrum width, W, return signals from ranges within the radar ground pattern are passed through devices that remove most of the signal. These clutter suppressors take advantage of statistical properties returned from stationary or clutter targets, which are usually different from the meteorological signals, in order to reject the clutter. The two most important properties are mean Doppler velocity and spectrum width or signal correlations.

Ground clutter is usually stationary, has near zero mean Doppler velocity, and has a small dispersion or spectrum width. Typical clutter spectrum widths range from <0.1 ms^{-1} (<0.2) to about 0.5 ms^{-1} (1). This is much smaller than the widths of most meteorological signals that have median values ranging from about 1 ms^{-1} (2 kts) for snow and stratiform rain to about 4 ms^{-1} (8 kts) for convective storms.

Thus, as can be visualized from the transfers shown in Figure 3-7, a band-reject filter with a notch around zero velocity will reject most of the clutter without seriously affecting the meteorological signal so long as the mean velocity of the reflecting particles is several times the notch width.

The WSR-88D Doppler channel clutter suppressor is equipped with selectable notch width ranging from about 0.5 ms^{-1} to 2.0 ms^{-1} (1 to 4 kts) with the filter controlled by a site selectable clutter map. In the Doppler channel, the unit will deliver a peak suppression of about 50 dB and an average suppression of about 40 dB.

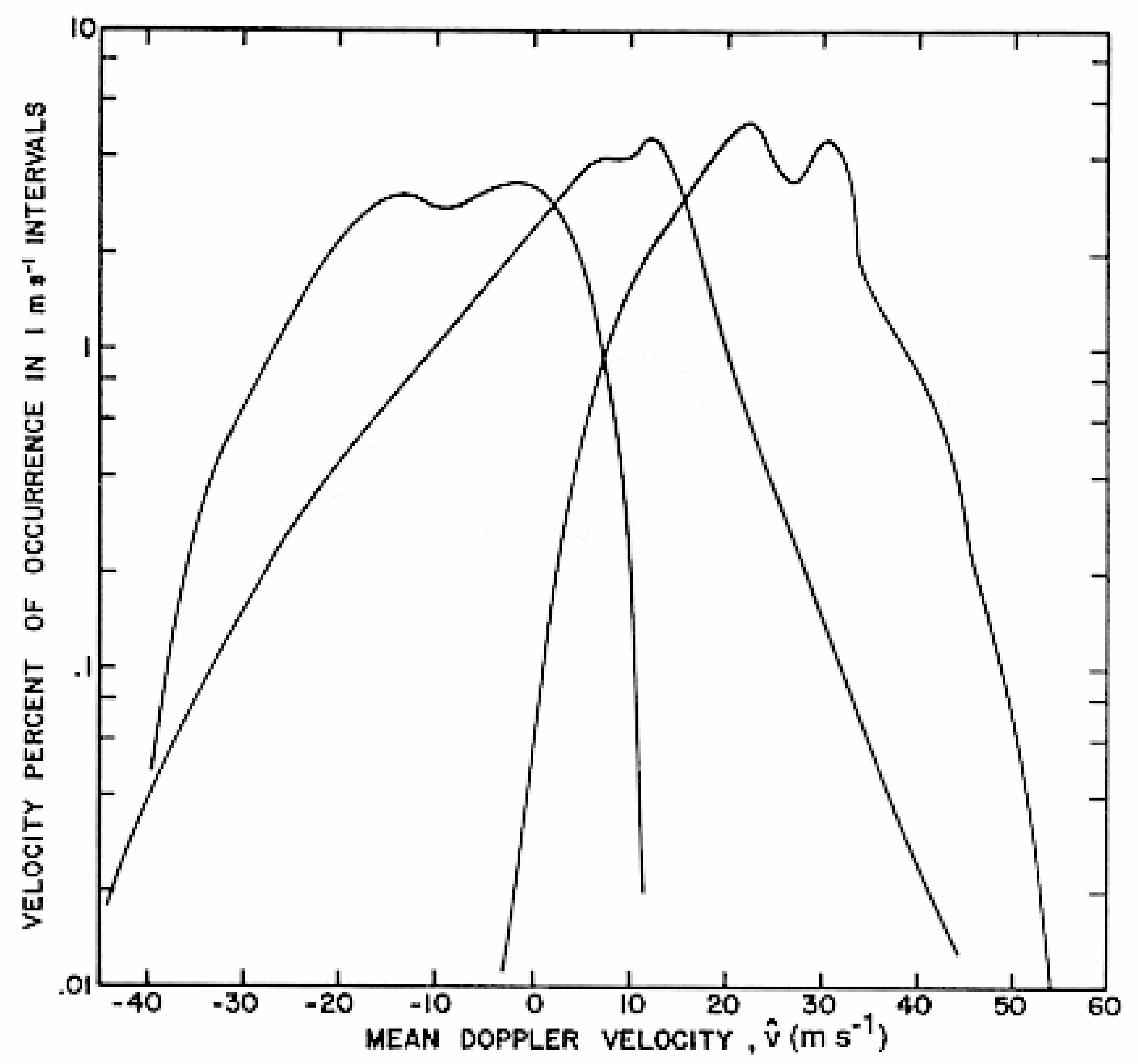

Figure 3-5
Histograms of Velocity for Three Tornadic Storms

The storm translation velocity has been removed.

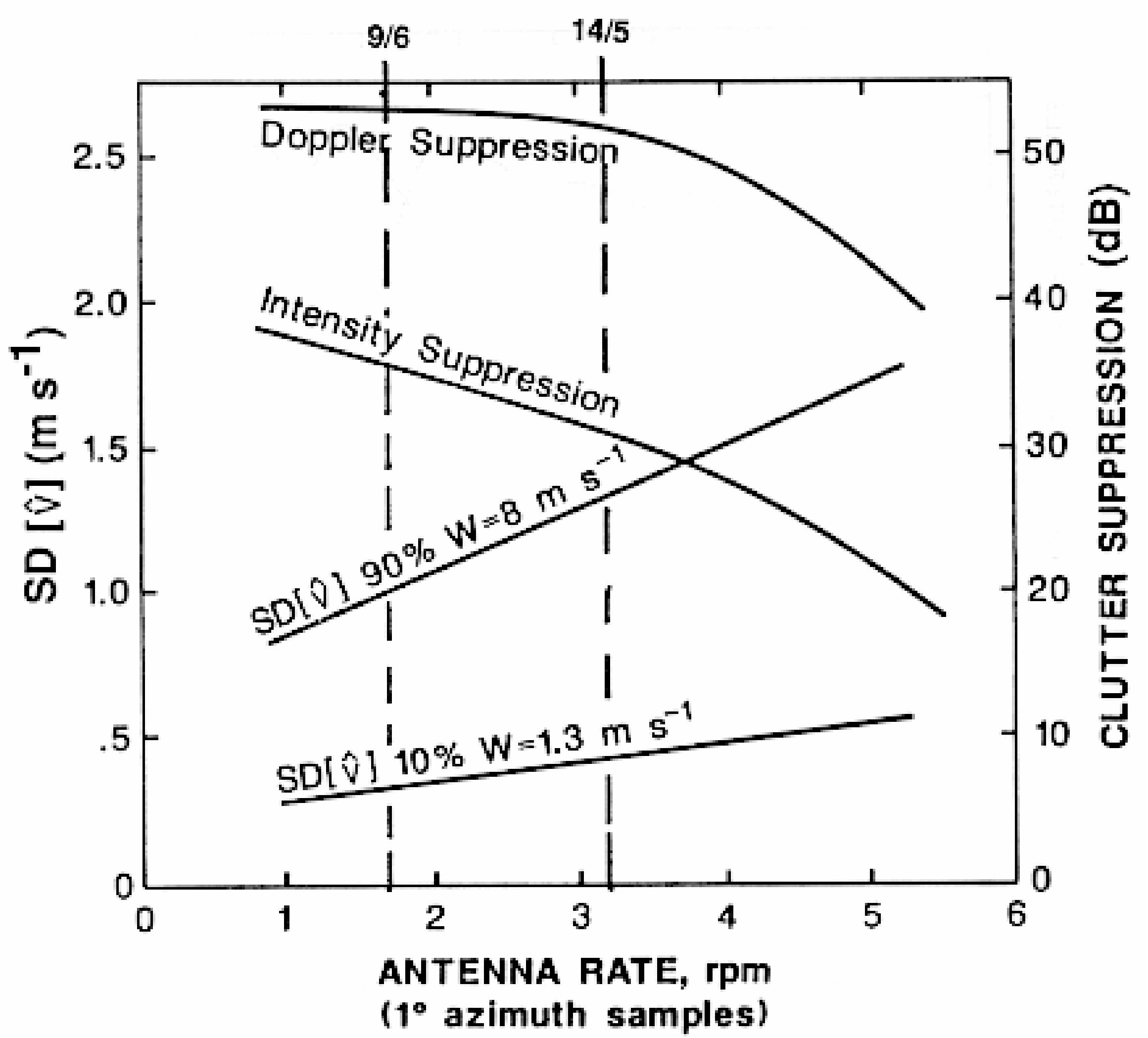

Figure 3-6
Standard Deviations of the Velocity Estimates
and Ground Clutter Suppression

Performance as a function of antenna speed with a one degree azimuth sample. Vertical lines intersect performance at throughput rates of 9 unique elevations in 6 minutes and 14 unique elevations in 5 minutes. Spectrum widths, W, of 1.3 ms^{-1} and 8 ms^{-1} are the 10 and 90 percentile widths expected in convective storms.

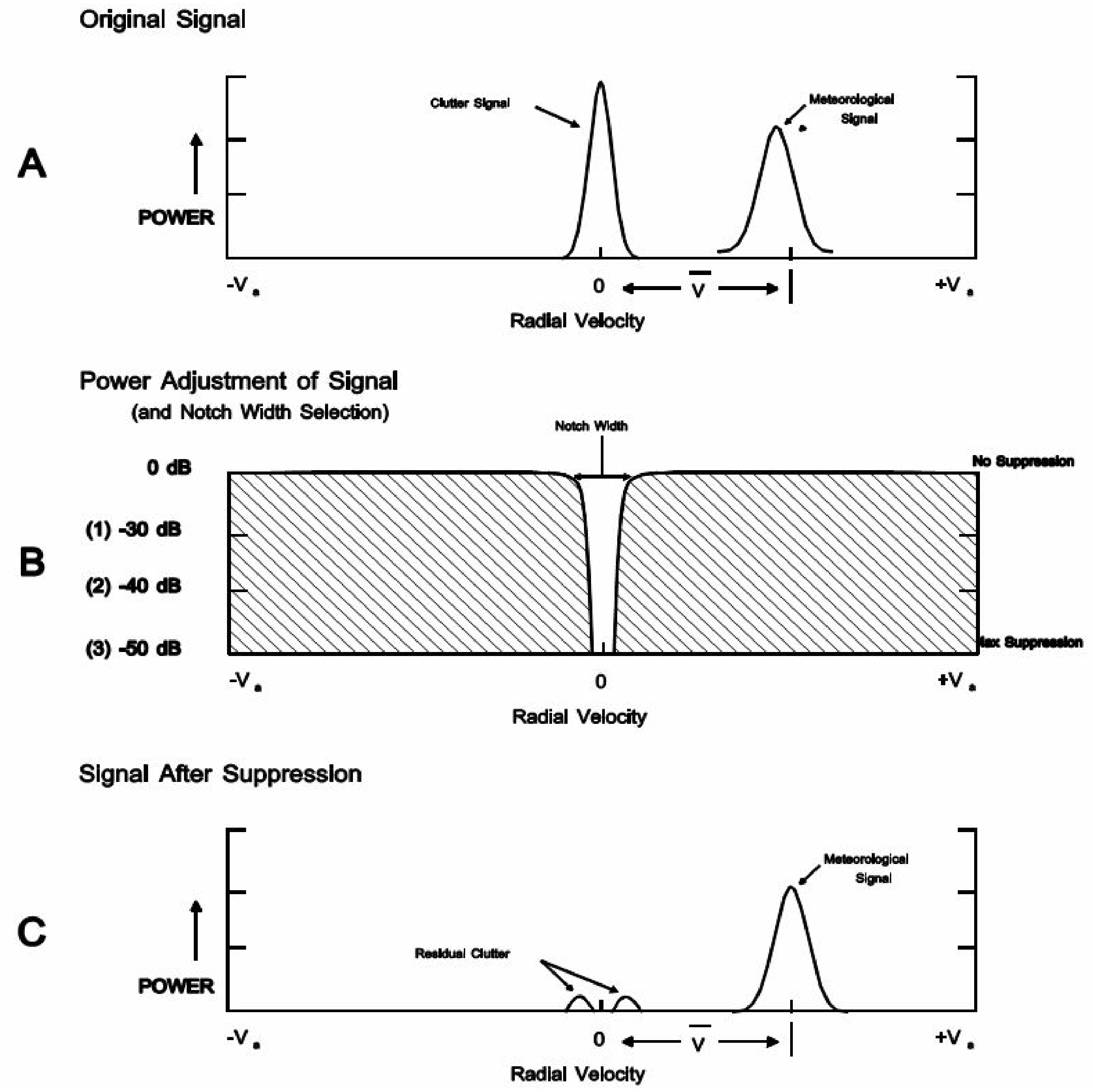

Figure 3-7
Simple Conceptual Model of Legacy Clutter Filter

(A) A depiction of the input power for a given range bin. The clutter signal has a radial velocity centered around zero and the meteorological signal is offset from zero due to its radial velocity. (B) Represents the clutter filter with a notch width centered on zero radial velocity. The scale represents the amount of power reduction, from 0 dB (no power reduction) to -50 dB (maximum power reduction), applied within the notch width. (C) A diagram of the resulting power after the algebraic addition of the signal from A and the power reduction factor from B (A+B=C). From Chrisman and Ray (2005).

Efficiency of the clutter removal depends on the notch depth and the relative width of the notch and clutter signal. In general, the wider the notch, the larger the clutter rejection is. However, in the Doppler channel, wider notches result in larger minimum velocities that will be passed unaffected. If the meteorological signal has a mean velocity at or near zero, a significant portion of this signal will also be rejected. The magnitude of rejection is generally less for the meteorological signal than a clutter signal of comparable strength since the width of the meteorological signal is usually much larger than the notch width. However, in situations where the width of the meteorological signal is small, such as snow or stratiform rain, rejection of the meteorological signal along the zero isotach can result in serious spectrum distortion or complete signal loss. This effect is shown in Figure 3-8, which gives the minimum usable velocity as a function of the suppression magnitude.

Another consideration is that residue from a strong clutter signal, in the presence of a weak meteorological signal can produce a significant bias in the signal estimate. Estimates of signal power, mean velocity, and spectrum width are all affected by the residue but the effect on the mean velocity estimate is probably the more important. Bias effects of clutter or clutter residue are shown in Figure 3-9 where it is seen that, if the residue power is 10 dB below the signal power, the maximum bias is about 1 ms^{-1} (2 kts--about the same as the standard deviation of the estimate). If the residue power is within 5 dB of the signal power, the bias is 2.5 ms^{-1} (5 kts) and probably unacceptable.

The clutter suppression in the reflectivity channel is of the same design as the Doppler channel, i.e. a band-reject filter with the notch around zero velocity.

The worst case, i.e., zero mean velocity, intensity estimate bias, as a function of spectrum width, is shown in Figure 3-10 where it is seen that this bias can be appreciable for spectrum widths less than about 2 ms^{-1} (4 kts). For most convective meteorology, the bias is small (less than 1 dB) and can be accounted for with a connection based on the spectrum width associated with the type of meteorological situation.

3.4 Propagation Considerations. In free space, radio waves travel in straight lines. In the Earth's atmosphere, however, electromagnetic waves are generally bent or curved downward due to the variation with height of the index of refraction. Index of refraction here is defined as the ratio of the velocity of propagation in free space to the velocity of propagation in the atmosphere.

Effects of refraction are the introduction of errors in measurement of radar range and elevation angle.

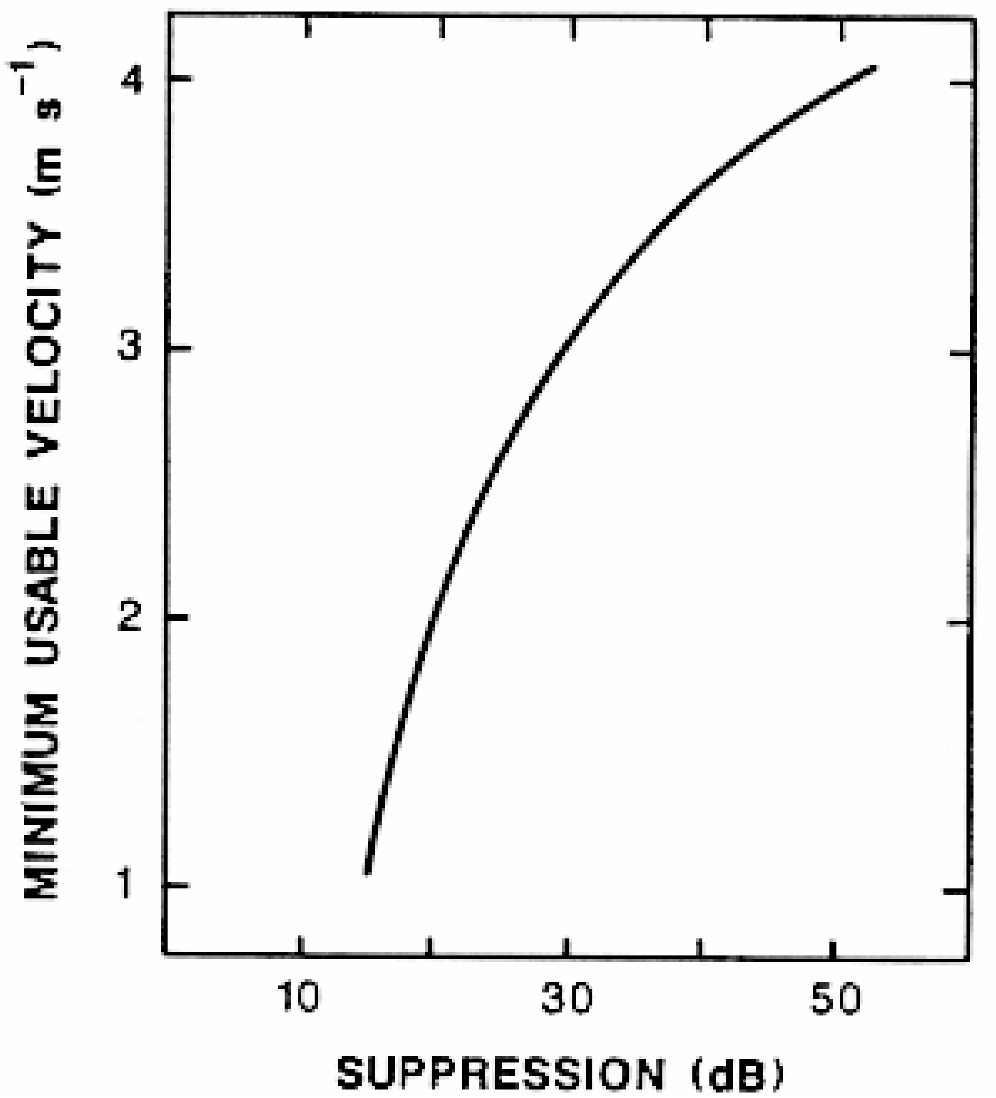

Figure 3-8
Minimum Usable Velocity Due to Suppressor Rejection

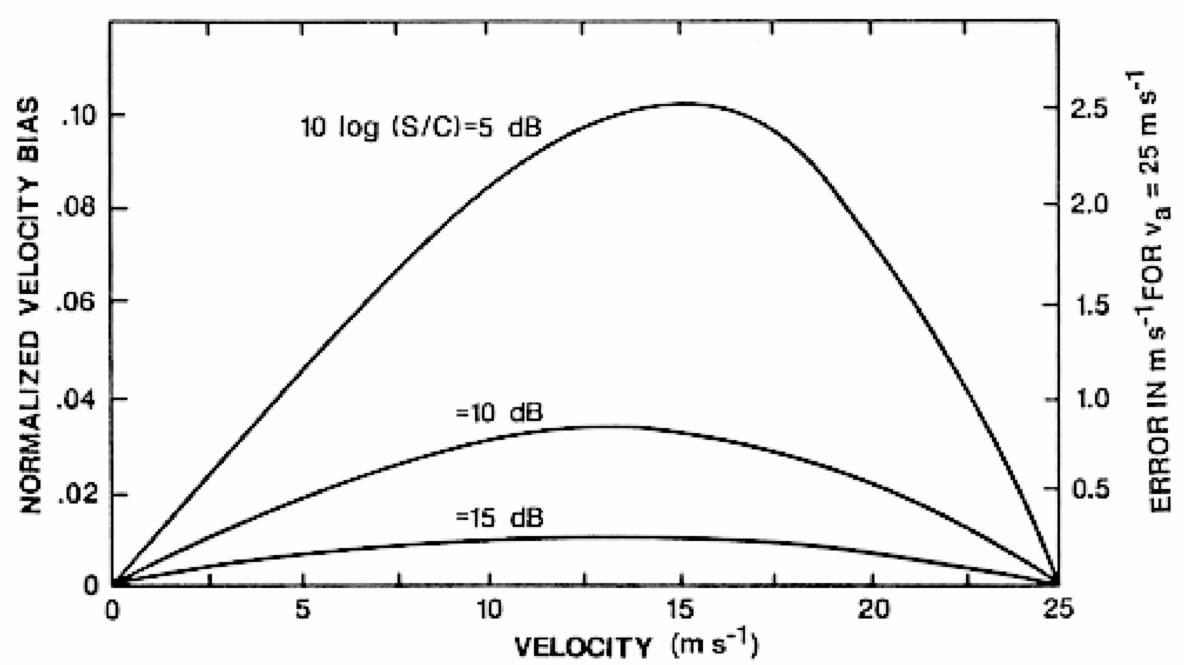

Figure 3-9
Bias of the Velocity Estimate Due to Clutter or Clutter Residue Signal

The bias for unambiguous velocities other than 25 ms^{-1} (13 kts) is equal to the normalized bias times the unambiguous velocity. (S/C = Ratio of Signal Power to Clutter Power)

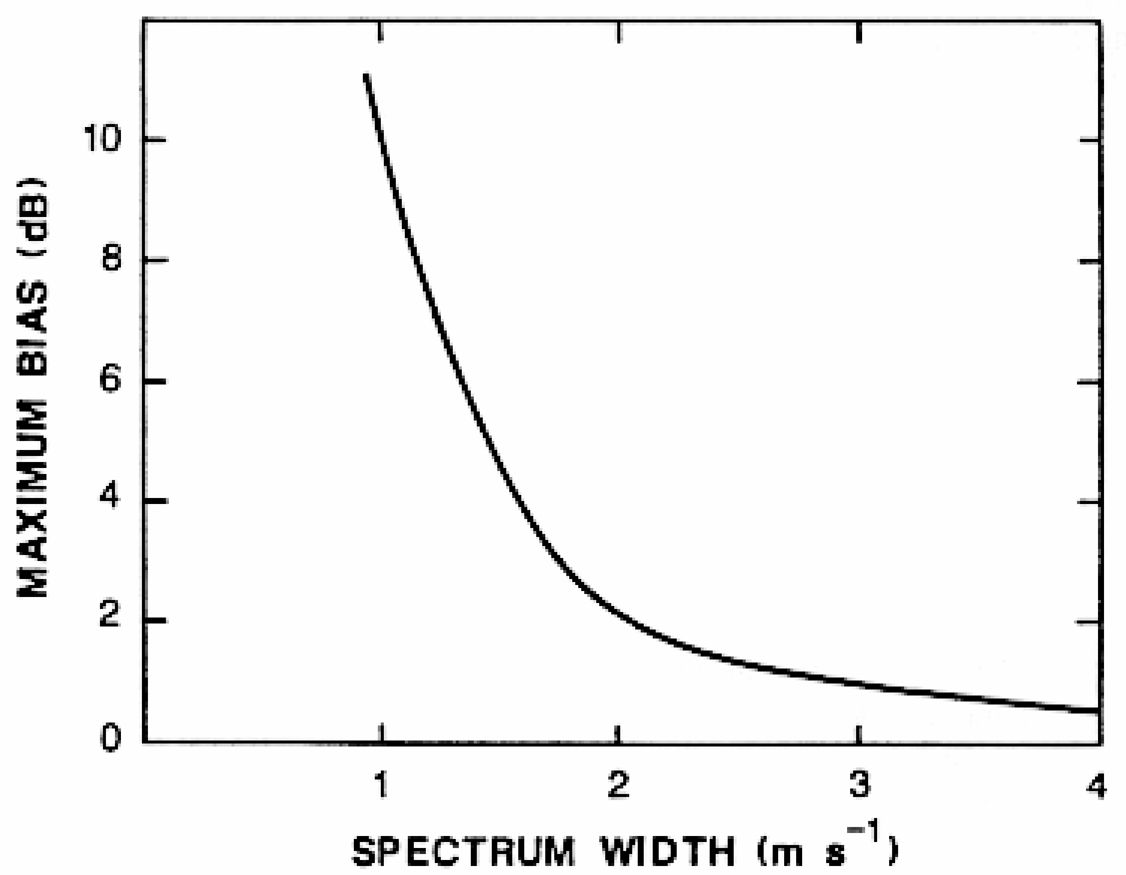

Figure 3-10
Bias of the Reflectivity Estimate Due to Suppressor Rejection as Related to Spectrum Width

Typical spectrum widths (median values) are 4 ms^{-1} (8 kts) for convective storms and 1 ms^{-1} (2 kts) for stratiform rain and snow.

3.4.1 Standard Propagation. At microwave frequencies, the index of refraction of air becomes smaller with decreasing pressure, smaller with decreasing moisture, and larger with decreasing temperature. In the standard atmosphere all three of these variables usually decrease with increasing altitude, but the increase in the index due to decreasing temperature is not sufficient to offset the decrease in the index due to decreasing pressure and moisture. The net result is an almost uniform decrease in refractive index with height up to altitudes of about 7600 m (24,934 ft) under normal conditions resulting in a beam propagation path that is curved downward but with less curvature than the Earth's surface (Figure 3-11).

The index of refraction, *n*, is a function of temperature, pressure, and water vapor and is usually expressed indirectly in a form such as:

$$(n-1)\times 10^{6} = N = \frac{77.6P}{T} + \frac{3.73\times 10^{5}\varepsilon}{T^{2}}$$

where:

N = Refractivity (unit of convenience)
T = Air temperature, °K
P = Pressure, millibars
ε = Partial pressure of water vapor, millibars

The first term of the above is the density applicable at all frequencies and the second term accounts for the polarization of water vapor at radio frequencies. Since pressure and water vapor decrease rapidly with height, the index of refraction normally decreases with height. In a standard atmosphere the index decreases at a rate of about $4(10^{-8})\ \mathrm{m}^{-1}$ in altitude. The typical value of n at the Earth's surface is of the order of 1.0003.

The classical method of accounting for refraction in radar-height computations is to replace the actual Earth radius, a, by an equivalent Earth with radius, k • a, and to replace the actual atmosphere by a homogeneous atmosphere in which electromagnetic waves travel in straight lines. It can be shown that the value of k that will result in straight ray paths is:

$$k = \frac{1}{1 + \frac{a}{n}\frac{dn}{dh}}$$

where dn/dh is the rate of change of the refractive index with height. Normally the vertical gradient of the refractive index is negative and, if it is assumed to be constant, the value k is 4/3. Because of its convenience and good accuracy for the normal atmosphere, the 4/3 Earth model is widely used. It is, however, only an approximation that may or may not be satisfactory in all applications.

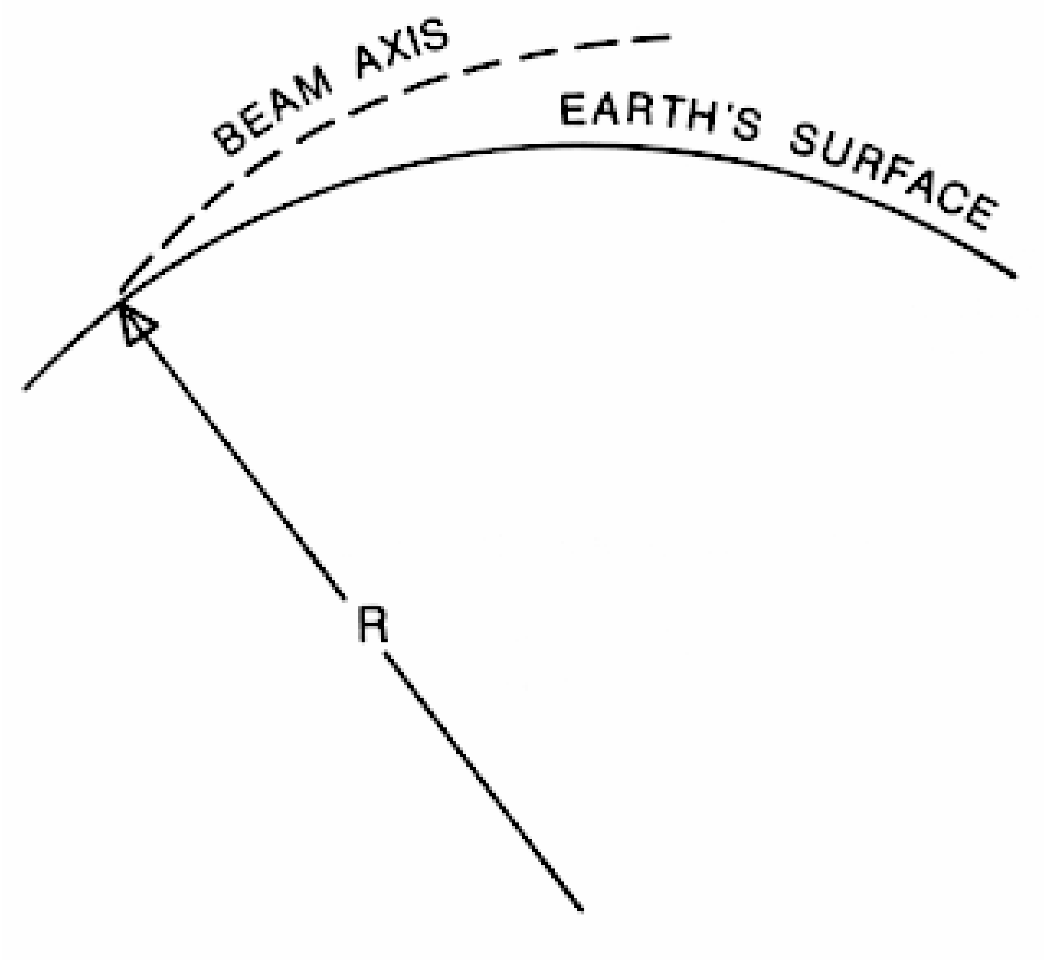

Figure 3-11
Beam Propagation Path Due to Refraction

Assuming standard atmospheric conditions, the nominal radar beam axis is schematically illustrated.

A similar approach to height determination is the use of nomograms such as the one given in Figure 3-12. Nomograms such as this account for the mean Earth curvature but not local terrain variation and assume a constant linear decrease of the refractive index with height.

A more rigorous model of the refractivity height function has been developed by the National Bureau of Standards, Central Radio Propagation Laboratory (CRPL).

The normalized refractive index, as a function of height in this model, is given by: $N = N_s \exp[-c_e(h-h_s)]$ where N_s and c_e are constants and h_s is the surface or initial height. This is referred to as the CRPL exponential reference model. The constants may be specified from surface refractivity. Values of $N_s = 313$ and $c_e = 0.1439$ are average values for the United States.

The differences in heights predicted by the 4/3 Earth or linear refractive index vertical gradient and the exponential gradient are usually negligible for the WSR-88D, i.e., small compared to radar beam dimension at the ranges of interest. A comparison of heights based on the two models is tabulated in Table 3-2.

Table 3-2
Height Based on Exponential Minus Height Based on 4/3 Earth Curvature

Elevation Angle	Slant Range 185 km/100nm		Slant Range 370 km/200nm	
	meters	feet	meters	feet
0	30	100	366	1200
0.5	61	200	610	2000
1.0	91	300	793	2600
2.0	152	500	1128	3700
4.0	244	800		
Radar two-way beam width	2257	7400	4511	14800

Ranging errors due to beam bending are also usually negligible (small compared to sample volume depth, Appendix A). This is shown in Figure 3-13 based on the CRPL model.

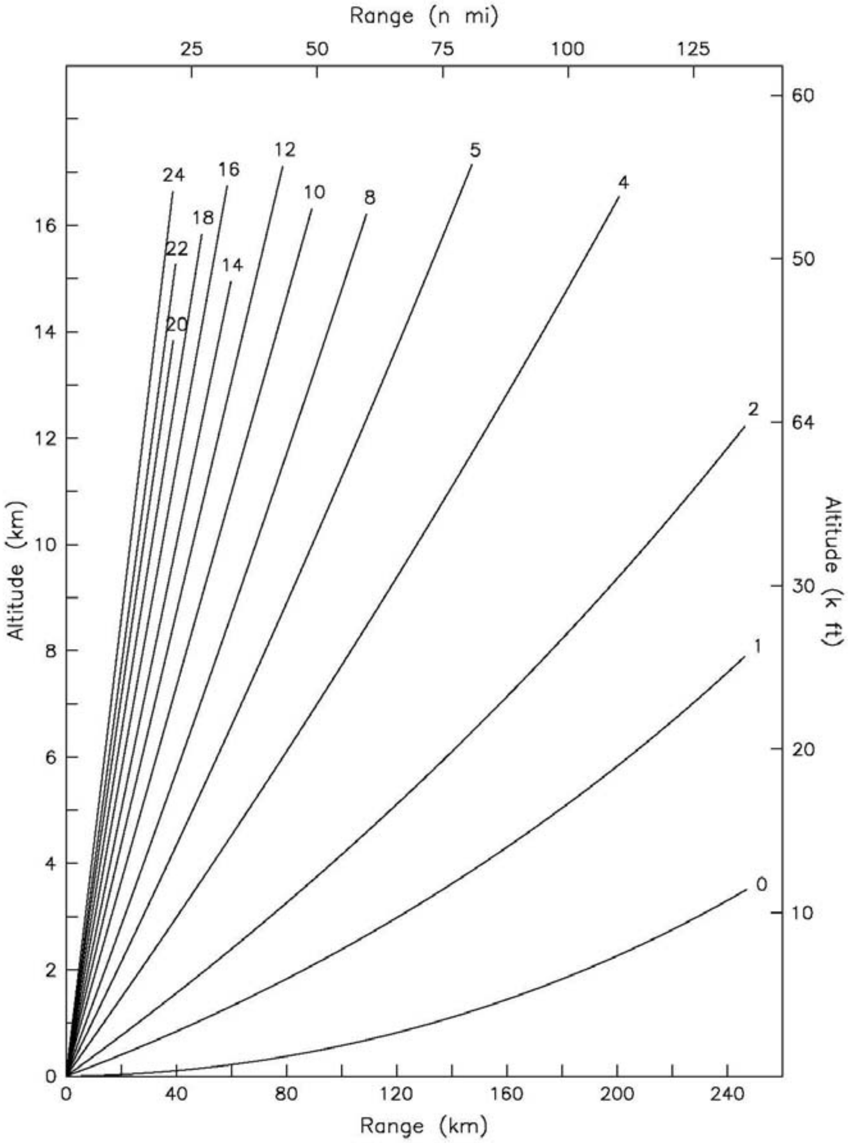

Figure 3-12
Range-Radar Beam Altitude Nomogram

(Standard Atmosphere)

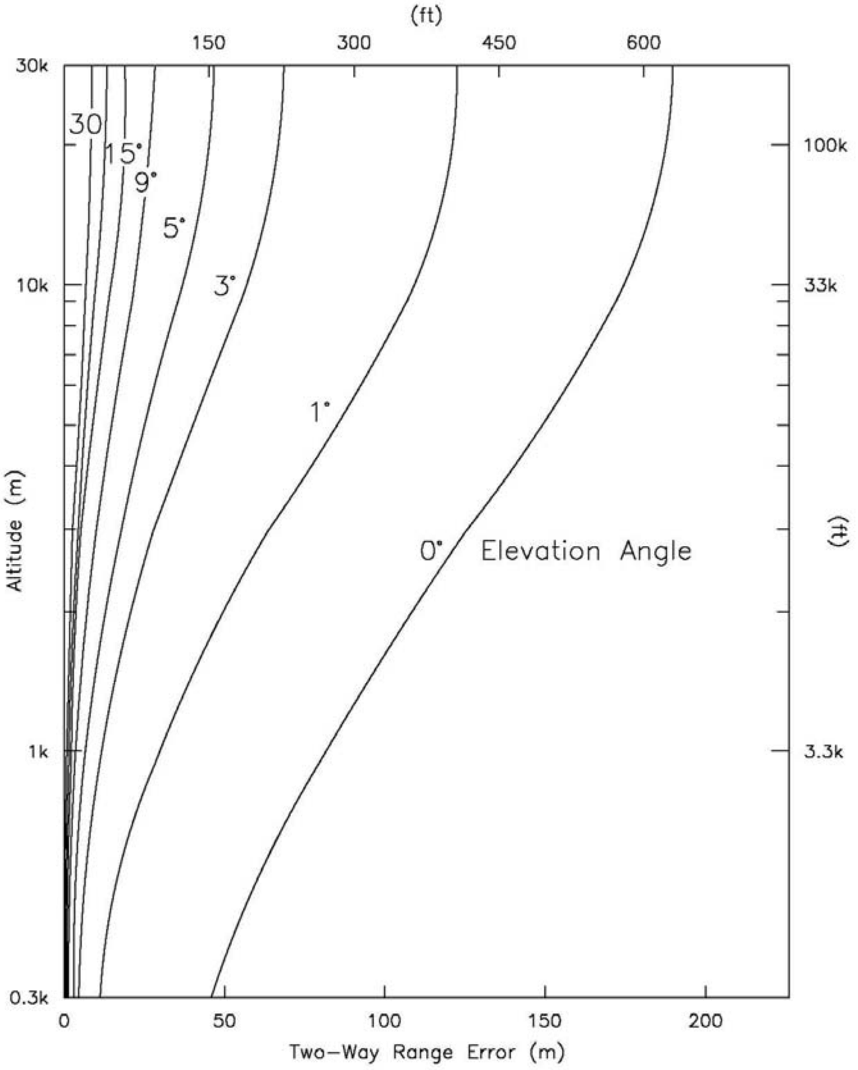

Figure 3-13
Range Error

Range error as a function of echo altitude and elevation angle due to beam bending in a standard atmosphere (CRPL model).

3.4.2 Anomalous Propagation. Normal atmospheric propagation conditions, however, may not be present at all times. In some cases the temperature may first increase with height and then decrease (temperature inversion), or the moisture content of the atmosphere may decrease very sharply close to the Earth's surface, or a combination of these atmospheric variations may occur such as to substantially perturbate the standard refractive index-height dependency. These anomalous conditions may modify the atmosphere in such a way as to provide a "duct," or propagation path, whereby the radio waves are bent substantially more than in the standard atmosphere and, in some cases, bent enough to intercept the Earth's surface. (While sub-refraction [beam bending less than standard] also occurs in the atmosphere, that condition does not result in anomalous propagation and is not treated here.)

In radio wave propagation work, the characteristic used to predict the probable degree of bending of the radio wave is the modified index of refraction curve. The modified index of refraction, M, combines the refractive index contribution from pressure, temperature, and moisture into an index-height relationship and subtracts this relationship from the standard atmosphere index-height relationship. Thus, M provides a measure of beam bending relative to the standard propagation.

Examples of temperature and specific humidity height distribution and the associated curves are given in Figure 3-14. Curve A is the distribution for the standard condition. Curves B, C, and D illustrate conditions under which anomalous propagation (AP) is likely to occur.

The condition shown in B is the most common duct-producing situation and is usually the result of one of the following meteorological conditions:

- Nocturnal radiation causing a temperature inversion near the ground and a sharp decrease in moisture with height.
- A flow of warm moist air over cooler surfaces, especially water, resulting in a cooling of the air in the lower layers and the addition of moisture.
- A diverging downdraft under a thunderstorm resulting in a temperature inversion in the lower few thousand feet as the cool air spreads out from the base of the storm. This is infrequent but can be very important because of its proximity to the storm.

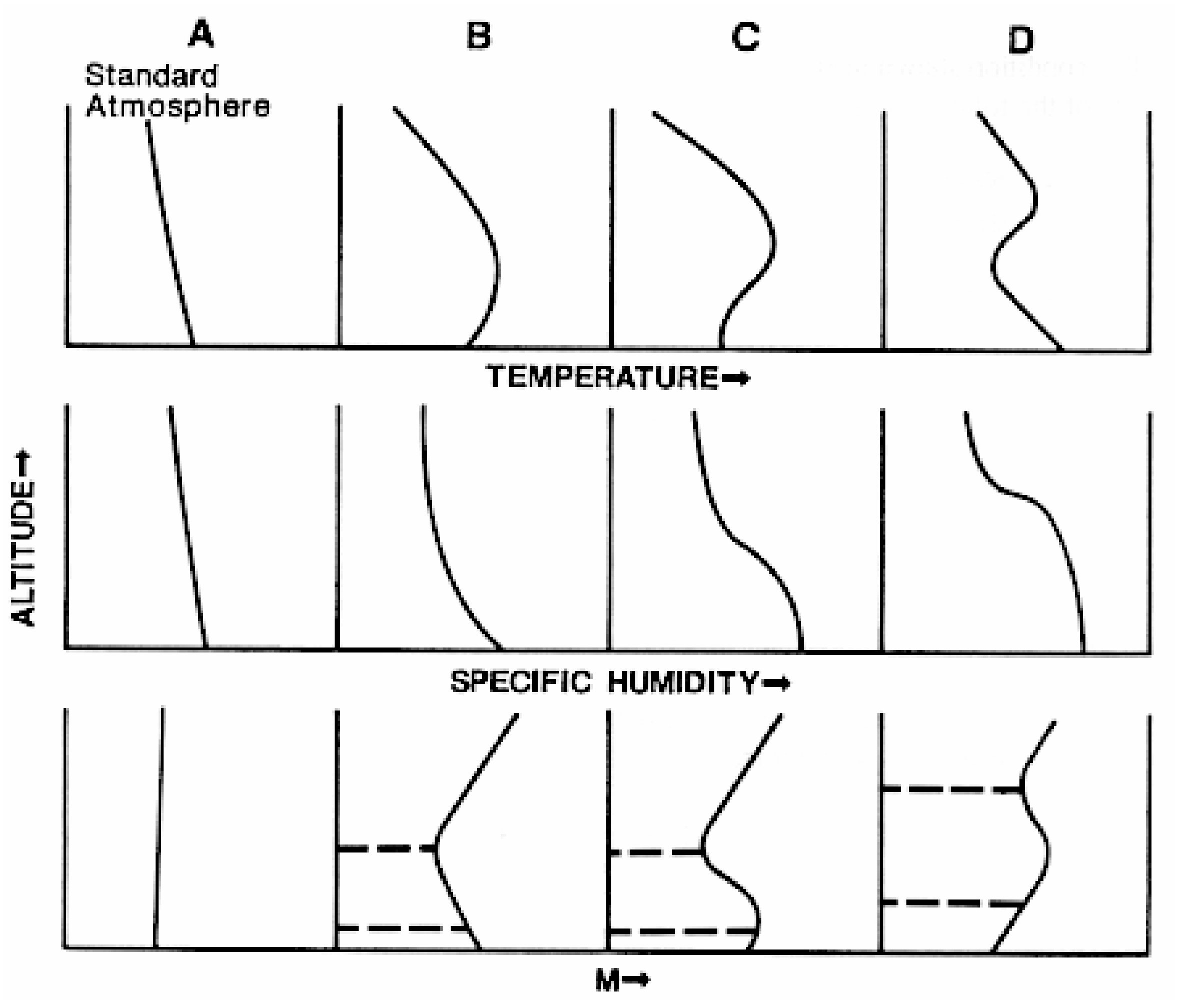

Figure 3-14
Meteorological Conditions Likely to Result in Anomalous Propagation

M is the modified index of refraction or deviation of beam bending from that under standard conditions. The duct, where ducting occurs, is shown by dashed lines. See text for a description of the meteorological conditions that can produce the profiles shown in B, C, and D.

Conditions shown in Curve C are less frequent than those shown in B and are sometimes associated with a low-level inversion through which the specific humidity decreases sharply. Meteorological conditions that can produce these are:

- A subsidence inversion close to the ground especially when the air close to the ground is initially very moist.
- A flow of warm moist air over a cool body of water by turbulent winds. Turbulence can cause the inversion to be lifted above the surface and a nearly adiabatic lapse rate in the lower layers.

The ducts shown in B and C occur at low levels and are of most concern to ground-based radars such as the WSR-88D. Conditions shown in Curve D result in an upper-level duct that seldom result in sufficient bending of the beam to cause interception with the Earth's surface. This is, however, a source of antenna pointing error.

The anomalous signal return is from the Earth's surface and, therefore, has statistical properties very similar to the normal clutter return. The significant differences in the normal clutter and the anomalous clutter signals are a slightly larger width and smaller reflectivity values associated with the anomalous signal. Generally, the AP will be removed by the ground clutter suppressor if the suppressor is active in the AP region. Activation of the suppressor may require manual intervention since AP will normally occur outside the ground clutter map.

Radar signals or echo properties that can be used to identify AP (in conjunction with knowledge of the meteorological situation conducive to the occurrence) are:

- Small temporal variability of the echo in reflectivity, velocity, and spectrum width.
- Large irregular areas of zero velocity.
- A larger number of small-scale features, particularly high-intensity cores in the reflectivity field.
- Vertical variability.
- Large reflectivity gradients, i.e., $dZ/d(r,\theta) > 20$ dB km^{-1}.
- Large gradients in the spectrum width field.

Occurrence of these features should be used in the decision to activate the intensity and Doppler suppressors, in the region outside the clutter map.

3.5 Signal Attenuation.

3.5.1 Atmospheric Attenuation.

3.5.1 Atmospheric Attenuation. Any atmosphere, standard or non-standard, is an attenuating medium at a 10 cm wavelength. In the clear atmosphere, an incident frequency of 3 GHz is well below the attenuation resonances associated with water vapor (first maxima at f $\simeq$ 23 GHz) or oxygen (first maxima at f $\simeq$ 62 GHz) but even the small attenuation associated with this wavelength can accumulate to significant values over the maximum range coverage of the WSR-88D.

Two-way attenuation by the International Civil Aviation Organization (ICAO) standard atmosphere is shown in Figure 3-15 and is accounted for in the WSR-88D signal intensity calculation.

Primarily due to oxygen and water vapor, the loss, L, (where L_a is the total loss) as a function of elevation angle, ϕ_e, is given approximately by:

$$L_a \cong L(\phi_e)\left[1 - \exp\left[-\frac{r}{r(\phi_e)}\right]\right]$$

$$L(\phi_e) = 0.4 + 3.45\exp\left[-\frac{\phi_e}{1.8}\right]$$

$$r(\phi_e) = 27.8 + 154\exp\left[\frac{\phi_e}{2.2}\right]$$

For $\lambda = 10$ cm and r <200km (108 nm), $\phi_e < 10°$, the above approximates the theoretical loss to within 0.2 dB.

3.5.2 Rainfall Attenuation. Signal attenuation due to rainfall is generally less than 1 dB and is accounted for in the WSR-88D.

For a temperature of 0°C and a modified Marshall-Palmer drop-size distribution, the two-way attenuation, K_p, at $\lambda = 10$ cm is given by:

$$K\,p = 6(10^{-5})\,Z_e^{\mathbf{0.62}}\ \text{dB km}^{-1}$$

and shown graphically in Figure 3-16.

Two-way attenuation will exceed 0.1 dB km^{-1} at reflectivity greater than 53 dBZ and, on occasion, the total attenuation can exceed several dB. Any correction for this effect must be made subjectively by the user.

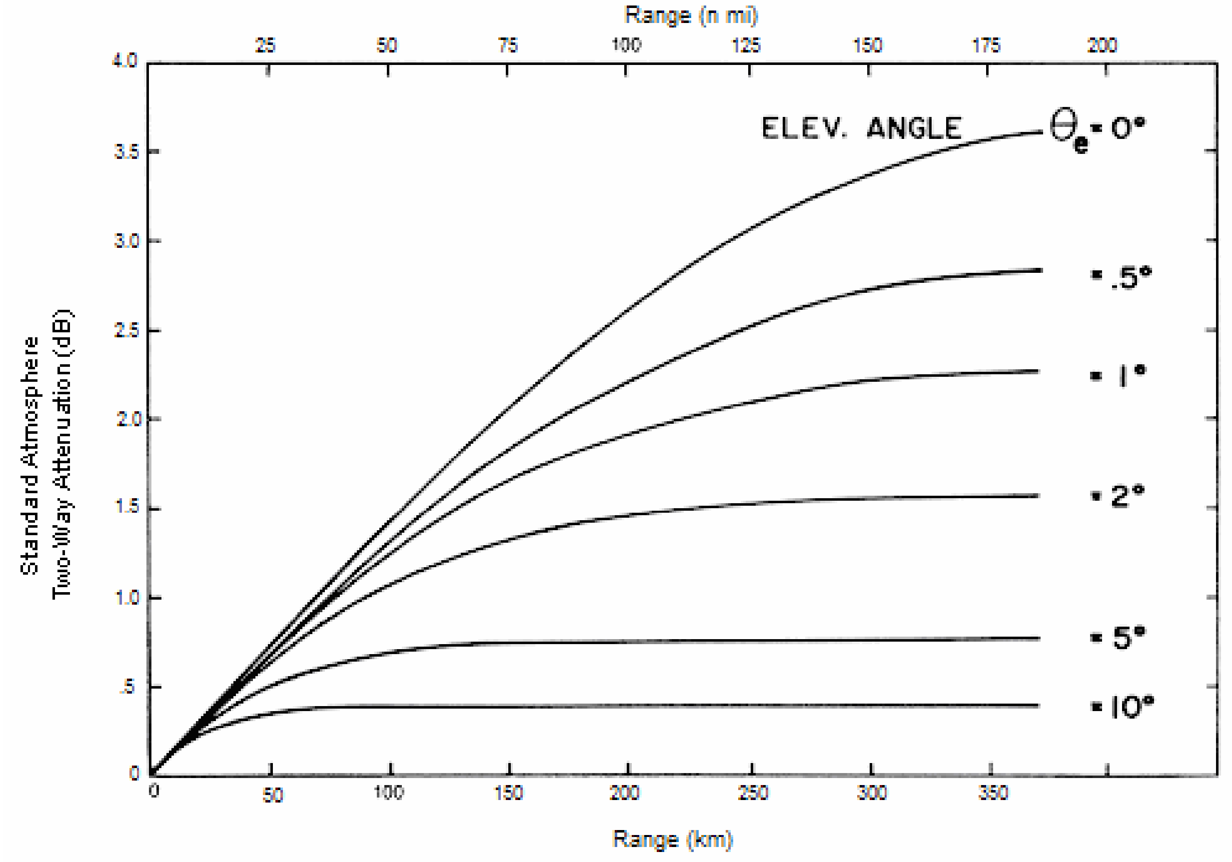

Figure 3-15
WSR-88D Signal Attenuation by the ICAO Standard Atmosphere

This attenuation is accounted for in the radar reflectivity estimate.

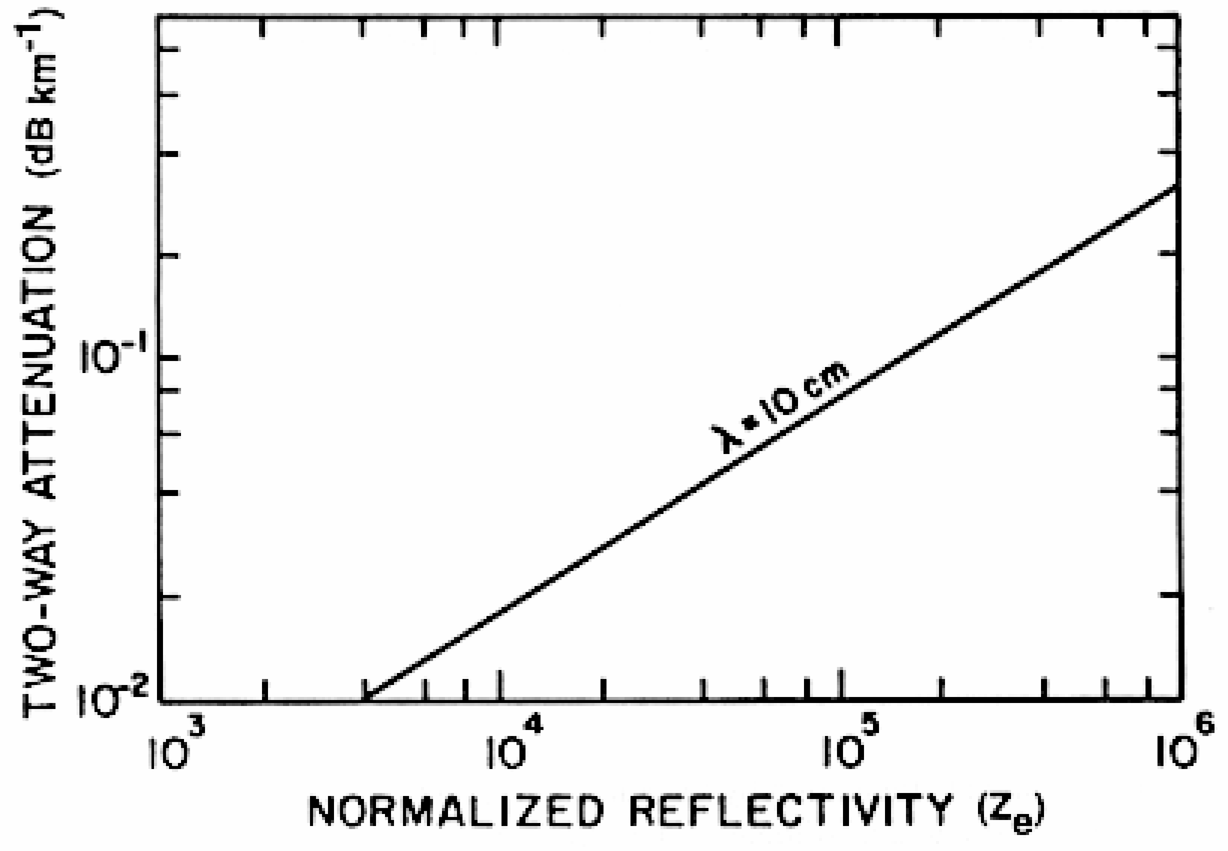

Figure 3-16
Attenuation of a 10 cm Signal by Rainfall

This attenuation is accounted for in the WSR-88D. For reflectivities greater than 53 dBZ, the user must subjectively make the correction.

3.5.3 Lack of Beam Filling. Another phenomenon, which is not attenuation but that also results in an underestimation of reflectivity, is the lack of beam filling, i.e., an apparent Z_e range dependency other than r^{-2}. (Recall that Z_e is interpreted as a volume reflectivity assuming homogenous reflectivity in the sample volume.) The effect can be visualized as an increase in the range exponent. The overall or average effect for a large number of situations is shown in Figure 3-17 for storms in the southern Great Plains. Although small scale meteorological features can fail to fill the horizontal dimension of the beam at the longer ranges, the predominant effect is the failure to fill the beam in the vertical.

The magnitude of underestimation is highly dependent on the particular meteorological situation and is usually more significant for non-convective precipitation systems, having low echo tops, than for convective storms.

In summary, signal attenuation by the atmosphere and rainfall or lack of radar beam filling all cause a systematic underestimate of the true signal strength. Attenuation by the atmosphere, usually the most appreciable effect, and attenuation by rainfall are objectively accounted for by the WSR-88D.

3.6 Data Contamination by Antenna Sidelobe Signal. An occasional source of data contamination is simultaneous reception of signals at comparable power levels through both the antenna pattern main lobe and its sidelobes. This occurs when the meteorological reflectivity gradient exceeds the two-way sidelobe/main lobe isolation.

Antenna sidelobe levels of the WSR-88D are described as follows:

> In any plane, the first sidelobe level is less than or equal to -27 dB relative to the peak of the main lobe. In the region between ±2 and ±10 degrees from the axis of the main lobe, the sidelobe level shall lie below a straight line connecting -29 dB at ±2 degrees and -34 dB at ±10 degrees. Between ±10 degrees and ±180 degrees the sidelobe envelope is less than or equal to -40 dB relative to peak of the main lobe.

These blanket criteria, along with a typical actual performance, are shown in Figure 3-18. Generally, the actual pattern is about 5 dB below the prescribed envelope in the region beyond ±2 degrees. Other characteristics of interest that are frequency dependent and vary across the operational band include:

- first sidelobe maximum is at about +1.5 degrees from the main lobe axis.
- first null is at about ±1.2 degrees.
- sidelobe periodicity is about 1.23 degrees.

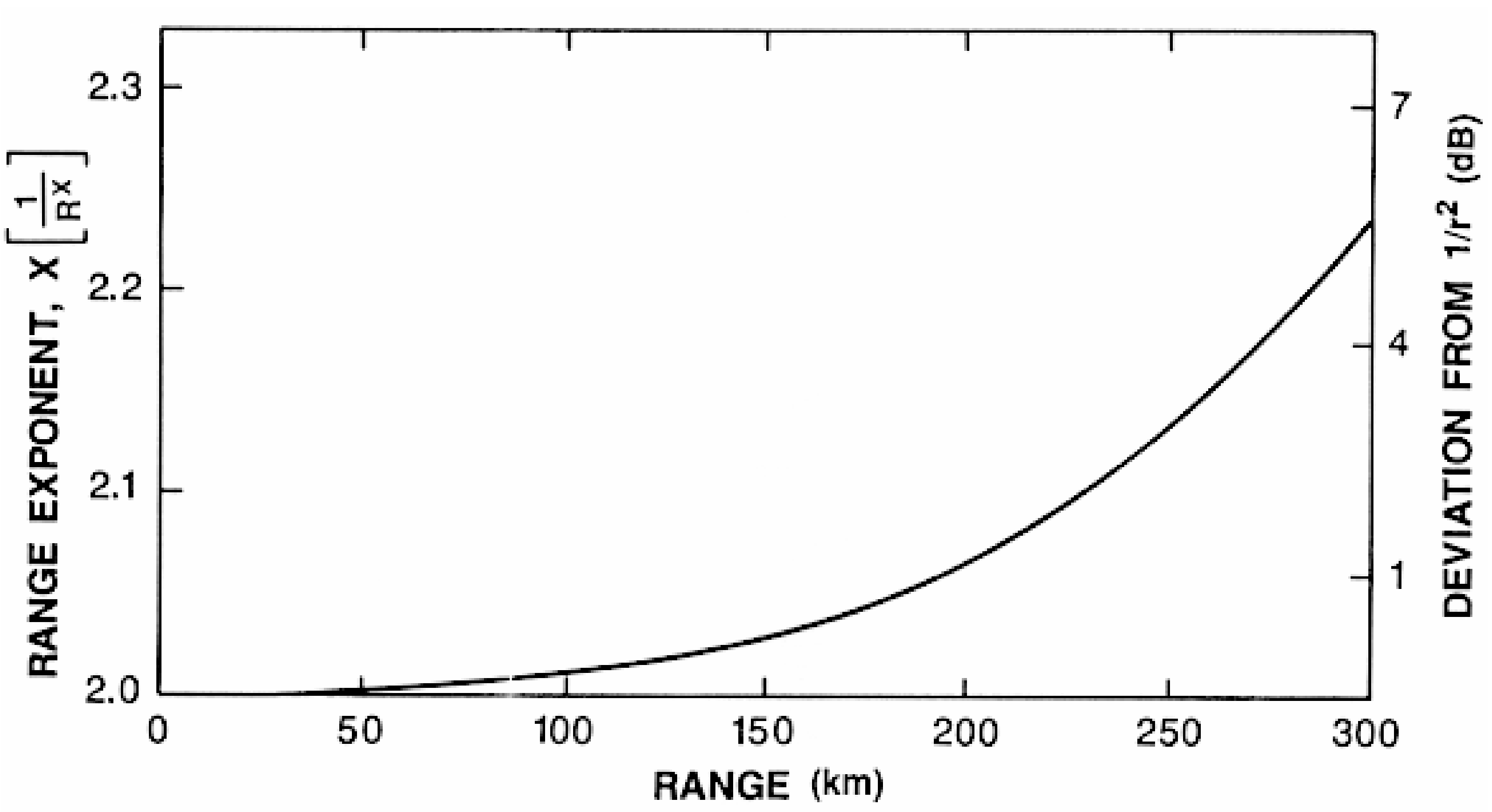

Figure 3-17
Deviation in Apparent Range Dependency of Z_e Due to Lack of Radar Beam Filling

Results shown are an empirical derivation for storms in the southern Great Plains and not valid for general application.

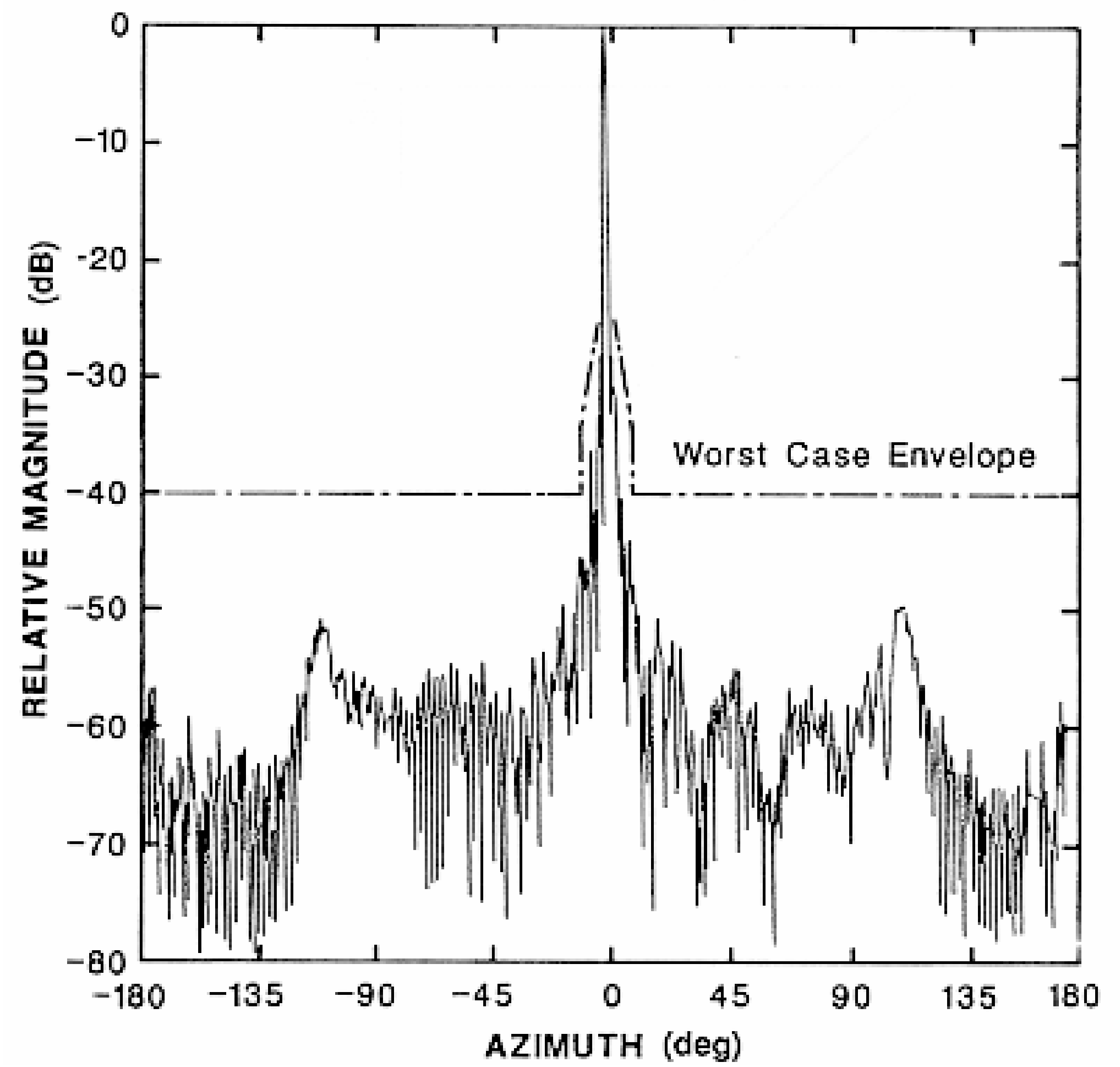

Figure 3-18
Typical Antenna Pattern for the WSR-88D and
Worst Case Sidelobe Envelope

Generally the sidelobe level is several dB below the envelope.

The two dimensional antenna pattern is given by the revolution of the pattern in a plane about the beam axis with the addition of the perturbations in sidelobe level due to antenna aperture blockage by non-symmetry of the feed and support spars. While the main lobe illuminates a circular region of space, the sidelobes illuminate an annulus and the sidelobe signals can originate from any portion or this entire region.

Conditions under which sidelobe detection will occur can be predicted from the known two-way antenna pattern. For example, in order to detect a signal through the first sidelobe, at signal strength equal to that detected through the main lobe, the reflectivity of the meteorological signal in the sidelobe (i.e., 1.2 degrees from the main lobe) must be stronger than the signal in the main lobe, by at least the two-way, first-sidelobe isolation (i.e., >50 dB). This requires a reflectivity gradient of greater than 50 dB per 1.2 degrees (greater than 40 dB degree^{-1} sustained over about 2 degrees). This is a rather large value and seldom-encountered in practice. However, at 6 degrees from the main lobe, the pattern envelope ensures that the sidelobe level is only 30 dB which, under the above criteria, requires a gradient of about 10 dB degree^{-1} sustained over about 6 degrees. Severe convective storms can occasionally support gradients of this magnitude. Beyond 10 degrees the sidelobe level is less than 40 dB with an isolation of 80 dB. As with the first sidelobe, meteorological signal coupling through these higher order sidelobes is rare.

From the prescribed envelope, the worst-case condition for signal detection through the antenna pattern sidelobes can be specified in terms of the reflectivity difference subtending a given angle. This is shown in Figure 3-19. In the use of this graph, it should be remembered that the actual antenna sidelobe level is probably several dB lower than the "worst-case envelope" and, therefore, the reflectivity difference required for coupling is several dB greater.

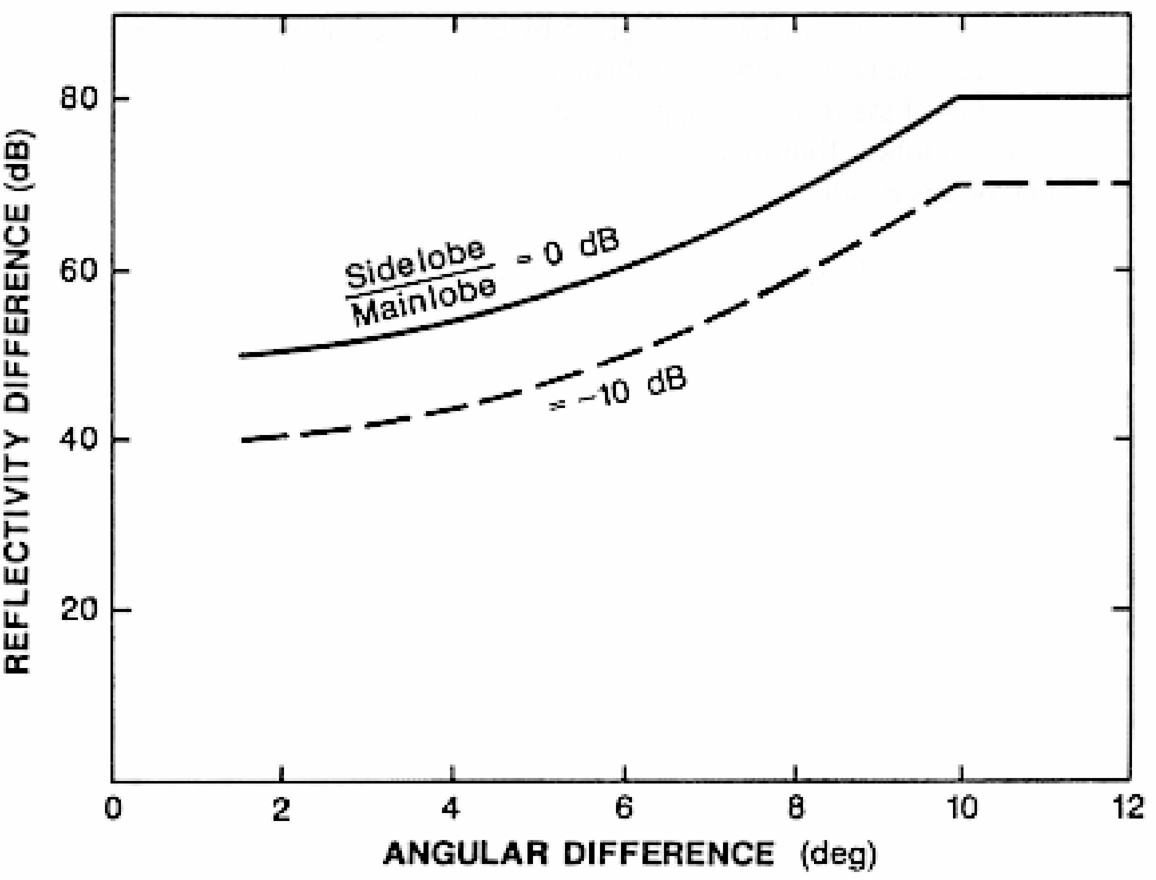

Figure 3-19
Reflectivity Difference and Angle Subtended Necessary for Signal Contamination Through Sidelobe Coupling

The ratio $\frac{\text{Sidelobe}}{\text{Main lobe}}$ is the relative power.

REFERENCES

Battan, L J., 1973: *Radar Observations of the Atmosphere*. Univ. of Chicago Press, Chicago, IL, 323 pp.

Baxter, T. L., 1966: An empirical determination of the WSR-57 radar range attenuation function for Oklahoma thunderstorms. Preprints, *12th Conference on Radar Meteorology*, Amer. Meteor. Soc.

Chrisman, J. N. and C. A. Ray, 2005: A first look at the operational (data quality) improvements provided by the Open Radar Data Acquisition (ORDA) system. Preprints, 3*2nd Conference on Radar Meteorology*, Albuquerque, NM, Amer. Meteor. Soc., paper P4R.10.

Doviak, R. J., and D. S. Zrnic', 1984: *Doppler Radar and Weather Observations*. Academic Press, Inc., Orlando, FL, 458 pp.

Johnson, J. C., 1962: *Physical Meteorology*. John Wiley & Sons, Inc., New York, NY, 393 pp.

Kerr, D. E., 1951: *Propagation of Short Radio Waves*. McGraw Hill Book Co., New York, NY, Chapter 7, 710 pp.

Marshall, J. S., and H. Hitschfeld, 1953: Interpretation of the fluctuating echo from randomly distributed scatterers, Part I., *Can. J. Phys.,* **31***,* 962-994.

Nathanson, F. E., 1969: *Radar Design Principles*. McGraw Hill Book Co., New York, NY, Chapter 6.

Skolnik, M. I., 1970: *Radar Handbook*. McGraw Hill Book Co., New York, NY, pp. 2-51 to 2-59.

CHAPTER 4

WSR-88D FUNCTIONAL OVERVIEW

4.1 Introduction. The meteorological situation determines the WSR-88D volume coverage patterns, measurement accuracy requirements, and analysis products required for maximum information extraction. The user must understand the physical processes that take place within the WSR-88D unit in order to optimize this information extraction.

The foundation for quantitative meteorological radar measurements was established in Chapters 2 and 3. Mathematical formulations were given describing the translation from the physics of radar sensing to a series of sensible meteorological measurements used for mapping the structure, motion, and magnitude of areas of precipitation. These concepts are the theoretical building blocks for utilizing the WSR-88D.

4.2 Simplified Radar System. The WSR-88D unit is configured functionally in three areas with functions as shown in Figure 4-1. (A description of the WSR-88D is given in Part D of this Handbook).

- The RDA detects and estimates the meteorological phenomenon.
- The RPG performs the meteorological data analysis and reformats the output products for remote display.
- The user display system provides the user interface.

Using the system nomenclature just described, the following sections trace the data from meteorological detection through the RDA, RPG, and the user display system. The focus is on signal flow and the step-wise processing of data.

4.3 Radar Data Acquisition. A block diagram of the RDA is shown in Figure 4-2. For purposes of signal flow, this function is divided into three areas: 1) antenna, transmitter, and receiver; 2) signal processing; and 3) data preprocessing.

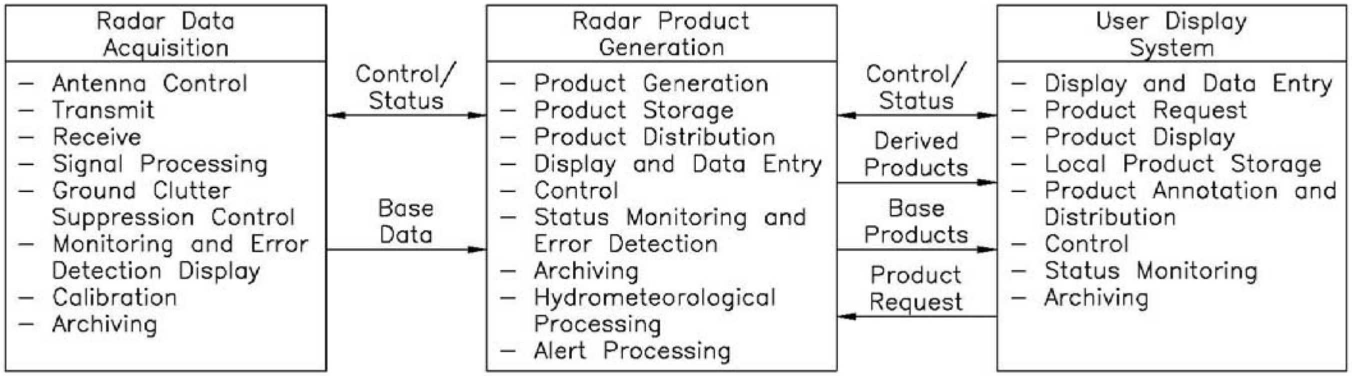

Figure 4-1
Functional Configuration of the WSR-88D Unit

The three major functional areas of the WSR-88D are shown along with the major data and messages transmitted among the functional areas.

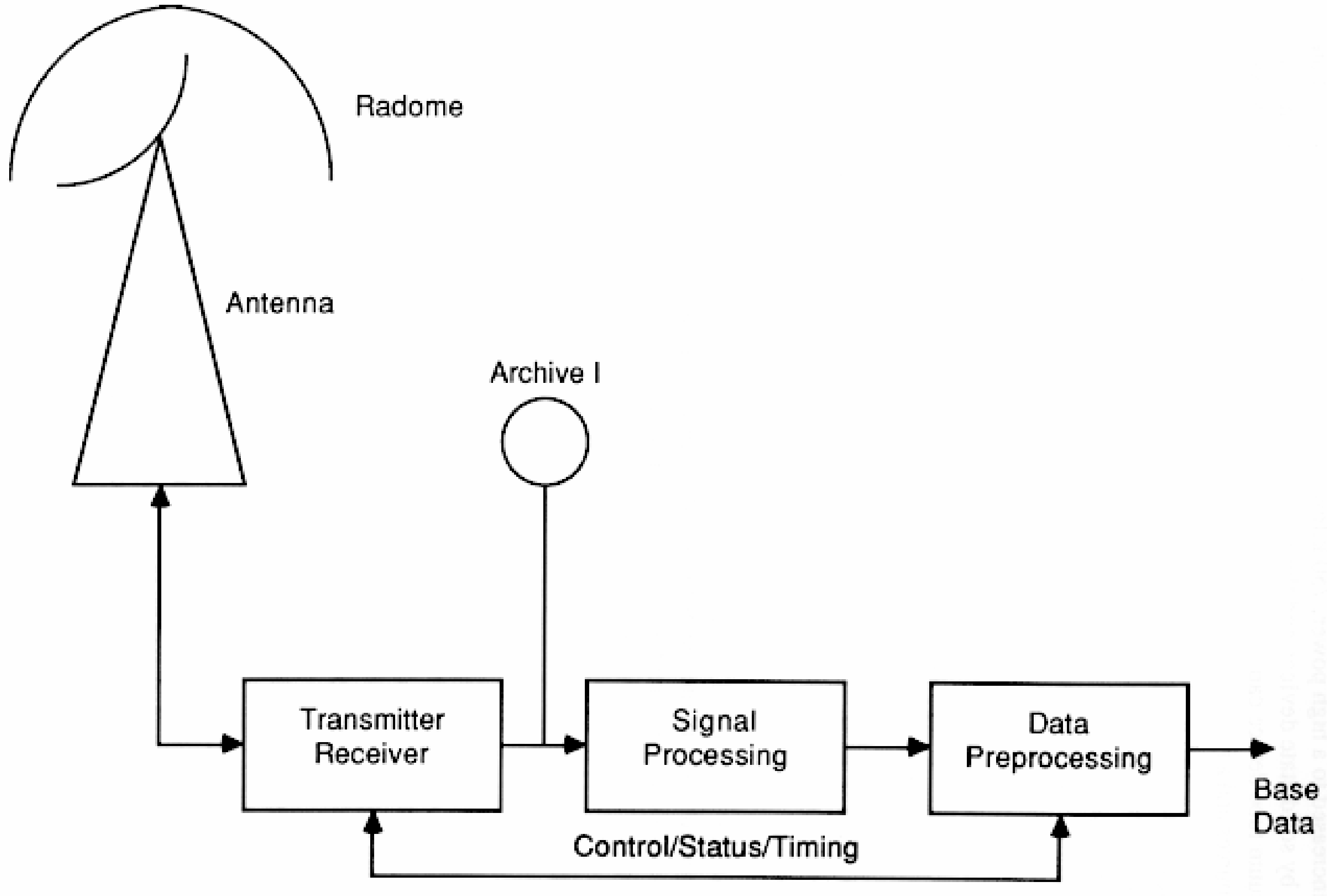

Figure 4-2
Block Diagram of the RDA

A complete tabulation of the radar system characteristics is given in Chapter 2. Some of the more important are: transmitter peak power of 750 Kw; a pulse width of 1.57 μs for the Precipitation Mode and 4.5 μs for the Clear Air Mode; and pulse repetition rates from about 300 to 450 Hz for surveillance and from about 1000 to 1300 Hz (short pulse) or 450 Hz (long pulse) for Doppler. The antenna main lobe one-way 3 dB beamwidth is 0.93 degree and the first sidelobe level is about 29 dB below the main lobe. The receiver has a dynamic range of about 100 dB and a bandwidth of 0.6 MHz. The radar system can detect a reflectivity of -8 dBZ_e at 27 nm (70 km), Figure 2-1, as per design, while actual tests indicate a somewhat better capability.

4.3.1 Basic Radar. The basic radar (antenna, transmitter, and receiver) is a coherent "chain-transmitter" design. Coherence, or phase information, in this design is maintained by very stable signal sources that operate continuously. These sources are used as the reference in extracting the Doppler shift of the back-scattered signal. A chain transmitter is one in which the transmitter signal is initially generated at a low power level, in this case a few hundred milliwatts, and increased to a high power, 750 kilowatts, by an amplifier chain. Intermediate amplification is by solid-state devices and the final high-power amplifier is a klystron. The klystron is a vacuum tube device capable of high amplification and efficiency. The WSR-88D uses two signal sources and a mixing scheme to generate the transmitter signal.

The receiver uses two frequency mixers to down convert the received signal to zero frequency carrier (video signal). The first conversion generates an intermediate signal carrier at which most amplification, bandpass filtering, and AGC are done. The second frequency conversion is synchronous detection (a detection that retains received signal amplitude and phase shift difference between received and transmitted signal phases but that removes the intermediate frequency carrier). This is a "complex" signal; complex meaning that it contains both amplitude and phase information and, for convenience of handling and analysis, is decomposed into its vector components, i.e., two signals (inphase and quadrature) having a phase difference of 90° that, when added vectorally, form the complex signal.

At this point the signal is still analog and carries the meteorological information as signal power, which is proportional to reflectivity, and the time rate of change of signal phase is proportional to target radial velocity.

4.3.2 Signal Processors. The "dedicated" signal processors calculate the electrical properties and translate them to the meteorological quantities of interest. Dedicated digital processors are processors designed and configured to perform a specific operation by implementing a specific algorithm with only limited changes in parametric values.

Reflectivity, Z, is estimated for each range interval from a linear average of several return pulses, usually about 25.

Velocity, v, is also estimated from an average of several pulses, usually 40 to 50. The mathematical quantity computed is the covariance of the return complex signal using a technique called "pulse-pair processing." The computation operates on two pulses (two consecutive signal returns from the same target). Physically, the covariance measures the rotation rate of the complex vector and represents the returned signal, which is directly related to the Doppler frequency.

Spectrum width, W, is estimated indirectly. The computation performed is the autocorrelation of the returned signal, which is related to the velocity spectrum standard deviation. It is also an average of the same number of pulses as the radial velocity. Physically the spectrum width is a measure of velocity dispersion within the radar sample volume. The signal from regions designated as being in the ground clutter by the site dependent clutter map is processed by a clutter filter that removes the clutter signal without serious degradation of the meteorological signal.

A comprehensive description of the signal processing and system performance is given in Chapters 2 and 3 and Appendices A and B.

4.3.3 Post Processing. Post-processing operations prepare the data for meteorological analysis and consist of unit conversion (from the normalized units used in signal processing to meteorological units used in analysis); specialized, highly redundant processing such as point target censoring and signal thresholding; and data conditioning such as range unfolding and velocity dealiasing.

Unit conversion consists of the following: signal power is converted to reflectivity by solving the radar equation for backscattering by hydrometeors (Appendix A.1); vector rotation rate is converted to velocity by multiplication by a constant derived from the Doppler equation, radar wavelength, and pulse repetition time; and spectrum width is converted from autocorrelation to velocity by multiplication by a constant derived from the radar wavelength and pulse repetition time under the assumption that the spectral density functional form is Gaussian (Appendix A.4).

Point target suppression is accomplished by an analysis routine that monitors the width and reflectivity gradient of the target and suppresses the return when these characteristics correspond to those of a point target.

Data thresholding consists of suppression of data points whose signal-to-noise ratios (2 dB for reflectivity and 3.5 dB for velocity and spectrum widths) fall below a user-specified value.

Range unfolding is achieved in the following manner. The occurrence of overlaid echoes (two or more echoes appearing at the same range due to the short unambiguous range of a high PRF) is detected by implementing a low PRF surveillance, range unambiguous, waveform along with the higher Doppler waveform. Determining the potential range ambiguities is accomplished by comparing power returned on a gate-by-gate basis for the higher Doppler PRF using the range unambiguous surveillance waveform. If the relative power of two or more potentially ambiguous range gates is within a user-specified difference (usually 5 dB), both echo regions are flagged as obscured and the Doppler velocities are suppressed for those same range gates. If the relative power is greater than the specified difference, the Doppler velocity and spectrum width data are assigned to that range gate having the greater power. The gate(s) having weaker power returned are then flagged as obscured and Doppler data is suppressed for those same gates.

The range-unfolding scheme is illustrated pictorially in Figure 4-3. Figure 4-3A shows the true range distribution of echoes as monitored by the reflectivity PRF [range folding is rare at this PRF with an unambiguous range of about 248 nm (460 km)]. Figure 4-3B shows the range distribution of normalized power (intensity) levels after folding where all echoes appear within the Doppler unambiguous range. Figure 4-3C shows the results of the range unfolding and suppression of data obscured by echo overlaying (in this case, echo 2 and echo 3).

Velocity dealiasing is accomplished by testing for velocity continuity along the radial and assuring true velocity gradients on the order of the Nyquist velocity co-interval, $\pm 2v_a$ do not exist. The measured velocities are checked gate-to-gate and measured differences greater than a specified value are assumed to be due to velocity aliasing. These large gradients are then reduced by adjusting the measured point velocity by $\pm 2v_a$ i.e., the radial velocity gradient is minimized by adjusting the measured adjacent range velocity values by $\pm 2v_a$ (Chapter 2).

The velocity dealiasing scheme is illustrated pictorially in Figure 4-4. Aliasing (Figure 4-4A) is recognized (Figure 4-4B) by velocity differences between adjacent range gates approaching $\pm 2v_a$. A running correction is made (Figure 4-4C) on all cells exhibiting this large velocity gradient by either adding $2v_a$ or subtracting $2v_a$ so as to minimize the gate-to-gate velocity difference.

4.3.4 Operational Scenario. The mode of radar operation is an automatic scanning sequence that provides the volumetric data for meteorological analysis. There is the design capability to have up to 20 predetermined volume coverage patterns available to the user allowing the data acquisition scheme to be varied with the meteorological situation.

There are several considerations in the selection of a data acquisition scheme (Chapter 3) with the governing considerations being the temporal and spatial scales of the meteorological situation (volumetric throughput rate) and the volume in space over which data are to be acquired (number of elevations). These two general considerations combine to specify the optimum antenna scan rate and, thus, dwell time for the data on the fixed 1° polar grid. Dwell time determines the system performance in terms of estimate accuracy, and estimate accuracy determines the quality of the output products.

The fastest acquisition scheme (VCP 12) is 14 unique elevations extending to 19.5° in a total time of 4.2 minutes. There is more than one scan at the lower elevation angles; the number of elevation angles is VCP dependent. A surveillance scan is made to obtain power return and target location information. A Doppler scan is made to obtain good velocity and spectrum width estimates. More samples of the atmosphere are obtained to provide better estimates of the three moments and to mitigate the effects of the Doppler Dilemma. Antenna rotation rate is dependent on number of elevations and the volume throughput time and may vary with elevation angle with maximum rates of about 5 revolutions per minute (rpm).

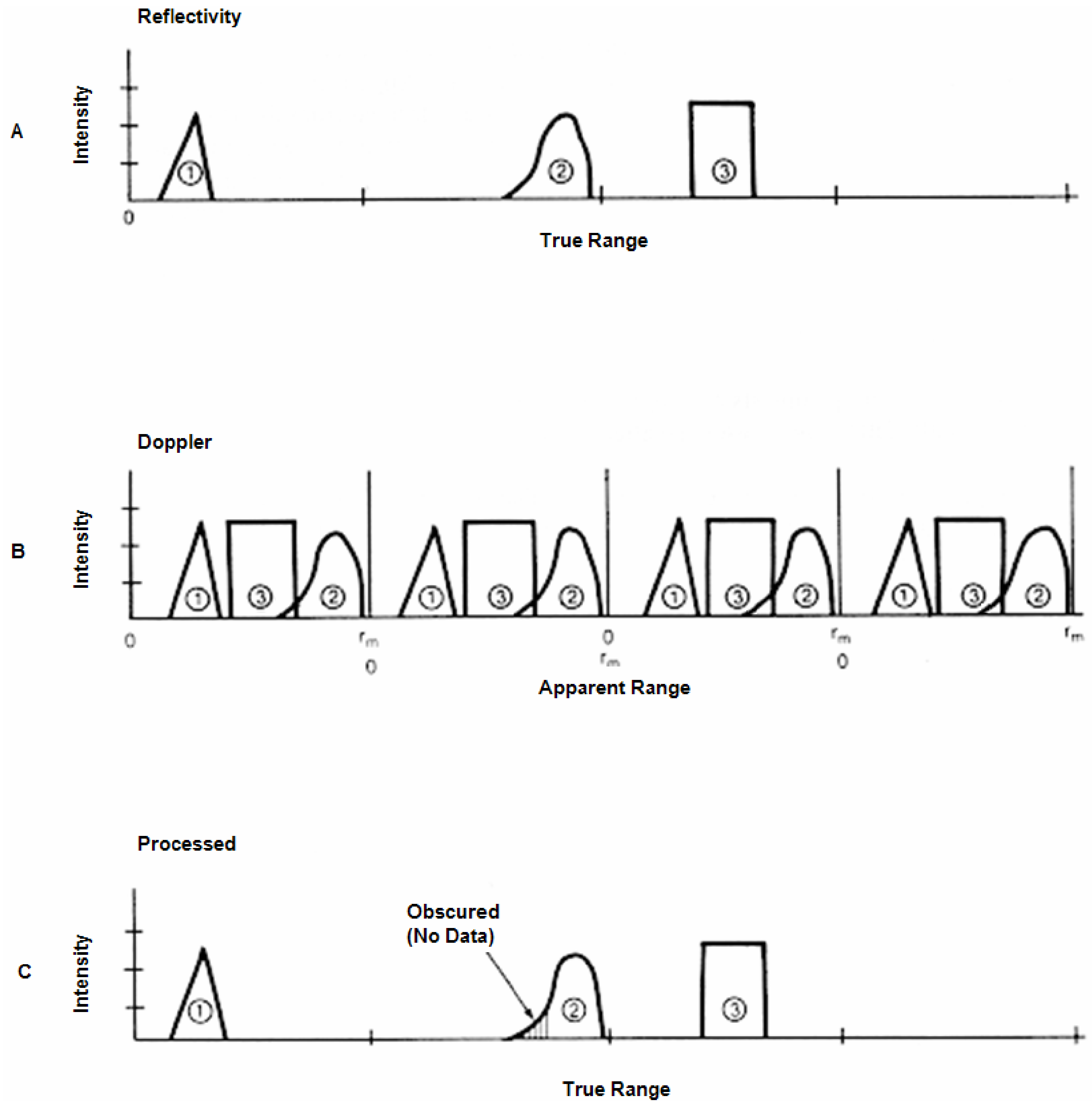

Figure 4-3
Range Unfolding/Obscuration Pictorial

See the text for a summary of the range-unfolding scheme operation.

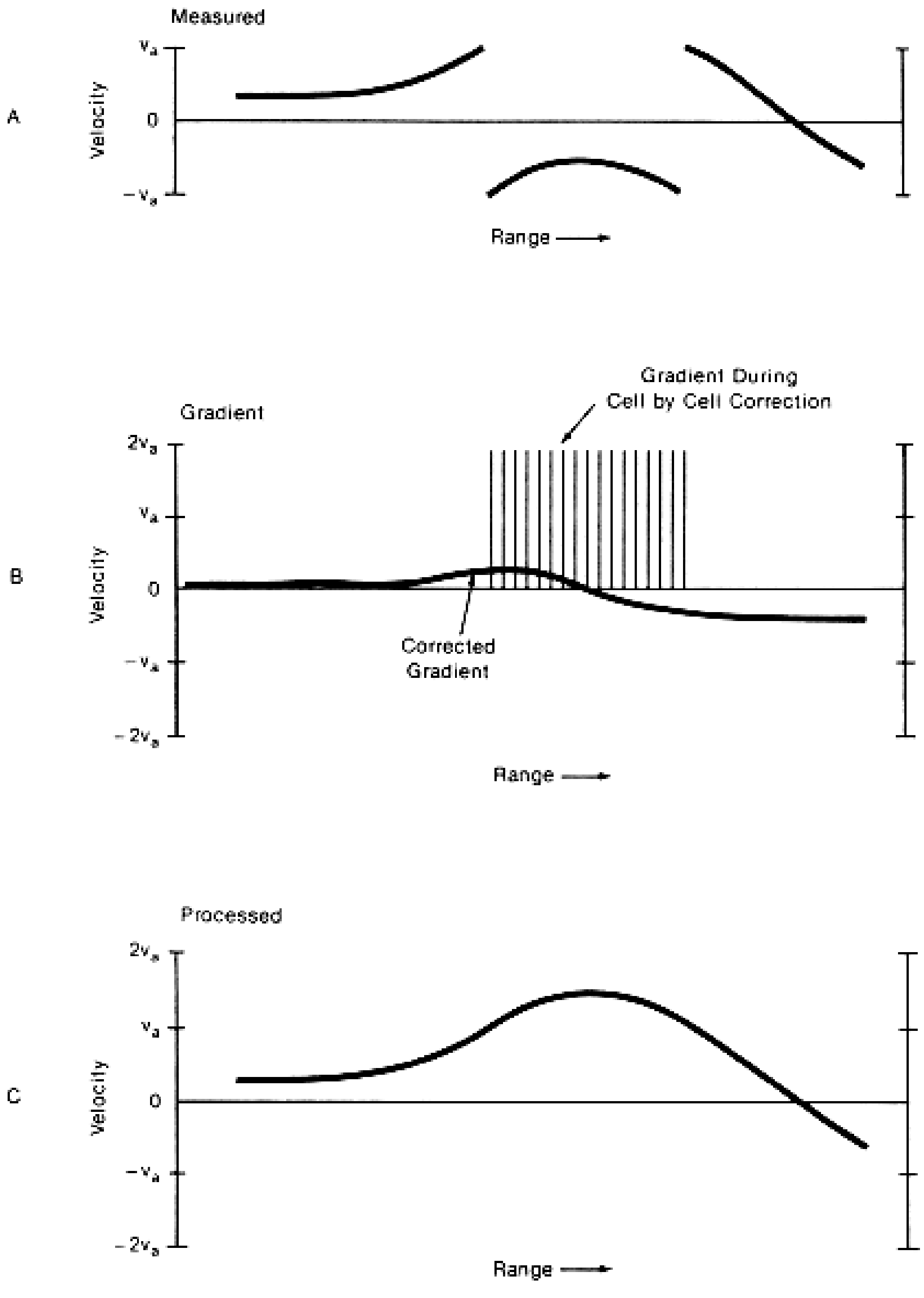

Figure 4-4
Velocity Dealiasing Pictorial

See the text for a summary of the velocity dealiasing scheme operation.

The transmitter PRFs are coupled to the scanning sequence providing long-range surveillance data at the low elevation angles where range folding is likely to occur and automatic selection of Doppler PRF (from the three choices available) that results in the minimum obscured echo area.

A representative fast scan sequence (VCP 12) is described in Table 4-1. The Batch Mode (B) technique uses alternating low and high PRFs on each radial for one full rotation at each elevation angle. (See Part C, Chapter 5, of this Handbook for discussions of "Batch" processing). The low PRF long-range surveillance is provided by redundant scans at the lower elevation angles, where the altitude of the maximum Doppler range is less than about 50,000 ft (15 km). The Doppler PRF is selected from minimum obscuration consideration from the preceding volume scan and is fixed for the sequence (may change from volume scan to volume scan). The average rotation rate is 4.1 rpm, but varies from scan to scan in order to optimize system performance. For example, ground clutter suppression would be enhanced and measurement accuracy increased by rotating slower at the low elevation angles (Figure 3-6) but at the expense of increased error with the faster rotation rates that become necessary at the higher elevation. Considerable versatility is available in the unit within the meteorological and performance constraints given in Chapters 2 and 3.

4.3.5 Base Data Summary. Data sent from the RDA (base data) to the RPG consist of estimates of the first three Doppler spectral moments Z, v, and W. Data are delivered to the RPG (Figure 4-1), radial-by-radial, spaced approximately 1° apart. Time between data blocks for adjacent radials is determined by the acquisition scan rate and usually varies between 39 and 166 milliseconds. In addition to the auxiliary or housekeeping information, each block consists of three data subsets (Z, v, W) each containing about 1024 entries corresponding to the individual range cells.

General characteristics of the base data are given in Table 4-2. Reflectivity products are now limited to displays of -28 dBZ and up to greater than +75 dBZ. In actual observations values as low as -30 dBZ have been observed (commonly) and rarely values as high as about +78 dBZ have been observed. In reality these are probably near the atmospheric limits.

With the default velocity resolution setting of ~ 1 kt (0.5 ms^{-1}), the RDA is limited to observing velocities within the range of +/- 123 kts (+/- 62 ms^{-1}). Thus, this would be a base data limitation. However, when wind speeds (and therefore velocities) in tropical storms or in other particular cases are expected to exceed these limits, the velocity resolution can be expanded by setting the RDA velocity resolution default to ~ 2 kts (1 ms^{-1}). In this case the system is then capable of measuring +/- 246 kts (+/- 126 ms^{-1}). The system in actual practice has already measured velocities in excess of 130 kts (67 ms^{-1}). There will probably be occasions when actual meteorological measurements will at least approach 246 kts (126 ms^{-1}). However, velocity products will have to be modified for display of such values. Therefore, base data characteristics may reach this value.

Table 4-1
Representative Fast Scan Sequence (VCP 12)

			Unambiguous Range		*Unambiguous Velocity		
Scan	Elev	PRF (Hz)	nm	km	kts	$m\ s^{-1}$	Data
1	0.5°	322	252	466			Surveillance
2	0.5°	1014	80	148	49.4	25.4	Doppler Moments
3	0.9°	322	252	466			Surveillance
4	0.9°	1014	80	148	49.4	25.4	Doppler Moments
5	1.3°	322	252	466			Surveillance
6	1.3°	1014	80	148	49.4	25.4	Doppler Moments
7	1.8°	1014	80	148	49.4	25.4	Batch
8	2.4°	1014	80	148	49.4	25.4	Batch
9	3.1°	1014	80	148	49.4	25.4	Batch
10	4.0°	1014	80	148	49.4	25.4	Batch
11	5.1°	1014	80	148	49.4	25.4	Batch
12	6.4°	1014	80	148	49.4	32.1	Batch
13	8.0°	1905	74	137	53.3	27.4	Doppler Moments
14	10.0°	1181	69	127	57.5	29.6	Doppler Moments
15	12.5°	1282	63	117	62.4	32.1	Doppler Moments
16	15.6°	1282	63	117	62.4	32.1	Doppler Moments
17	19.5°	1282	63	117	62.4	32.1	Doppler Moments

* At $\lambda=10$ cm
Average rotation rate = 4.1 rpm
Dwell time = 39 milliseconds per degree
Doppler Moments = Contiguous Doppler waveform
Batch = Alternating low and high PRFs on each radial for one full rotation at each elevation angle.

Table 4-2
Base Data Characteristics

Data	Dynamic Range	*Estimate Standard Deviation	Range Coverage	Range Increment	*Data Resolution
Z	< -28 to > +75 dBZ	1 dB	0 to 248 nm (0 to 460 km)	0.54 to 248 nm (1 to 460 km)	0.3 dB
	**		***		
v	> +/- 123 kts (> +/- 62 ms^{-1})	1.9 kts (1 ms^{-1})	0 to 124 nm (0 to 230 km)	820 ft (250 m)	0.49 kt (0.25 ms^{-1})
			***		
W	0 to 35 kts (0 to 18 ms^{-1})	1.9 kts (1 ms^{-1})	0 to 124 nm (0 to 230 km)	820 ft (250 m)	0.2 kt (0.1 ms^{-1})

*	typical value
**	after velocity dealiasing and with a velocity resolution of about 1 kt (0.5 ms^{-1})
***	after range unfolding

4.4 Radar Product Generator. The digital base data generated within the RDA is sent via a wideband communications system (by fiber optics, wire, commercial T-1 circuits, or microwave line of sight) to the RPG where a larger computer system digests the full 3-dimensional volume of polar scan data.

As shown in Table 4-2, the reflectivity data are in a matrix of 360 degrees by 248 nm (460 km) in range; whereas the radial velocity data are in a matrix of 360 degrees by 124 nm (230 km) in range. The resolution of the reflectivity data is 0.54 nm (1 km); the velocity and spectrum width resolution is 0.13 nm (0.25 km or 820 ft).

The RPG computer system processes more than 250,000 lines of code to produce and transmit meteorological products. These products are derived from algorithms that enjoin several fundamental relationships among reflectivity and radial velocity patterns to provide users with conclusions concerning the locations, movement, and severity of meteorological phenomena.

4.4.1 Interactive Control. The control of the WSR-88D unit is linked through software resident in user terminals. The Master System Control Function (MSCF), a graphical user interface, is used to set all adjustable parameters that determine pulse repetition frequency, antenna motion, and all processing thresholds and limits, including the setting of adjustable parameters that affect the seasonal and geographical performance of the hydrometerological algorithms.

The RPG controls all analysis procedures. The products generated from the algorithms are queued, according to operational priorities, and sent to requesting displays at user workstations.

4.4.2 Meteorological Analysis Products. The graphic products are displayed after the analysis of multiple data fields in the RPG. Several of them are made directly from the polar scan data. For example, the base products of reflectivity, radial velocity, and spectrum width are truncated and scan converted to produce polar matrices [reflectivity, 0.54, 1.1, or 2.2 nm (1, 2, or 4 km) x 1^{o}; velocity and spectrum width, 0.13, 0.27, or 0.54 nm (0.25, 0.5, or 1 km) x 1^{o}] that can be color coded or grey-scaled to enhance their operational use. Other products are generated after analysis algorithms composite the data geometrically into layers, or transform them to other identities--such as shear, which is derived from the velocity field. Still other algorithms search the base data for specific reflectivity and velocity signatures that, when found, mark the hazards to be depicted as symbols or alphanumeric labels on the user display systems. Critical data thresholds are established and data is filtered for all products limiting displays to what is believed to be noise free and accurate data.

Products can be grouped generally into three areas of application: 1) Wind Profiling--which includes the measurement of wind velocity and shear in the optically clear boundary layer, in dense cloud layers that contain only extremely light precipitation, and in areas of heavy rain in stratiform and convective storms; 2) Precipitation Measurement--which includes quantitative data gridded for mapping on the national scale, and localized data that will allow local meteorologists and hydrologists to project the movement of areas of precipitation over specific watersheds; and 3)

Storm Warning--which provides location and tracking information on severe thunderstorms and estimates the likelihood of hail and tornadoes.

4.5 User Display Systems. The users of WSR-88D data have developed their own systems to display meteorological products generated by the RPG. A summary of the current systems in place to meet unique NEXRAD agency user needs is provided in Part D, Chapter 2, of this Handbook.

The original WSR-88D baseline display system, deployed to all NEXRAD agency user locations, was the Principal User Processor (PUP). The last of the PUPs will be decommissioned in 2006. The PUP has been replaced by an open-systems based architecture version termed the Open PUP. The Open PUP is considered the new WSR-88D baseline display device and is used by the ROC for implementing new product displays. Only DoD users operate the Open PUP.

REFERENCES

JSPO Staff, 1980: *Next Generation Weather Radar (NEXRAD) Joint Program Development Plan*, JSPO report. Silver Spring, MD, 102 pp.

JSPO Staff, 1984 and 1986: *NEXRAD Technical Requirements*, JSPO report, Silver Spring, MD, 144 pp.

CHAPTER 5

ESTIMATION OF PRECIPITATION BY RADAR

5.1 Introduction. The accurate measurement of precipitation plays a very important role in hydrology, agriculture, weather modification, climatology, and weather forecasting. The primary requirement of radar for hydrological purposes is to provide estimates of the amount and the temporal and spatial distribution of precipitation that falls over a watershed. For many agricultural applications and climatic studies, precipitation data are needed over large areas for long periods (days or weeks) and a relatively sparse network of rain gages reporting once per day may be adequate. In contrast, measurements from many closely spaced stations are required to forecast flash floods on streams, where data are required for short time intervals (<6 hours) and over small areas [<1000 km^2 (<290 nm^2)]. Also, to evaluate weather modification experiments, high-resolution spatial and temporal data are needed. However, it is generally not practical to install and to maintain a sufficient number of closely spaced in situ observation sites that transmit timely data to a central processing facility. Hence, weather radar precipitation estimates provide a practical data source not available by other means. Development of procedures for using radar as a tool to measure precipitation has progressed from the subjective manual techniques, first used in the late 1940s, through the semi-automatic techniques, to the fully automatic techniques of today.

Radar does not measure precipitation rate directly, but rather estimates that rate from the backscattered energy received from precipitation particles in an elevated volume. Consequently, radar estimates of precipitation, due to the variability in the relationship between the backscattered energy and precipitation rate, are subject to sampling and measurement errors. Other errors also potentially come into play when estimating precipitation by radar as well as by the combination of radar and rain gages. These will be discussed in subsequent sections of this chapter.

5.2 Physical Principles of the Measurement Process. A more detailed description of the physics pertaining to the measurement process is provided in Appendix A. The following discussion highlights the relationship between the meteorological quantities of particle size distribution, radar reflectivity factor, and precipitation rate.

5.2.1 Particle Size Distributions. Except for small diameters (D <1 mm), particle size distributions for rain and snow can be approximated by:

$$N\,(D) = N_{\mathbf{o}}\, e^{-\Lambda D} \qquad (5\text{–}1)$$

where N (D) is the number concentration of size D droplets per volume interval, Λ is the mean drop size, and $N_{\mathbf{o}}$ is the number of particles per unit volume (Marshall and Palmer 1948). For a snow particle, D is the diameter of a droplet of equal mass. From raindrop records collected on dyed filter paper for an entire summer, Marshall and Palmer determined N_o to be 8000 m^{-3} mm^{-1} and Λ to be 4.1R$^{-2.1}$ mm^{-1}, where R is the rainfall rate (mm h^{-1}). Of course, there are significant departures from these parametric values for other precipitation regimes and, in fact, the relationship may differ markedly from a simple exponential relationship with individual drop size samples and with certain types of precipitation. Numerous other investigations have reemphasized that Λ and N can vary from storm to storm and that N_o is also a function of precipitation rate. In general, both parameters, N_o and Λ, are needed to specify the size distribution.

5.2.2 Radar Reflectivity Factor. When the drop size distribution is known, radar reflectivity factor, Z, in a unit volume can be calculated from:

$$Z = \int_{0}^{\infty} D^{6} \; N(D)dD \tag{5–2}$$

Alternatively, Z can be estimated using the radar equation:

$$Z = \frac{2^{10}(\ln 2)}{\pi^{3} c}\left[\frac{\lambda^{2}}{P_{t}\tau G^{2}\theta^{2}_{3dB}}\right]\left[\frac{r^{2}\,\bar{P}_{r}}{|K|^{2}}\right] \tag{5–3}$$

where:

P_r = average return power, watts

P_t = peak transmitted power, watts

G = antenna gain, dimensionless

λ = radar wavelength, meter

θ_{3dB} = antenna half-power beam width, radian

τ = pulse duration, second

c = electromagnetic propagation constant (speed of light) = 3(10^{8}) m s^{-1}

r = range to target, meter

K = complex index of refraction; $|K|^2$ is conventionally taken to be 0.93 for water and 0.2 for ice

Z = radar reflectivity factor

This equation assumes that:

- The particles are small, homogeneous spheres conforming to Rayleigh scattering principles;
- The particles are spread uniformly throughout the contributing region;
- The reflectivity factor, Z, is uniform throughout the contributing region and constant over the sampling interval;
- All particles have the same dielectric constant, $|K|^2$, i.e., it is not mixed precipitation;
- The main lobe of the antenna beam pattern is described adequately by a Gaussian function;
- Microwave attenuation and multiple scattering are negligible; and
- Incident and back-scattered waves are linearly polarized.

If all assumptions were able to be met and if no measurement errors existed, the radar measured Z (Eq. 5-3) would conform to the meteorologically defined Z (Eq. 5-2). However, this is not the case and it is, therefore, customary to use Z_e, the equivalent radar reflectivity factor, in the radar equation as shown in Appendix A, which can be simplified as:

$$\bar{P}_r = \frac{C\,Z_e}{r^2} \tag{5–4}$$

where C is a combination of all known constants in the equation. Z_e can be calculated if P_r and r are known.

In the same way that Z can be related to drop size distribution, the precipitation rate, R, when the vertical airspeed is zero, as it is at the ground, can be given by:

$$R = \frac{\pi}{6}\int_{\circ}^{\infty} D^3 v_t \quad (D)N(D)\,dD \tag{5–5}$$

Attempts have been made to combine Eqs. (5-2) and (5-5) in order to obtain an analytical relationship between Z and R, but a number of problems are encountered. First, spatial and temporal variations of particle size distributions are rarely known and, second, vertical air motions are frequently of the same magnitude as the particle terminal fall speeds (particularly in thunderstorms). Finally, different drop size distributions can result in the same Z yielding different values of R.

5.2.3 Reflectivity-Precipitation Relationship. A unique relationship between Z and R does not actually exist. But if all the assumptions introduced to develop Eqs. (5-2) and (5-5) hold true and one assumes that N_o is constant, then a single parameter relationship R = R (Z) is implied. This relationship is generally expressed in the form:

$$Z = AR^b \tag{5–6}$$

There has been much empirical study to identify values of the coefficient (A) and exponent (b) in Eq. (5-6). The parameters for rainfall reported by different investigations range from less than 20 to more than 1000 for the coefficient and from 1.11 to 3.05 for the exponent In most cases, as the Z-R's coefficient increases the exponent decreases.

5.3 <u>Error Sources in Radar Measurements</u>. The factors causing errors in the radar measurement of surface precipitation can be grouped into four broad categories: 1) estimating equivalent radar reflectivity factor, 2) variations in the Z-R relationship, 3) time and space averaging of precipitation measurement by radar, and 4) below-beam effects. These categories are described in the following sections.

5.3.1 Estimating Equivalent Radar Reflectivity Factor. The equivalent radar reflectivity factor may be biased by a number of factors such as incorrect hardware calibration, ground clutter, anomalous propagation, partial beam filling, and wet radome attenuation.

System errors (bias) in the measurement of reflectivity arise from incorrect hardware calibration. Even after careful electronic system calibration, large, inexplicable errors in precipitation estimates occasionally remain. Usually, losses are greater than estimated and precipitation amounts are underestimated accordingly, although the opposite effect is also possible.

A potentially serious source of error, not associated with hardware, is blockage by ground targets close to the radar site such as trees, buildings, and ridges that can severely reduce the effective transmitted and received power and cause recurring shadows in precipitation patterns. Correction for blockage can be performed by addition of an adjustment factor or interpolation with neighboring bins as described in Part C, Chapter 3, of this Handbook.

Vertical gradients in atmospheric temperature, humidity, and pressure cause a gradient in the refractive index. This causes the radar beam to be bent in a characteristic manner for standard atmospheric conditions. Non-standard atmospheric conditions, and the associated non-standard gradient in the refractive index, can result in AP (Part D, Section 4.2.1 and Part B, Section 3.4.2 of this Handbook) of the radar beam and can produce significant errors in reflectivity estimates. Temperature inversions, with decreasing moisture with height, cause bending or even ducting of radar signals, resulting in ground target returns from extended ranges. This condition is sometimes widespread; a local condition, dubbed thunderstorm super-refraction, occurs when local temperature inversions and specific humidity fluctuations are produced by downdrafts spreading beneath thunderstorms. In regions of super-refraction and their attendant shadow zones, precipitation estimates may be significantly reduced. AP can often be identified by a large variance of spatial reflectivity and by a small rate of echo fluctuations.

Ground clutter and AP are most likely to corrupt reflectivity estimates from radar signals at lower elevations. As a result, these effects can be reduced by an appropriate selection of reflectivity data from four sequentially obtained contiguous low elevation scans (Fulton et al. 1998). Development of the "hybrid scan" is described in Part C, Chapter 3, of this Handbook.

Signal degradation, partial beam filling, and radar horizon reduce precipitation rate estimates at longer ranges (Wilson 1975; Hudlow et al. 1979). This is known as the range effect. The range effect has been found to be correlated with echo intensity (or precipitation rate) and is greater in shallow precipitation regimes. The hybrid scan significantly reduces the range effect, but an additional range-dependent, site-varying correction is also applied to the precipitation rate data (Ahnert et al. 1983). (An exception to the range effect is seen with convective storms which normally are characterized by an elevated reflectivity maximum. The radar horizon will then lead to rainfall overestimation in convective storm situations at longer ranges.)

When the radome that encloses the radar antenna is wet, attenuation of the radar signal increases. This increased attenuation is a function of water film thickness and radar wavelength and may approach 1 dB for the WSR-88D. Because this temporary condition is difficult to describe quantitatively and because recovery is rapid once precipitation has ended, usually no attempt is made to account for this loss for S-band radars. Since wet radome attenuation introduces systematic bias, adjustment with rain gage data helps via the adjustment algorithm and the external bias factor generated externally to the radar system.

5.3.2 Variations in the Z-R Relationship. Many studies of the relationship between Z and R have been made, especially for rain. If the particle size distribution were a unique function of the precipitation rate, a universal Z-R relationship for rain would exist. However, it has been amply demonstrated that there is no unique particle size distribution for a given precipitation rate or even for a given storm. The literature on the subject of Z-R relationships for rain is too extensive to be reviewed in detail in this section; however some of the more significant results are discussed below.

One of the earliest and most familiar relations is:

$$Z = 200R^{1.6} \tag{5–7}$$

following the work of Marshall and Palmer (1948).

Numerous measurements of drop size distributions have been made in stratiform rain, rain showers, and thunderstorms; and the characteristic Z-R relationships are reported in the literature (e.g., Battan 1973). Ordinarily the coefficient in Eq. (5-6) increases as the precipitation becomes more convective. For example, Joss et al. (1970) gave:

Drizzle $Z = 140R^{1.5}$ (5–8)

Thunderstorms $Z = 500R^{1.5}$ (5–9).

The presence of larger raindrops in thunderstorms causes the coefficient to be larger.

Drop size measurements beneath a large Oklahoma thunderstorm (Martner 1977) yielded these relationships:

Leading portion $Z = 667R^{1.33}$ (5–10)

Central core $Z = 124R^{1.64}$ (5–11)

Trailing portion $Z = 436R^{1.43}$ (5–12).

A mean Z-R relationship for snow, where R is an equivalent rain rate, is:

$$Z = 2000R^2 \quad (5\text{–}13).$$

Hail Z-R relationships depend upon the stone density, i.e., whether growth has been dry or wet, and the thickness of water films. Douglas (1963) found:

Wet growth $Z = 84000R^{1.29}$ (5–14)

Dry growth $Z = 22500R^{1.17}$ (5–15).

Considering all of the above, the coefficient and exponent in the Z-R relationship used with the WSR-88D hydrologic software are adaptable parameters with default values set at:

$$Z = 300R^{1.4} \quad (5\text{–}16)$$

or for tropical convective systems, particularly during land falling hurricanes and tropical storms (Rosenfeld et al. 1993)

$$Z = 250R^{1.2} \quad (5\text{–}17).$$

Based on several years of WSR-88D experience and studies of cool season stratiform rain events (Super and Holroyd 1998; Carins et al. 1998; Huggins and Kingsmill 1998; and Quinlan and

Sinsabaugh 1999) have shown that the best Z-R relationship depends significantly on geographic location. The ROC recommends the following Z-R relationships:

Winter stratiform precipitation (east of Continental Divide) and orographic rain (East)

$$Z = 130R^{2.0} \tag{5–18}$$

Winter stratiform precipitation (west of Continental Divide) and orographic rain (West)

$$Z = 75R^{2.0} \tag{5–19}$$

Figure 5-1 gives examples of Z-R relationships for various forms of precipitation. As can be seen in Figure 5-1, use of Eq. (5-16) with the WSR-88D hydrologic software should provide a good average for different precipitation types.

Though the multiplicative coefficient chosen for Eq. (5-16) strongly affects the accuracy of the estimates, this coefficient can be adjusted using coincident rain gauge observations (Seo et al. 1999). This was done in establishing the default tropical relationship of Eq. (5-17). Of course this assumes that a reasonable number of rain gages are available under the radar umbrella to satisfactorily removing the mean bias. Also, assuming that the mean bias is removed, the error associated with the exponent is not excessive if a nominal value is chosen (e.g., 1.4) since errors caused by the Z-R relationship tend to cancel as data are averaged over greater space and time scales as shown in Figure 5-2 (Hudlow and Arkell 1978).

Physical mechanisms that can alter particle size distribution and, consequently, a Z-R relationship include: evaporation, accretion, coalescence, breakup, size sorting, and vertical and horizontal wind motion. Non-spherical ice particles and the flattening of raindrops as their size increases can enhance or reduce radar reflectivity measurements several decibels, depending on the radar polarization, and contribute errors to estimates of the precipitation rate. Mixed precipitation types, e.g., rain and hail in thunderstorms or rain and snow, can significantly alter a Z-R relationship. One means of minimizing the hail effect is to impose a maximum threshold on the precipitation rate (often ~ 53 dBZ). The threshold should be based on a maximum precipitation rate that can be expected in a given area. The presence of radar echoes beyond the threshold would then indicate the probability of hail and that specified upper limits of precipitation rate should not be exceeded.

Attempts have been made to determine Z-R variations based on other meteorological information such as storm type and various weather conditions; however, limited benefit was derived for reducing precipitation rate uncertainty (Stout and Mueller 1968).

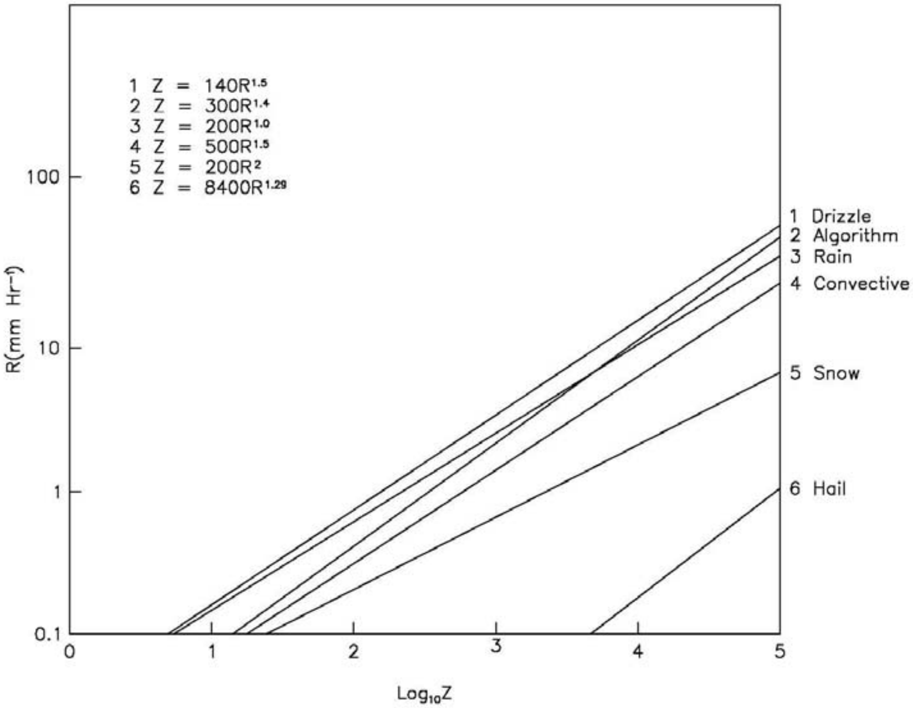

Figure 5-1
Plots of Z-R Relationships Illustrate the Variability of Various Forms of Precipitation

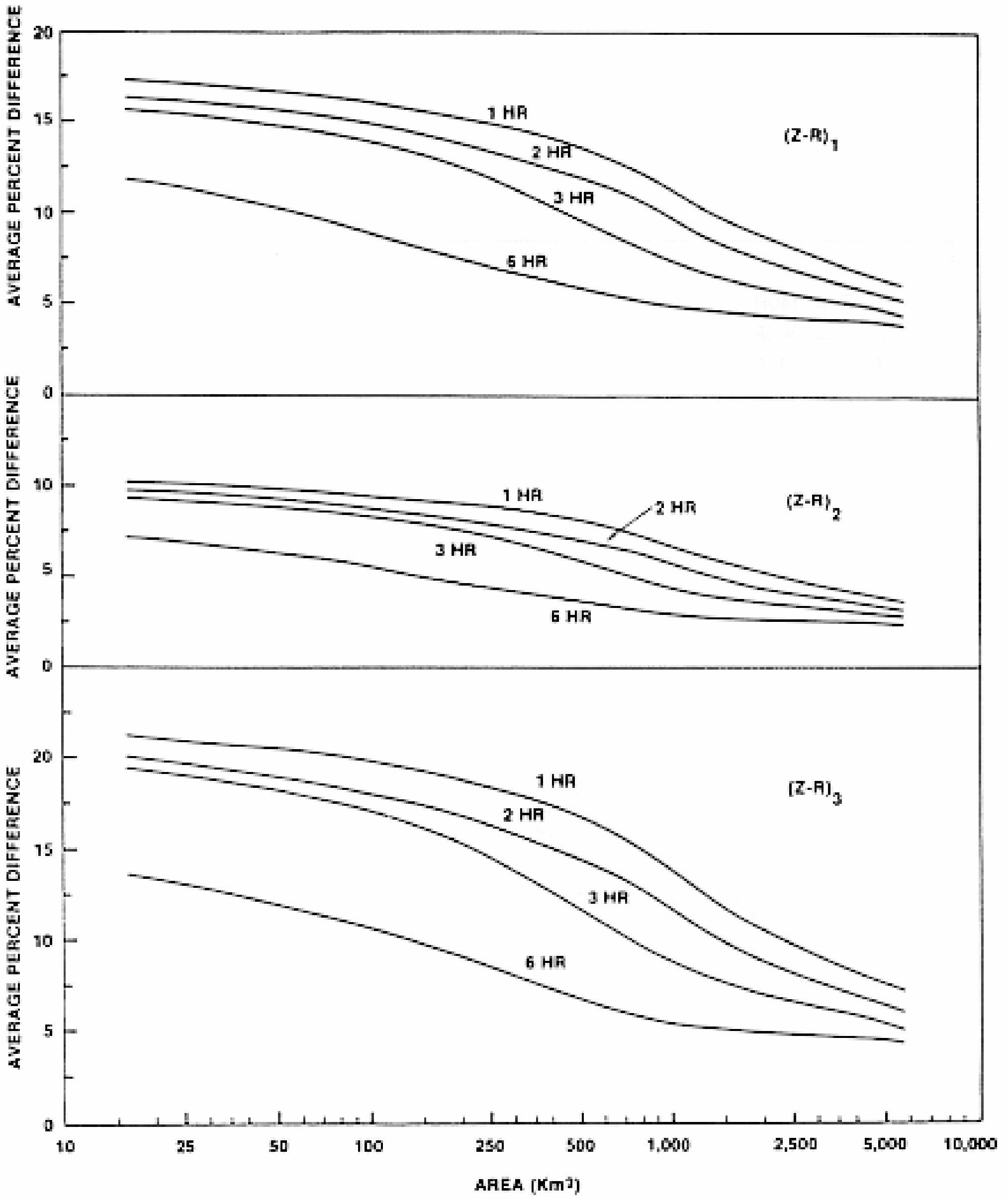

Figure 5-2
Mean Absolute Percent Difference Between Rainfall Estimates
Based on Z-R Relationships

Differences from a Z-R relationship of $Z = 230R^{1.25}$ and $(Z\text{-}R)_1$ of $Z = 170R^{1.52}$, $(Z\text{-}R)_2$ of $Z = 300R^{1.4}$, and $(Z\text{-}R)_3$ of $Z = 200R^{1.6}$, for a range of spatial averaging and temporal integration scales. Phase mean biases were removed before compilation of differences. This figure is based on the analysis of GARP Atlantic Tropical Experiment (GATE) data (Hudlow and Arkell 1978).

The previous discussion assumes that the precipitation estimates are based on radar pulses with a single polarization, usually horizontal. The introduction of dual-polarization capability promises to significantly increase the accuracy of precipitation identification and quantitative measurement (Rhyzhkov and Zrnic 1996). In a dual-polarization system, the separate returned power estimates in both the horizontal and vertical sense can be used to infer the aspect ratio of the backscatterers. For example, small raindrops are nearly spherical, and yield nearly identical backscatter in both channels (Schuur et al. 2001). Larger raindrops tend to be more oblate due to viscous drag effects, and therefore yield significantly larger backscatter in the horizontal channel than in the vertical. The dual-polarization capability also greatly facilitates discrimination among different hydrometeor types, and between hydrometeors and other common targets such as birds, insect, and radar-cloaking chaff.

5.3.3 Time and Space Averaging. WSR-88D data are obtained by scanning in azimuth at a series of low elevation angles and making measurements at discrete range and angular intervals. The equivalent reflectivity factor values are converted to rainfall rate with an appropriate Z-R relationship and accumulated in time to yield a spatial distribution of precipitation depth.

Regardless of the Z-R relationship used, this procedure results in time and space sampling errors. Figure 5-3 illustrates the increase in these errors as the sampling interval is increased over the various averaging areas. For example, the top graph in Figure 5-3 shows for this data set that increasing the sampling interval from 5 to 10 minutes increases the hourly precipitation estimate error on the average of about 5 to 15 percent, depending on the averaging area. For a given sample interval, the percent differences decrease with increasing averaging area and integration time.

5.3.4 Below-Beam Effects. Below-beam effects result from the evaporation or growth of precipitation below the radar beam as well as horizontal motion of descending precipitation. At greater radar ranges with larger sampling volumes and with increasing beam height, the correlation between radar estimated and measured ground-level precipitation diminishes. An extreme example of below-beam effects is total evaporation of precipitating water. Thus, precipitation shown on the radar display at far ranges may not reach the ground at all. Comparison with rain gage observations and other surface synoptic data can offer help in identifying this problem. In many cases, access to other radars closer to the area of rainfall ambiguity is better at estimating accumulated rainfall than a distant radar.

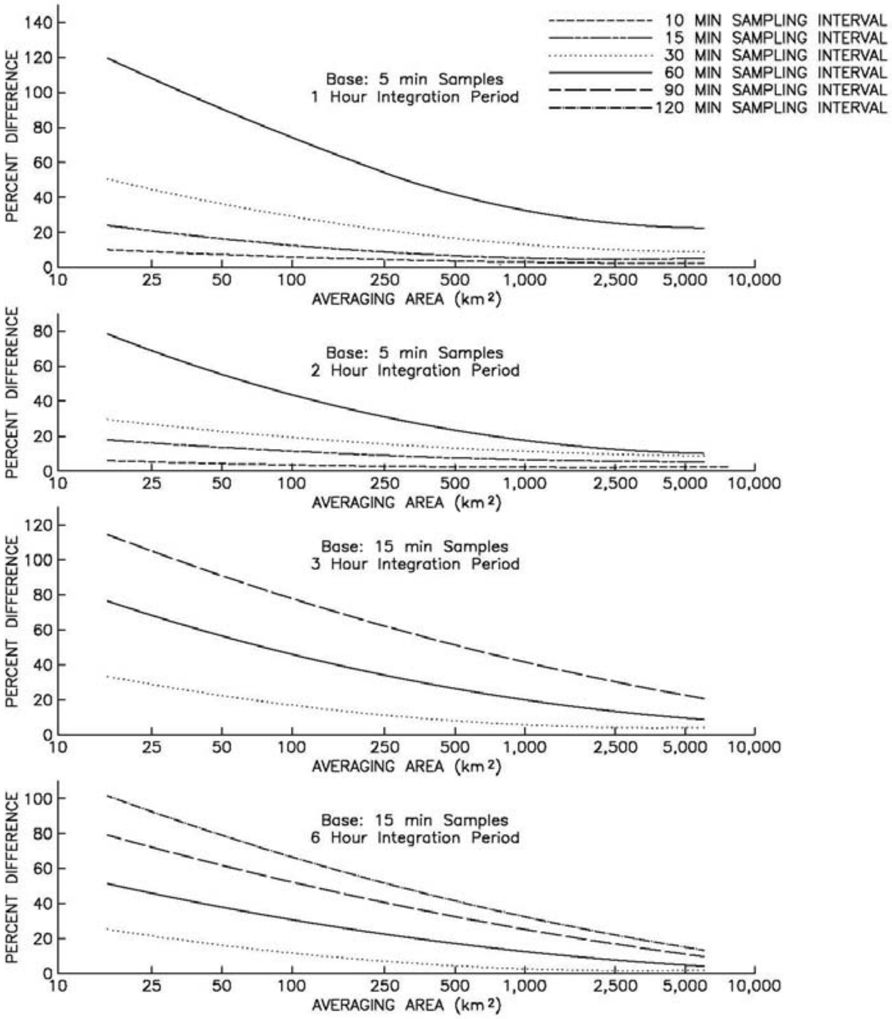

Figure 5-3
Mean Absolute Percent Difference Between Rainfall Estimates Based on Sampling

Upper two panels: Using five-minute base sampling intervals and those from coarser sampling intervals for spatial averaging and temporal integration scales. Lower two panels: Same as upper two, except 15-minute base sampling interval was used and longer integration periods were included. This figure is based on the analysis of GARP Atlantic Tropical Experiment (GATE) data (Hudlow and Arkell 1978).

5.3.5 Effects of the Vertical Reflectivity Profile. In addition to near-surface evaporation or raindrop growth below the radar beam, precipitation systems generally feature a nonuniform reflectivity profile in the vertical. Most surface rainfall originally forms as snow above the freezing level. In stratiform rain situations, the radar detects dry snowflakes at longer ranges where the lowest beam is centered above the freezing level. Since ice hydrometeors return less radio power than liquid water, the estimated rainfall rate is significantly smaller than that observed at the surface. There is enhanced reflectivity due to melting, water-coated snowflakes in the layer just below the freezing level, and thus where the lowest beam intersects the melting layer the surface rain rate is overestimated (the bright-band effect). These effects become apparent with increasing radar range, and are often referred to collectively as range effects.

Correction for range effects is possible through the application of a climatic vertical profile, or through objective identification of the profile in real time, based on volumetric scanning. Both methods have achieved some success (Seo et al. 2000).

5.4 Adjustment of Radar-Derived Precipitation Estimates.

Very large storm-to-storm and within storm errors in radar precipitation estimates can result from error sources described above. Errors of up to a factor of 2 are not uncommon; errors up to a factor of 5 or more sometimes occur (of course, as illustrated above, many factors affect the magnitude of the errors, especially the spatial and temporal scales over which the precipitation estimates are averaged). These errors can be reduced to various degrees by a number of adjustments and corrections to the radar-derived precipitation estimates. The simplest of these adjustments are applied to the radar parameter itself. More sophisticated procedures combine radar estimates with other hydrological and meteorological data. These adjustments are described in the following sections.

5.4.1 Adjustments Using Radar Parameters Alone. Many of the error sources discussed in Section 5.3 can be reduced by quality control and adjustment procedures operating on the radar data alone. Examples include the following:

- Oxygen absorption corrections
- Assignment of zero values to all reflectivities below a given noise threshold
- Ground clutter suppression procedures
- Corrections for beam blockage
- Isolated bin and other outlier checks
- Use of multiple elevation angles
- Adjustment of Z-R relationship for precipitation type and/or climatology and season

The precipitation estimation procedures of the WSR-88D employ many of these quality control and adjustment procedures (Part C, Chapter 3, of this Handbook).

5.4.2 Adjustment with Rain Gages. Techniques for adjusting radar precipitation estimates with rain gage observations take advantage of the superior ability of the radar to sample comprehensively the temporal and spatial precipitation distribution and the ability of the rain gages to measure relatively accurately the precipitation depth at the surface. Such adjustment, if carried out properly, will reduce errors in radar precipitation estimates caused by all the factors described previously, including those caused by an inadequate Z-R relationship (Anagnostou et al. 1998; Seo et al. 1999).

One must keep in mind that even if there were no actual errors in either gage or radar measurements, there are still discrepancies that result from differences in sampling mode (Anagnostou and Krajewski 1999). The radar beam and pulse volume samples instantaneously a large volume of atmosphere that may be several thousands of feet above ground and may have a surface projection of more than a square mile. The radar measurements are repeated at intervals of 4 to 10 minutes. The gage continuously records precipitation falling on an area that is smaller than a square foot. Precipitation intensity often varies significantly over distances of less than a mile and may change during time intervals of less than a minute. Therefore, the precipitation sampled by the gage may not be representative of that in the entire area beneath the radar-sampled volume. (Additionally, wind flow over rain gages and gage sampling techniques will also contribute to gage errors.) Similarly, rain rates observed instantaneously by the radar in any given measurement bin may not be representative of intensities during the intervals between observations (Austin 1987). These sampling-related discrepancies are very important to procedures that adjust radar estimates to match gage data. Techniques that force agreement at a few gage sites and extend the correction outward to adjacent measurement bins are especially sensitive to these discrepancies.

Intuitively, we expect the radar, even if only roughly calibrated, to measure the precipitation over the entire area observed by the radar to be better than a single gage. Conversely, if the network of calibrating gages were very dense under the entire radar umbrella, we would not expect the addition of radar to provide significant improvement (Wilson and Brandes 1979).

Procedures used to adjust radar precipitation estimates with rain gage data involve a variety of spatial adjustment techniques; some of the more notable will be discussed next.

5.4.2.1 Single-Parameter Rain Gage Data Adjustments. The simplest class of adjustments compares radar with rain gages to come up with a single "correction factor" that is then applied uniformly to the radar precipitation estimate**.** A common approach has been to compute the mean radar bias by averaging the sum of the Gage/Radar (G/R) ratios over some interval of time. Two major issues are whether the single correction factor is assumed to change with time and whether the procedure for estimating the correction factor is suitable for real-time applications (as opposed to post analysis). The adjustment procedure planned for eventual use in the WSR-88D hydrologic software is in the class of time-varying, single-parameter rain gage data adjustments and is described in Part C, Chapter 3, of this Handbook.

5.4.2.2 Multi-parameter Rain Gage Data Adjustment. Various multiparameter procedures have been devised to combine radar observations routinely with distributed calibrating gages. With some procedures, local adjustments are made by computing G/R ratios at nearby calibration sites and then extrapolating the appropriate weights inversely by distance. In essence, the radar observations are molded to the gage observations by a plane-fitting technique while retaining the radar-indicated precipitation variability between gages. More sophisticated multivariate objective analysis approaches are also possible. A common multivariate objective analysis approach involves an optimal interpolation procedure that merges the radar and rain gage data in a multivariate analysis framework (Seo and Breidenbach 2002).

While multi-parameter rain gage data adjustments offer the promise of higher quality precipitation estimates, they are more computational demanding (sometimes much more) than single-parameter methods. They also tend to be more sensitive to the distribution in space and the accuracy of each gage data value used. For these reasons, the WSR-88D does not use multi-parameter rain gage data adjustments. However, such multivariate techniques have been implemented within the Advanced Weather Interactive Processing System (AWIPS), and have been used successfully as input to hydrologic models (Seo 1998).

5.4.3 Adjustments with Other Data. Clearly, the most accurate possible estimates of precipitation would optimally combine all available sources of information (e.g., radar, rain gage, satellite imagery, soundings, and surface data). Such a processing system would have to be extremely sophisticated, but the first steps in this direction will probably use satellite data along with radar and gage data. These types of procedures are considered to be outside the scope of the processing of the WSR-88D.

5.5 Concluding Remarks.

As has been shown in the preceding discussion, there are many limitations in trying to correlate equivalent radar reflectivity factor with precipitation rate. Radar error patterns suggest that discrepancies occur from storm-to-storm in a systematic and perhaps predictable manner. The search for systematic error patterns and causes holds promise, but until this knowledge can be applied fully to radar measurements, the use of gage data to calibrate radar data is the most promising approach. Such approaches, however, must be applied with great care, and the adjustment procedure adopted must be formulated to ensure numerical stability and physically meaningful corrections.

The current operational WSR-88D processing system (Fulton et al. 1998) features many internal quality control measures and can be adapted to use several Z-R relationships. Radar-only precipitation estimates are likely to become substantially more accurate with the introduction of dual-polarization capabilities in the 2009 time frame.

REFERENCES

Anagnostou, E. N, W. F. Krajewski, D.-J. Seo, Dong-Jun, and E. R. Johnson, 1998: Mean-field rainfall bias studies for WSR-88D. *J. of Hydrologic Engrg,* **3**, 149-159.

Anagnostou, E. N., and W. F. Krajewski, 1999: Uncertainty quantification of mean-areal radar-rainfall estimates. *J. Atmos. Oceanic Technol.,* **16**, 206-215.

Ahnert, P. R., M. D. Hudlow, E. R. Johnson, D. R. Greene, and M. Diaz, 1983: Proposed "on-site" precipitation processing system for NEXRAD, Preprints, *21st Conference on Meteorology*, Edmonton, Canada, Amer. Meteor. Soc., 378-385.

Austin, Pauline M., 1987: Relation between Measured Radar Reflectivity and Surface Rainfall. *Mon. Wea. Rev*., **115,** 1053-1070.

Battan, L. J., 1973: *Radar Observations of the Atmosphere*. Univ. of Chicago Press, 323 pp.

Cairns, M.A., Huggins, and S. Vasiloff, 1998: Precipitation algorithm improvements in the Eastern Sierra. NWS Western Region Technical Attachment, No. **98-08**, Salt Lake City, UT, 5 pp.

Douglas, R. H., 1963: *Size distribution of Alberta hail samples*. Sci. Rept. MW-36. Montreal: Stormy Weather Group, McGill Univ., 71 pp.

Hudlow, M., and R. Arkell. 1978: Effect of Temporal and Spatial Sampling Errors and Z-R Variability on Accuracy of GATE Radar Rainfall Estimates. Preprints*, 18th Conference on Radar Meteorology*, Atlanta, GA*,* Amer. Meteor. Soc. 342-349.

Hudlow, M. D., R. Arkell, V. Patterson, P. Pythowany, F. Richards, and S. Goetis, 1979: *Calibration and intercomparison of the GATE C-band radars.* NOAA Tech. Report EDIS 31, NTIS, Springfield, VA.

Huggins, A. and D. Kingsmill, 1998: Improvements of WSR-88D algorithms in the intermountain west with applications to flash flood forecasts and wintertime QPFs. CIASTA Annual Report on Progress under Task II: Weather Research, Desert Research Institute, Dandini Research Park, Reno, NV, 26 pp.

Joss, J. K., K. Schram, J. D. Thams, and A. Waldvogel, 1970: *On the quantitative determination of precipitation by radar.* Wissenschaffliche Mineilungen Nr. 63, Eidgenossisichen Komission Zum Studium der Hagelbildung und der Hagelawehr, 38 pp.

Marshall, J. S., and W. M. Palmer, 1948: The distribution of raindrops with size. *J. Appl. Meteor*., **5,** 165-166.

Martner, B. E., 1977: A field experiment on the calibration of radars with raindrop disdrometers. *Appl. Meteor*., **16,** 451-454.

Quinlan, J.S. and E.J. Sinsabaugh, 1999: An evaluation of the performance of the snow algorithm at NWFO Albany, NY during the 1997-98 winter season. Preprints, *29th Int. Conf. on Radar Meteorology.,* Montreal, Quebec, CA, Amer. Meteor. Soc., 794-979.

Schuur, T. J., A. V. Ryzhkov, D. S. Zrnić, and M. Schönhuber, 2001: Drop size distributions measured by a 2D video disdrometer: Comparison with dual-polarization radar Data. *J. App Meteo.*, **40**, 1019-1034.

Seo, D. J., J. P. Breidenbach, and E. R. Johnson, 1999: Real-time estimation of mean field bias in radar rainfall data. *J. Hydrology*, **223**, 131-147.

Seo, D. J., 1998: Real-time estimation of rainfall fields using radar rainfall and rain gage data. *J. Hydrology*, **208**, 37-52.

Seo, D. J., J. Breidenbach, R. Fulton, and D. Miller, 2000: Real-time adjustment of range-dependent biases in WSR-88D rainfall estimates due to nonuniform vertical profile of reflectivity. *J. Hydrometeorology*, **1**, 222-240.

Seo, D. J., and J. P. Breidenbach, 2002: Real-Time Correction of Spatially Nonuniform Bias in Radar Rainfall Data Using Rain Gauge Measurements. *J. Hydrometeorology*, **3**, 93-111.

Stout, G. E., and E. A. Mueller, 1968: Survey of relationships between rainfall rate and radar reflectivity in the measurements of precipitation. *J. Appl. Meteor*., **7,** 465-474.

Wilson, J. W., 1975: *Radar-gage precipitation measurements during the IFYGL.* The Center for the Environment & Man, Inc., Report 4177-540.

Wilson, J. W., and E. A. Brandes 1979: Radar measurement of rainfall--a summary. *Bull. Amer. Meteor. Soc.*, **60,** 1048-1058.

CHAPTER 6

INTERPRETATION OF DOPPLER VELOCITY PATTERNS

6.1 **Introduction.** Although a single Doppler radar observes only the component of the wind in a radial direction from the radar, a wide variety of weather features of great importance can be identified. In this chapter, subjective and objective interpretations of Doppler velocity patterns produced by vertical and horizontal variations of simulated horizontal wind fields are discussed. For the simulated WSR-88D data, Doppler velocity data points were produced at 1.0^o increments in the azimuthal direction and 0.13 nm (0.25 km) increments in range. With interest in signature interpretation, an infinitesimally narrow radar beam was used for the simulations so there would not be the increased smearing with range that ordinarily occurs since beam width broadens with increasing range.

Online:

- (From the University of Illinois) Interpreting Doppler Radar Velocities: speed shear wind patterns.

  http://ww2010.atmos.uiuc.edu/(Gh)/guides/rs/rad/ptrn/ptrn1.rxml

- (From the Weather Decision Training Branch) Go to the updated version of the IC5.4.

  http://wdtb.noaa.gov

6.2 Patterns Due to Vertical Variations of the Wind.

Winds that vary with height produce Doppler velocity patterns on a display at a constant elevation angle that can be uniquely interpreted. In these situations, the radar return may be from some combination of refractivity gradients, insects, and/or particulate matter in optically clear air (Appendix B) or from wide-spread stratiform precipitation. Random noise was added to the simulated Doppler velocity fields to produce more realistic looking Doppler velocity displays.

Consider, for instance, a vertical wind profile where the speed is a constant 45 kts (23 ms^{-1}) and the direction changes uniformly from southerly at the ground to westerly at a height corresponding to the edge of the display (Figures 6-la and b). With the center of the display representing the radar location, winds that have a component away from the radar have a positive Doppler velocity value (red and orange in Figure 6-1d). Those toward the radar have a negative Doppler velocity value (blue). When the wind direction is normal to the radial direction from the radar, the Doppler velocity component is zero (gray).

Figure 6-lc indicates how to interpret wind direction along the gray zero Doppler velocity band.

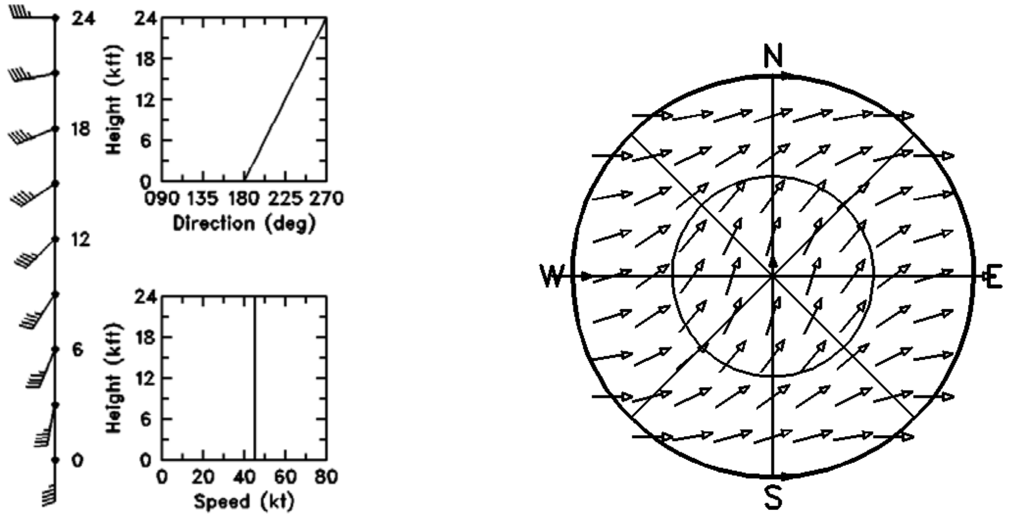

(a) Wind profile

(b) Winds on PPI surface

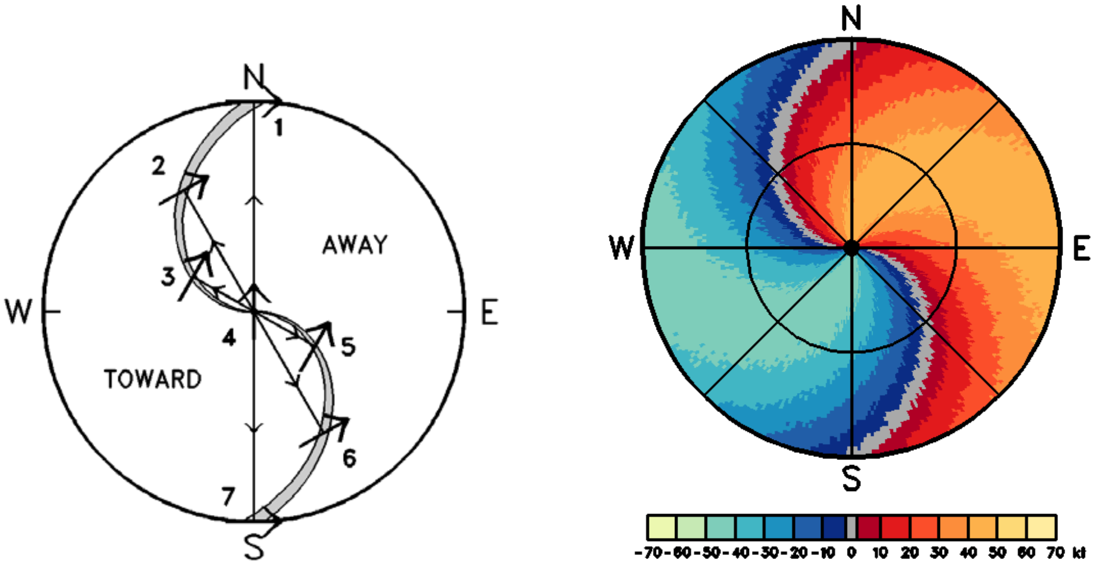

(c) Interpretation of display

(d) Doppler velocity display

Figure 6-1
Environmental Wind

Vertical profile (a) of uniform wind speed (45 kts, 23 ms^{-1}) that veers with height and (b) corresponding horizontal wind vectors on a conical Plan Position Indicator (PPI) surface where height increases from the center of display (ground level) outward. Interpretation of wind direction along the zero Doppler velocity (gray) band in (d) is shown in (c) where bold arrows represent wind vectors. Positive Doppler velocities (red, orange) represent flow away from the radar (at center of display) and negative Doppler velocities (blue) represent flow toward radar.

The presence of the zero band indicates that the wind direction is perpendicular to the radial viewing direction from the radar at that location (that is, wind direction is tangent to the circle at that radius). For example, along the outer edge of the display, the Doppler velocity is zero when the radar points toward the north (point 1) and the south (point 7). This means that the wind is blowing either from west to east or from east to west at the height corresponding to the edge of the display. Since Doppler velocities are negative (component toward the radar) along the western edge of the display and positive (component away from the radar) along the eastern edge, the wind obviously is blowing from west to east at the height of the edge of the display.

When the radar aims toward point 2 on the zero band, it is pointing toward 330°. The wind direction at that point is 330° ± 90°. Since the wind is blowing generally from west to east, the wind at point 2 must be from 330° - 90° = 240°. Similar arguments at points 3, 5, and 6 result in wind directions of 300° - 90° = 210°, 120° + 90° = 210°, and 150° + 90° = 240°, respectively. At the radar location on the ground (point 4), the zero band is oriented east-west. Since the wind is approaching the radar from the south, wind direction is from 180°.

Wind speed at a given height (slant range) is determined by the extreme Doppler velocity values around a constant slant range circle. In Figure 6-1d, maximum flow away from the radar (light orange) and maximum flow toward the radar (light blue) indicate that wind speed is constant from the ground to the height corresponding to the edge of the display. Thus, the Doppler velocity pattern in Figure 6-ld uniquely represents an environmental wind profile where wind speed is constant and wind direction veers uniformly from southerly at the ground through southwesterly to westerly at the edge of the display.

Doppler velocity displays corresponding to a variety of vertical profiles of wind speed and direction are shown in Figure 6-2. When wind speed is constant (non-zero) with height (Figures 6-1d and 6-2a), all of the color velocity bands converge to the radar location at the center of the display. Curvature of the zero Doppler velocity band indicates the change of wind direction with height. Veering winds produce an S-shaped profile (Figure 6-1d) and backing winds produce a backward S-shaped profile (Figure 6-2c). When the wind direction veers then backs with height, an S-shaped profile changes into a backward S-shaped profile with increased range from (height above) the radar (Figure 6-2a).

Doppler velocity patterns associated with the same wind direction at all heights always have a straight zero line (Figure 6-2b). The rest of the pattern reflects the vertical profile of the wind speed. When a wind speed maximum exists within the height interval represented by the display, a pair of quasi-elliptical bull's-eyes appears on the display (Figure 6-2b). The centers of the bull's-eyes are positioned upwind (negative) and downwind (positive) of the radar at the slant range equivalent to the height of the wind maximum. Note that only the zero band passes through the radar location at the center of the display when wind speed is zero at the ground and increases with height.

When wind speed at the ground is less than the maximum value (but still greater than zero), those colors corresponding to wind speeds less than or equal to the surface value converge to the center of the display (Figure 6-2c). Those colors corresponding to greater speeds converge toward the center but never reach it. With wind direction varying with height, the bull's-eye pattern of Figure 6-2b becomes distorted.

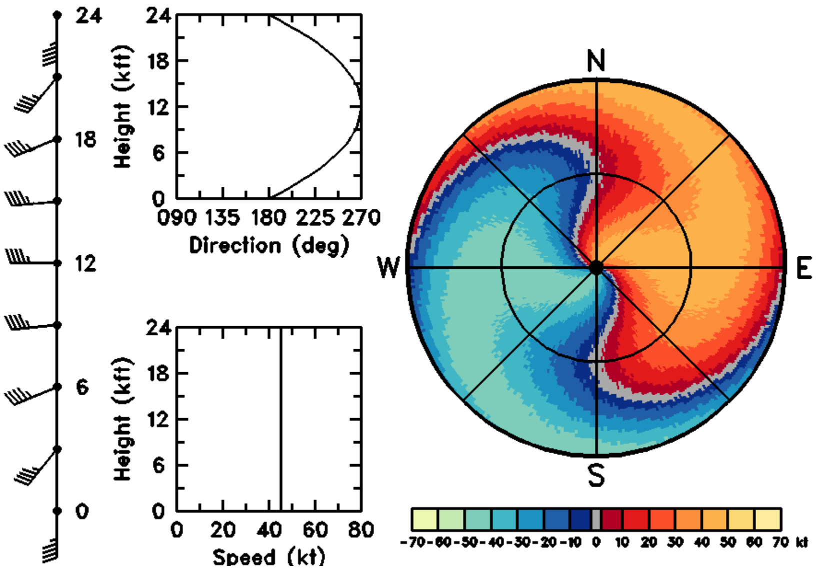

(a) Constant wind speed; wind direction veering, then backing

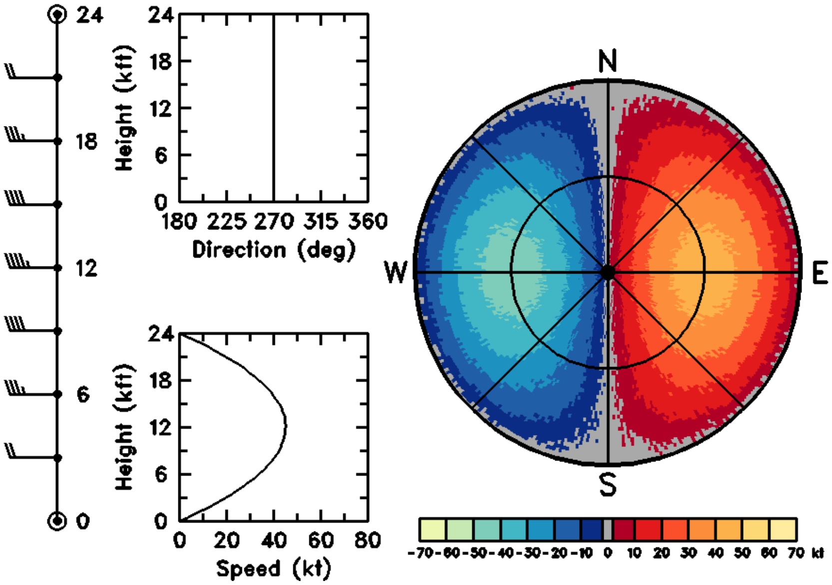

(b) Constant wind direction, middle-altitude speed maximum

Figure 6-2
Variety of Doppler Velocity Displays

Doppler velocity displays corresponding to (a) constant wind speed 45 kts(23 ms^{-1}) with veering at lower altitudes and backing at higher altitudes. (b) Constant wind direction (270°) and middle-altitude speed maximum with calm winds at the ground (display center) and edge of display.

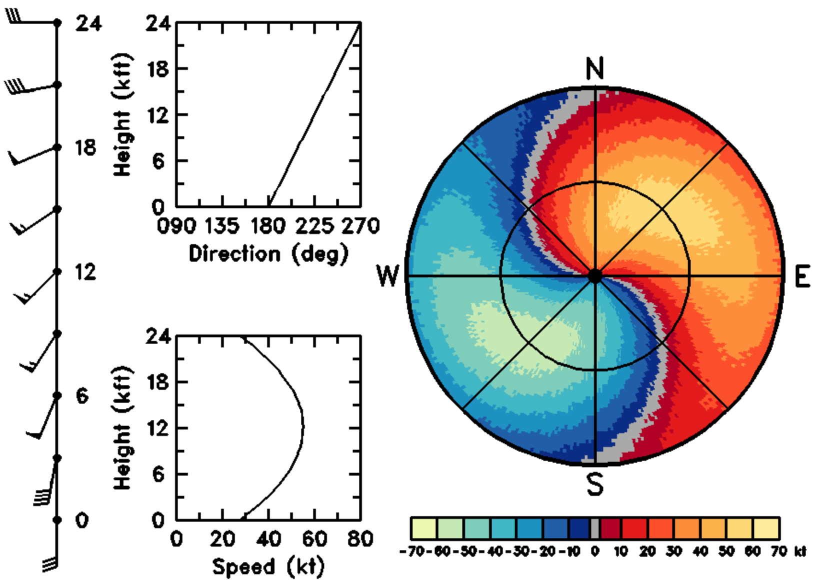

(c) Veering wind direction with middle-altitude speed maximum

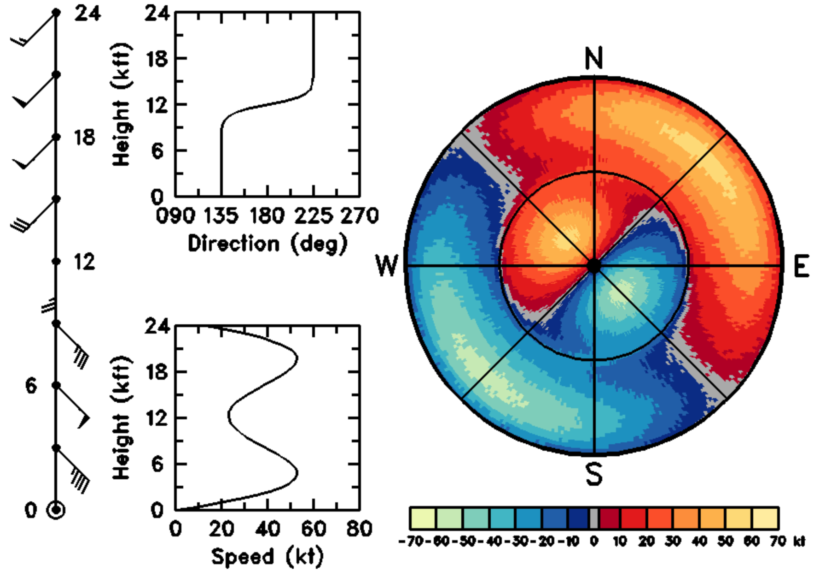

(d) Two-layer wind regime, each having constant wind direction and a speed maximum

Figure 6-2
Variety of Doppler Velocity Displays
(concluded)

(c) Veering wind direction and middle-altitude speed maximum 55 kts (28 ms^{-1}) with 30 kts (23 ms$^{-1)}$ winds at the ground and edge of display. (d) Two-layer wind regime with each layer having constant wind direction and a speed maximum 55 kts (28 ms^{-1}) in mddle of layer.

Figure 6-2d illustrates an example of Doppler velocity fields through a horizontal surface that separates two different atmospheric flow regimes. There is a wind speed maximum within each wind regime and wind directions differ by 90°. The discontinuity region could represent a frontal surface or it could represent the top of the boundary layer in clear air. Note the variation of the zero Doppler velocity band. It is oriented northeast-southwest through the center of the display indicating a constant wind direction in the lower layer. The inner pair of bull's-eyes indicates that the wind is blowing from the southeast to the northwest at 50–60 kts (26–31 ms^{-1}). The zero velocity band indicates a 90° shift in wind direction through a narrow height interval, with the wind direction becoming constant again above the discontinuity region. The second pair of bull's-eyes indicates that the upper layer winds are from the southwest at 50–60 kts (26–31 ms^{-1}).

There are two important points to remember when attempting to interpret Doppler velocity patterns such as those in Figures 6-2a through d. The first point is that the vertical profile of wind speed is responsible for producing the overall pattern. The surface wind speed is equal to the largest Doppler velocity color band that converges to the radar location at the center of the display. The second point is that the vertical profile of wind direction controls curvature of the color bands. The most informative velocity for interpreting wind direction is the zero Doppler velocity band.

Discontinuities in Doppler velocity patterns frequently are associated with frontal boundaries. With adequate signal return, it is possible to determine characteristics of the flow field both ahead of and behind a front. For example, the pattern in Figure 6-3d clearly indicates that the frontal zone is marked by a rapid change of Doppler velocity over a narrow transition region. As indicated in Figures 6-3a through c, the wind backs and increases in speed with height behind the front and veers and increases with height ahead of the front.

6.3 Quantitative Measurements of Vertical Profiles of the Horizontal Wind. The qualitative interpretation of single Doppler velocity patterns obtained by rotating the radar antenna at one elevation angle has been discussed in Section 6.2. This section investigates a technique for making quantitative measurements from the same data in either optically clear air or widespread precipitation at multiple elevation angles. For this approach, the velocity field is assumed to vary linearly in space. Also, the vertical air motion is assumed to be negligible. The Velocity Azimuth Display (VAD) Algorithm that makes these quantitative measurements on an operational basis is discussed in Part C of this Handbook.

The basic radar scanning geometry is shown in Figure 6-4a. The Doppler velocity, v_d, measurement at height $h = r \sin \alpha$, can be computed from:

$$V_d = V_t \sin \alpha - V_h \cos \alpha \cos \beta,$$

where V_h is the horizontal wind velocity (a positive quantity) at height h and azimuth angle β measured from the upwind direction (maximum flow toward the radar), V_t is the terminal fall velocity (a negative quantity) for precipitation particles in the absence of vertical air motion, and α indicates the elevation angle of the radar antenna.

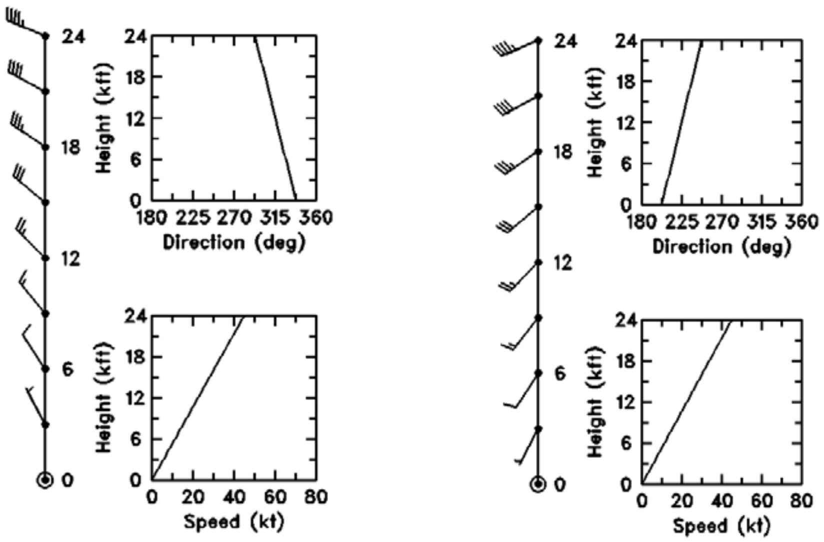

(a) Behind front (b) Ahead of front

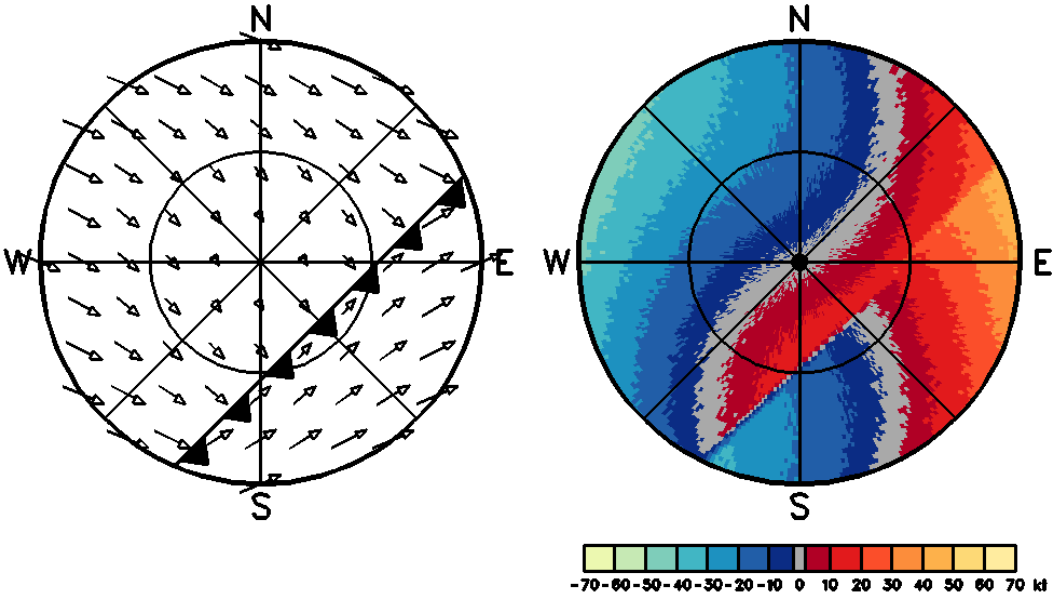

(c) Winds on PPI surface (d) Doppler velocity display

Figure 6-3
Frontal Discontinuity

Vertical profiles of (a) backing winds that increase speed with height behind front and (b) veering winds that increase speed with height ahead of front. Doppler velocity values on PPI display in (d) correspond to Doppler components of wind vectors (length proportional to speed) in (c). Positive Doppler velocities (red, orange) are away from the radar (at center of display) and negative velocities (blue) are toward the radar.

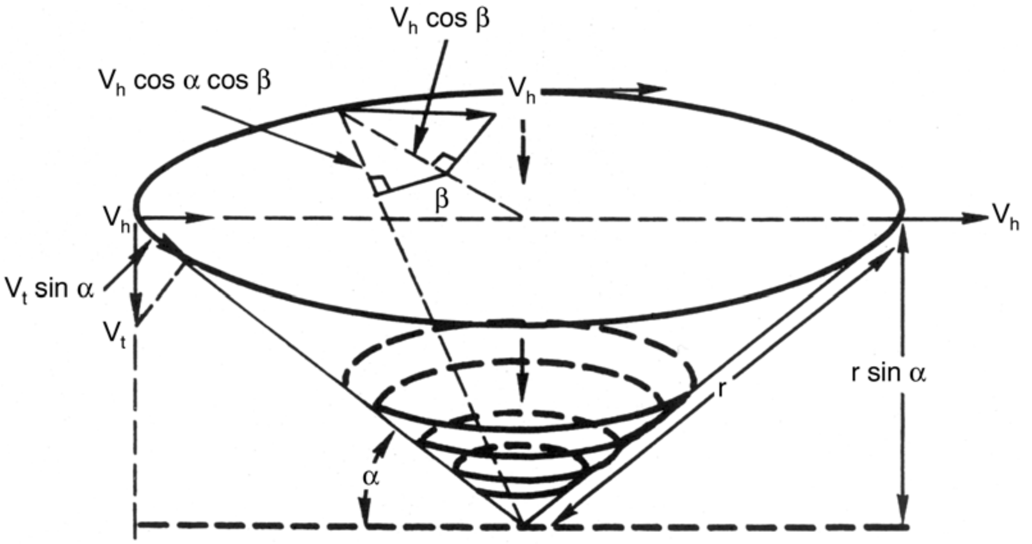

(a) Geometry of VAD scan

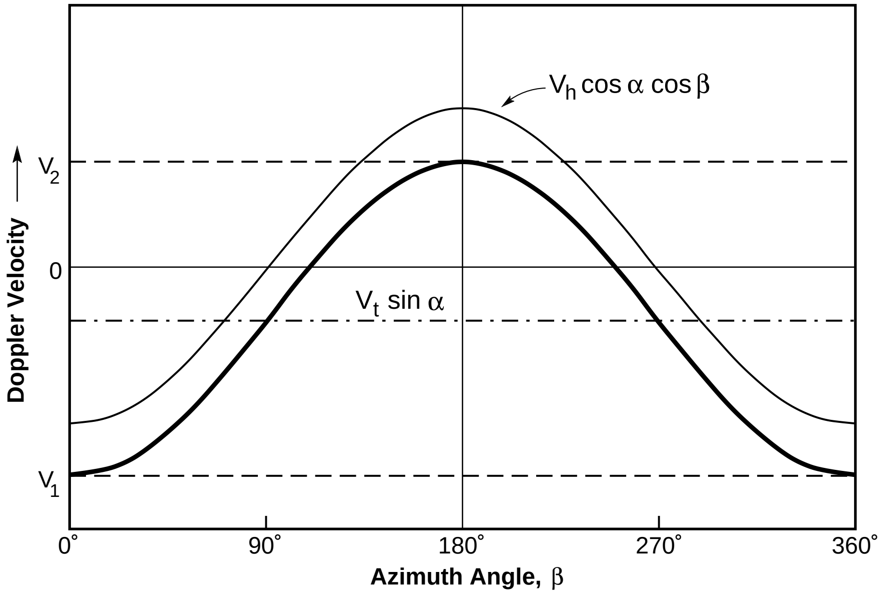

(b) Velocity Azimuth Display

Figure 6-4
Wind Measurements Using the VAD Technique

The thicker sinusoidal curve in (b) represents Doppler velocity values as a function of azimuth, β, measured in (a) at slant range, r, and elevation angle, α. The thicker curve is the sum of the Doppler component of the uniform environmental wind ($V_h \cos \alpha \cos \beta$, thin sinusoidal curve) and the Doppler component of the precipitation terminal fall velocity ($V_t \sin \alpha$, dash-dot line). After Atlas (1964).

If the horizontal wind and terminal fall velocity are constant around the scanning circle, Doppler velocity will vary sinusoidally as the radar antenna rotates through 360°. The plot of Doppler velocity as a function of azimuth in Figure 6-4b is called a velocity azimuth display (VAD). The sinusoidal curve will be off centered by an amount $v_t \sin \alpha$ due to the contribution of the terminal velocity of the precipitation particles. When the antenna points upwind ($\beta = 0$), the Doppler velocity value is:

$$v_1 = (v_t \sin \alpha - v_h \cos \alpha) < 0 .$$

and when the antenna points downwind ($\beta = 180°$), the value is:

$$v_2 = (v_t \sin \alpha + v_h \cos \alpha) > v_1 .$$

Combining these equations, velocity at height h is:

$$\hat{v}_h = \frac{v_2 - v_1}{2\cos\alpha}$$

By making similar computations at a number of heights along the radar beam, a vertical profile of environmental winds is produced.

One finds that the variation of Doppler velocity with azimuth at a constant height is not exactly sinusoidal. If the terminal velocity of the scatterer is assumed to be uniform around the scanning circle (as in the case of clear air or stratiform precipitation), divergence also can be computed across the circle (Browning and Wexler 1968). This quantity is included in the VAD algorithm discussed in Part C, Chapter 3, of this Handbook.

6.4 <u>Patterns Associated with Convective Storms</u>. Doppler radar data collected in convective storms can be displayed in windows covering a limited area of interest. Here we display horizontal flow fields and corresponding Doppler velocity patterns within a 27 x 27 nm (50 x 50 km) window located 65 nm (120 km) due north of the radar (Figure 6-5). Except as noted, the simulated flow fields represent basic features without the addition of environmental winds and storm motion.

Horizontal variations of the wind within convective storms produce single Doppler velocity patterns that reveal important storm characteristics. Two important storm features are those of axisymmetric rotation and axisymmetric divergence as shown in Figure 6-5. In both cases, the flow is zero at the center, increases linearly to a maximum value at core radius, r_c, and then decreases beyond r_c, with the change being inversely proportional to distance from the center as indicated by the Rankine combined velocity profile in Figure 6-6.

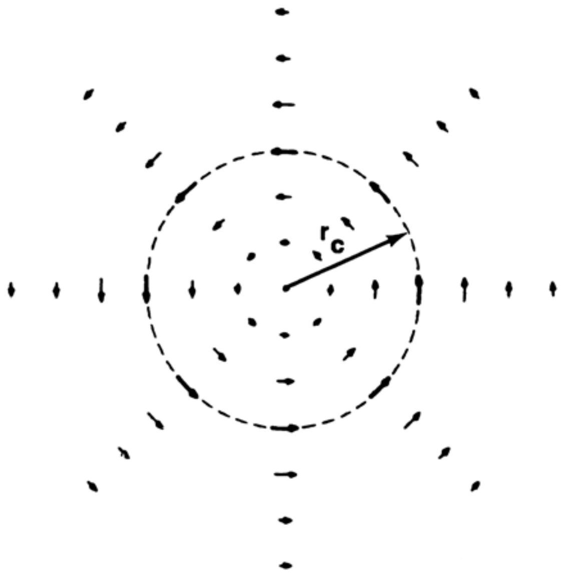

(a) Axisymmetric rotation

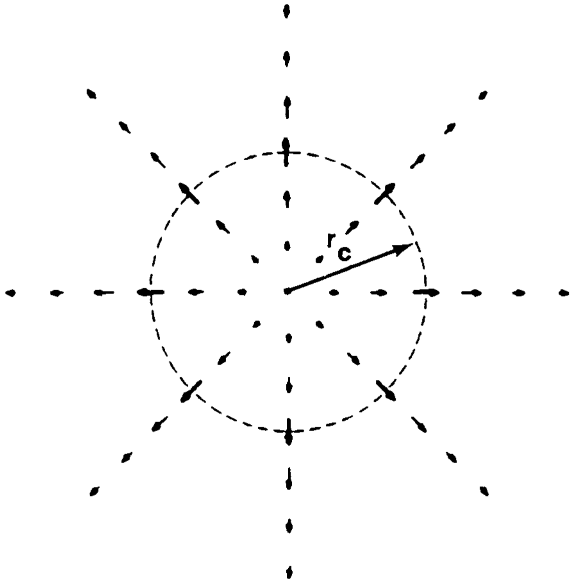

(b) Axisymmetric divergence

Figure 6-5
Horizontal Axisymmetric Flow Fields

Bold arrows represent maximum wind velocities at core radius, r_c, of axisymmetric (a) rotation and (b) divergence fields having Rankine combined velocity profiles (see Figure 6-6). Vector length is proportional to speed.

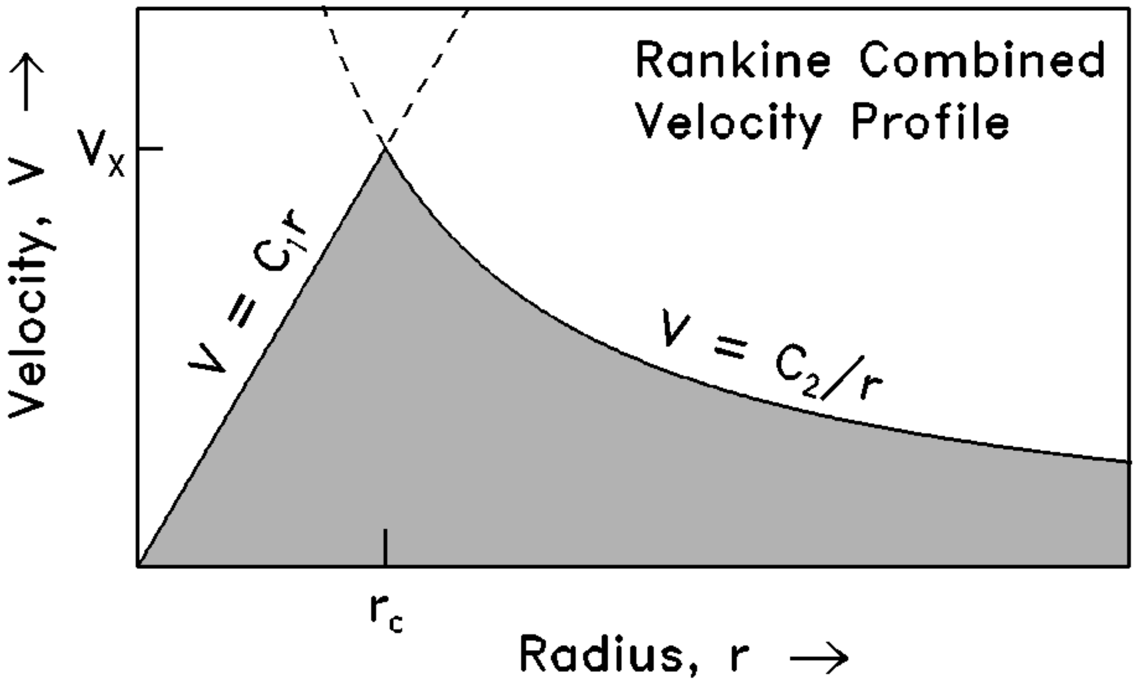

Figure 6-6
Combined Rankine Velocity Profile

Maximum velocity, V_x, occurs at core radius, r_c. Constant C_1 equals V_x/r_c and constant C_2 equals $V_x\ r_c$.

The rotation field in Figure 6-5a is a good approximation for the mesocyclone that is a prominent feature of the supercell stage of severe thunderstorms. When a distant Doppler radar scans through a mesocyclone to the north of the radar, patterns similar to those in Figure 6-7 are produced. Since a Doppler radar senses only the component of flow in the radar viewing direction, the gray area in Figure 6-7a represents zero Doppler velocity because flow there is perpendicular to the viewing direction. To the right of the mesocyclone center, flow is away from the radar (red, orange). To the left of the center, flow is toward the radar (blue). Whereas a Doppler radar senses none of the flow when viewing a vortex through the circulation center, it senses the complete flow on both sides of the center where flow is directly toward or away from the radar.

Therefore, the single Doppler velocity signature of a mesocyclone (or any vortex) has a pattern that is symmetrical about the radar viewing direction through the vortex center and has peak values of opposite sign at the core radius, r_c, either side of the center. When the vortex is embedded in a uniform motion field (representing some combination of environmental wind and mesocyclone movement), the circulation is no longer circular but the basic *vortex signature pattern* remains unchanged (Figure 6-7b); the only difference is that the colors have changed and the center of the signature no longer has a Doppler velocity value of zero. Note that the apparent rotation center in the combined flow field (left side of Figure 6-7b) is displaced to the left of the center of the vortex signature pattern (black dot). Algorithms that are used for detecting mesocyclones include the legacy Mesocyclone Algorithm and the more recent Mesocyclone Detection Algorithm is discussed in Part C of this Handbook.

The axisymmetric divergence field in Figure 6-5b also is a good approximation for divergence in the upper region of thunderstorm updrafts and within downdrafts near the ground. This field is reproduced in Figure 6-8a, along with the corresponding single Doppler velocity pattern. Note that the divergence signature is similar to a mesocyclone signature that has been rotated counterclockwise by 90°. Here the zero region is aligned perpendicular to the radar viewing direction because the radar does not sense motion toward the left or right of the divergence center. Maximum flows toward and away from the radar are measured along the viewing direction that passes through the divergence center; these peak velocities occur at the core radius. When the divergence field is embedded in a uniform motion field (representing some combination of environmental wind and motion of the divergence pattern), the flow field changes and the Doppler velocity values change but the basic Doppler velocity *pattern* remains unchanged.

For the mesocyclone and divergence Doppler velocity patterns discussed thus far, the radar was located 65 nm (120 km) south of the center of the flow features. When the features are much closer to the radar, the patterns become more distorted. We now investigate convergence patterns that are like divergence patterns, except that the positive and negative Doppler velocities are reversed. In Figure 6-9a, the radar is only 10 nm (19 km) south of the center of the mesocyclone (left) and the convergence region (right). The weaker Doppler velocities associated with the mesocyclone signature extend southward and converge at the radar position. The boundaries between colors in the core region are along imaginary lines radiating out from the radar location.

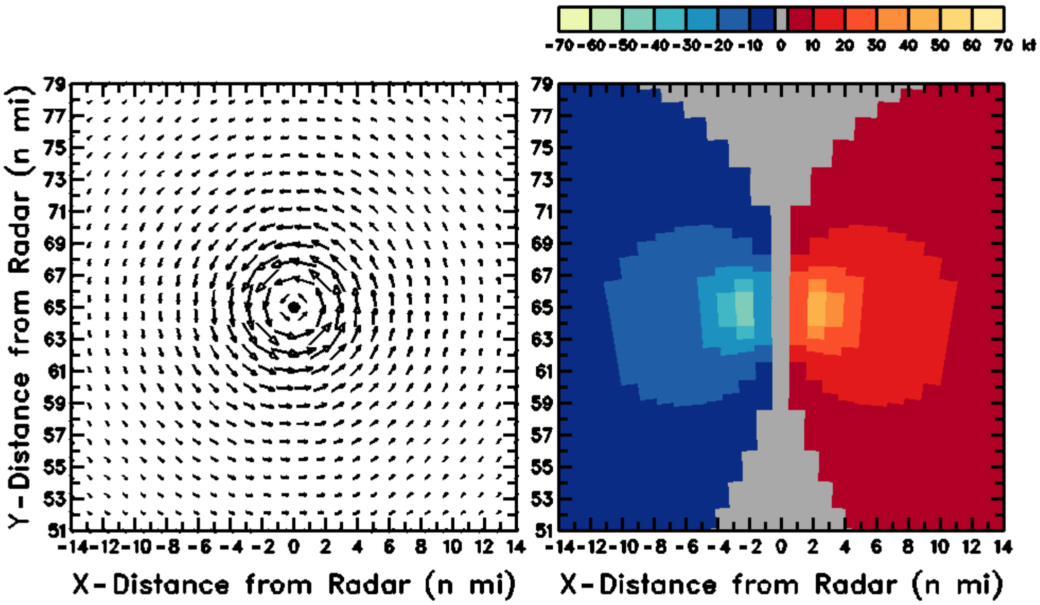

(a) Axisymmetric rotation

(b)

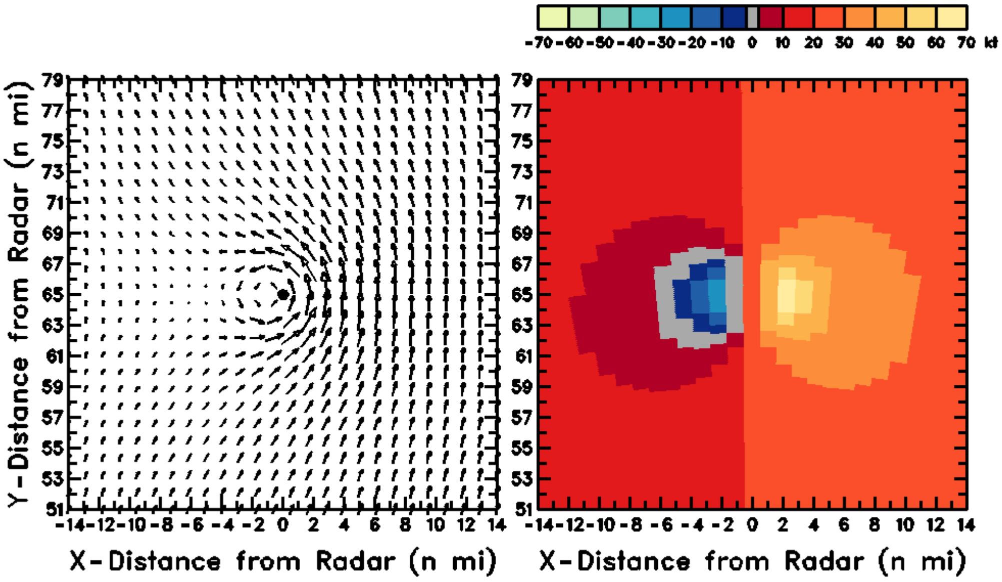

(b) Axisymmetric rotation with superimposed motion field

Figure 6-7
Axisymmetric Mesocyclone Signature

(a) Doppler velocity pattern for a stationary mesocyclone (right) corresponding to an axisymmetric horizontal flow field (left, dot at center) where the peak rotational velocity of 45 kts (23 ms^{-1}) is at a core radius of 2.5 nm (4.6 km). Center of panel is 65 nm (120 km) north of radar. (b) Same as (a) except for addition of a uniform motion field from the south at 20 kts (10 ms^{-1}). Vector length is proportional to speed.

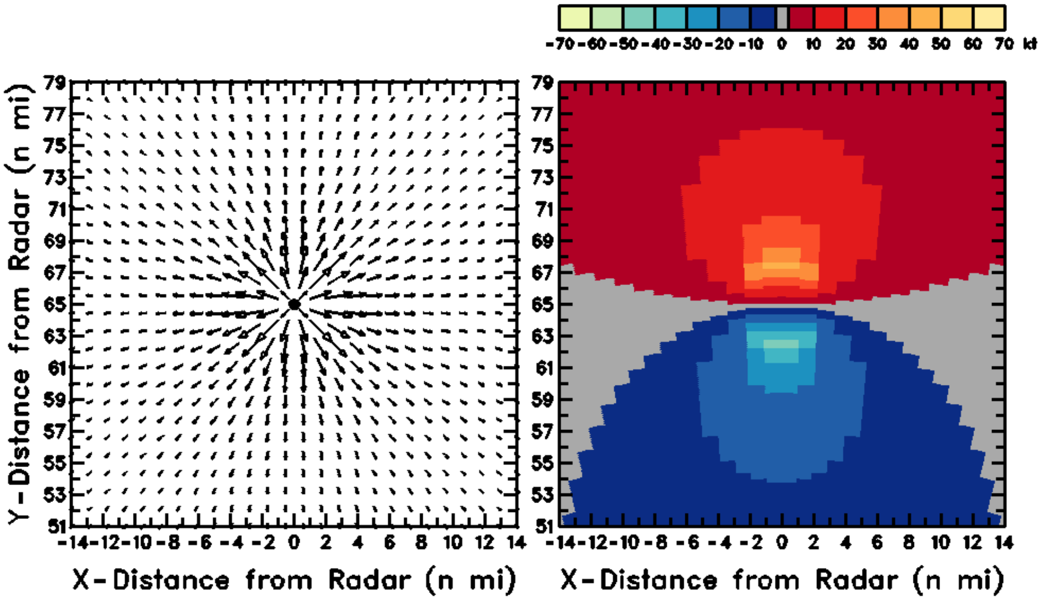

(a) Axisymmetric divergence
(b)

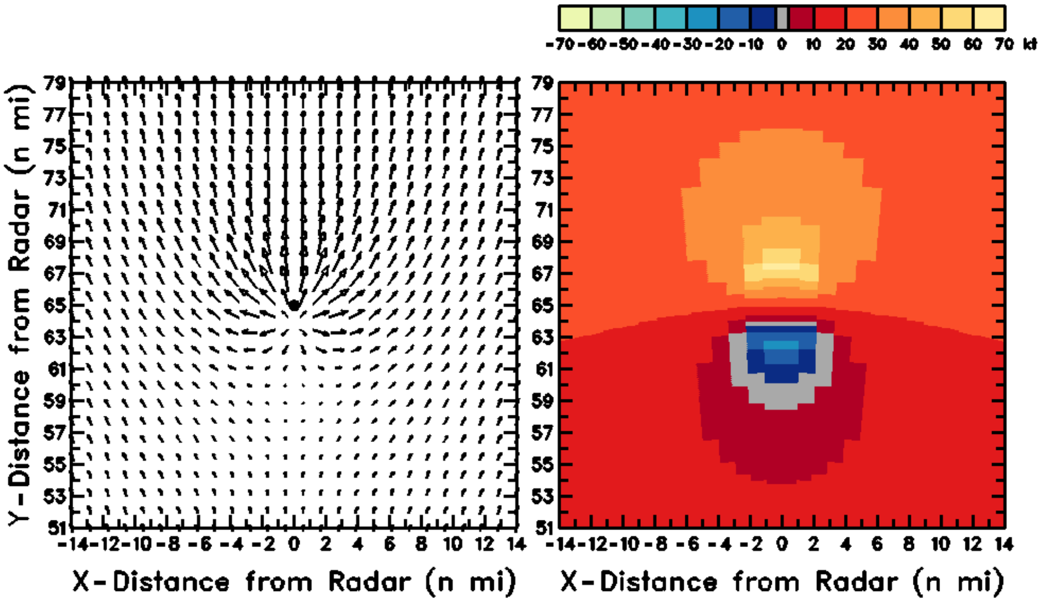

(b) Axisymmetric divergence with superimposed motion field

Figure 6-8
Axisymmetric Divergence Signature

(a) Doppler velocity pattern for a stationary region of axisymmetric divergence (right) corresponding to an axisymmetric horizontal flow field (left) where the peak radial velocity of 45 kts (23 ms^{-1}) is at a core radius of 2.5 nm (4.6 km). (b) Same as (a) except for addition of a uniform motion field from the south at 20 kts (10 ms^{-1}).

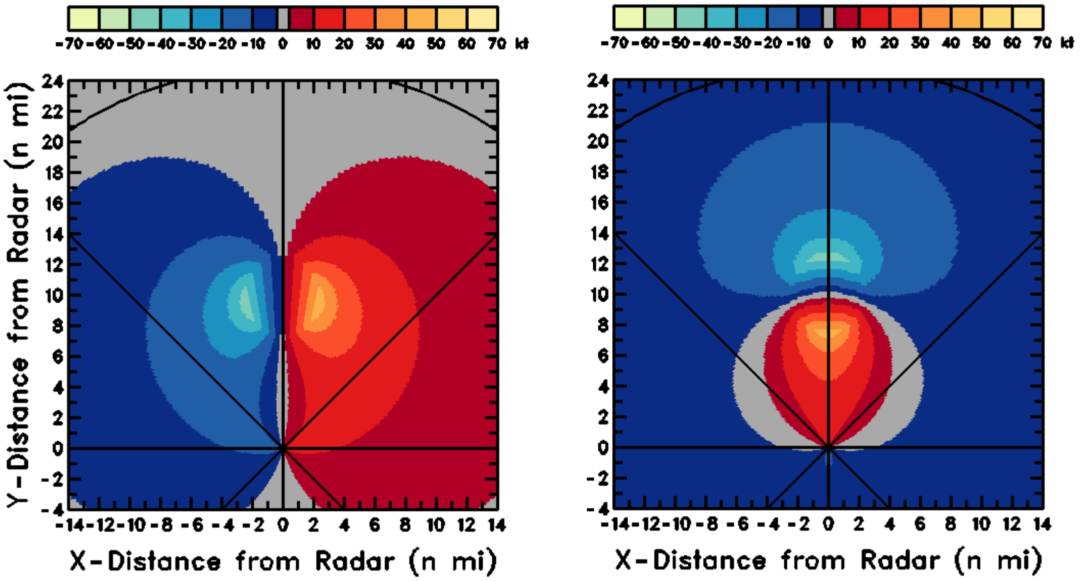

(a) Center of window 10 nm (19 km) north of radar

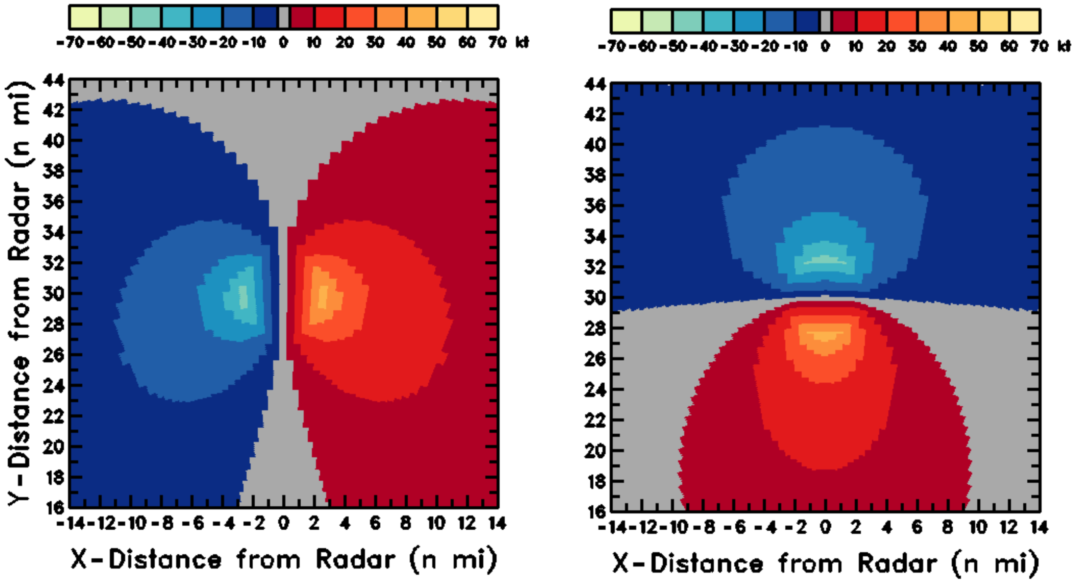

(b) Center of window 30 nm (56 km) north of radar

Figure 6-9
Distortion of Doppler Velocity Patterns due to Proximity of Storm to Radar

(a) Doppler velocity patterns for a mesocyclone (left) and convergence (right) when the center of the flow feature (at center of window) is 10 nm (19 km) north of the radar (located where radial lines converge). Core radii are 2.5 nm (4.6 km) and peak velocities are 45 kts (23 ms^{-1}). (b) Same as (a) except that the center of the flow feature is 30 nm (56 km) north of the radar.

The weak Doppler velocity band (gray) for convergence in the right part of Figure 6-9a has a unique shape—the center of the band (where the zero Doppler velocity contour would be located) is a circle passing through the radar and the convergence center. The chord connecting the radar and the convergence center is the diameter of the circle. From plane geometry we know that any angle inscribed in a semicircle is a right angle. Therefore, at the point along the radar viewing direction where a radial line from the radar intersects the expected circular zero Doppler velocity contour, the line is perpendicular to a convergent streamline flowing straight into the center of convergence signature.

At a range of 30 nm (56 km), the mesocyclone and convergence signatures are less distorted (Figure 6-9b). The Doppler velocity areas outside the mesocyclone's core region extend southward to some extent toward the radar. For convergence, the weak Doppler velocity band is less curved since it now surrounds the circular zero Doppler velocity contour (not shown) whose diameter is 30 nm (56 km). Consequently, the positive and negative Doppler velocity regions are more nearly symmetric than those found in Figure 6-9a.

When rotation and divergence/convergence fields having the same core radius are combined, the resulting Doppler velocity pattern still resembles a Rankine velocity profile. The primary distinction is that the zero band is neither parallel to nor perpendicular to the radar viewing direction. Instead, the zero band is at an intermediate angle depending on the relative strength of the two flow field components.

Figure 6-10a shows the combination of cyclonic rotation and convergence where the core radii are the same and the peak velocities are the same. In this case, the pattern is rotated 45°, midway between the Doppler velocity patterns for cyclonic rotation and convergence. Similarly, in Figure 6-10b the combination of cyclonic rotation and divergence is midway between the respective separate Doppler velocity patterns in Figures 6-7a and 6-8a.

The mesocyclone is the parent circulation within which significant tornadoes form. The resulting tornadoes typically are found within the mesocyclone's core region. Since all but the largest and closest tornadoes are smaller than the width of the radar beam, the tornado's rotational velocities are greatly smoothed within the beam. Doppler velocities within the resulting tornado vortex signature (TVS) do not reflect either the size or strength of the tornado but rather some indeterminable combination of the two parameters (e.g., Brown et al. 1978). The one consistent feature of the TVS is that the peak Doppler velocities toward and away from the radar are approximately one beamwidth apart.

A strong TVS is simulated at the edge of the core region of the parent mesocyclone in Figure 6-11a. Though it is small, the TVS is a prominent feature where the packing of colors represent extreme Doppler velocity values of opposite sign. The presence of a strong TVS located 0.5 nm (0.9 km) east of the parent mesocyclone, as illustrated in Figure 6-11b, also is very evident within the parent mesocyclonic circulation. Owing to the smearing effect of an ever-widening radar beam with increasing range, a tornado of a given size and strength produces a Tornado Vortex Signature (TVS) that is progressively weaker with increasing distance from the radar. Only the strongest tornadic vortex signatures are evident beyond 60–70 nm (111–130 km) from a WSR-88D.

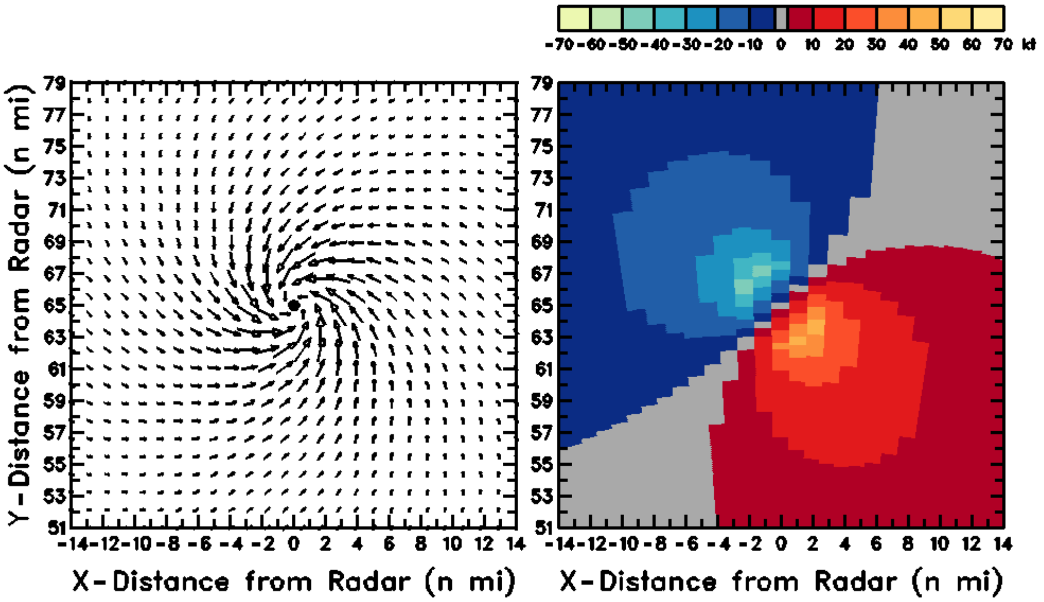

(a) Axisymmetric cyclonic rotation and convergence

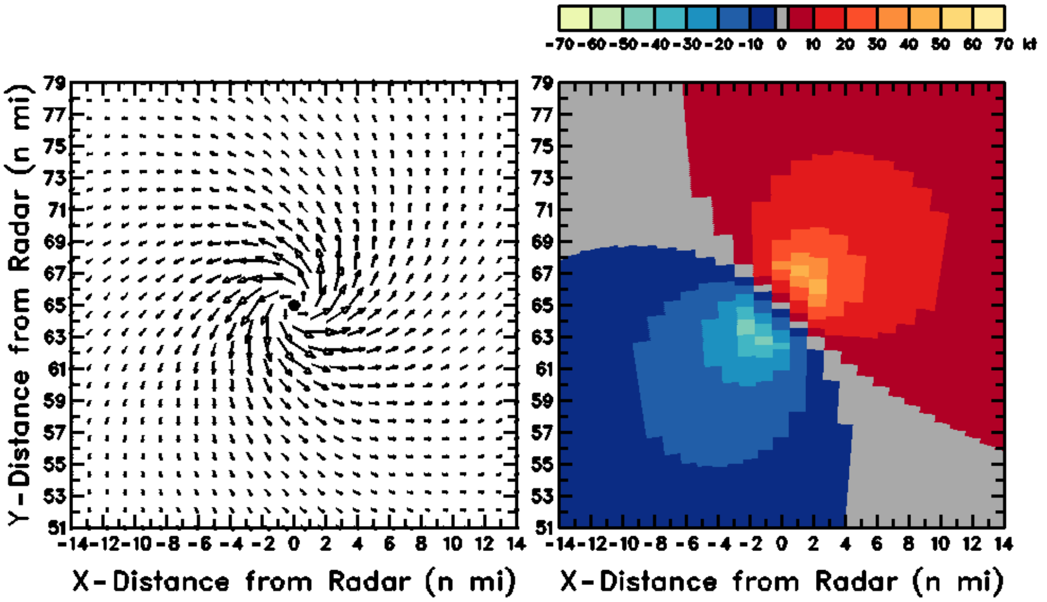

(b) Axisymmetric cyclonic rotation and divergence

Figure 6-10
Combinations of Axisymmetric Rotation and Convergence/Divergence

(a) Doppler velocity pattern (right) corresponding to combination of convergence and cyclonic rotation fields (left) having same core radii 2.5 nm (4.6 km) with maximum inflow velocity equaling maximum rotational velocity 31.8 kts (16.4 ms^{-1}). Dot in left panel is center of combined flow. (b) Same as (a) except for combination of divergence and cyclonic rotation.

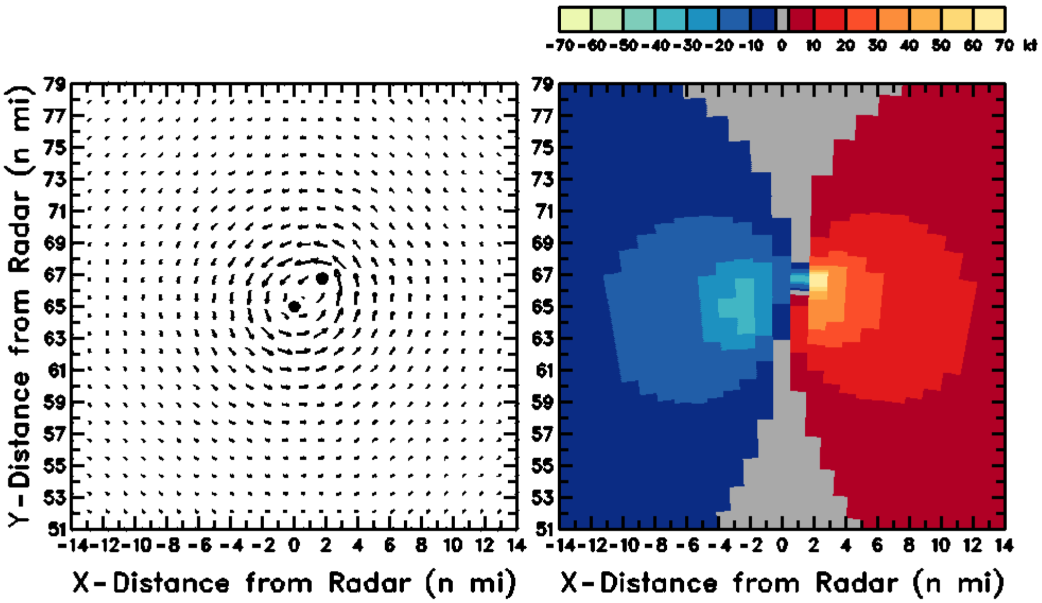

(a) TVS at edge of mesocyclone core region

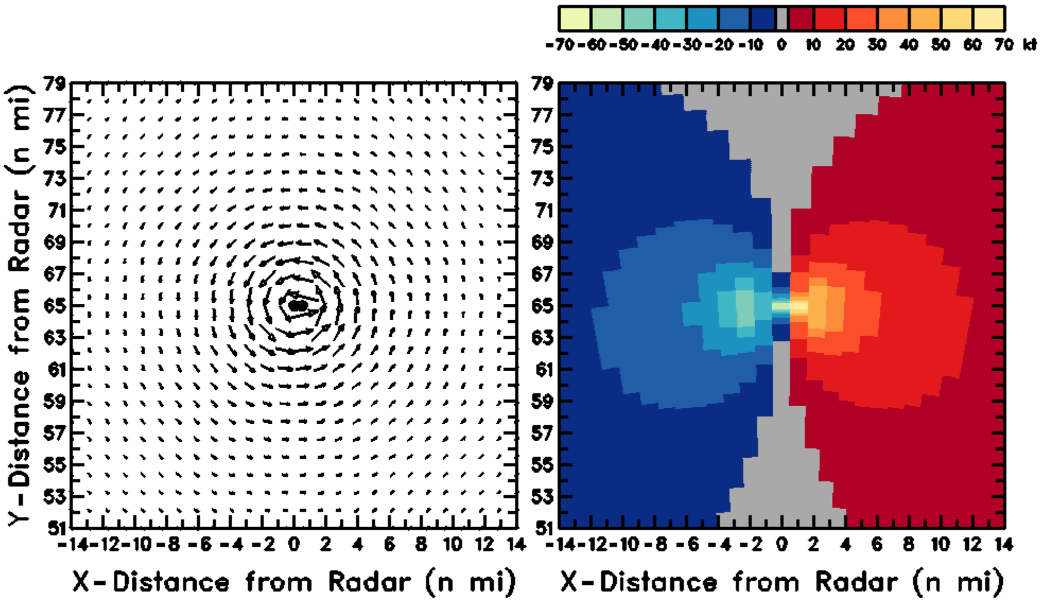

(b) TVS located 0.5 nm (0.9 km) east of mesocyclone center

Figure 6-11
Tornadic Vortex Signature within Mesocyclone Signature

(a) Doppler velocity pattern (right) corresponding to a TVS (peak rotational velocity of 60 kts (31 ms^{-1}), core radius of 0.5 nm (0.9 km) located 2.5 nm (4.6 km) northeast of the mesocyclone center (peak rotational velocity of 35 kts (18 ms^{-1}), core radius of 2.5 nm (4.6 km). (b) Same as (a) except that TVS is located within core region 0.5 nm (0.9 km) east of mesocyclone center.

6.5 Concluding Remarks. The Doppler velocity patterns presented in this chapter represent some of the more straightforward patterns that will be encountered. The development of expertise in display interpretation requires detailed training and extensive experience. The basic principles that have been presented in this chapter can be used to infer the basic components of the observed flow.

REFERENCES

Atlas, D., 1964: Advances in radar meteorology. *Adv. Geophysics*, **10**, Academic Press, 317–478.

Battan, L. J., 1973: *Radar Observations of the Atmosphere*, University of Chicago Press, 323 pp.

Brown, R. A., and V. T. Wood, 1991: On the interpretation of single-Doppler velocity patterns within severe thunderstorms. *Wea. Forecasting*, **6,** 32–48.

Brown, R. A., L. R. Lemon, and D. W. Burgess, 1978: Tornado detection by pulsed Doppler radar. *Mon. Wea. Rev.*, **106,** 29–38.

Browning, K. A., and R. Wexler, 1968: The Determination of kinematic properties of a wind field using Doppler radar. *J. Appl. Meteor.*, **7,** 105–113.

Donaldson, R. J., Jr., 1970: Vortex signature recognition by a Doppler radar. *J. Appl. Meteor.,* **9,** 661–670.

Doviak, R. J., and D. S. Zrnić, 1993: *Doppler Radar and Weather Observations*, 2nd ed., Academic Press, 562 pp.

Wood, V. T., and R. A. Brown, 1986: Single Doppler velocity signature interpretation of nondivergent environmental winds. *J. Atmos. Oceanic Technol.*, **3,** 114–128.

CHAPTER 7

MORPHOLOGY OF LARGE-SCALE PRECIPITATING WEATHER SYSTEMS

7.1 Introduction. The character of precipitation is largely controlled by vertical air motions, static stability, horizontal kinematics (e.g., deformation and vorticity), and shear of the horizontal winds in the vertical. Radar observations of the aerial extent, intensity, and lifetime of precipitation systems are evidence of the physical processes at work in the atmosphere. Depending on the dominant mechanism responsible for the vertical air motion, precipitation is usually classified into one of these two types:

Stratiform	- Widespread, continuous precipitation produced by large-scale ascent due to warm advection, positive vorticity advection, deformation, frontagenessis, topographical lifting, or large-scale horizontal air convergence caused by other means.
Convective	- Localized, rapidly changing, showery precipitation produced by cumulus-scale convection in unstable or conditionally unstable air.

The distinction between stratiform and convective precipitation is not always clear in practice. Widespread precipitation, for example, is often accompanied by fine-scale structures, or embedded convective elements. In fact, precipitation systems generally are composed of a broad spectrum of vertical motion scales and intensities. Nevertheless, it is usually possible to classify precipitation patterns by their dominant scale.

7.1.1 Stratiform Rain and Snow. Stratiform precipitation is most often produced in nimbostratus clouds or cumulus cloud shields such as those with Mesoscale Convective Systems (MCSs) or in the cold sectors northwest through east of warm fronts and ExtraTropical Cyclone (ETC) centers. Upward air motions are relatively weak (a few cm s^{-1} to a few ms^{-1}) and the vertical structure of the reflectivity pattern is closely related to the precipitation growth process during gravitational settling.

The presence of stratiform precipitation facilitates wind measurements with the Velocity Azimuth Display (VAD) technique and the VAD Wind Profile (VWP) products (Chapter 6) to much higher altitudes than possible in clear air. The wind profiles observed during precipitation are useful in determining the nature of thermal advection, jets, slantwise flow, fronts, accuracy of numerical models, etc.

On most occasions, mesoscale precipitation bands form not only along boundaries such as fronts but also within the stratiform precipitation area of ETCs. These bands arise from warm advection, local slantwise vertical motion, deformation zones, gravity waves, as well as variable instabilities and wind shears generated within large-scale systems. Such a mesoscale band within a larger precipitation echo is shown in Figure 7-1. The band is within a cold frontal region. Other bands have different orientations with respect to the shear profiles and zones of deformation. Bands also occur in the vicinity of and north of warm frontal zones. Embedded convective regions are also common in these same precipitation regions.

7.1.2 Bright Band. Apparently the bright band was first documented by the Canadian Army Operational Research Group during WW II (Atlas 1990). It was notably absent within convective storms. In stratiform precipitation where lower portions of the echo are at or above freezing temperatures and higher levels are below freezing, a thin layer of relatively high reflectivity (bright band) is often observed just below the level of 0° C in the phase transition region (Figure 7-2). As snowflakes descend into this layer they become wet and begin to coalesce developing larger, wet flakes of snow that begin to melt and coalesce still further. This highly reflective mixture warms still further and changes completely into rain. The radar reflectivity of the large, wet snowflakes is up to 15 dB higher, principally because of their large size and because the dielectric constant of water (0.93) exceeds that of ice (0.19) by a factor of nearly five. Descending further below the bright band, the raindrops accelerate their fall speed (to 5 ms^{-1}) exceeding the fall-speed of snowflakes (1.3 ms^{-1}) above resulting in a diminished hydrometeor concentration. This decrease in size and number of hydrometeors accounts for the lower reflectivity just below the bright band. Table 7-1 summarizes the physical causes of bright bands by accounting for the changes in backscatter echo intensity.

Table 7-1
Average Echo Intensity Change (dB) Due to
Physical Factors Above and Below the Bright Band

	Dielectric	Fall Velocity	Coalescence	Shape	Growth	Total
Snow to bright band	+4	-1.5	+3	+1.5	0	+7
Bright band to rain	+1	-5.5	-1	-1.5	0.5	-6.5

Figure 7-2 is an example of a bright band within generally stratiform precipitation.

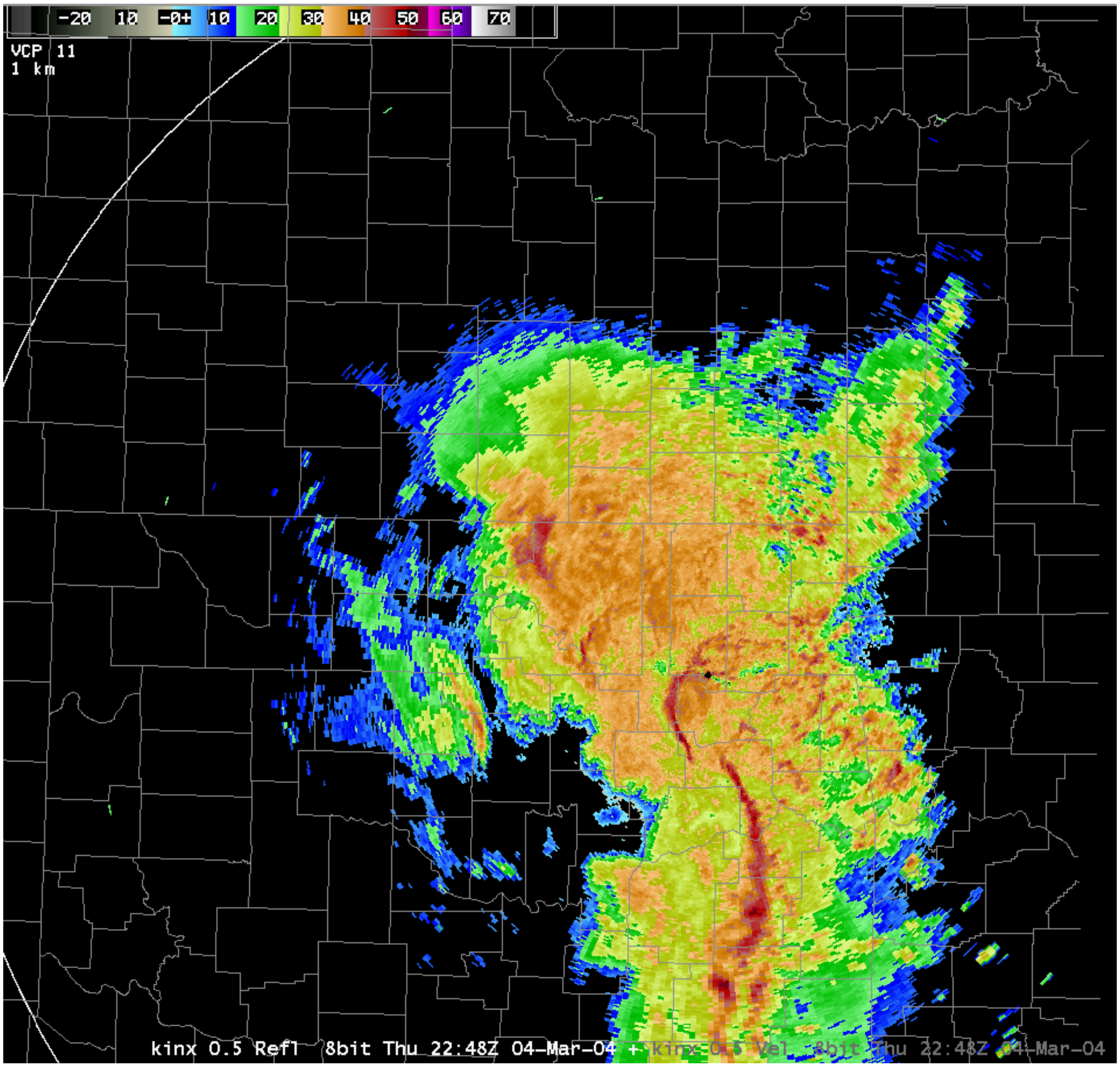

Figure 7-1
Precipitation Band Along a Cold Front Within an ETC

Tulsa, OK WSR-88D Reflectivity Data Array product at 22:48 UTC on 4 March 2004 (AWIPS display). The mesoscale precipitation band is along a cold front extending southward from the surface circulation center located about 80 nm (148 km) north northwest of the radar.

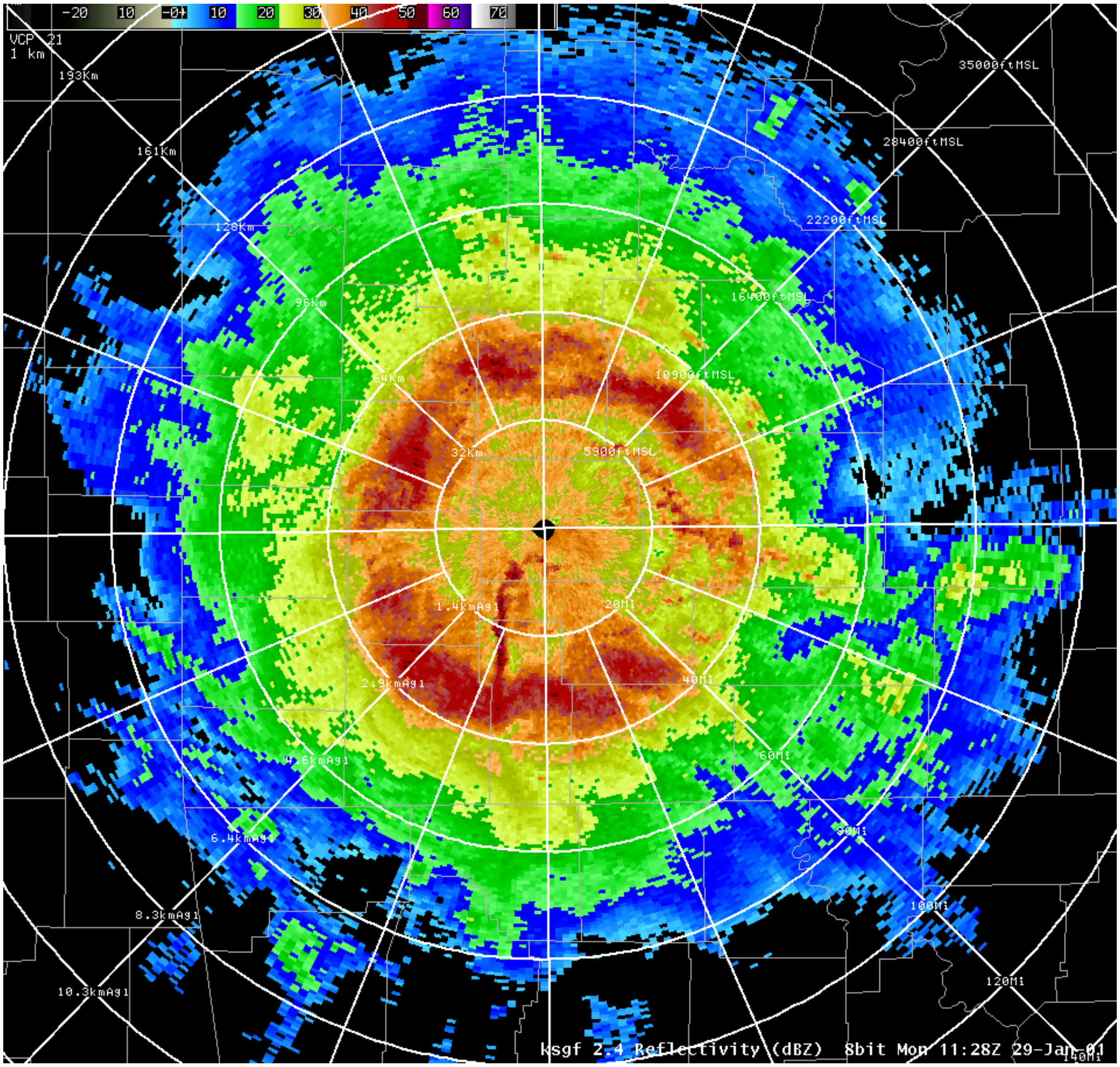

Figure 7-2
Bright Band

Springfield, MO WSR-88D Reflectivity Data Array product at 11:28 UTC on 29 January 2003 (AWIPS display). Note the bright band reflectivity varies from ~ 35 dBZ to 50 dBZ and the height averages ~ 9000 ft (2700 m). A nearby sounding indicated the environmental freezing level at 9440 ft (2877 m).

7.2 Mesoscale Convective Systems. Some large-scale precipitating systems begin as combinations of a number of convective elements. The resulting system, although still feeding on unstable air, takes on a character much different from typical cumulus-scale convection yet it can still be considered a multicell system. Regions of strong convection and heavy showers can become distributed in bands within a larger area of developing stratiform precipitation or the strong convection can be limited to the large system's leading edge with the rest of the system primarily composed of stratiform rain. However, the convective line can, at times, be near the trailing edge as well. When organized in a linear fashion, the multicell convective elements are typically distributed along a band about 20 km (11 nm) wide and hundreds of kilometers long. The bands are related to the low-level “cold pool,” convergence, both low-level and deep layer wind flow and shear, the Earth's topography, and the rotation of elements within the line itself can all affect the structure of the rain areas. The characteristics of precipitation bands have been categorized, but it is not completely understood why precipitation has the strong tendency to become organized into the characteristic scales and patterns that are observed.

Precipitation areas can be grouped into categories of size and lifetime. Observations show that synoptic areas that are larger than 10^4 km^2 (2915 nm^2) have lifetimes of one day or longer; large mesoscale areas that range from 10^3 to 10^4 km^2 (291 to 2915 nm^2) last several hours; small mesoscale areas that cover 100 to 400 km^2 (29 to 116 nm^2) last about an hour; and elements that are about 10 km^2 (2.9 nm^2) in size usually last no longer than half an hour. Along with the larger mesoscale features, typically the smaller deep moist convective elements have the highest rain rates and supply the major contribution to the total rainfall.

Multicell storms are a common occurrence when deep, moist, convection organizes in clusters, lines, or areas. Multicells are defined in this text as a group of cells in close proximity sharing a common cold pool and precipitation area. In Maddox's (1980) classification of the Mesoscale Convective Complex (MCC), multicells could be thought of as belonging to both Linear and Circular types (Figure 7-3).

The term Mesoscale Convective System (MCS) (Zipser 1982) includes all precipitation systems 20 to 500 km (11 to 270 nm) wide that contain deep convection. Examples in middle-latitudes are large isolated thunderstorms, squall lines, MCCs, and rain bands. The aerial extent of these systems is often too large to be covered by a single radar. Examination of mosaic maps from a network of radars is required to capture the full extent of many MCSs.

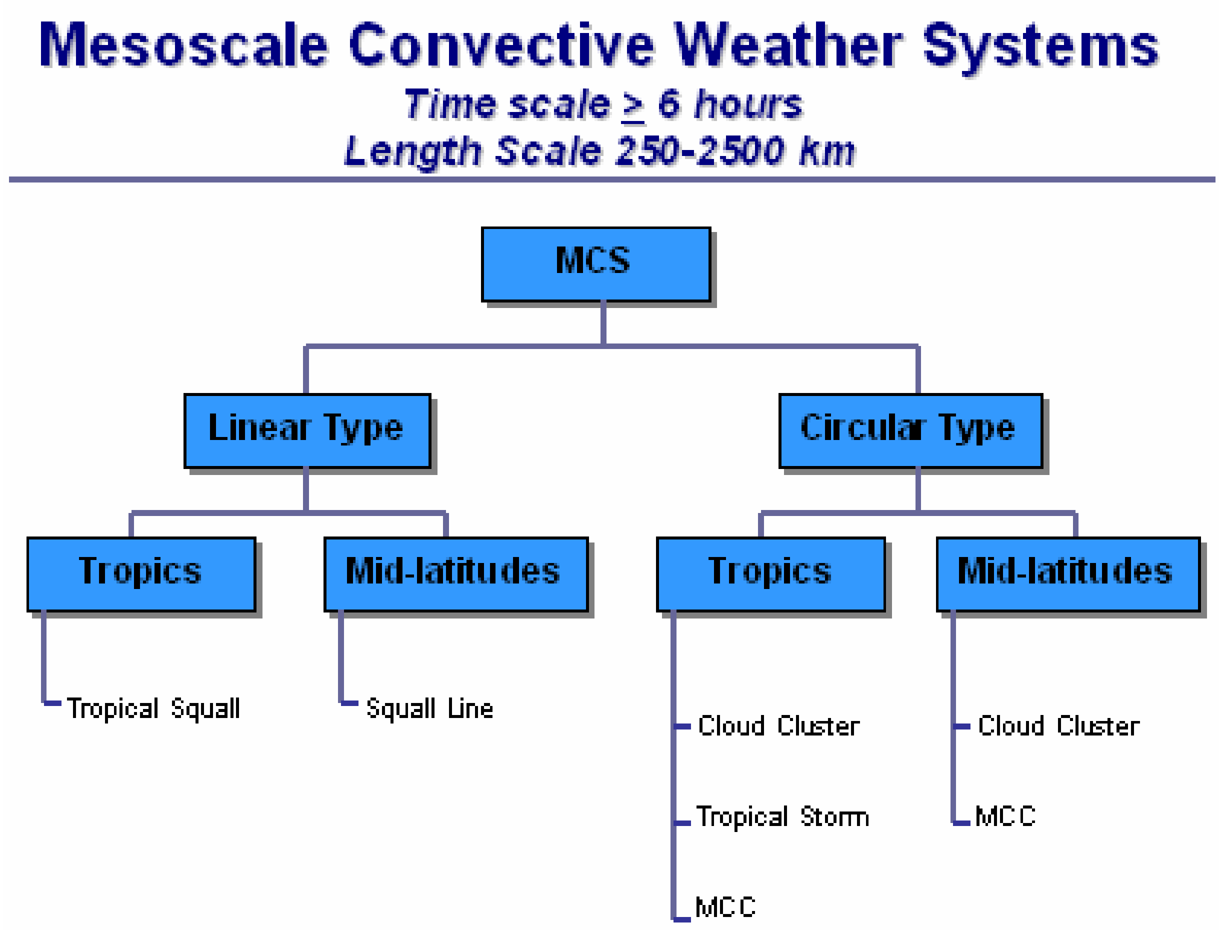

Figure 7-3
Schematic of Mesoscale Convective Weather Systems Classification

From Maddox (1980).

7.3 Squall Lines and Mesoscale Convective Systems. There is the potential for confusion when the terms "squall line", “Mesoscale Convective Complex” and “Mesoscale Convective System” are used. (See the discussion of Doswell (2001) as applied to this subject.) In summary, the term “squall line” was originally applied to the cold front and associated with gusty winds. However, the term now applies to linear convective storm systems or almost any thunderstorm line. With this organization the convective elements interact and often have a common cold pool and outflow (gust front) boundary. The initiation mechanism is often a synoptic or mesoscale boundary such as a dryline, trough, or front. Gaps between adjacent convective elements often fill in to form a nearly two dimensional line of storms (a quasi linear convective system) that may or may not be severe. This is especially true when environmental shear profiles are oriented more parallel to the line orientation, thus encouraging storms that interact or seed and overlap adjacent storms. The definition for the MCC was originally based upon infrared (IR) satellite imagery (Maddox 1980). Maddox chose the largest, most circular, and longest-lasting systems for study. Certain aerial coverage criteria, a duration criterion, and a shape criterion were to be satisfied in order to be labeled a MCC. Essentially, the system’s cold cloud shield must surpass a size threshold, persist for at least 6 hours, and must be characterized by a circular shape. Now the entire class of mesoscale systems observed by IR, whether linear or quasi-circular, have come to be termed Mesoscale Convective Systems (Zipser 1982). Almost any squall line, especially those with large mesoscale rain areas are MCSs. Examples of squall lines with large trailing regions of stratiform precipitation have been summarized in conceptual models by Houze et al. (1989) (Figure 7-4), Kessinger et al. (1983), and Parker and Johnson (2000, 2004c) (Figure 7-5).

Conceptual models of squall lines and the MCS have evolved over the years based on studies from higher-resolution satellite, radar, and surface observations. The MCS classification continues to develop from relatively recent studies of convective systems using satellite and radar information, as well as comprehensive field programs such as BAMEX (Davis et al. 2004; Parker and Johnson 2004a, b, c; Wakimoto 2004). There are many convective systems that could be considered as both MCSs and/or squall lines. In fact, linear squall lines are considered as a phase in the development of many MCSs by Parker and Johnson (2004a, b, c). Comprehensive studies, such as those above, of the internal dynamics of MCSs and squall lines and the conditions in which they form, are establishing their similarities and differences.

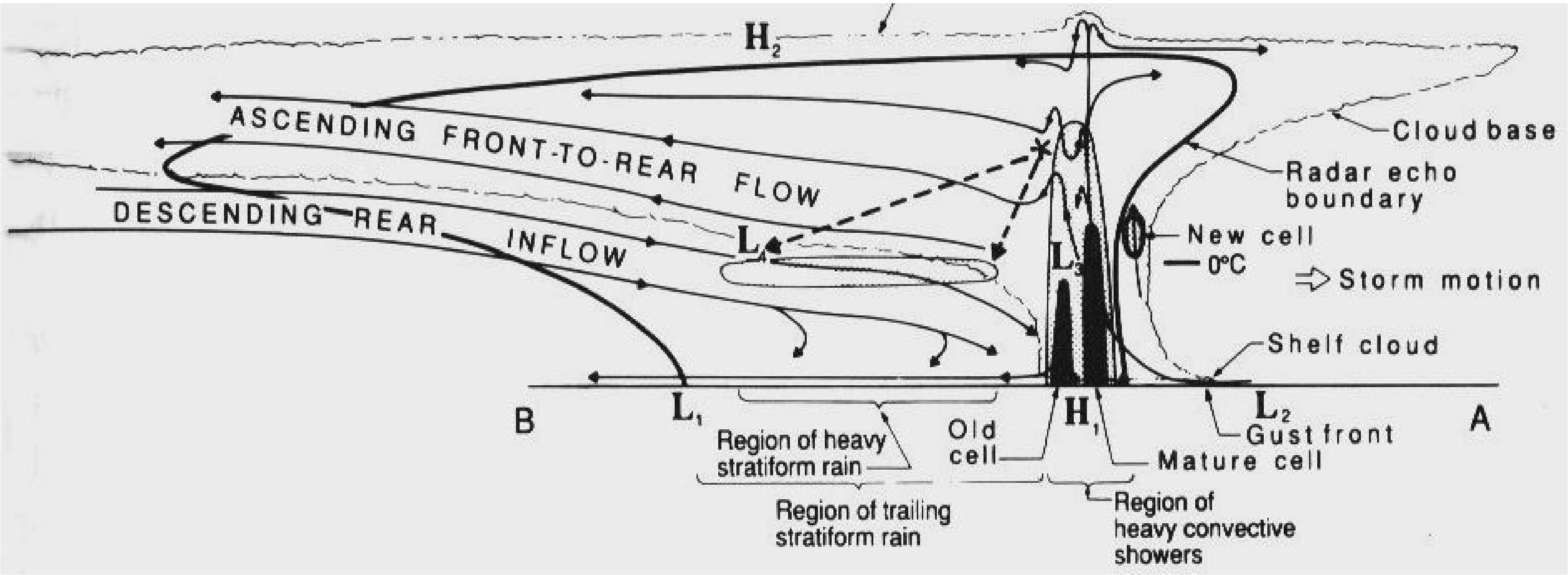

Figure 7-4
Conceptual Model of a Squall-Line System

See the text for a discussion of this model from Houze et al. (1989).

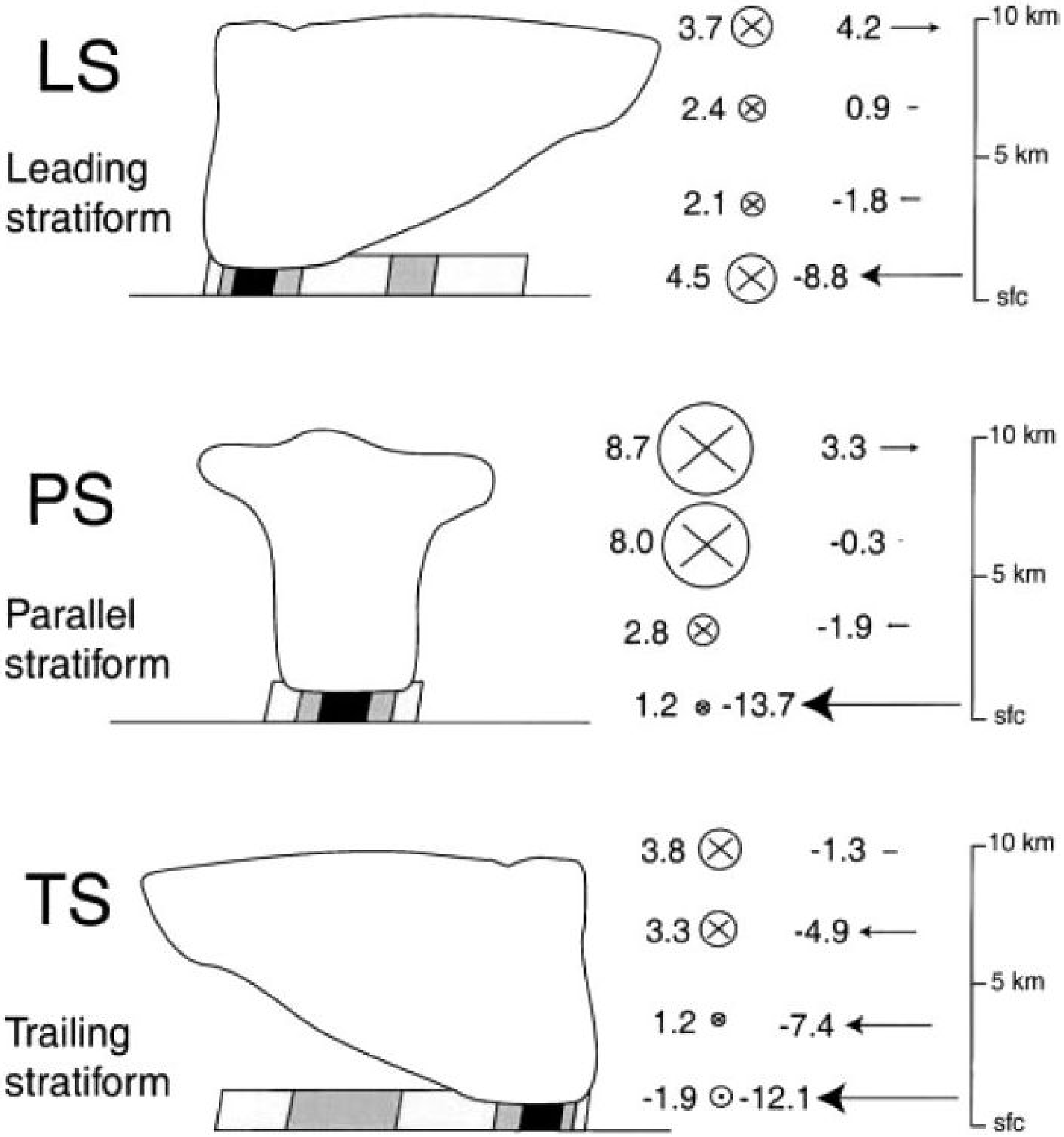

Figure 7-5
A Schematic of Mesoscale Convective System Archtypes

Vertical profiles of layer-mean storm-relative pre-MCS winds for linear MCS classes. Wind vectors are depicted as line-parallel (vectors with arrow) and line-perpendicular (encircled X) components in m s^{-1}. Layers depicted are 0–1, 2–4, 5–8, and 9–10 km (AGL). Typical base scan radar reflectivity patterns (shading) and hypothetical cloud outlines are drawn schematically for reference. MCSs' leading edges are to the right (after Parker and Johnson 2000).

Fritsch and Forbes (2001) point out that there are essentially two classes of MCSs. Type 1 has its origin within a baroclinic system, i.e., an ETC. It results when a mesoscale ribbon of low-level potentially unstable air is forced to ascend in a frontal zone or other region of baroclinic forcing. Type 2 results when the outflow of thunderstorms developing in a more barotropic environment congeal forming a cold pool that interacts with the environmental shear profile in such a way that continuing convection is encouraged and organized along and above the cold pool. One of the dominant characteristics of both types is that they tend to be nocturnal. Often, the nocturnal forcing for the low-level jet downstream from north-south mountain range is important to MCS genesis and maintenance. The surface-based baroclinity facilitates slantwise ascent (warm advection) of the lowest few thousand feet of warm sector air. Continuing ascent saturates this air as it overruns low-level colder more stable air. This process often results in scattered, elevated, deep convection in an along-front direction over a considerable distance which organizes into a "squall line."

Thus, squall lines that occur within extratropical cyclones may initiate as elevated convection in the warm advection area north of the warm front. This same area is often the focus of potential temperature ridges, (a warm and moist tongue) accompanied by a low-level jet (Johns and Hirt 1987; Johns and Doswell 1992). These same authors also addressed those squall lines that are most often located in the warm sector, where the air mass is most unstable. As indicated, a common initiating mechanism is convergence along fronts or discontinuities. Once formed, the squall line provides its own propagating mechanism in the form of convergence along the cold pool and gust front, which maintains ascent into existing updrafts and initiates convection ahead of storms.

Both squall lines (mid-latitude and tropical) and Mesoscale Convective Systems contain multicell characteristics (e.g., cells developing along the leading edge of the line and moving rearward into the large stratiform rain regions). Some distinction is needed in the two classes (of MCS and squall line) to account for the unique three-dimensional attributes often found in MCSs. Some of the MCSs' unique nature of storm structure is based on the environmental conditions and longevity that tend to influence evolution of these large convective systems. These are examined in detail in COMET's web-based instructional component, Mesoscale Convective Systems: Squall Lines and Bow Echoes, available at: http://meted.ucar.edu/convectn/mcs/index.htm. The COMET MCS web module also explains the development of MCSs from initiation to mature phase.

Two of the more widely accepted conceptual models of the complex flow structure for squall lines are from Houze et al. (1989); (see Figure 7-4) and Biggerstaff and Houze (1991).

In the Houze et al. (1989) model of a mature MCS, development of the Rear-Inflow Jet (RIJ) is attributed to mid-level mesoscale areas of low pressure (labeled L3 & L4). The mesolow "L3," which forms immediately behind the leading line convection, is a hydrostatically-induced negative pressure perturbation that develops under the upshear tilted warm convective updrafts and above the evaporatively cooled downdrafts. Mid-level mesolow "L4" forms in the stratiform region in between the warm buoyant air which gets pulled rearward past the cool and the dry descending air flow. Although MCSs develop in a number of ways, all mature systems eventually develop convective regions and stratiform precipitation regions to some degree. The eventual MCS type is determined to a large extent by the environmental wind and deep layer shear conditions in which it develops and the strength of the system's cold pool. Parker and Johnson (2000) studied MCS types and determined the distribution of precipitation and stratiform region shapes were largely a result of mean storm-relative winds (Figure 7-5). The speed and direction of the environmental mid- and upper-level winds relative to the system's motion affect the resulting evolution of the MCS. Thus, storm- (or system-) relative wind fields are critical to the evolution and movement of multicell systems. According to their studies, Parker and Johnson (2000) found MCSs evolve into three major archetypes: 1) trailing stratiform, 2) leading stratiform and 3) parallel stratiform. The main distinction arises from storm-relative flow fields. The leading stratiform precipitation MCS archetype (also see Parker and Johnson 2004a, b), which is typically slower-moving than trailing stratiform systems, was characterized by stronger mid- and upper-level storm-relative flow (often described as rear-to-front flow) than any of the other types (Figure 7-5). The trailing stratiform MCS type has a sloped front-to rear flow produced by stronger system-relative flow.

These multicell storms may consist solely of simple ordinary cells, or they may also contain embedded supercells. These multicell storm systems contain a wide variety of configurations and multiple mechanisms may exist for determining their movement. These mechanisms include, but are not limited to:

- shear-cold pool interactions,
- low-level convergence,
- instability gradients, and
- three-dimensional boundary interactions.

Some of MCS's unique nature of storm structure is based on the environmental conditions that tend to influence evolution and longevity of these large convective systems. These are examined in detail in COMET's web based instructional component, Mesoscale Convective Systems: Squall Lines and Bow Echoes, available at this web address: http://meted.ucar.edu/convectn/mcs/index.htm. The module is highly recommended reading to complement this Handbook. However, of equal importance is some of the more recent work that has emphasized not only the low-level shear interaction with the cold pool, but also the importance of deep-layer shear (Congilio et al. 2004a, b).

Derecho events, as we will see, are defined as a series of damaging wind episodes, Johns and Hirt 1987), which are the fastest moving multicell systems, can last from 2 to over 20 hours and can travel across multiple County Warning Areas if downstream instability remains sufficient. Additionally, those MCSs/squall lines containing embedded supercells are very often associated with high-end (extreme but non-tornadic) damaging wind events (Miller and Johns 2000; Miller et al. 2002). Those events are associated with the supercells themselves.

A wave in a line of thunderstorms that is sometimes associated with one or more bow echoes is called a Line Echo Wave Pattern (LEWP) (Figure 7-6). Nolen (1959) found that these echo structures were often associated with damaging winds and other potential servere weather. Multiple bow echoes within a squall line may sometimes result in a LEWP. Many features of bow echo evolution which cause a typical LEWP structure (such as the rotating comma head and the cyclonic/anticyclonic rotating vortices) are based on the conceptual model from Fujita (1978), (Figure 7-7).

Fujita found that the initial echo started as a strong isolated cell or a small line of cells. The initial cells then evolved into a quasi-symmetric bow-shaped segment of cells over a period of an hour or two, and eventually into a comma-shaped echo over several hours. More recently, Burke and Schultz (2004) documented several other modes of bow-shaped echo development such as the latter stages of some supercells.

A distinction should be made between a squall line that contains closely spaced interactive cells with nearly continuous precipitation throughout its length and one consisting of a line of isolated or quasi-isolated storms. These two types differ both in appearance and other characteristics. It is not uncommon for a line of isolated cells with severe weather to evolve into a solid line by a progressive filling of gaps in the line. This is typically the case when the deep layer shear vector is oriented largely parallel to the line. In the case where the initially isolated cells were tornadic, this evolution often signals the end of tornadic activity, although damaging straight-line winds, hail, and heavy rains may persist. (Note, however, as explained previously, squall lines in the form of bows or LEWPs and those containing embedded supercells may still be significantly tornadic despite being members of quasi linear convective systems [QLCS].) Tornadic activity frequently, but not always, shifts to isolated cells ahead of the line or cells that occur at the southern or southwestern end of the squall line and/or on the northern end of a gap in a line. Existing lines sometime increase in length by new cell development on the southern or western end of the line.

Updrafts often form a nearly continuous curtain along the advancing edge of the QLCS echo. Downdrafts form in the precipitation echo to the rear of the leading updrafts. That portion of the line often with the most intense gust front and updrafts is identified by a strong reflectivity gradient at low altitude, echo overhang and related forward WER, and a shift of echo top from over the storm core to along the leading edge of the line. Sometimes the surface gust front surges ahead of the leading edge of the echo and, if close enough to the radar, can be observed as a thin line echo (Figure 7-6).

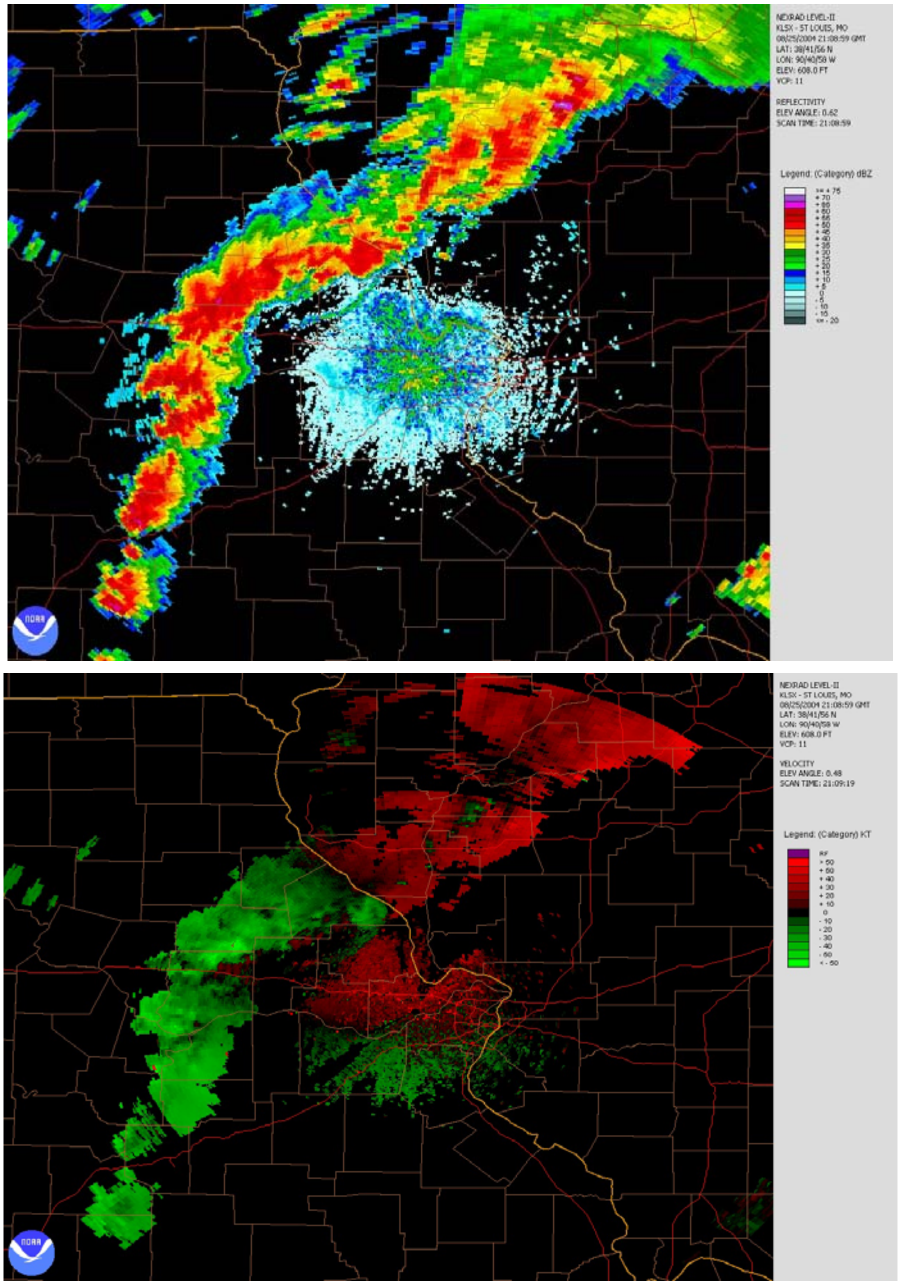

Figure 7-6
Line Echo Wave Pattern

St. Louis, MO WSR-88D Reflectivity product (top) and Mean Radial Velocity product (bottom), both at 0.5° elevation, and at 21:08 UTC on 25 August 2004 (NCDC NEXRAD Viewer graphic). A squall line in the form of a Line Echo Wave Pattern (LEWP) is north and west of St. Louis. A gust front can be seen northwest of the radar in both reflectivity and velocity imagery.

Rear-Inflow Jets (RIJs) are common with large QLCSs or MCSs. However, numerical simulations suggest the RIJs do not descend in the most severe squall lines (Weisman 1992). According to Weisman (1992), most squall lines become upshear-tilted as the cold pool dominates environmental shear and the non-descending RIJ restores balance, allowing the squall line updraft to remain nearly vertically erect for longer periods of time. Non-descending RIJs are found in environments where deep layer shear and conditional available potential energy (CAPE) are high.

A radar signature which is often associated with the RIJ and with high winds and tornadoes is the Mid-Altitude Radial Convergence Signature (MARC). This is a signature very similar to the Deep Convergence Zone, or DCZ, identified by Lemon and Burgess (1993) and Lemon and Parker (1998) that is also found to be associated with strong and damaging surface winds. However, those authors emphasized the extreme depth and convergence sometimes associated with the MARC. Observations of a MARC have been noted by Przybylinski (1998) as a precursor to the descent of the elevated RIJ. Enhanced velocity differentials (areas of strong convergence) are often located just downwind of high reflectivity cores along the leading edge of the convective line. Persistent areas of MARC greater than 25 ms^{-1} at 3-5 km AGL can sometimes provide lead time for the first report of wind damage (often before a well-defined bow echo with bookend vortex develops). On either end of mature squall lines and flanking the RIJ, can sometimes be found "book-end" vortices (and sometimes supercells), cyclonic on the north end and anticyclonic on the south end. Squall line segments exhibiting line-end vortices and a localized RIJ in between the vortices and directed toward the leading edge are often called bow echoes based on their bowing configuration (Figure 7-8). Bow echoes intensify the RIJ between the vortices, often leading to localized areas of maximum wind damage. Small tornadoes may occur just to the left of the maximum wind in an RIJ and with leading edge mesocyclones given enough low-level helicity and instability in the environment. The line-end vortices in bow echoes (Figure 7-7 and Figure 7-8) develop in one of two ways; by either tilting negative storm induced vorticity at the top end of the cold pool from the storm updraft, and/or by tilting positive environmental vorticity downward by the downdraft in the back end of a bow echo. More will be said about bow echoes and these line-end vortices shortly.

Bow echoes and RIJs are sometimes associated with Derechos. Johns and Hirt (1987) studied warm-season Derechos. They defined the Derecho as:

1). A concentrated area of convectively induced wind damage and/or gusts >50kts ($25ms^{-1}$) that has a major axis length of at least 250 nm (463 km).

2). Reports must show a pattern of chronological progression.

3). At least 3 reports of convective gusts >65kts ($33ms^{-1}$) and/or F1 intensity damage. These 3 reports must be separated by 40 nm (74 km) or more.

4). No more than 3 hours can elapse between successive wind damage (gust) events.

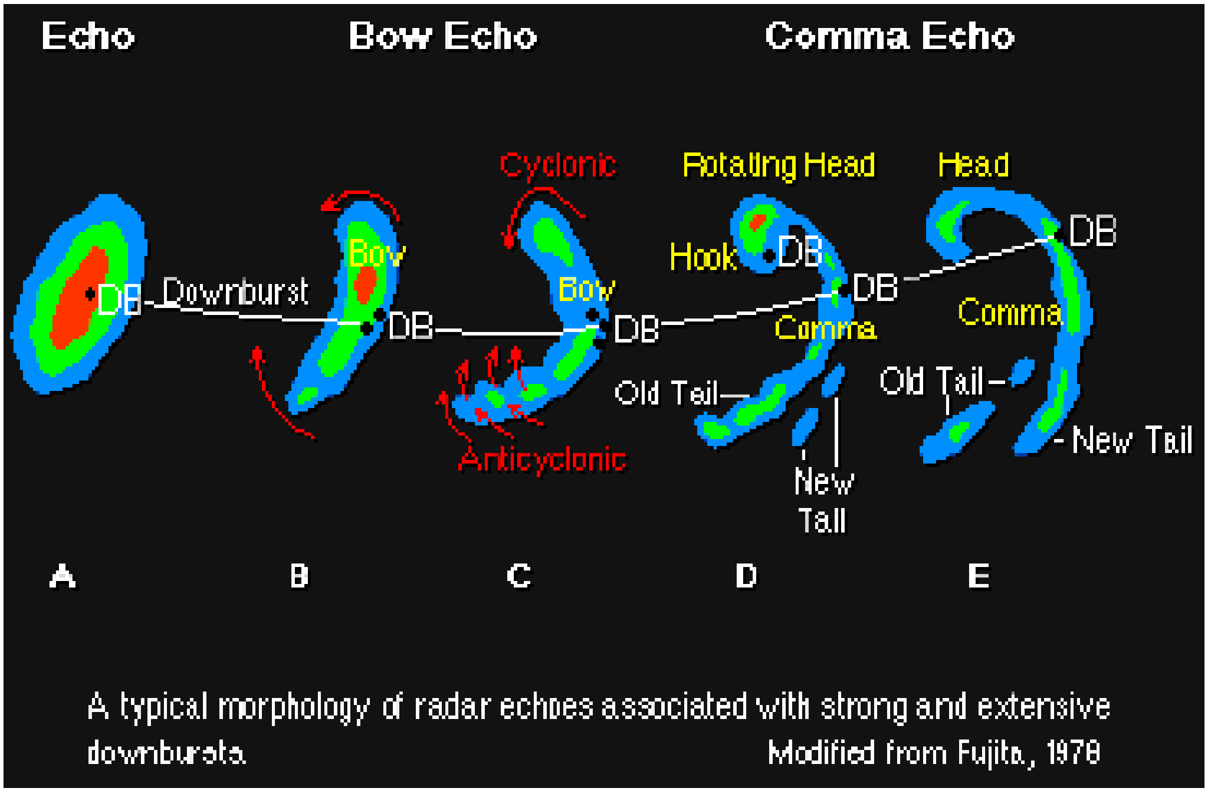

Figure 7-7
Conceptual Bow Echo Evolution

Conceptual model of a bow echo evolution. Adapted from Fujita (1978) and COMET (1999).

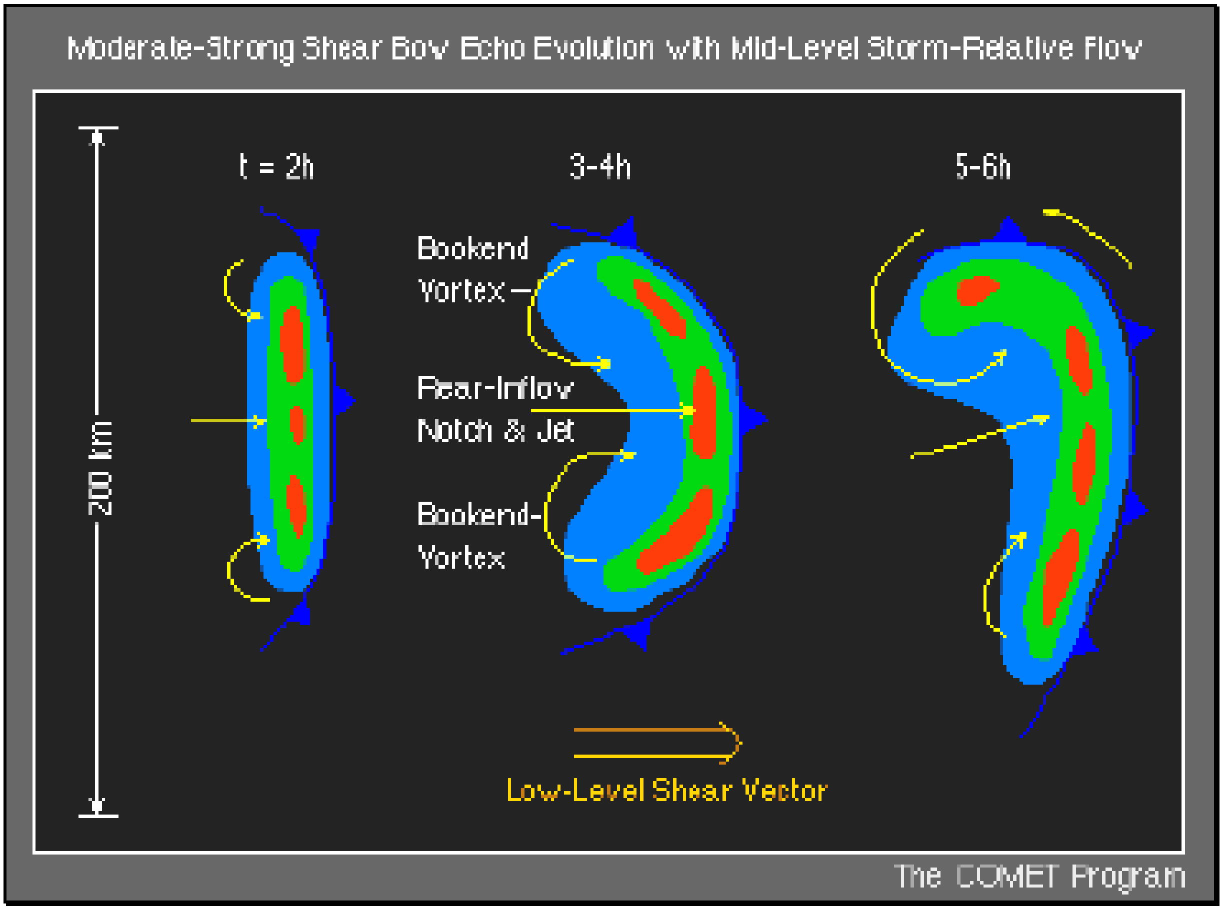

Figure 7-8
Conceptual Bow Echo Model

Conceptual model of a strong bow echo evolution showing bookend vortices and development of a Rear-Inflow Notch (RIJ). From COMET (1999).

They found that Derecho environments were characterized by copious moisture at low levels and extreme convective instability. However, in synoptically forced cases, lesser instability accompanied the "strong" 500 mb shortwave troughs in their data set. Similarly, Johns et al. (1990) examined 14 very intense Derechos during the months of June and July and found that CAPE values were generally greater than 2400 J/kg near the genesis region, but increased to an average CAPE maximum of 4500 J/kg as the convective system moved eastward. In fact, the studies by Miller and Johns, 2000, and Miller et al. 2002 found that those high-end Derechos occurred within the same types of environments associated with outbreaks of tornadic storms (strong CAPE and strong deep-layer shear).

Evans and Doswell (2001) also studied CAPE distributions in squall lines (via proximity soundings) and found a much greater range of values for Derecho events. They found that in most cases which were weakly-forced, the instability (and CAPE) were generally larger than in those cases where the forcing was "strong" (SF). For SF, there were a number of Derecho systems that developed and persisted in environments with low values of CAPE. A few Derechos developed and persisted within regions of conditionally stable surface air. Thus, squall lines have been observed over a wide range of environmental CAPE (and vertical wind shear). For any given CAPE, the intensity and longevity of linear convective systems seem to increase with increasing synoptic scale forcing, which includes depth and strength of the vertical wind shear.

Bluestein and Jain (1985) studied squall lines in Oklahoma and found that the magnitude of the vertical wind shear on average was stronger for severe lines than for the non-severe lines. In their study, the average CAPE for severe lines was significantly larger than for the non-severe lines (2260 J/kg versus 1372 J/kg), which agrees with other studies.

While we have omitted other discussion that can be found elsewhere (see IC 5.7, WDTB web site) we can summarize the relationship between CAPE and shear. The intensity and longevity of squall lines and bow echoes occur within a wide range of environmental conditions and shear/buoyancy parameters. As in supercell environments, for stronger synoptic forcing, deep layer shear is usually stronger and CAPE is smaller. The converse holds true as well; in weaker synoptic forcing, higher CAPE and Downdraft CAPE (DCAPE) are necessary to maintain the strong winds at the surface. Thus, there is a greater dependence, in weak (0-6 km) flow situations, on strong downdrafts and cold pools for maintaining severe surface winds.

Given the same buoyancy for updrafts and cold pools, shear can modulate the intensity of the RIJ. According to numerical simulations, as shear increases, the updraft along the leading edge becomes more erect and stronger. More heat is pumped into the anvil just behind the leading edge causing a stronger hydrostatic low in the mid-levels. The more intense precipitation from the stronger updraft is hypothesized to create a stronger cold pool and gust front as well.

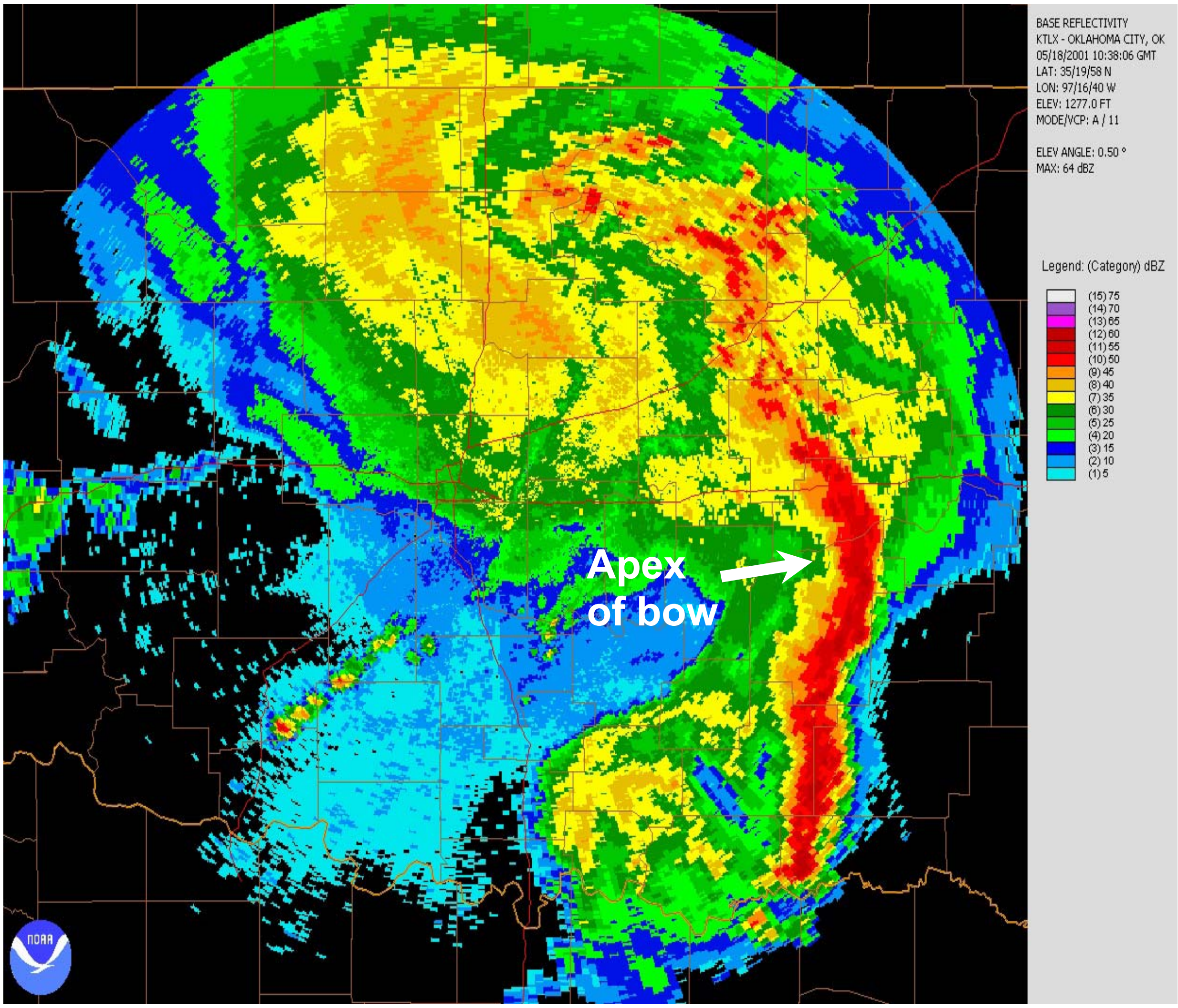

Figure 7-9
Reflectivity Image of a Bow Echo

Oklahoma City, OK WSR-88D 0.5° Reflectivity product at 10:38 UTC on 18 May 2001 (NCDC NEXRAD Viewer graphic). This image is of a bow echo in Eastern Oklahoma as annotated.

While the role of vertical wind shear in the strength, structure, and maintenance of MCSs has been examined by many, much of this work focuses on the interaction of the low-level shear with the circulation induced by the cold thunderstorm outflow (see a summary in Weisman and Rotunno 2004). However, the relative importance of upper-level wind shear has been neglected until more recently. Coniglio et al. (2004a, b), via simulations, as well as observations, has shown convincing evidence that deep layer shear helps to organize and maintain the MCS and the Derecho associated MCS, especially in situations involving weak forcing and the lack of a strong low-level jet. Furthermore, this work also helps explain the demise in these systems when wind shear in the 7 to 9 km AGL range weakens.

When the squall line is trailed by stratiform precipitation, the first indication that a bow echo is about to develop is sometimes the erosion of the back edge of the adjacent stratiform echo, accompanied by the strong velocities of the RIJ directed toward the forward convective-line flank. Figure 7-9 is a mature squall line with an embedded, developing bow echo. Some line echoes evolve into the comma shape that shows rotation within the “book end” vortices.

While the presence of bow echoes and LEWPs are often used by the meteorological practioner as a severe weather indicator, this does not guarantee that a severe storm is imminent. Confirmation can be obtained via the updraft flank signatures of the Weak Echo Region (WER) and the Bounded Weak Echo Region (BWER) associated with the mid-level echo overhang, strong low-level reflectivity gradients, and the displaced echo top are all signatures associated with intense updrafts (e.g., Lemon 1980) and severe weather. This is the case for nearly all severe storms that are severe by virtue of intense updrafts, even with squall lines (Figure 7-10). The radial velocity data from low altitude scans sufficiently close to the radar can be used to estimate the intensity of surface winds associated with thunderstorm outflows and to determine if mesocyclone development accompanies storms within the line. Further, at longer ranges, mid-level convergence identified in radial velocity fields and associated with the Deep Convergence Zone, or DCZ, (Lemon and Burgess 1993; Lemon and Parker 1998) and the related Mid-Altitude Radial Convergence (MARC) (Schmocker et. al. 1996) can be used to infer strong downdrafts and associated strong, damaging surface winds.

7.4 Storm Development on Airmass Boundaries. New convective cells commonly develop along gust fronts, outflow boundaries, mesoscale and synoptic scale boundaries, boundaries of all types. A large fraction of non-frontal thunderstorms form on these boundaries and at the intersection of existing boundaries as detected on visible satellite photographs. These boundaries are most often associated with density discontinuities. The boundaries can often be detected on radar and are commonly known as thin or fine lines. However, it should be noted that the effective range for boundary layer probing is limited by the Earth's curvature (radar horizon) and the finite beam width. Reflectivity is enhanced not only by turbulent mixing of warm and cool air along the discontinuity, but by insects carried into the boundary by the airflow as well as their predators, birds (Figure 7-11). At times, migratory birds will use the wind-flow behind fronts to aid them in their migratory journeys. This can create significant echo return behind the boundary, as well, and is also seen in Figure 7-11. As the front passes, the birds at the surface will take to flight. Clouds (containing precipitation size hydrometeors) need not be present as the echoes are from refractive index perturbations associated with the mixing and the insects and birds themselves.

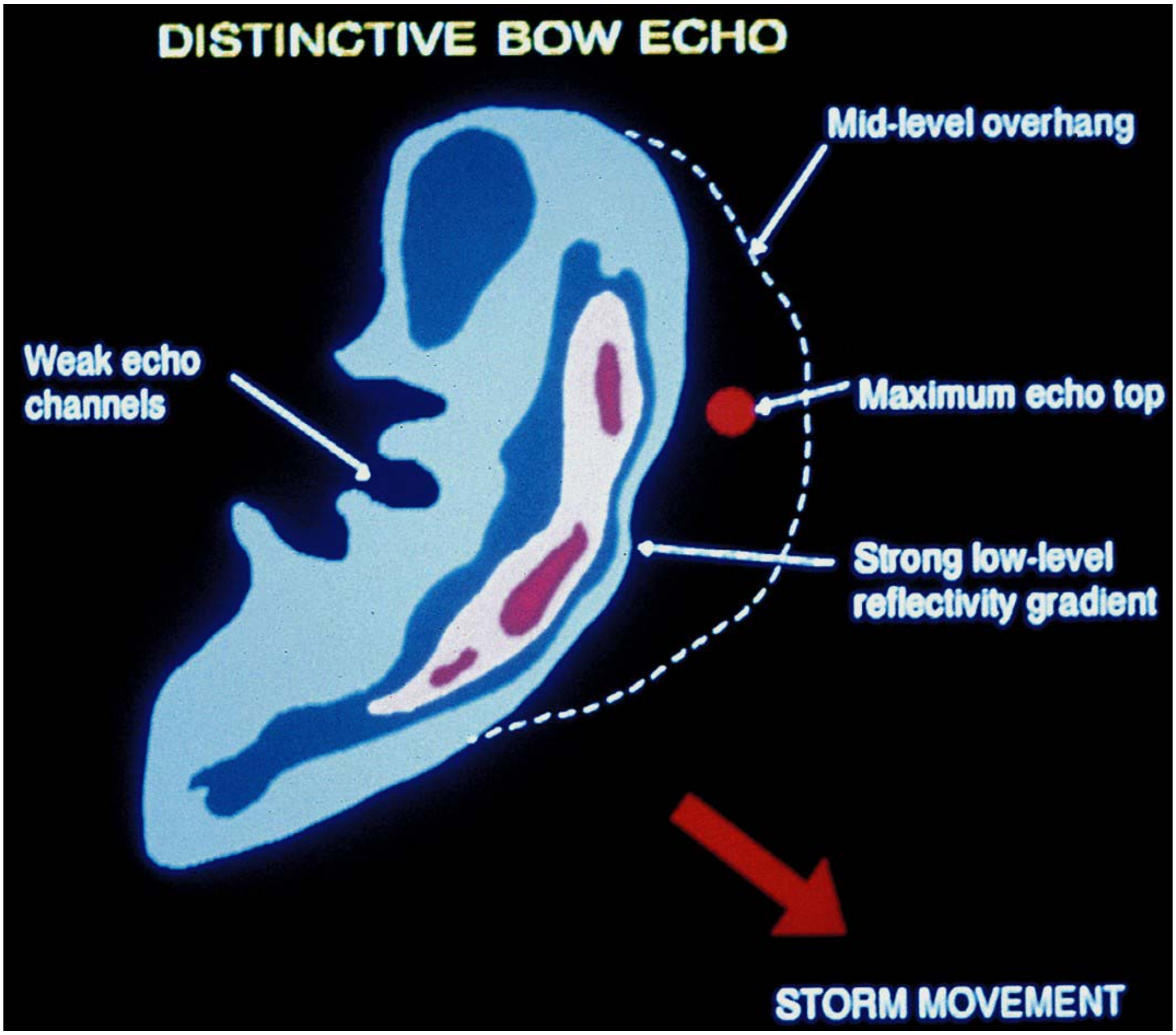

Figure 7-10
Schematic Diagram of a Distinctive Bow Echo

Features associated with the strong updraft along the leading edge of the Distinctive Bow Echo including the mid-level echo overhang, displaced echo top, and strong low-level reflectivity gradient. (After Przybylinski and Gery 1983).

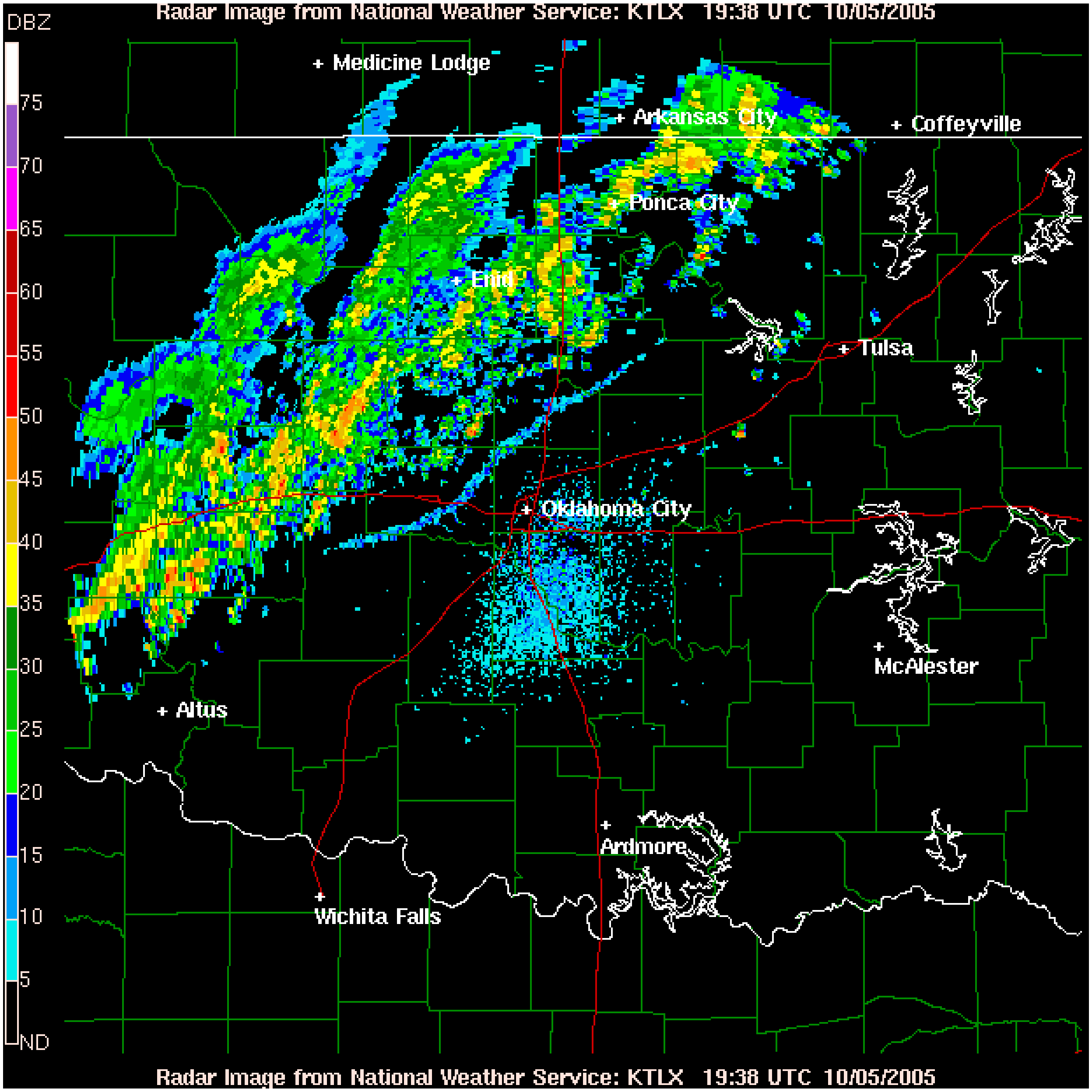

Figure 7-11
Base Reflectivity Product with a Cold Front

A cold front approaching the Oklahoma City, OK WSR-88D at 19:38 UTC on 5 October 2005 is shown on this 0.5° Reflectivity product. The cold front is the northeast – southwest oriented line (predominantely blue color/reflectivities less than 20 dbZ) northwest of the radar and southeast of the broader area of convection. This image was taken from the NWS Radar Image web page.

Thunderstorm development can, in many cases, be anticipated by identifying the intersection of boundaries tracked by radar or by enhanced reflectivity along these lines. In some cases, boundaries are not traceable to thunderstorms or other causes and may not be accompanied by density gradients. WSR-88D velocity data can be used to determine if such lines are accompanied by wind shifts and convergence that may trigger storms.

Also, general lifting of air above a front can sometimes be estimated from Doppler data using the VAD algorithm (Part C, Chapter 3, of this Handbook).

Once these boundaries have passed a location and sufficient precipitation exists behind the boundary, the VAD Wind Profile (VWP) can be applied to monitor the nature of the thermal advection, the depth of cold air, numerical model performance and the vertical depth of echo (precipitation, and in clear air situations, non-precipitation particles) (Figure 7-12). When convection generated in association with boundaries surrounds or is nearby the radar, often the VWP winds will not be representative of the environment. However, the VWP seen in Figure 7-12 was made by a radar located north of a warm front and within a developing ETC. Note that, in this case, the depth of the cold air can be determined beneath the wind shift at ~5,000 ft (~1500 m). Notice, too, that in the colder air beneath the frontal surface, winds are from a northeasterly direction. Within the frontal zone, winds veer in direction to southerly and then to the southwest. Stratiform precipitation echo extends to ~ 24,000 ft (~7300 m) ahead of an advancing mid-level short wave.

The subject of the Morphology of Large-Scale Precipitating Weather Systems is admittedly broad and is only partially discussed here. The reader may wish a more detailed treatise and is urged to obtain text books on the subject (e.g., Bluestein 1992; Shapiro and Gronas 1999; Carlson 1998). The following Internet and references are also available:

- Mesoscale Meteorology Severe Convection II: Mesoscale Convective Systems – Bibliography:

  http://meted.ucar.edu/mesoprim/severe2/print_version/_p_9.0Bibliography.htm.

- Cold Pool/Shear Interactions in Mesoscale Convective Systems:

  http://www.hprcc.unl.edu/nebraska/pool-shear.html,

- References:

  http://www.hprcc.unl.edu/nebraska/references.html.

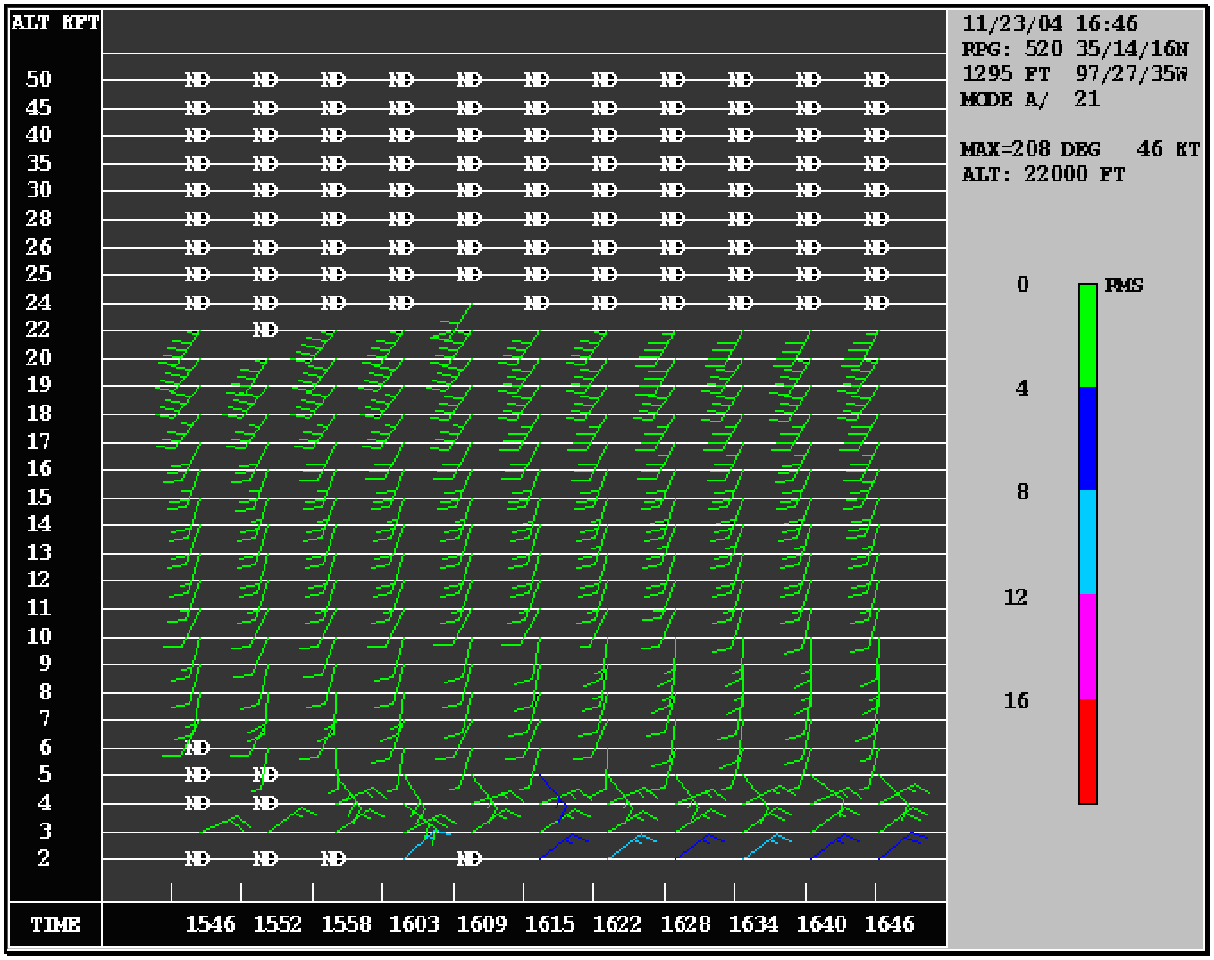

Figure 7-12
VAD Wind Profile

This VWP product was collected by the Wichita, KS WSR-88D at 16:52 UTC on 23 November 2004 (NCDC NEXRAD Viewer graphic). Note the wind shift from northeast at 20 kts (10 ms-^{1}) at 4,000 ft (~1200 m) to south at 5 kts (2.5 ms^{-1}) at 6,000 ft (~1800 m). This wind shift marks the frontal surface near 5,000 ft (~1500 m).

REFERENCES

Atlas, D. (Ed), 1990: *Radar in Meteorology*. Amer. Meteor. Soc., Boston, MA., 773 pp.

Bluestein, H. B., 1992: *Synoptic-Dynamic Meteorology in Midlatitudes*, Vol. I and II, Oxford University Press, 1015 pp.

Bluestein, H. B. and M. H. Jain, 1985: Formation of mesoscale lines of precipitation: Severe squall lines in Oklahoma during the spring. *J. Atmos. Sci*., **42**, 1711-1732.

Burke, P. C. and D. M. Schultz, 2004: A 4-yr climatology of cold-season bow echoes over the continental United States, *Wea. Forecasting*, **19**, 1064-1071.

Carlson, T. N., 1998: Mid-Latitude Weather Systems. Amer. Meteor. Soc., Boston, MA, 507 pp.

COMET, Mesoscale Convective Systems: Squall lines and Bow Echoes, 1999, Cooperative Program for Operational Meteorology, Education and Training, Distance Learning Program. http://www.meted.ucar.edu/convectn/mcs/.

Coniglio, M. C., D. J. Stensrud, and L. W. Wicker, 2004: How mid- and upper-level shear can promote organized convective systems. Preprints, *22nd Conf. on Severe Local Storms,* Zurich, Amer. Meteor. Soc., paper 10.5.

Coniglio, M. C., D. J. Stensrud, and M. B. Richman, 2004: An observational study of derecho-producing convective systems. *Wea. Forecasting*, **19**, 320-337.

Doswell, C. A. III, 2001: Severe Convective Storms – An overview, *Severe Convective Storms*, *Meteor. Monogr*., **50**, C. A. Doswell (Ed.), Amer. Meteor. Soc., Boston, MA, 561 pp.

Evans, J., and C.A. Doswell III, 2001: Examination of derecho environments using proximity soundings. *Wea. Forecasting*, **16**, 329-342.

Fritsch, J. M., and G. S. Forbes, 2001: Mesoscale convective systems. *Severe Convective Storms, Meteor. Monogr.,* No. **50**, Amer. Meteor. Soc., 323–357.

Fujita, T. T., 1978: Manual of downburst identification for Project NIMROD. SMRP Res. Pap. 156, University of Chicago, 104 pp.

Hane, C. E., 1984: Extratropical Squall Lines and Rainbands. AMS Intensive Course on Mesoscale Meteorology and Forecasting, Boulder, CO.

Houze, R. A., Jr., S. A. Rutledge, M. I. Biggerstaff, and B. F. Smull, 1989: Interpretation of Doppler weather radar displays in midlatitude mesoscale convective systems. *Bull. Amer. Meteor. Soc*., **70**, 608-619.

Johns, R. H., and W. D. Hirt, 1987: Derechos: Widespread Convectively Induced Windstorms. *Wea. Forecasting*, **2**, 32-49.

Johns, R. H., K. W. Howard, and R. A. Maddox, 1990: Conditions Associated with Long-Lived Derechos - An Examination of the Large-Scale Environment. Preprints, *16th Conf. on Severe Local Storms*, Kananaskis Park, AB, Canada, Amer. Meteor. Soc., 408-412.

Jorgensen, D., 1982: The Organization and Structure of Hurricane Convective Bands with Applications to NEXRAD. *NEXRAD Doppler Radar Symposium/Workshop*, Univ. of Oklahoma, Norman, OK, pp. 68-81.

Kessinger, C. J., P. S. Ray, and C. E. Hane, 1983: *An Oklahoma Squall Line: A Multiscale Observational and Numerical Study,* Cooperative Institute for Mesoscale Meteorological Studies Report No. 34, 211 pp.

Kessinger, C. J., P. S. Ray, and C. E. Hane, 1987: The Oklahoma squall line of 19 May 1977. Part I: A multiple Doppler analysis of convective and stratiform structure. *J. Atmos. Sci*., **44**, 2840-2864.

Koscielny, A. J., R. J. Doviak, and R. M. Rabin, 1982: Statistical considerations in the estimation of divergence from single-Doppler radar and applications to pre-storm boundary layer observations. *J. Appl. Meteor*., **21,** 197-210.

Lemon, L. R., 1980: Severe thunderstorm radar identification techniques and warning criteria. NOAA Tech. Memo. NWS NSSFC-3, 60 pp.

Lemon, L. R., D. W. Burgess, 1993: Supercell associated deep convergence zone revealed by a WSR-88D. Preprints, *26th Inter. Conf. on Radar Meteorology*, Norman, OK, Amer. Meteor. Soc., 206-208.

Lemon, L. R., and S. Parker, 1996: The Lahoma storm deep convergence zone: Its characteristics and role in storm dynamics and severity. Preprints, *18th Conf. on Severe Local Storms*, Atlanta, GA, Amer. Meteor. Soc., 70-75.

Maddox, R. A., 1980: Mesoscale convective complexes. *Bull. Amer. Meteor. Soc.,* **61,** 1374–1387.

Maddox, R. A., K. W. Howard, and D. L. Bartels, and D. M. Rodgers, 1986: Mesoscale convective complexes in the middle latitudes. *Mesoscale Meteorology and Forecasting* P. S. Ray, Ed., Amer. Meteor. Soc.

Miller, D.J., and R.H. Johns, 2000: A Detailed Look at Extreme Wind Damage in Derecho Events, Preprints, *20th Conf. on Severe Local Storms*, Orlando, FL, Amer. Meteor. Society, 52-55.

Miller, D.J., D.L. Andra, J.S. Evans and R.H. Johns, 2002: Observations of the 27 May 2001 High-End Derecho Event in Oklahoma, Preprints, *21st Conf. on Severe Local Storms*, San Antonio, TX, Amer. Meteor. Society, 13-16.

Nolen, R. H., 1959: A radar pattern associated with tornadoes. Bull. Amer. Meteor. Soc., 40, 277–279.

Ogura, Y., and M. T. Liou, 1980: The structure of a mid latitude squall line: A Case Study. *J. Atmos. Sci*., **37,** 553-567.

Parker, M.D., and R.H. Johnson, 2004a: Simulated convective lines with leading precipitation. Part I: Governing dynamics. *J. Atmos. Sci.,* **61**, 1637-1655.

Parker, M. D., and R. H. Johnson, 2004b: Simulated convective lines with leading precipitation. Part II: Evolution and maintenance. *J. Atmos. Sci.,* **61**, 1656-1673.

Parker, M. D., and R. H. Johnson, 2004c: Structures and dynamics of quasi-2D mesoscale convective systems. *J. Atmos. Sci*., **61**, 545-567.

Parker, M. D. and R. H. Johnson, 2000: Organizational modes of midlatitude mesoscale convective systems. *Mon. Wea. Rev*., **128**, 3413-3436.

Przybylinski, R. W., and W. J. Gery, 1983: The reliability of the bow echo as an important severe weather signature. Preprints, *13th Conf. On Severe Local Storms*, Tulsa, OK, Amer. Meteor. Soc., 270-273.

Rabin, R. M., D. E. Engles, and A. J. Koscielny, 1987: Applications of a Doppler radar to diagnose a frontal zone prior to thunderstorms. *Mon. Wea. Rev*., **115,** 2674-2686.

Rogers, R. R., 1976: *A Short Course in Cloud Physics*, Pergamon Press, 224 pp.

Schmocker, G. K., R. W. Pryzbylinski, and Y.J. Lyn, 1996: Forecasting the initial onset of damaging downburst winds associated with a mesoscale convective system (MCS) using the mid-altitude radial convergence (MARC) signature**.** Preprints**,** *15th Conf. on Wea. Analysis and Forecasting,* Norfolk, VA, 306-311.

Shapiro, M. A., and S. Grønås, (Ed.), 1999: The Life Cycles of Extratropical Cyclones. Amer. Meteor. Soc. Boston, MA, 359 pp.

Wakimoto, R. M., C. Huaqing, and H. V. Murphey, 2004: The superior, Nebraska supercell during BAMEX. *Bull. Amer. Meteor*. Soc., **85**, 1095-1106.

Weisman, M.L., and R. Rotunno, 2004: “A theory for strong, long-lived squall lines” revisited. *J. Atmos. Sci*., **61**, 361-382.

Wilson, J. W., R. E. Carbone, H. Baynton, and R. J. Serafin, 1980: Operational applications of meteorological Doppler radar. *Bull. Amer. Meteor. Soc.*, **61,** 1154-1168.

CHAPTER 8

MORPHOLOGY OF INDIVIDUAL THUNDERSTORMS AND ATTENDANT PHENOMENA

8.1 Thunderstorm Cells and Their Evolution. Refer to Part D, Chapter 4, of this Handbook for operational application of the WSR-88D to convective and severe convective storms which also contains a discussion of the critical velocity signatures and morphology associated with severe convective storms. The following discussion applies primarily to the distribution, character, and changes in the water substance within convective storms via detection by radar.

The dynamical building block of a thunderstorm is the cell. A cell is a compact region of relatively strong vertical air motion (many meters per second). With radar, cells are identified by their associated volumes of precipitation.

Most thunderstorms are composed of several short-lived cells known as ordinary cells. At any given time, such storms consist of a succession of ordinary cells at different stages of evolution. There are three stages in the evolution of ordinary cells (Figure 8-1): cumulus, mature, and dissipating.

The cumulus stage is characterized by updrafts throughout the cell. As the cell builds upward, moisture condenses and precipitation particles grow. The precipitation begins descending within the cloud and an associated downdraft begins to develop. This downdraft is forced by: 1) the drag exerted on the air by the precipitation particles and 2) negative buoyancy due to evaporational cooling as cloud and some of the condensate evaporates in dryer air that has been entrained into the storm from outside. The downdraft signifies the beginning of the mature stage.

The mature stage is characterized by precipitation reaching the ground. Updraft and downdraft coexist side by side, the downdraft being best developed in the lower portions of the precipitation shaft. With increasing downdraft development, cloud and more of the descending precipitation evaporates resulting in much of the downdraft displaced adjacent to, but outside of, the visual cloud. The downdraft brings evaporatively cooled air in the rain area toward the ground, where it produces a diverging pool of cold air. The leading edge of the cold air forms a micro cold front called a “gust front,” characterized by a sudden onset of shifting and gusty cool winds and rising pressure. New cells tend to form above and along this outflow.

The cell enters the dissipating stage when the updraft is replaced by downdraft, which spreads throughout the entire cell before weakening and disappearing. Simultaneously, the cold dome of downdraft air near the surface continues to spread outward becoming increasingly shallow and the winds behind the gustfront decrease. At this point, all that is left of the original cumulonimbus is often an “orphan anvil.” In other words, only the anvil aloft remains and the lower level cumulus cloud has dissipated.

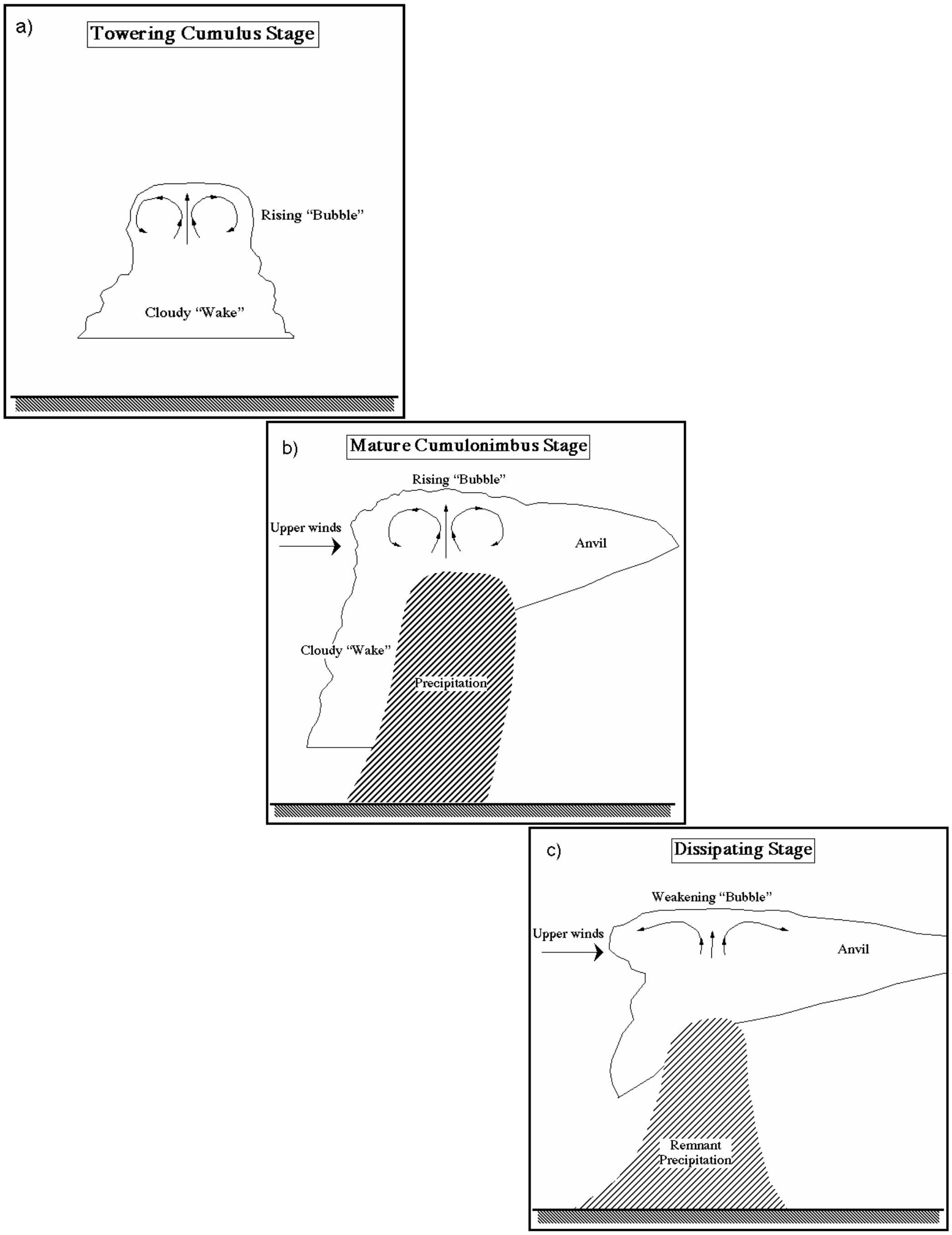

Figure 8-1
Ordinary Cell

The three stages of an ordinary cell life cycle, a) towering cumulous, b) mature, c) dissipating. Features of the figure are labeled showing distributions of cloud (outlined) encompassing updraft and precipitation encompassing downdraft. (From Doswell 2001, after Byers and Braham 1949).

The lifetime of an individual cell averages about 40 minutes, during which it may travel about 15 to 30 km (8 to 16 nm) in the general direction of the mean upper winds in which it is embedded. A storm consisting of a sequence of several such cells may, however, persist for several hours.

In the presence of considerable atmospheric instability and vertical shear of the horizontal wind, an extremely vigorous unit of convection known as a supercell may develop (Figures 8-2a through c). Supercells are relatively uncommon, evolve only slowly, and are often multicellular but dominated by a single large cell. These storms tend to be large, often 20 to 30 km (11 to 16 nm) or more in diameter. They are long-lasting (sometimes up to 6 or more hours) and cause a disproportionate amount of severe weather such as very large hail, damaging winds, and are often consistent tornado producers. Radar features of supercells are described in Section 8.5.4. The supercell's basic distinguishing feature is a deep, persistent "mesocyclone" in which vertical velocity and vertical vorticity are correlated, with vorticity magnitude of $\sim 1 \times 10^{-2}\ s^{-1}$ or greater within such a storm (e.g., Klemp 1987). Thus, significant vorticity is present within the updraft and perhaps the "Rear Flank Downdraft" (RFD). At times the RFD is a significant portion of the mesocyclone. The mesocyclone is seen as cyclonic shear in the radial velocity pattern (Figure 8-2a). (Note the bright red color coded velocity adjacent to the bright green.) Additionally, the air circulation is only slowly evolving, with updraft and downdraft coexisting in a symbiotic manner for long periods. Essentially, the supercell is a prolonged version of the mature stage of an ordinary cell, but with the addition of the mesocyclone in which the updraft-downdraft couplet takes on a stable and mutually beneficial configuration.

Unlike ordinary cells that tend to drift with the cloud-bearing winds, supercells travel with motion significantly different from the mean wind in the atmospheric layer that contains them, often moving markedly to the right or left of the mean wind.

In some cases and at times, without a Doppler radar, an observed cell may be difficult to classify as either an ordinary cell or supercell because there is not always a clear-cut and easily determined distinction within the reflectivity field. For further detail concerning severe convective storms, the reader is referred to Browning (1977), Lemon and Doswell (1979), Doswell and Burgess (1993), and Doswell (2001) as well as many of their references.

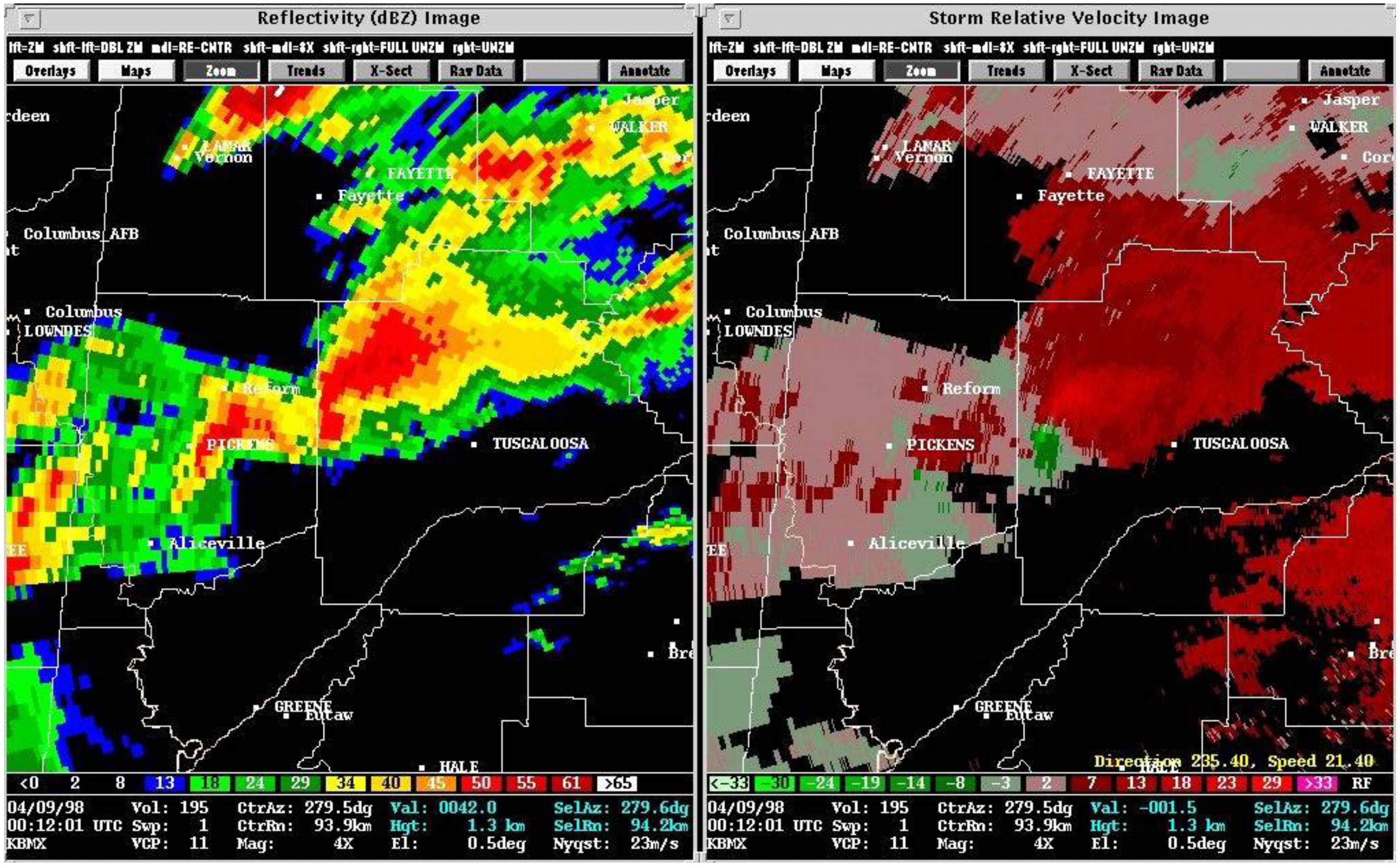

04/09/98 Vol: 195 CtrAz: 279.5dg Val: 0042.0 SelAz: 279.6dg
00:12:01 UTC Swp: 1 CtrRn: 93.9km Hgt: 1.3 km SelRn: 94.2km
KBMX VCP: 11 Mag: 4X El: 0.5deg Nyqst: 23m/s

04/09/98 Vol: 195 CtrAz: 279.5dg Val: -001.5 SelAz: 279.6dg
00:12:01 UTC Swp: 1 CtrRn: 93.9km Hgt: 1.3 km SelRn: 94.2km
KBMX VCP: 11 Mag: 4X El: 0.5deg Nyqst: 23m/s

Figure 8-2a
Doppler Radar Display of a Supercell at a Low Elevation

Seen here (storm in display center) is a mature supercell storm northwest of Tuscaloosa, AL, at 00:12 UTC on 8 April 1998 as scanned by the Birmingham, AL WSR-88D (WDSS display). Left display provides a view of the reflectivity field and the right, the Mean Radial Velocity. The velocity color code is in knots with the red colors signifying flow moving away from the radar and flow approaching the radar in green. Brighter colors are higher velocities. The color changes abruptly from red to green at the storm's right rear marks the position of the mesocyclone.

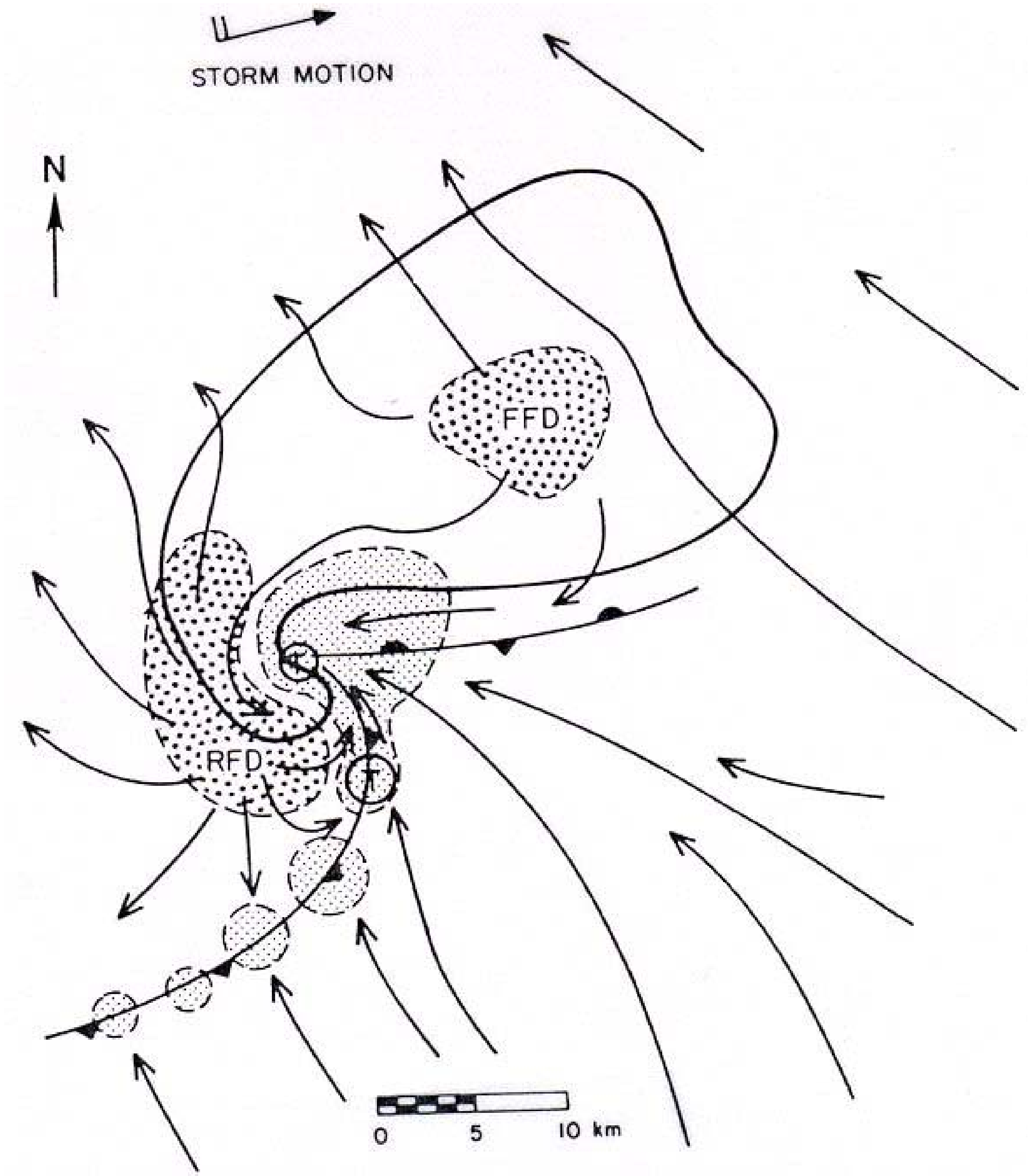

Figure 8-2b
Schematic Plan View of an Isolated Classic Supercell Storm Near the Surface

Thick line encompasses radar echo (note hook on southwest side). The wave-like gust front structure, resembling a synoptic scale cyclone, is depicted by classical frontal symbols and is part of the mesocyclone circulation. Low-level positions of the updraft and forward flank downdraft (FFD) and rear flank downdraft (RFD) are shown. Favored locations for tornadoes are near mesocyclone center (T) and along bulge in “pseudo-cold" front. Thin arrows depict storm-relative streamlines. (Adapted from Lemon and Doswell 1979).

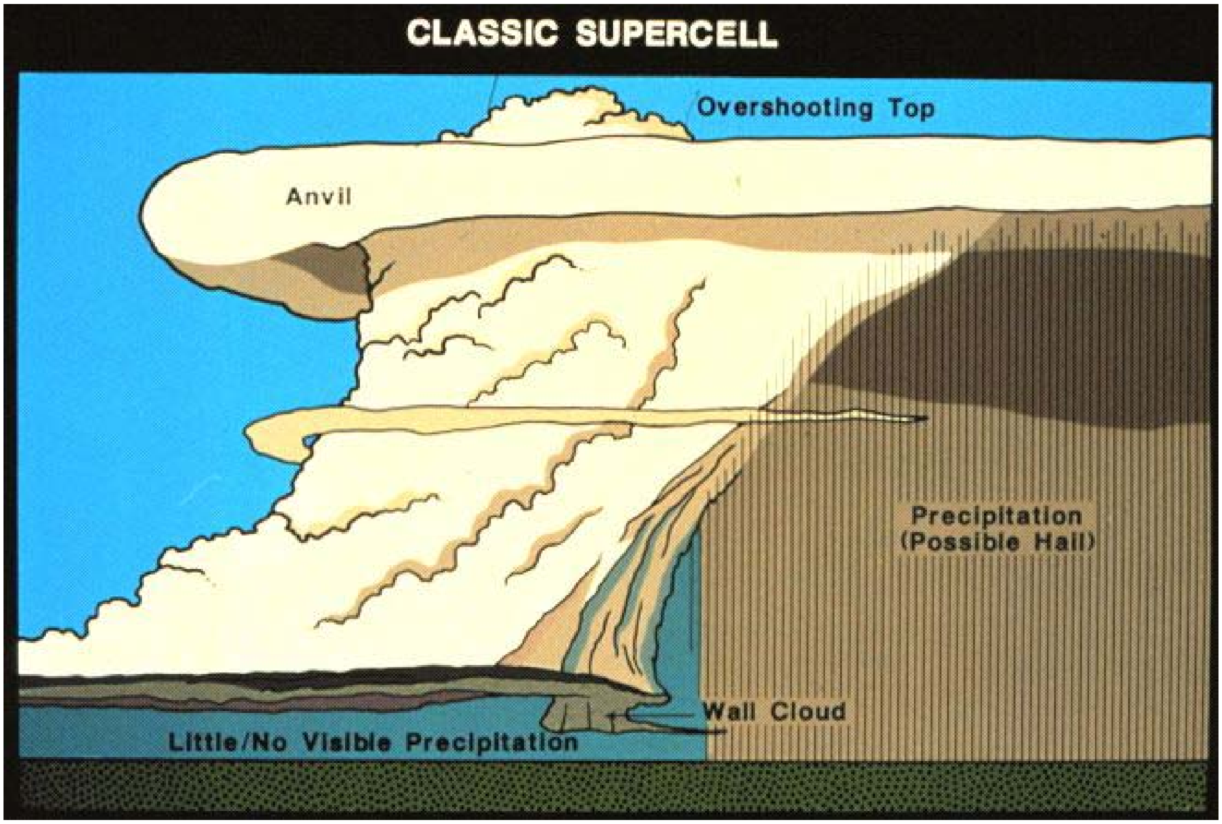

(Reproduced/modified by permission of American Geophysical Union.)

Figure 8-2c
Vertical View of Typical Classic (Supercell) Tornado-Producing Cumulonimbus

As seen from a southeasterly direction. Horizontal scale is compressed. All the features shown cannot be seen simultaneously from a single direction. Shelf cloud may not be present or may be to the left of the wall cloud. With time, spiral precipitation curtain wraps cyclonically around wall cloud from right to left. (From Doswell and Burgess 1993)

8.2 Types of Thunderstorms. In this document as in the science, we attempt to classify storms by storm "type." Over the years there have been attempts to develop a thunderstorm taxonomy such as that which began with the thunderstorm project of Byers and Braham (1949). Other attempts, Marwitz (1972) and Browning (1977), built upon the early "cellular" convection concept and further expanded it. This has been done in order to facilitate our convective storm understanding and to better discuss these storms in a meaningful and more utilitarian manner. But these taxonomies are conceptual in nature and should not be taken too literally or dogmatically. Real storms resist being placed in orderly and neat bins or categories. As will become clear, these conceptual models tend to deal with the degrees of draft steadiness and strength, especially the updraft. In some cases the updraft is seen as a "bubble" of weakly rising air and in other cases as a more-or-less steady and strong current. In reality there is probably a continuum ranging from the bubble at one end and the steady current at the other end of a broad spectrum. Furthermore, in reality there is a broad convective storm spectrum ranging from the single ordinary cell or storm at one end to the multicell, and finally to the true, quasi-steady state supercell. Moreover, this spectrum of storms is continuous in nature with categories considerably blurred and blended. In the study of convective storms we have somewhat arbitrarily chosen to divide this spectrum into individual categories. That is what has been done in this Handbook. The reader is reminded that reality will support these conceptual models only so far.

Browning (1977) introduced the storm classification system that consisted of basically two types of convective storms, the ordinary, and the supercell (Figure 8-3). However, for our purposes, we will also retain certain portions or aspects of the standard classification of Marwitz (1972) and divide thunderstorms into three basic categories as follows:

1. The supercell storm. It consists of one dominant cell (often with smaller cells embedded within the echo) that includes cyclonic (anticyclonic) turning of the mid-level updraft, i.e., the deep, persistent mesocyclone (mesoanticyclone) and continuously propagates to the right (left) of the mean winds. It often progresses steadily but slowly through a somewhat predictable evolution (Lemon and Doswell 1979; Burgess et al. 1982; Dowell and Bluestein 2000, 2002a) for 1 to 6 hours, or more (Figures 8-2a through c). A sub-classification is often recognized that includes the "Classic" (CL), the "Heavy Precipitation (HP), and the Low Precipitation (LP) supercell storms (Moller et al. 1990).

2. The multicell storm. It consists of several ordinary cells, and propagates discretely as new cells develop and old cells dissipate, sometimes in an organized fashion (Figure 8-4a, b).

3. The squall line. It consists of ordinary cells and sometimes supercells that are arranged in a linear fashion (Figure 8-5). Squall lines and MCS's are discussed somewhat in Section 8.5.7 and in Part B, Chapter 7, of this Handbook.

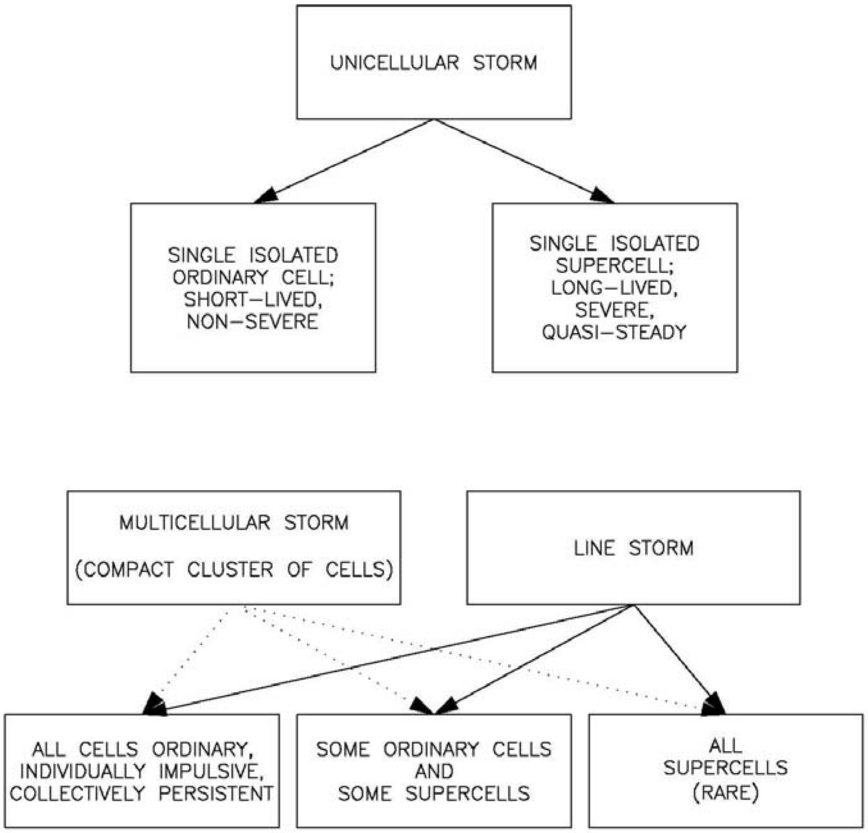

Figure 8-3
Browning's Classification of Thunderstorm Types

(From Browning 1986).

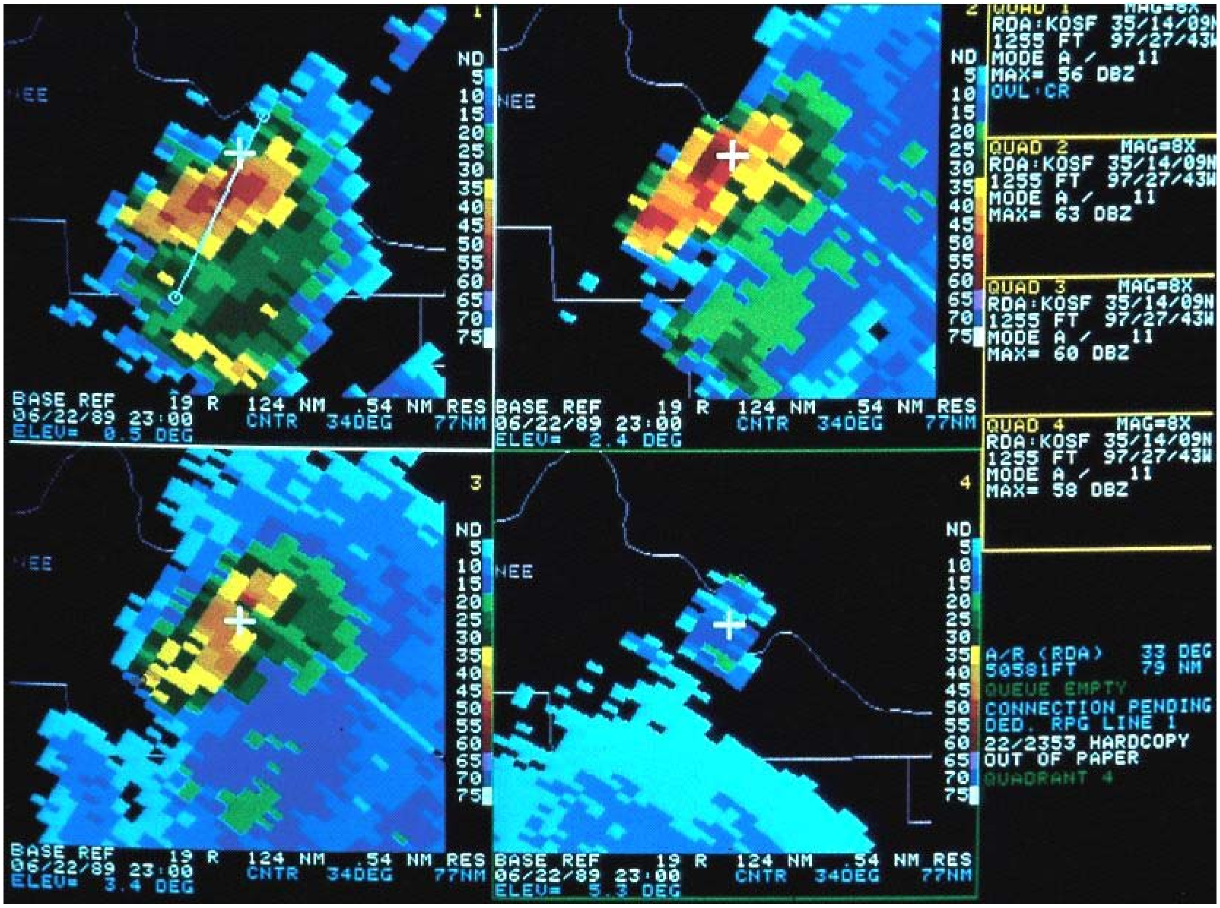

Figure 8-4a
Display of a Multicell Storm (4 - Panel)

An Oklahoma City, OK WSR-88D quarter screen Reflectivity product display of a multicell storm (PUP display) at 23:00 UTC on 22 June 1989. The magnified product elevations are as follows: upper left, 0.5°, upper right 2.4°, lower left, 3.4°, and lower right, 5.3°. Note the vertical cross section axis overlaid on the echo in the upper left quadrant or quadrant 1 (see Figure 8-4b). The white cross is at the same geographical location in all four panels.

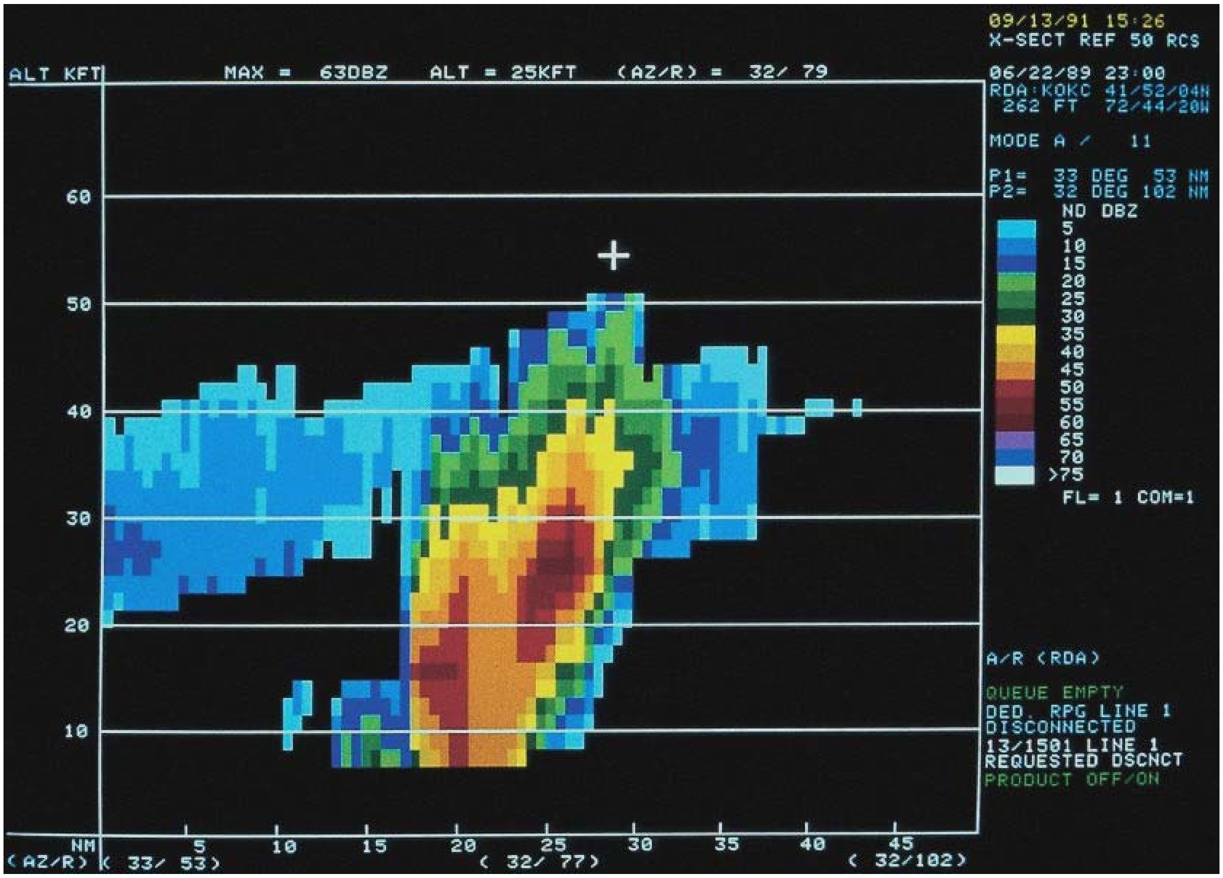

Figure 8-4b
Display of a Multicell Storm (Vertical Cross Section)

The Reflectivity (vertical) Cross Section along the axis shown in Figure 8-4a showing the structure of this multicell storm (PUP display).

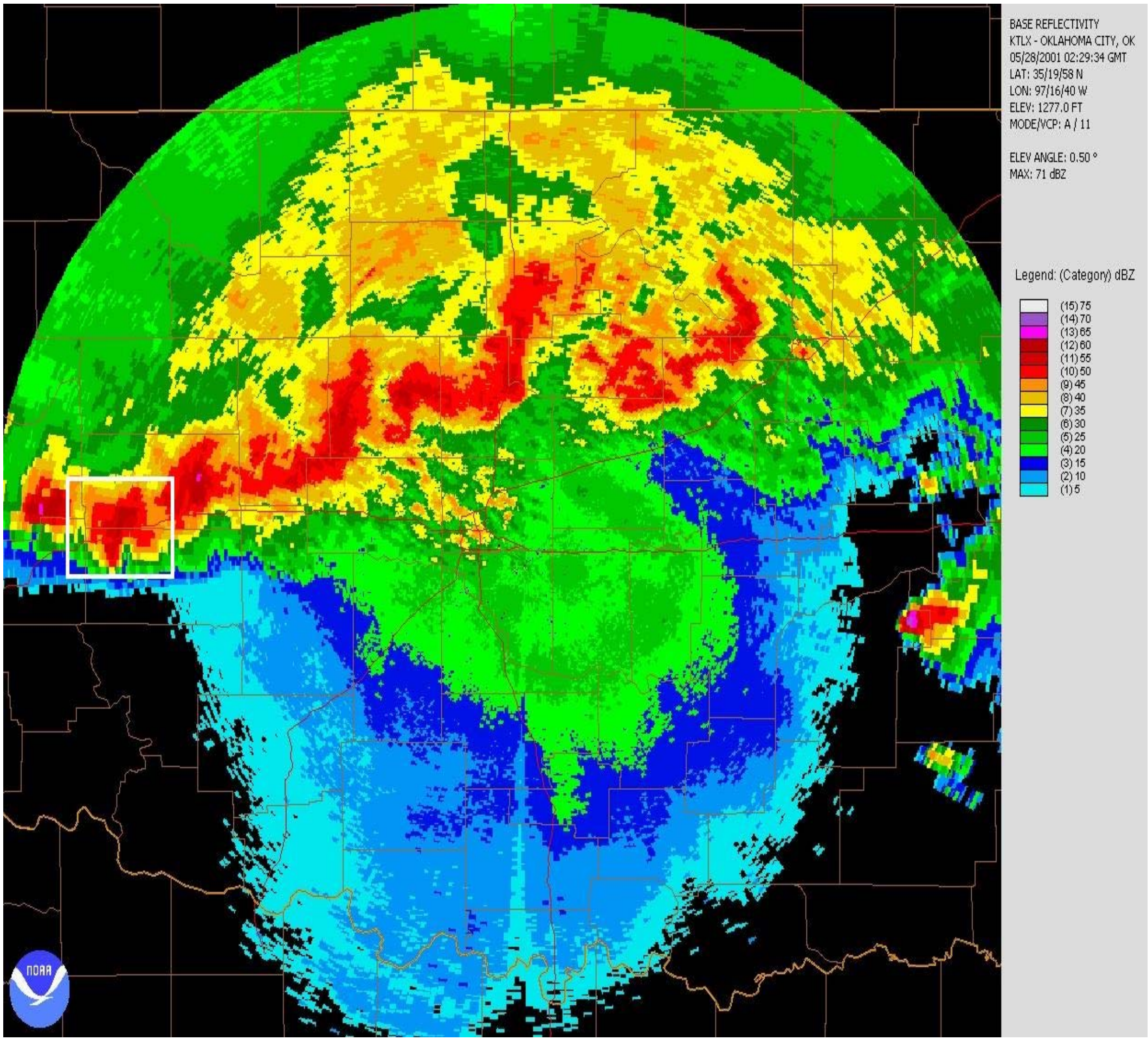

Figure 8-5
Display of a Squall Line at Low Elevation Angle

This line of thunderstorms consisted of both supercells and ordinary cells. This image os from the Oklahoma City, OK WSR-88D at 02:29 UTC on 28 May, 2001 (NCDC NEXRAD Viewer graphic). Note one of the supercells enclosed in the white box west of the radar. Reflectivity data levels are as labeled.

Browning (1986) points out some weaknesses of the above scheme; in particular, both multicell storm clusters and squall lines may contain supercells. Browning prefers the following classification (Figure 8-3).

1. Unicellular storm (e.g., Figures 8-1, 8-2a through c).
2. Multicellular storm (with a cluster of cells, not forming in a distinct line, such as in Figures 8-4a, b).
3. Line storm, i.e., squall line (containing cells along a line as in Figure 8-5).

Unicellular storms may consist theoretically of either a single ordinary cell of short duration or ideally, a supercell of long duration. (True unicellular storms, whether ordinary or supercell, are likely very rare if they do actually occur at all in nature.) Unicellular supercell storms are generally referred to simply as supercell storms (ignoring any multicellular characteristics that might be present). Multicell clusters and line storms may contain all ordinary cells, a mixture of ordinary and supercells, or (rarely) all supercells (Figure 8-5). Most supercell storms start and end life as none severe evolving multicellular storms.

8.3 Environmental Factors Governing Storm Type. Supercells form when the environmental deep layer vertical wind shear (horizontal vorticity) reaches a critical range such that it can be tilted into the vertical and stretched by strong thunderstorm updrafts supported by sufficient thermal instability (Klemp 1987; Johns et al. 1993) (Figure 8-6). Storms are weak when the instability and shear are slight. When the instability is high but the shear is low, storms consist of ordinary cells that are sometimes strong for short time-periods, either in isolation (the "pulse storm") or in disorganized multicellular clusters. Strong shear and weak instability can lead to supercell storms that are sometimes called "severely sheared" storms and/or short lived ordinary cells.

When the shear and thermal instability are both moderate or strong, the storms that develop tend to be well organized, supercells, multicell clusters, or squall lines and can produce very severe weather. Given that convective storms will occur with sufficient instability and deep layer shear (generally seen as shear from the surface to 6 km AGL) of greater than about 15-20 ms^{-1} (~30-40 kts), then supercells are the favored mode of organized convection and often produce very severe weather (Figure 8-6). With insufficient shear, storms are likely to be less organized multicell clusters or line storms, depending on whether the atmospheric mechanism that triggers the storms is confined to a local area or linear, such as along a dryline or front.

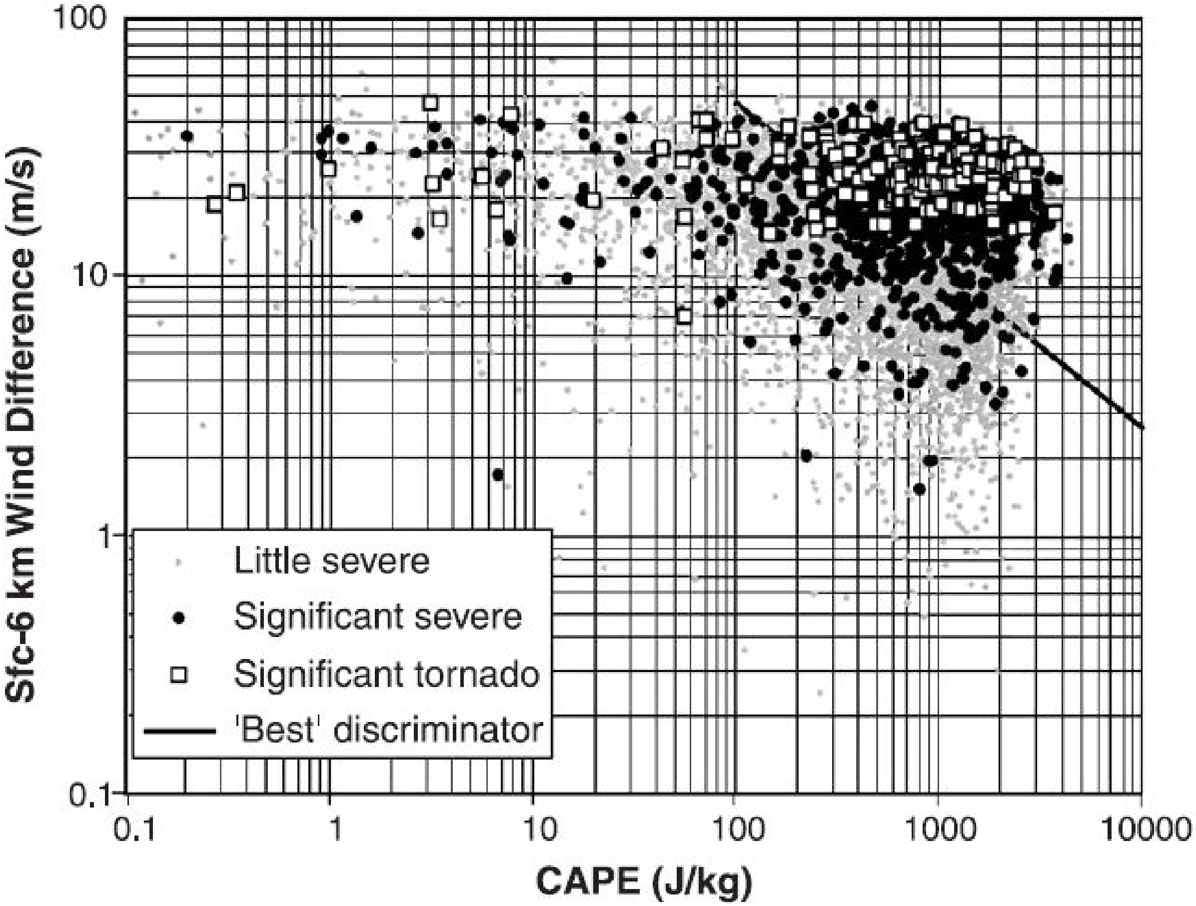

Figure 8-6
Surface to 6 km Wind Difference Versus CAPE

Magnitude of the vector wind difference (shear) between the surface and 6 km (ms^{-1}) and CAPE ($J\ kg^{-1}$) for all reanalysis soundings associated with severe thunderstorms in the US for 1997– 1999, segregated by weather type: non-significant severe weather (small gray dots), significant, non-tornadic severe weather (large black dots), and significant tornadoes (open squares). Solid black line is best discriminator between soundings associated with significant severe thunderstorms of any kind and other soundings. Note that non-severe soundings are not included in the figure. From Brooks et al. (2003).

As storms develop along a linear discontinuity, such as a boundary, and if the deep-layer shear vector tends to parallel the boundary, then adjacent storms interfere with one another such that precipitation from the up-shear storm will fall within (or seed) the down-shear storm. This typically leads to quasi-linear, two-dimensional, or continuous squall lines with few, if any breaks in the line. On the other hand, if the shear vector tends to be oriented more normal or perpendicular to the boundary, then individual storms will tend to be more isolated leading to scattered or broken lines of storms. If both instability and shear are sufficient, these individual storms developing within the line have a better chance of becoming supercells. Due to storm evolution, local meteorological conditions, and terrain effects, the dominant storm type may change over short distances and times.

Obviously, greater thermal instability means more potential energy available for storms to convert into kinetic energy and strong updrafts. The presence of dry air at mid-levels contributes to this available energy because it favors more intense downdrafts through increased evaporative cooling.

Shear has an important effect on storms for several reasons. First, precipitation is carried away from the updraft and allowed to cascade into the downdraft region favoring coexistence of both updraft and downdraft. Thus the storm's updraft and downdraft may co-exist side-by-side in a stable symbiotic configuration for prolonged periods. Second, the resulting storm-relative winds favor sustained and augmented low-level inflow into the updraft. This also helps keep the gust front from moving out away from the storm. Further, the interaction between the sheared environmental winds and the storm updraft causes a dynamic pressure gradient to develop that favors updraft propagation on one flank of the storm and decay on the other flank. Third, the presence of favorable vertical shear (often veering winds with increasing height) creates low-level horizontal vorticity that can be aligned with storm-relative inflow and tilted into the vertical. This can also eventually develop from unidirectional but sheared flow. The result is creation of substantial vertical vorticity within the updraft. Supercell storms and strong tornadoes require this vital raw ingredient.

Let's consider the development of vorticity in a little more detail. As an updraft extends into a sheared environment, horizontal vorticity tilting acts to create two vertical "vortices" in storm mid-levels. (While sometimes we use the term "vortices" or "rotation," in actual fact we are speaking of enhanced vertical vorticity and not necessarily true, closed, vortices or rotation.) The strength of these vortices depends on the strength of the shear and the intensity of the updraft. Facing toward the direction of the shear, on the right side of the updraft lies enhanced cyclonic vertical vorticity or vortex while on the left is found enhanced anticyclonic vertical vorticity. Initially, the vortices lie along the periphery of the updraft, and thus contain little updraft within them. However, the presence of this enhanced mid-level vorticity on either flank creates dynamically driven low pressure coincident with these vortices, thus creating vertically directed upward motion on either side of an initial large updraft. With the dynamic pressure at its lowest aloft, this enhanced upward directed pressure gradient force promotes the development of new updraft within enhanced vorticity centers. The effect is a widening of the updraft, new updraft growing on the flanks, and increasing correlation between updraft and vorticity on both flanks. For more detail the reader is encouraged to examine *Anticipating Convective Storm Structure and Evolution* and *A Convective Storm Matrix: Buoyancy/Shear Dependencies*. COMET (1996).

8.4 Storm Motion. Individual ordinary cells tend to move with the mean wind of the atmospheric layer that contains them (usually the entire troposphere). This is not surprising.

In a squall line, ordinary cells move roughly with the velocity of the mean wind, while the line as a whole moves roughly normal to its orientation and at a different speed. But this is understood since the motion of a two-dimensional feature can only be defined normal to its axis. Consider an example where the individual cells are arranged in a north-south line and cell motion is northeastward. Due to new cells developing on the southern end of the line and decaying on the northern end, the entire line moves eastward. Each individual cell is born at the southern tip of the line, moves up the line with time due to the organized pattern of birth and decay, and dies at the northern end.

Multicellular storm clusters (with all ordinary cells), in an environment with significant wind shear, have a similarly organized structure. The difference between individual cell motion and overall storm motion is again due to discrete cell and updraft propagation (Figure 8-7).

The motion of supercell storms also deviates from the mean wind. As explained above, interaction of the storm with the vertical shear profile generates a vertically directed dynamic pressure gradient force that continuously promotes new updraft on the flanks of the initial updraft. In addition, the manifestation of vertical vorticity within the mid-level updraft further promotes dynamic lift on the updraft flanks. The greatest tilting of horizontal vorticity occurs right and left of the shear vector. This means that the development of rotation and new updrafts also occur to the right and left of the shear vector. Precipitation developing in the middle of the widening updraft acts to develop a downdraft which, in turn, helps to split the widening updraft into two parts. The cyclonically (anticyclonically) rotating member moves to the right (left) of the shear vector. Since both the cyclonic and anticyclonic updrafts experience similar upward dynamic pressure forcing, they are equally strong supercells in a straight hodograph environment. The rightward deviating storm contains a cyclonic mesocyclone and the left deviating supercell or “left mover” contains an anticyclone or mesoanticyclone.

Once these supercells deviate off the hodograph, it experiences streamwise vorticity, and storm-relative helicity in its inflow layer. Tilting of the streamwise vorticity into the updraft immediately produces vertical vorticity well correlated with updraft. The processes that develop rotation in the unidirectional hodograph, also apply to curved hodographs. However, a curved hodograph implies that streamwise vorticity and helicity are available for the updraft to directly ingest upon its initial growth. In other words, the vorticity acts in the direction of the flow as in the thrown, spinning football. This represents the available streamwise vorticity that merely needs to be tilted into the vertical by the updraft in order for enhanced vorticity to be well correlated with the updraft. Therefore, the evolution from ordinary cell to supercell is much more rapid.

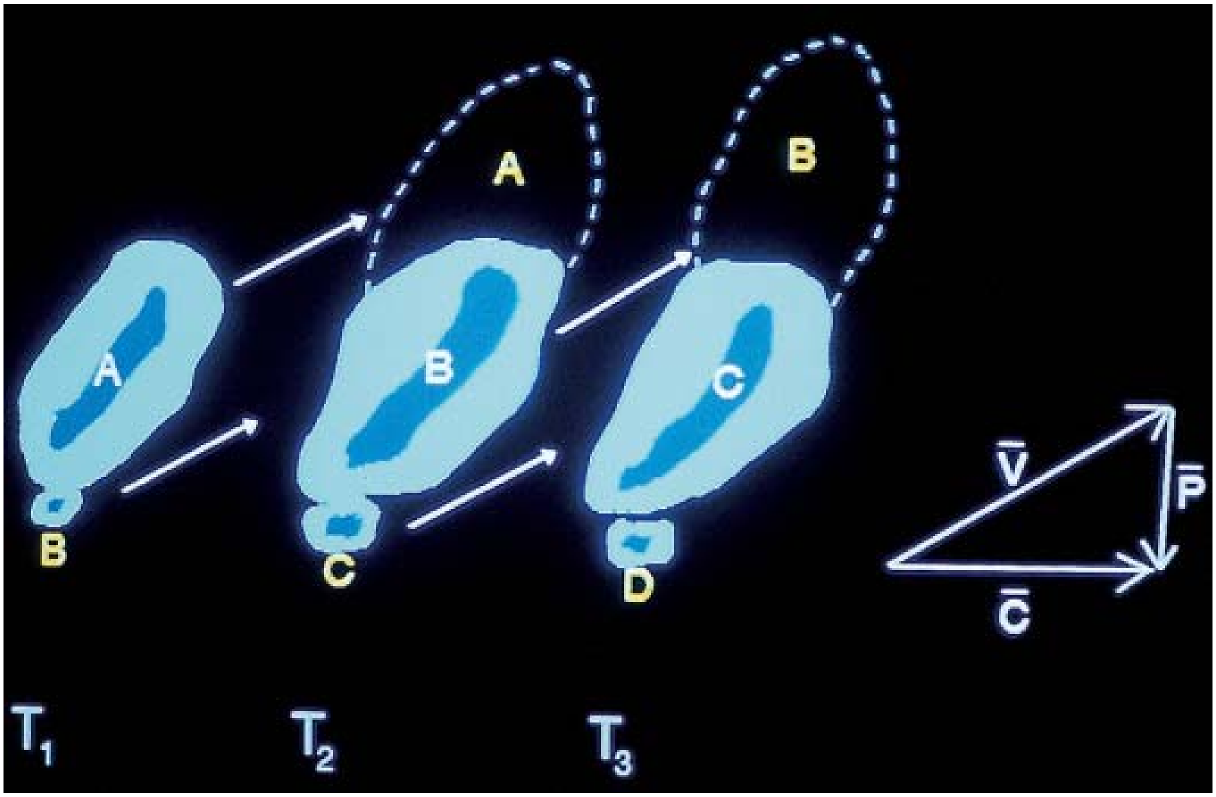

Figure 8-7
Conceptual Storm Motion Diagram

A schematic depicting storm motion where A – D are cells, V (bar) is cell advection, C (bar) is storm motion vector, and P (bar) is the propagation vector. Note that cells develop on the right flank, mature, and dissipate on the left flank in this example. However, there are almost an infinite number of variations, e.g., new development (propagation) may be occurring on the left forward flank with storm motion to the left of cell advection.

Finally, the presence of the gust front very near the edge of the precipitation cascade region and the RFD typically places it on the right rear storm flank (of the cyclonic supercell) where this further promotes boundary layer convergence. From there the gust front trails to the southwest or to the right rear of the mesocyclonic supercell storm. Thus, in the northern hemisphere, new updraft formation is strongly favored on the updraft flank, typically on the mesocyclonic supercell storm's right rear flank (especially for the Classic (CL)) and on the forward left flank of the left moving mesoanticyclonic supercell. The propagation is not only continuous, but it is often also discrete as new cells develop along the gust front and move into the storm complex. Thus, new updraft continuously, and often discretely, develop on the updraft flank strongly "driving" or "pulling" the storm significantly toward the updraft flank, on the right flank of the rightward deviating storm as compared to the prevailing environmental winds. The new growth on one side is balanced by decay in the region of downdrafts on the opposite side. Usually, mesocyclonic supercells move to the right of and slower than the mean wind while mesoanticyclonic supercells move to the left and faster than the mean wind. Such storms were originally called SR, Severe Right moving supercells by Browning (1964). As just explained, occasionally, SL, Severe Left moving supercells are observed. On those days when the vertical wind shear is strong and practically unidirectional, storms may split into SR and SL unidirectional supercells which follow highly divergent paths.

Therefore, and as explained above and by Klemp (1987), there is a close association between vertical vorticity within the updraft and anomalous motion, as exemplified by the mesocyclones (mesoscale anticyclonic circulations) observed in SR (SL) storms. For greater detail and illustration, the reader is encouraged to review *Anticipating Convective Storm Structure and Evolution* and *A Convective Storm Matrix: Buoyancy/Shear Dependencies*. COMET (1996).

8.5 Radar Reflectivity Structure of Thunderstorms.

The three-dimensional reflectivity field of a storm's radar echo and its evolution contain a great deal of information about the storm's intensity and severe weather potential (tornado, hail, strong winds, turbulence).

8.5.1 Weak Echo Regions.

An important concept in the interpretation of radar echoes is that of the WER associated with a strong updraft (Figure 8-8). The WER is created in part as a direct result of the updraft. A portion of the WER results when there is a sparsity of radar-detectable precipitation particles within the rapidly rising air in the updraft column. The echo weakness is due to the air rising so rapidly that precipitation does not have time to grow to detectability within the lower and mid-levels of the updraft. Additionally, precipitation formed elsewhere is unable to penetrate or fall through the updraft (Browning 1977).

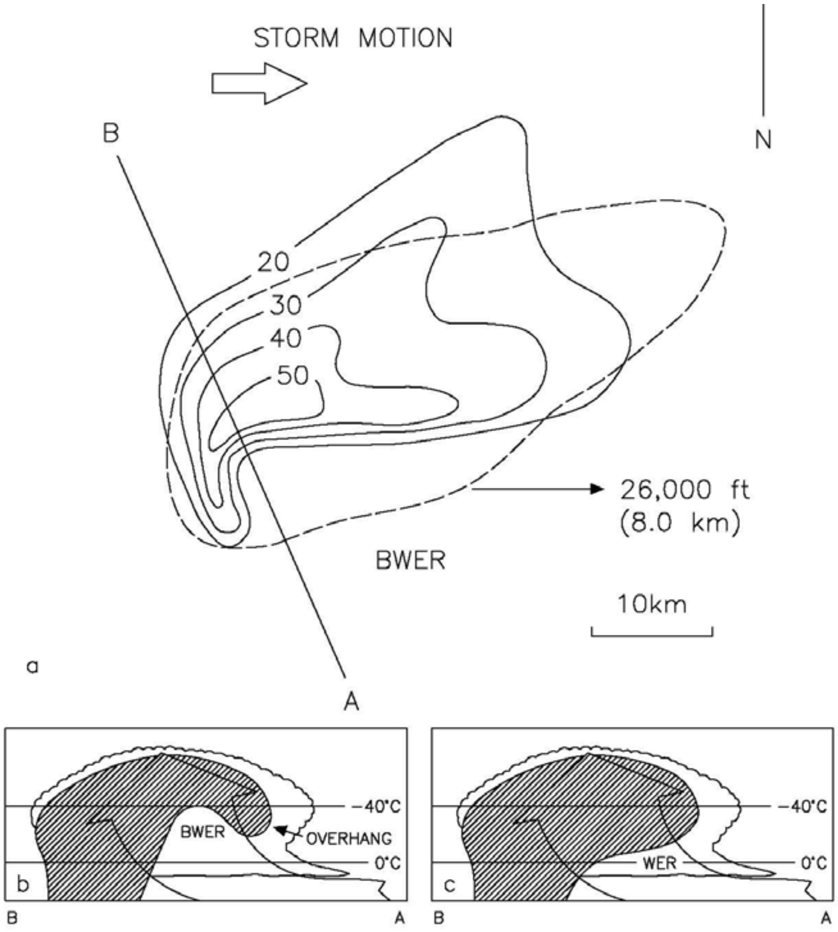

Figure 8-8
Schematic Diagrams Illustrating Bounded and Unbounded Weak Echo Regions

(a) Plan view of a right-moving supercell with a BWER. Solid lines are low-level and dashed lines are mid-level reflectivity in dBZ. Black dot is storm top (Lemon 1980). (b) Vertical cross section along line AB in (a). The extent of the radar echo (nominally 20 dBZ) is indicated by hatched shading and the location of the steady-state updraft and inflow is denoted by a bold arrow. Cloud outlines are also sketched (Browning 1977). (c) Vertical section along AB for a lesser developed storm than depicted in (a) and (b); here the weak echo region is unbounded.

However, the majority of the WER results when strong upper level divergence from the updraft summit transports large amounts of precipitation to high levels and is blown by the storm's relative winds (Lemon 1998). The result is a canopy of strong echo aloft with little or only weak echo beneath. As this precipitation descends from the cumuliform anvil aloft into the ambient environmental flow it forms what Browning termed the "slopping echo overhang." This should not be confused with the downstream anvil that may contain substantially weaker precipitation that evaporates as it descends but is still found aloft.

With increasing updraft (or sometimes as a result of better resolution at closer range), a bounded weak echo region (BWER) appears because air within the updraft core ascends still higher in the updraft before radar detectable precipitation particles form (Figure 8-8a). In a horizontal cross section, the weak echo region is completely surrounded, or bounded, by higher radar reflectivity values and results in the BWER. The acronym WER is reserved for unbounded weak echo regions (Figure 8-8b).

8.5.2 Ordinary Multicellular or Unicellular Storms in Weak Shear. The cumulus stage of each cell of an ordinary storm in weak shear begins on radar when the first echo develops aloft at temperatures between 0° C and -15° C or a height of 3 to 6 km (10,000 to 20,000 ft). The mature stage is marked by the tallest tops and highest reflectivities. The dissipating stage is associated with weakening reflectivities as the remaining precipitation developed aloft falls out. In the multicellular cluster, there are several cells at various stages of their life cycles. The complex of cells may last several hours due to new cells forming on the gust fronts of the mature storm cells.

8.5.3 Ordinary Multicellular Storms in Moderate to Strong Shear. In moderate to strong shear, an ordinary multicellular storm consists of an organized group of cells that develop and move in a consistent manner (Figure 8-9). Typically, the storm contains two to four cells at any given time. New cells develop from cloud towers a few kilometers in diameter, rising at 10 to 15 ms^{-1} (19 to 29 kts) in a preferred region on the updraft flank (see cell 3 at time 0 in Figure 8-9). The newly formed cell does not move into the storm complex but rather grows rapidly and becomes the storm center. Meanwhile, the previous cell (cell 2) begins to decay while another (cell 4) forms. New cells continue to form in this way at intervals of 5 to 15 minutes and each cell is identifiable on radar for about 40 minutes. A total of 30 or more cells may develop during a typical storm's lifetime.

The evolution of one of the cells (cell 3) is depicted by the vertical sections at the bottom of Figure 8-9. The first echo appears in the mid troposphere about 10 minutes after the associated daughter cloud starts rising rapidly. Soon afterward, the echo develops an inverted cup-like shape, partially encompassing a WER that lasts for several minutes until the entire echo has descended to the ground. The WER is associated with a moderately strong updraft reaching 20 to 30 ms^{-1} (39 to 58 kts) before diminishing with the descent of precipitation through it. The storm, as a whole, propagates to the right of the mean troposphere wind.

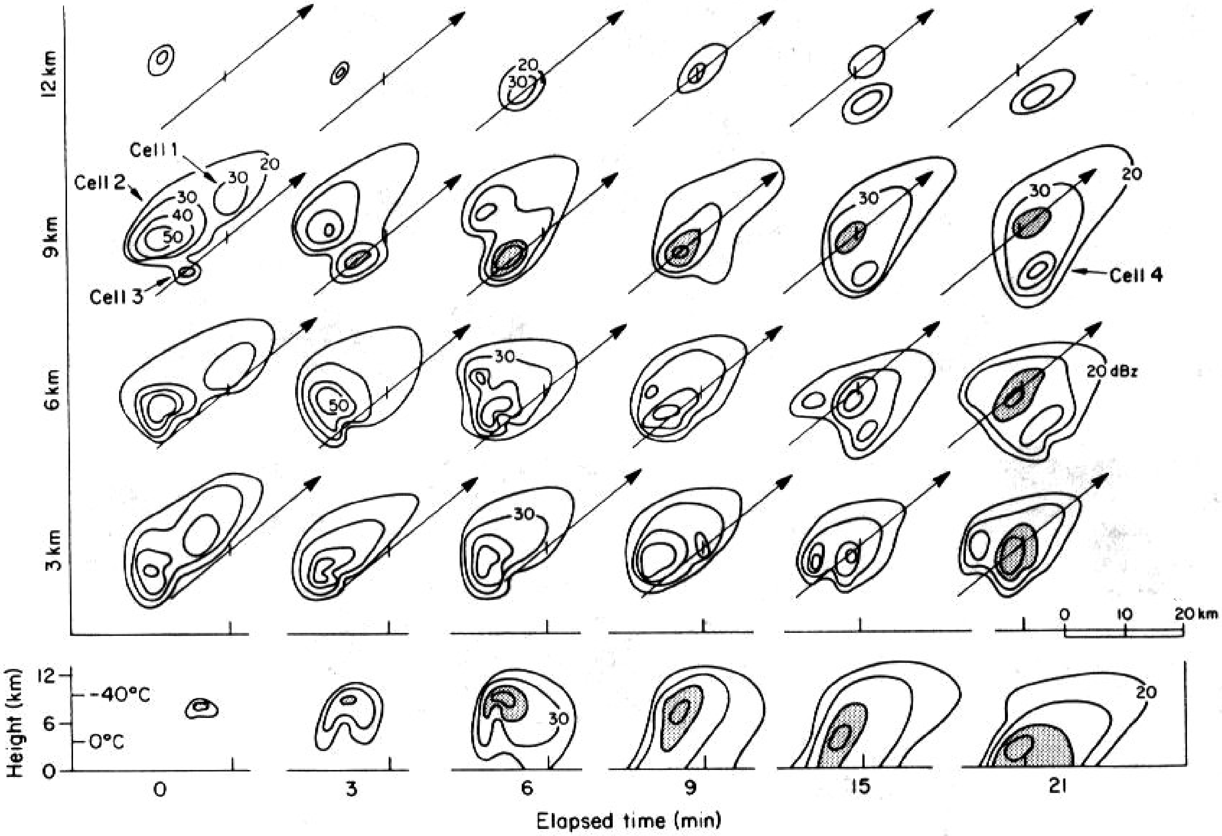

Figure 8-9
Schematic Horizontal and Vertical Radar Sections
for an Ordinary Multicell Storm

Various stages during a storm's evolution showing reflectivity contours at 10 dBZ intervals. Horizontal sections are illustrated for four altitudes (3, 6, 9, and 12 km AGL) at six different times. The arrow superimposed on each section depicts the direction of cell motion and is also a geographical reference line for the vertical sections at the bottom of the figure. Cell 3 is shaded to emphasize the history of an individual cell and the vertical cross-sections are also of cell 3 (Chisholm and Renick 1972).

Often in an environment with at least moderate shear, there are storms that appear to be hybrids between ordinary multicellular cluster storms and supercells. These storms have been labeled as weak evolution storms that gradually evolve from their initial multicellular state to the hybrid or weakly evolutionary supecells (Foote and Frank 1983). While individual small cells remain identifiable for brief periods as perturbations, these storms also develop supercelluler characteristics such as a deep persistent mesocyclone that move to the right (or left for mesoanticyclonic storms) of the mean environmental wind (Vasiloff et al. 1986). The majority of supercells have multiple cells, although one cell dominates.

Note that for the sake of the following discussion we are considering the CL supercell storm. We have already mentioned the spectrum of supercell storms including the CL, HP and LP supercell storms. However we have not considered that the Classic in particular also comes in the form of smaller and even very small storms called "mini-supercells" that are much smaller in all dimensions but can be just as severe (Figure 8-10). The "low-topped" supercell is similar except for other than having a shallower depth; other dimensions may be larger than the mini. The low-topped supercells may exhibit wide mesocyclones, and similarly, high-topped supercells may contain narrow mesocyclones. By definition, a mini-supercell is one with the depth and width substantially reduced and includes a narrow mesocyclone.

Low topped and mini supercells can reach anywhere from 20-30 kft (6.1–9.1 km) AGL. Mesocyclone diameters in mini-supercells typically are less than 3 nm (5.6 km). There are no structural differences between low topped, mini, and the more typical large supercells. There are differences in the expected severe weather. Giant hail (>2", 5 cm) is rare because of limited updraft depth, strength, and smaller dimensions. Poor radar sampling of small mesocyclones means that it is more difficult to measure high rotational velocities even when the circulations are relatively near the radar. To illustrate the variability of supercell size, the main supercell in each panel of Figure 8-10 is tornadic, yet only the largest supercell (right panel) was large enough for the radar mesocyclone algorithm to resolve the circulation as a mesocyclone. Therefore, it is important to recognize mini-supercells and be more sensitive to the fact that weak circulations (rotation less than 30 kts (15 ms^{-1})) can carry a significant tornado risk (Grant and Prentice 1996). Moreover, it is important to realize that the limitations of radar, primarily those dealing with beamwidth and aspect ratio and radar horizon, will often prevent the identification of mini-supercells at even modest ranges (greater than about 45 nm (83 km)).

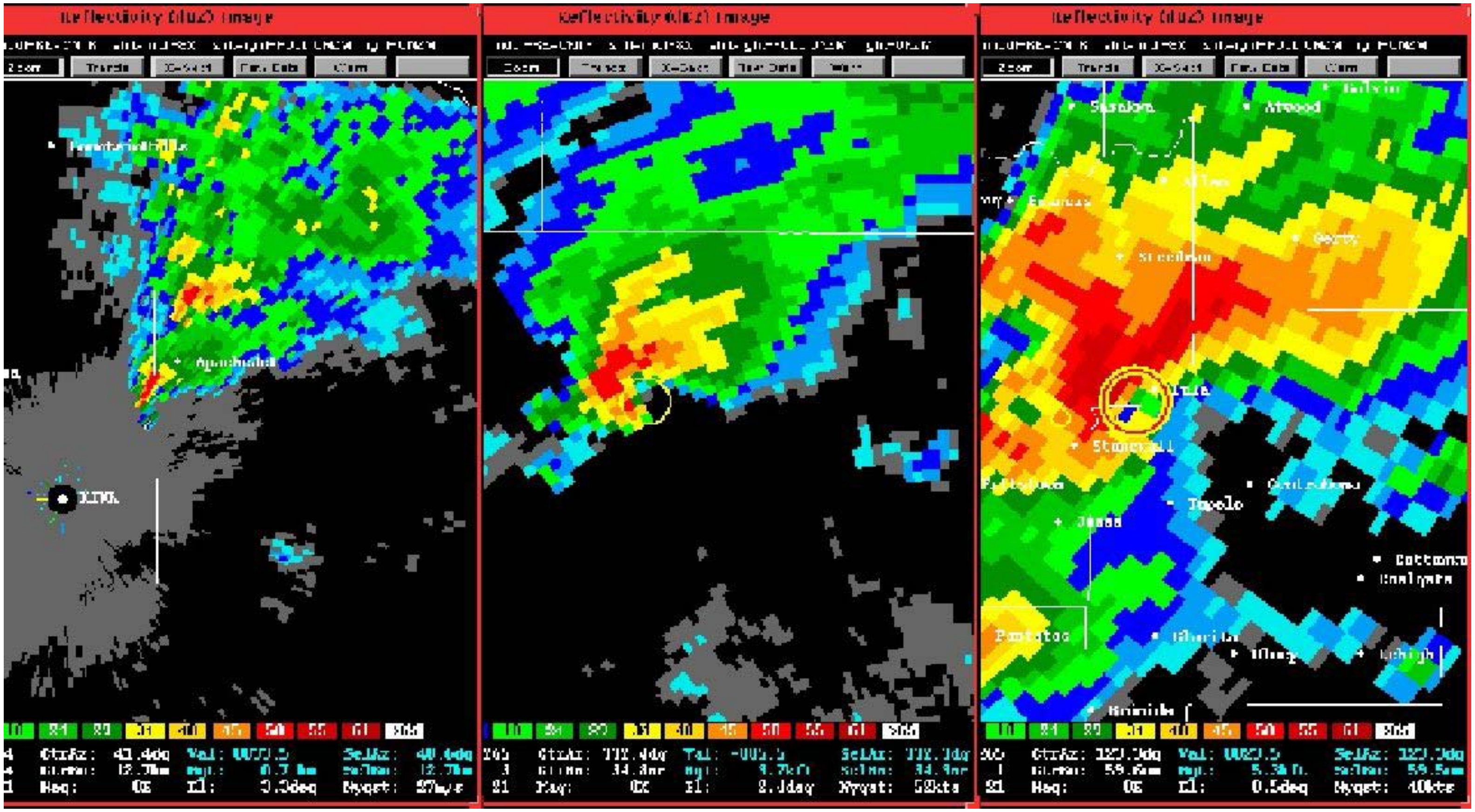

Figure 8-10
Reflectivity Imagery of Supercell Storms

All of these WSR-88D Reflectivity products are the same scale and all are severe, supercell storms. A mini-supercell is pictured left; a mini/low-topped supercell is at the center, and a large, classic supercell, at the right. Note the typical "V-notch" in the upper right of each echo in the 35 dBZ - 40 dBZ echo contours. The red ring in the two right panels indicates a mesocyclone detection by the Mesocyclone Algorithm (WDSS display).

8.5.4 Isolated Supercell Storms. Supercell storms display some basic and persistent characteristics that are often strikingly similar from storm to storm. These characteristics are as follows for a CL type supercell:

1. An approximately elliptic horizontal cross section aloft, often larger in all dimensions than the typical non-severe storm (Figures 8-2a through c). These storms are often characterized by a down-shear "V-notch" or "winged" appearance (Figure 8-10). An extensive plume is observed on radar and this forms part of a much larger visible anvil that extends downstream from the main storm core aloft. At low levels, the echo is situated mainly on the storm's left flank coincident with the forward flank downdraft but the echo may extend toward the right in the form of a hook-shaped appendage that is located mainly in the region of the rear flank downdraft.

2. A persistent WER/BWER is found on the updraft flank. A WER is very common for most supercells, even those with weak mesocyclones. A WER is persistent, and capped by high reflectivities (>45 dBZ) above. The WERs not overlaid by strong reflectivities imply weak or no updraft, such as an overspreading, down-shear, anvil layer. The WER is immediately adjacent to the low-level reflectivity core and bounded with high reflectivity gradients and on the storm-relative low-level inflow side.

   The BWER is less common but may also develop within the WER of the supercell. The BWER is conically shaped and decreases in width with height, extending to a height one-half to two-thirds of the storm depth. The BWER is indicative of a broad, strong (25 to perhaps 60 ms^{-1}; 49 to 115 kts) updraft that contains small cloud particles but little precipitation (Figures 8-11a through c). The storm top is located directly over the BWER and is over the updraft storm flank. When the storm is at moderate to long distances the BWER may not be detectable.

3. A high-reflectivity core (the hail zone) extending all the way to the ground borders the BWER on its left and rear flank resulting in a strong reflectivity gradient there. The largest hailstones are typically located in the strong reflectivity gradient next to the BWER, with smaller hail and rain at increasing distances to the left and left forward of the BWER. This is a size sorting effect associated with the descent of hail within rising air that is also flowing toward the storm's left flank.

   The precipitation cascade downdraft owes its existence to precipitation falling out of the tilted updraft and evaporating in the midlevel stream of environmental air that enters the storm on the right flank (Figure 8-11). However, the primary downdraft, the RFD, is along the storm rear flank and extending into the hook echo. The RFD has proven to be crucial to the production of tornadoes but its origin is still unknown.

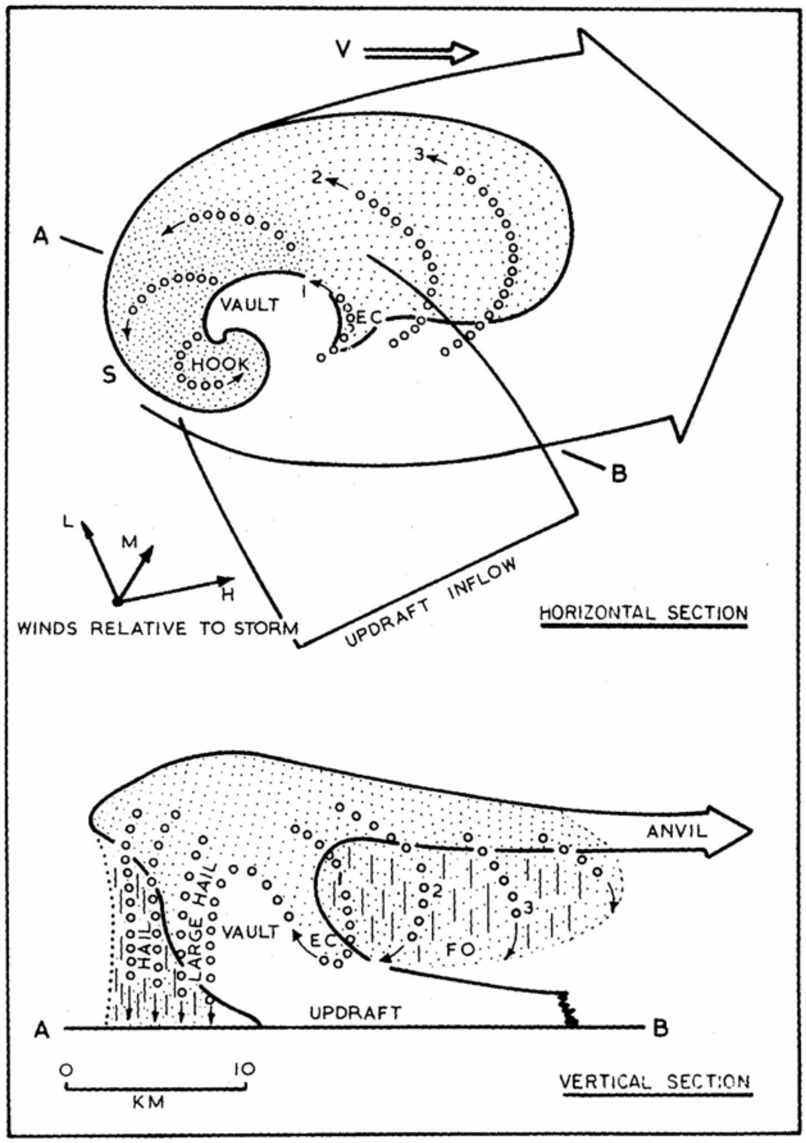

Figure 8-11a
Supercell Storm Illustration - Horizontal and Vertical Sections

Horizontal and vertical sections illustrating relation of updraft to the radar echo in Classic Supercell storm. Solid curves: extent of the updraft air; dotted curves: trajectories of some precipitation particles accounting for the characteristic shape of the radar echo. Horizontal section: light and heavily stippled shading denotes extents of rain and hail in the lower troposphere, respectively; AB oriented in the direction of the mean tropospheric wind shear, into which the updraft is inclined at low levels. Vertical section: broken vertical hatching denotes downdrafts. Characteristic features of the echo pattern referred to in the text are the BWER, hook, and forward overhang (FO) (Browning 1986).

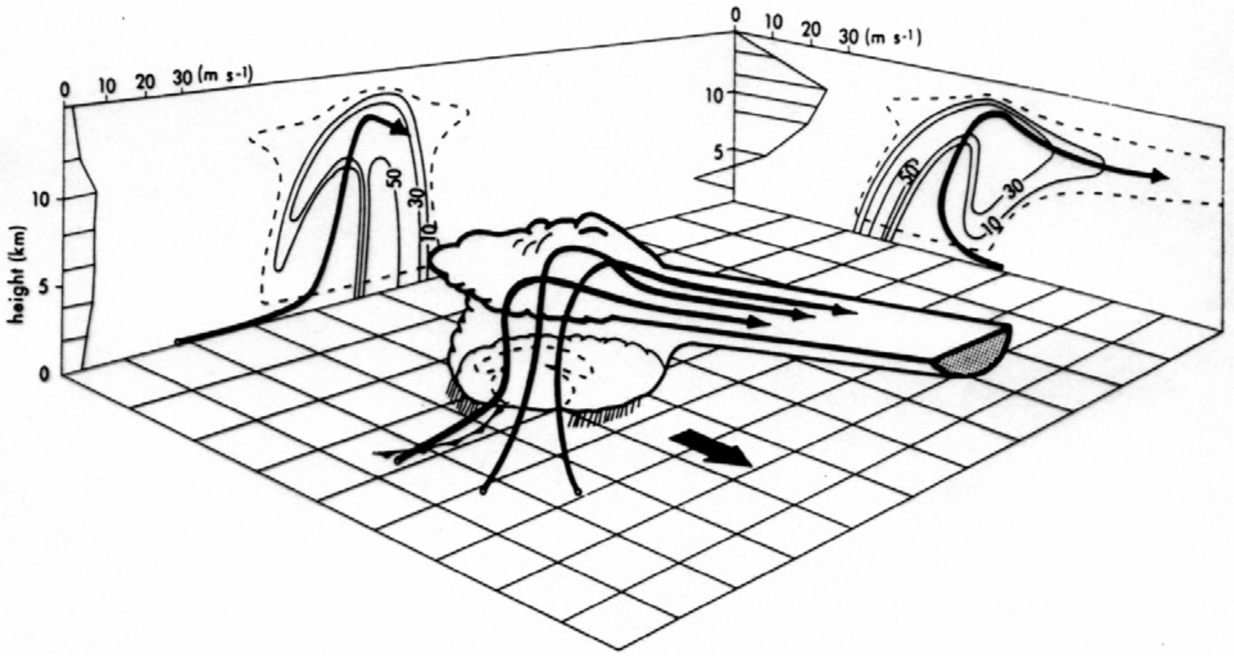

Figure 8-11b
Supercell Storm Illustration - Perspective View

A perspective view of a supercell storm depicting storm airflow and reflectivity structure (Chisholm and Renick 1972). The reflectivity contours are 10, 30, and 50 dBZ.

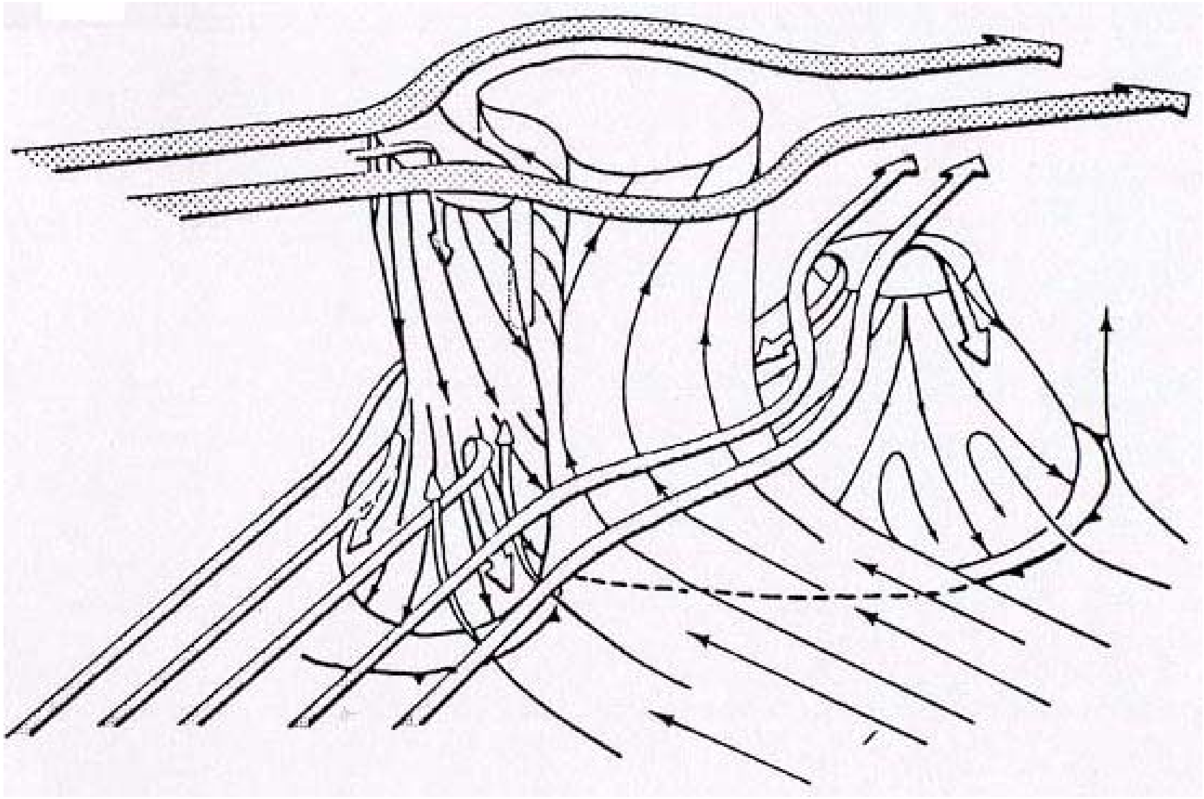

Figure 8-11c
Classic Supercell Storm Draft and Flow Illustration – Three-Dimensional Model.

Model schematic depiction of the drafts, tornado, and mesocyclone in an evolving CL supercell storm. Low-level flow is seen approaching the storm from the right front flank and rising and turning within the updraft in a cyclonic manner. Mid-level flow is shown approaching the storm from the right rear and flowing around the updraft region. A portion of the flow is shown descending into the RFD and the forward flank downdraft (FFD). While high-level flow is depicted as being involved in the RFD that is now in question. Its height of origin and the cause of the associated forcing is unknown at this time. Flow lines throughout the figure are storm relative and conceptual only, not intended to represent flux, streamlines, or trajectories. Conventional frontal symbols are used to denote outflow boundaries at the surface. From Lemon and Doswell (1979).

4. An important period in the life cycle of the CL is the collapse phase. During this phase the echo top lowers, the BWER and WER disappear or are reduced, reflectivity and VILs often decrease, and the hook echo often "wraps up" and disappears. The echo then resembles the ordinary cell, rather than the supercell. While hail size decreases during this period the storm is often undergoing tornadogenesis and producing downburst and microburst winds. The tornado, if it develops, will often reach its maximum size and strength. After collapse, the storm often resembles a typical multicell cluster storm, but may recycle and become a reinvigorated supercell.

The typical visual appearance of an isolated Classic supercell storm is illustrated by Figure 8-2c. For sake of clarity not all features are included, such as the spiraling rain curtain that gives rise to the hook on radar.

The relatively rarer "Left moving" supercell is almost a mirror image to the Classic supercell; thus its "mesocyclone" rotates anticyclonically and can be called a "mesoanticyclone." The "mirror" is in a vertical plane, parallel to the mean shear vector. Left moving storms often (but not necessarily) move faster and to the left of the mean wind and are notorious "hailers" but usually do not produce tornadoes, in contrast to most CL and HP supercell storms that commonly produce all forms of severe weather.

8.5.5 High Precipitation (HP) Supercell Storms. High Precipitation supercells may be the most common of all supercells. Admittedly, many of the features or characteristics of HP supercells are subjective in nature. These storms are efficient precipitation producers and often associated with strong downdrafts and outflows as well as very large hail. Large amounts of precipitation are available within these storms to wrap around the mesocyclone, producing large, high reflectivity hook echoes. Occasionally, the RFD gust front associated with the hook is sufficiently intense to generate strong convection along its leading edge. The result is that the strongest core can be behind and to the right of the mesocyclone path. Occasionally, this process leads to supercells being part of a much larger line of storms and they occasionally evolve into bow echoes.

There is a wide variety of possible HP supercell configurations (Figure 8-12). However, they all share traits common to supercells – an echo overhang and WER (sometimes a BWER), a displaced echo top and an inflow concavity, often on the front storm flank.

As with the Classic supercell, the inflow and mesocyclone are well correlated with primary updraft and the RFD and are typically long lived. The mesocyclone with the HP is usually well sampled by radar owing to the high reflectivities in the hook and circulation. But the correlation of the RFD with the precipitation cascade in the HP apparently often lead to a relatively cold RFD. Spotters in the field often have a difficult time observing the mesocyclone area most favorable for tornadogenesis. The updraft with its associated WER and BWER are often on the front storm flank. HP environments typically show more boundary layer moisture than that of LP or even CL. However, high boundary layer moisture is not necessary for HP occurrence. Another possibility includes low anvil-level, storm-relative flow (<18 ms^{-1}) that apparently sometimes allows precipitation to reseed the updraft, improving precipitation efficiency (Rasmussen and Straka 1998). A Classic supercell can evolve into an HP if it is being seeded by aggressive cells on its flanking line or adjacent storms. HP storms carry all threats of severe weather including strong tornadoes. However, the threats of large hail, damaging winds, and flooding are much larger than the tornado threat**.** Recent findings (Markowski 2001; Markowski et al. 2002) suggest that the RFD must be characterized by positive buoyancy and positive CAPE. Most often the RFD within HP supercells is heavy rain and hail laden and frequently “cold,” lacking the needed buoyancy for tornado development.

8.5.6 Low Precipitation (LP) Supercell Storms. The LP supercell storm was identified in the 1970s (Davies-Jones et al. 1976; Burgess and Davies-Jones 1979; Bluestein and Parks 1983). LP supercells are generally dominated by updraft with little precipitation reaching the ground. These storms are visualized by exposed updrafts and translucent to essentially transparent precipitation cores. They have small, less reflective and benign-looking radar echoes; produce little precipitation at the ground; lack a rain-cooled downdraft; and the updraft lies behind the radar echo at low levels (Figures 8-13 and 8-14). The relative lack of precipitation leads to poor downdraft development and thus these storms could be said to be outflow deficient. LP supercell updrafts often show significantly midlevel mesocyclones. However, low-level mesocyclones are rare owing to the lack of a well defined RFD. There is rarely a hook echo detected unless the radar is very near the storm, and most of the precipitation is carried well downstream of the updraft by the storm-relative upper-level winds. Maximum reflectivities in LP storms can be weak (< 50 dBZ), however, the reflectivity maximum likely consists of a few large hailstones.

Low Precipitation supercells require significant instability and shear; however, other conditions help to reduce precipitation efficiency. Relatively shallow moisture and abundant dry air aloft reduce available moisture and add to entrainment. However, LP storms can also exist where boundary layer moisture is high. Additionally, very high storm-relative anvil-layer winds (>30 ms^{-1}) transport rising hydrometeors well away from the updraft before they descend from the anvil (Rasmussen and Straka 1998). Hydrometeors may have little chance of recycling back into the updraft, especially if the mid-levels are dry. LP storms are severe and produce large hail and, although rare, can produce weak to moderate tornadoes while appearing innocuous on radar. Significant tornadoes appear to be rare but they have occurred (Burgess and Davies-Jones 1979). LP storms that move into a region of deeper, low-level moisture may transform gradually into CL or even HP supercell storms.

8.5.7 Squall Lines and Mesoscale Convective Systems (MCS). Most occurrences of multicell storms are in the form of clusters and of squall lines (both mid-latitude and tropical), but MCSs also contain multicell characteristics (e.g., convective storms with large stratiform rain regions). Some MCSs' and the related squall line’s unique nature of storm structure is based on the environmental conditions and longevity that tend to influence evolution of these large convective systems. This topic has been considered in some detail in the previous chapter (Part B, Chapter 7, of this Handbook) and, thus, will not be covered here.

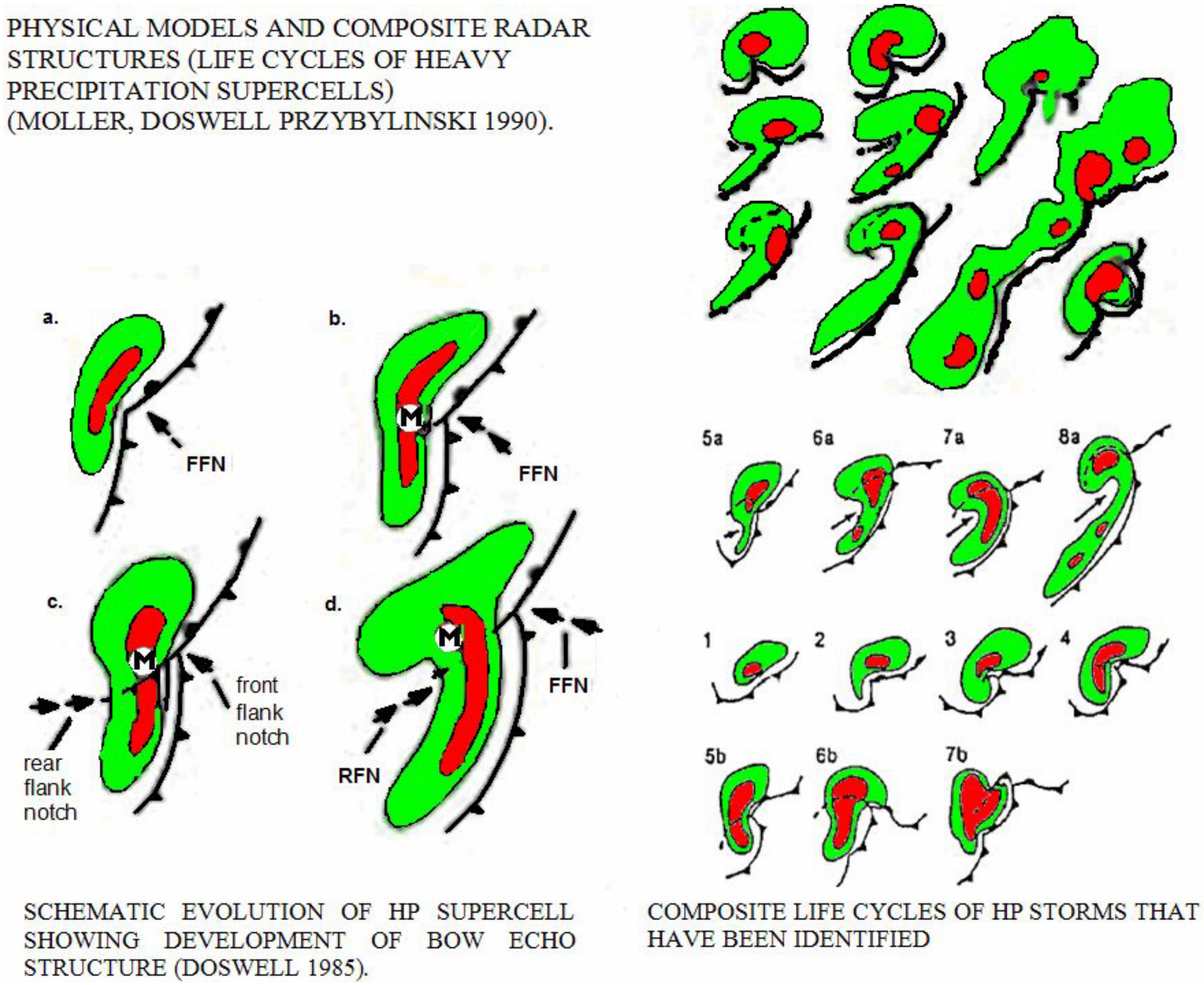

PHYSICAL MODELS AND COMPOSITE RADAR STRUCTURES (LIFE CYCLES OF HEAVY PRECIPITATION SUPERCELLS) (MOLLER, DOSWELL PRZYBYLINSKI 1990).

SCHEMATIC EVOLUTION OF HP SUPERCELL SHOWING DEVELOPMENT OF BOW ECHO STRUCTURE (DOSWELL 1985).

COMPOSITE LIFE CYCLES OF HP STORMS THAT HAVE BEEN IDENTIFIED

Figure 8-12
A Variety of Documented HP Supercell Reflectivity Configurations

Adapted from Moller et al. 1990 and Doswell 1985.

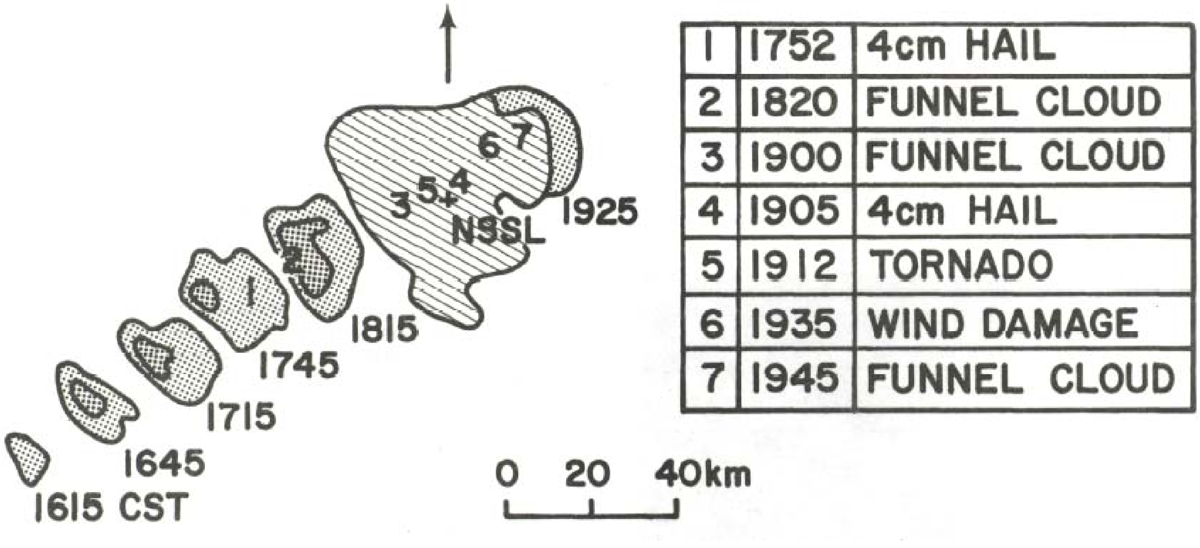

1	1752	4cm HAIL
2	1820	FUNNEL CLOUD
3	1900	FUNNEL CLOUD
4	1905	4cm HAIL
5	1912	TORNADO
6	1935	WIND DAMAGE
7	1945	FUNNEL CLOUD

Figure 8-13
Radar Chronology of an LP Storm

Radar chronology of an LP storm and a list of severe weather events associated with that storm. Reflectivity contour values are 20 and 40 dBZ, respectively. Hatching represents ground clutter (from Davies-Jones et al. 1976).

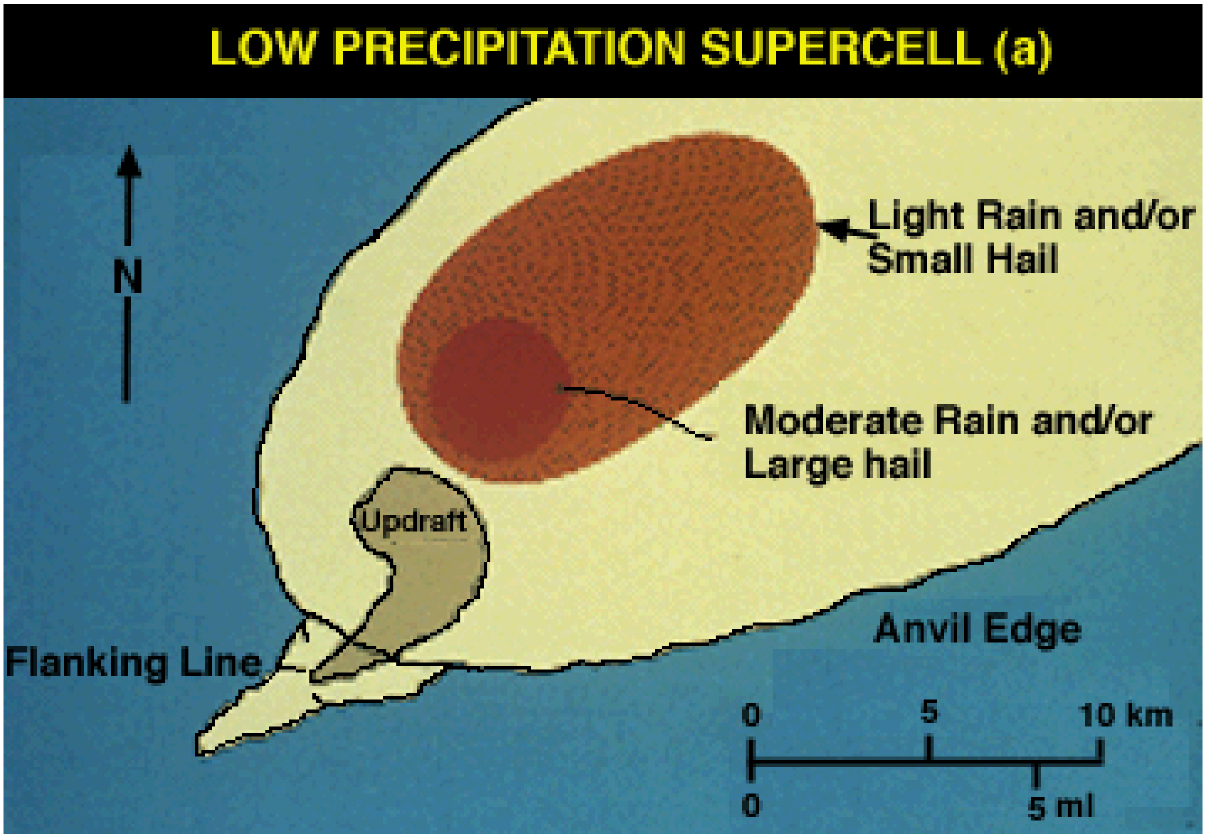

(Reproduced/modified by permission of American Geophysical Union.)

Figure 8-14
Top View of an LP Supercell

Low Precipitation supercell schematic. (After Doswell and Burgess 1993)

8.5.8 Transformation From One Type of Storm to Another. Deep convection frequently begins in mid-afternoon as isolated ordinary storms, some of which evolve into severe multicell cluster or supercell storms. Often more storms form, their outflows combine into a large cold pool and resulting gust front, and a squall line of ordinary cells eventually develops. However, even these squall lines that take on an appearance of a two-dimensional quasi-linear system can also become tornadic. Godfrey et al. (2004) found that these tornadic systems tend to occur when the environment is characterized by strong low-level bulk shears and high low-level CAPE. Supercells generally end their lives by reverting to an ordinary multicellular state or by becoming an ordinary member of a squall line. LP storms may evolve into CL supercells if they move into a more moist environment, but many dissipate in the LP state or occasionally merge into squall lines.

Occasionally, a reverse transformation takes place with a solid squall line of ordinary cells evolving into a short line of a few very intense supercells. In one well-documented case, this transformation occurred after dark as an intense short wave trough aloft overtook the squall line. The resulting supercells produced violent and deadly tornadoes (Burgess and Curran 1985).

The collapse phase of a supercell storm, including those associated with MCSs, is often accompanied with severe winds due to strong downdrafts or downbursts and, perhaps, strong tornadoes. This stage is marked by a dramatic weakening or overall collapse of a portion of the main updraft and greatly enhanced downdrafts (Lemon and Doswell 1979; Dowel and Bluestein 2000). On radar, it can be recognized by sharp declines in storm top, maximum reflectivity aloft, and vertical extent of the WER or BWER (Lemon and Doswell 1979; Dowel and Bluestein 2002a, b). However, as the reflectivity structure weakens, the low-level mesocyclone is strengthening with amplifying rotational velocities. Thus, to discriminate this collapse phase from a true general weakening of the storm, the mesocyclone is revealed by the velocity data to be intensifying. In fact, the TVS, if within range, may also be detected at this time.

8.5.9 Additional Information. For more information on the subject of severe convective storms and their operational identification, the reader is referred to Part D, Chapter 4 and Part B, Chapter 7, of this Handbook and the following web sites.

Warning Decision Training Branch – Courses & Workshops

http://www.wdtb.noaa.gov/courses/index.html

Warning Decision Training Branch – Distance Learning Operations Course

http://www.wdtb.noaa.gov/DLCourses/dloc/dlocmain.html

University of Illinois Dept. of Atmos. Sciences – Severe Storms: Online Meteorology Guide

http://ww2010.atmos.uiuc.edu/(Gh)/guides/mtr/svr/home.rxml

REFERENCES

Bluestein, H. B., and C. R. Parks, 1983: A synoptic and photographic climatology of low-precipitation, severe thunderstorms in the southern plains. *Mon. Wea. Rev.*, **111,** 2034-2046.

Brady, R. H., and E. Szoke, 1988: The landspout--a common type of northeast Colorado tornado. Preprints, *15th Conf. on Severe Local Storms*, Baltimore, MD, Amer. Meteor. Soc., 312-315.

Brooks, H. E., J. W. Lee, and J. P. Carven, 2003: The spatial distribution of severe thunderstorm and tornado environments from global reanalysis data. Atmospheric Research, pp. 67-68 and 73-94.

Brown, R. A., L. R. Lemon, and D. W. Burgess, 1978: Tornado detection by pulsed Doppler radar. *Mon. Wea. Rev*., **106,** 29-38.

Browning, K. A., 1964: Airflow and precipitation trajectories within severe local storms which travel to the right of the winds. *J. Atmos. Sci*., **21,** 634-639.

Browning, K. A., 1977: The structure and mechanism of hailstorms. *Hail: A Review of Hail Science and Hail Suppression, Meteor. Monogr.,* Amer. Meteor. Soc., **16,** 1-43.

Browning, K. A., 1986: General circulation of middle-latitude thunderstorms. *Thunderstorm Morphology and Dynamics*, E. Kessler (Ed). Univ. of Oklahoma Press, Norman, OK, pp. 133-152.

Burgess, D.W., 1974: Study of a right-moving thunderstorm utilizing new single Doppler radar evidence. M. S. Thesis, Dept. of Meteorology, Univ. of Oklahoma, 77 pp.

Burgess, D. W., 1976: Single Doppler radar vortex recognition: Part I Mesocyclone signatures. Preprints, *17th Conf. on Radar Meteorology*, Seattle, WA, Amer. Meteor. Soc., 97-103.

Burgess, D. W., and R. P. Davies-Jones, 1979: Unusual tornadic storms in eastern Oklahoma on 5 December 1975. *Mon. Wea. Rev*., **107,** 451-457.

Burgess, D. W., V. T. Wood and R. A. Brown, 1982: Mesocyclone evolution statistics. Preprints, *12th Conf. on Severe Local Storms, San Antonio, TX,* Amer. Meteor. *Soc*., 422-424.

Burgess, D. W., and E. B. Curran, 1985: The relationship of storm type to environment in Oklahoma on 26 April 1984. Preprints, *14th Conf. on Severe Local Storms*, Indianapolis, IN, Amer. Meteor. Soc., 208-211.

Burgess, D. W., and P. S. Ray, 1986: Principles of radar. Chapt. 6, Mesoscale Meteorology and Forecasting, P.S. Ray, (Ed), Amer. Meteor. Soc., 85-117.

Byers, H. R., and R. R. Braham. 1949: *The Thunderstorm*. U.S. Govt. Printing Office, Washington, D.C, 287 pp.

COMET, 1996: Anticipating Convective Storm Structure and Evolution and A Convective Storm Matrix: Buoyancy/Shear Dependencies, Cooperative Program for Operational Meteorology, Education and Training, Distance Learning Program. http://www.meted.ucar.edu/convectn/mcs/.

Chisholm, A. J., and J. H. Renick, 1972: The kinematics of multicell and supercell Alberta hailstorms. Alberta Hail Studies, 1972, Research Council of Alberta Hail Studies, Rep. No. 72-2, 24-31.

Davies-Jones, R. P., D. W. Burgess, and L. R. Lemon, 1976: An atypical tornado-producing cumulonimbus. *Weather*, **31,** 336-347.

Davies-Jones, R. P., 1982: Tornado interception with mobile teams. *Instruments and Techniques for Thunderstorm Observation and Analysis,* E. Kessler, (Ed). U.S. Govt. Printing Office, pp. 33-46.

Davies-Jones, R. P., 1984: Streamwise vorticity: The origin of updraft rotation in supercell storms. *J. Atmos. Sci*., **41,** 2991-3006.

Davies-Jones, R. P., 1986: Tornado dynamics. *Thunderstorm Morphology and Dynamics*, E. Kessler, (Ed). Univ. of Oklahoma Press, pp. 197-236.

Doswell, C. A. III, 1985: The operational meteorology of convective weather. Vol. II: Storm scale Analysis. NOAA Tech. Memo. ERL ESG-15, 240 pp.

Doswell, C. A. III, and D. W. Burgess, 1993: Tornadoes and tornadic storms. A review of conceptual models. *The Tornado: Its Structure, Dynamics, Hazards, and Prediction,* (C. Church et al, Eds), Geophys. Monogr. 79, Amer. Geophys. Union, 161-172.

Doswell, C. A. III, 2001, Severe convective storms – An overview. Severe Convective Storms, *Meteor. Monogr*., ***50,*** Ed. C. A. Doswell, Amer. Meteor. Soc., Boston, MA, pp. 1-26.

Dowell, D. C., and H. B. Bluestein, 2000: Conceptual models of cyclic supercell tornadogenesis. Preprints*, 20th Conf. on Severe Local Storms*, Orlando, FL, Amer. Meteor. Soc., 259-262.

Dowell, D. C., and H. B. Bluestein, 2002a: The 8 June 1995 McLean, Texas, Storm. Part II: Cyclic Tornado Formation, Maintenance, and Dissipation, *Mon. Wea. Rev.*, **130**, 2649-2670.

Dowell, D. C., and H. B. Bluestein, 2002b: The 8 June 1995 McLean, Texas, Storm. Part I: Observations of Cyclic Tornadogenesis, *Mon. Wea. Rev.*, **130**, 2626-2648.

Foote, G. B. and H. W. Frank, 1983: Case study of a hailstorm in Colorado. Part III: Air flow from triple-Doppler measurements. *J. Atmos. Sci*., **40,** 686-707.

Godfrey, S., R. J. Trapp, H. E. Brooks, 2004: A study of the pre-storm environment of tornadic quasi-linear convective systems. Preprints*, 22th Conf. on Severe Local Storms*, Hyannis, MA, Amer. Meteor. Soc., 259-262.

Fujita, T. T., 1978: Manual of downburst identification for Project NIMROD. SMRP Res. Pap. 156, University of Chicago, 104 pp.

Fujita, T. T., 1985: *The Downburst*. Satellite and Mesometeorology Research Project. Research Paper No. 210, University of Chicago, 122 pp.

Grant, B. N., and R. Prentice, 1996: Mesocyclone characteristics of mini supercell thunderstorms. Preprints, *15th Conf. on Wea. Anal. and Forecasting*, Norfolk, VA, Amer. Meteor. Soc., 362-365

Johns, R.. H., J. M. Davies, and P. W. Leftwich, 1993: Some wind and instability parameters associated with strong and violent tornadoes. 2. Variations in the combinations of wind and instability parameters. *The Tornado: Its Structure, Dynamics, Hazards, and Prediction* (Geophys. Monogr. 79) (C. Church, D. Burgess, C. Doswell, and R. Davies-Jones, Eds.), Amer. Geophys. Union, 583-590.

JDOP Staff, 1979: Final Report on Joint Doppler Operational Project (JDOP) 1976-1978. NOAA Tech. Memo. ERL NSSL-86, 84 pp.

Klemp, J. B. 1987: Dynamics of tornadic thunderstorms. Annual Reviews Fluid Mechanical, 19, 369-402.

Lemon, L. R., 1980: Severe thunderstorm radar identification techniques and warning criteria. NOAA Tech. Memo. NWS NSSFC-3, 60 pp.

Lemon, L. R., and C. A. Doswell, III, 1979: Severe thunderstorm evolution and mesocyclone structure as related to tornadogenesis. *Mon. Wea. Rev*., **107**, 1184-1197.

Lemon, L. R., 1998: Updraft identification with radar. Preprints, *19th Conf. on Severe Local Storms*, Minneapolis, MN, Amer. Meteor. Soc., 709-712.

Maddox, R. A., 1976: An evaluation of tornado proximity wind and stability data. *Mon. Wea. Rev*., **104**, 33-142.

Markowski, P. M., 2002: Hook echoes and rear-flank downdrafts: A review. *Mon. Wea. Rev*., **130**, 852-876.

Markowski, P. M., J. M. Straka, and E. N. Rasmussen, 2002: Direct surface thermodynamic observations within the rear-flank downdrafts of nontornadic and tornadic supercells. Mon. Wea. Rev., **130,** 1692-1721.

Marwitz, J. D., 1972: The structure and motion of severe hailstorms. Part III: Severely sheared storms. *J. Appl. Meteor*., **11,** 189-201.

Moller, A.R., C.A. Doswell III and R. Przybylinski, 1990: High-precipitation supercells: A conceptual model and documentation. Preprints, *16th Conf. on Severe Local Storms,* Kananaskis Park, AB, Amer. Meteor. Soc., 52-57.

NOAA, 1980: Tornado: A Spotter's Guide (Slide series supplement to movie). Available from Weather and Flood Warnings Coordination Program. NWS, NOAA, Silver Spring, MD.

Rasmussen, E. N.**,** and J. M. Straka, 1998: Variations in supercell morphology. Part I: Observations of the role of upper-level storm-relative flow. *Mon. Wea. Rev.*, **126**, 2406-2421.

Vasiloff, S. V., E. A. Brandes, R. P. Davies-Jones, and P. S. Ray, 1986: An Investigation of the transition from multicell to supercell storms. J. Climate Appl. Meteor., **25,** 1022-1036.

Witt, A., and S. P. Nelson, 1984: The relationship between upper-level divergent outflow magnitude as measured by Doppler radar and hailstorm intensity. Preprints*, 22nd Conf. on Radar Meteorology*, Zurich, Amer. Meteor. Soc., 108-111.

APPENDIX A

PHYSICS OF METEOROLOGICAL RADARS

A.1 <u>Detection of Precipitation</u>. Consider a monostatic radar such as the WSR-88D with peak transmitted power, P_t, and antenna gain, G, illuminating a single target cross section, σ_b, at range, r.

The incident power density, P_i, assuming no intervening losses, is:

$$P_i = P_t G / 4 \pi r^2$$

If the target does not absorb power and reradiates isotropically the return power, P_r, intercepted by the receiving antenna is:

$$P_r = \frac{P_t G}{4\pi r^2}\sigma_b \frac{1}{4\pi r^2} A_e$$

Where A_e is the effective aperture area of the antenna. From antenna theory, the effective area is related to the gain and wavelength, λ, by:

$$A_e = \frac{G\lambda^2}{4\pi}$$

Thus,

backscattered power ↓ power collected by the antenna ↓

$$P_r = \left|\left\{\left[\left(\frac{P_t G}{4\pi r^2}\right)\sigma_b\right]\frac{1}{4\pi r^2}\right\}\frac{G\lambda^2}{4\pi}\right|$$

↑ incident power density ↑ power density at receiving antenna

In the case of precipitation, the radar illuminates a large number of targets (raindrops) at the same time (Figure A-1) and the average return power is:

$$\overline{P}_r = \frac{P_t G^2 \lambda^2}{(4\pi)^3 r^4} \sum_i \sigma_{bi}$$

The summation is over the volume from which power is received simultaneously. This volume is proportional to the horizontal and vertical half-power beamwidths, θ_{3dB}, ϕ_{3dB}, and the radar sample volume depth, cτ/2, i.e.:

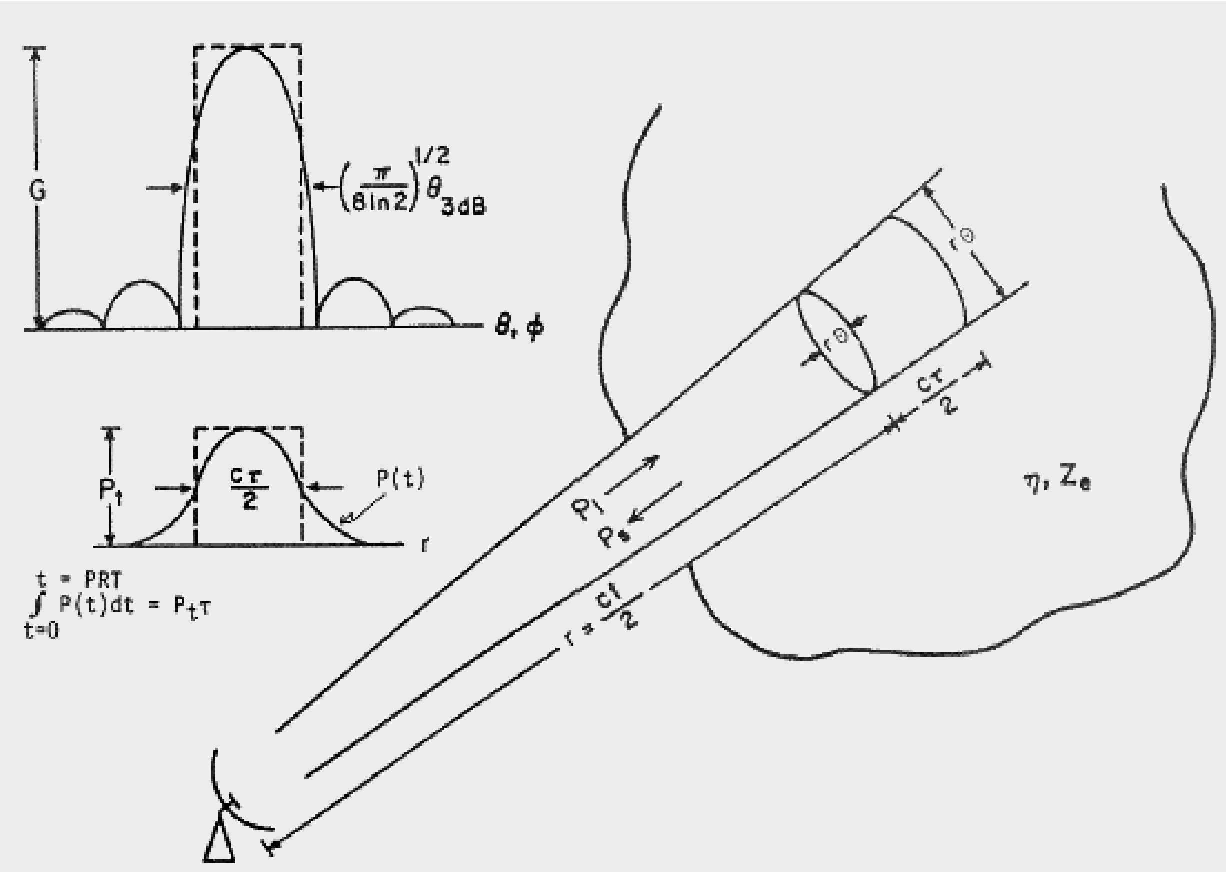

Figure A-1
Schematic for Radar Detection of a Distributed Target

The volume illuminated by the radar subtends an equivalent angle of $(\pi/8\ln 2)^{1/2}$ times the antenna one-way 3 dB beamwidth (upper inset) and has a depth equal to the equi-energy pulse width that is very close to half the power width for the WSR-88D.

$$\mathrm{Vol} \propto \pi\left(\frac{\mathrm{r}\,\theta_{3dB}}{2}\right)\left(\frac{\mathrm{r}\,\phi_{3dB}}{2}\right)\frac{\mathrm{c}\,\tau}{2}$$

If targets are uniformly distributed over the volume, the total back-scattering cross section can be expressed as:

$$\sum_{\mathrm{i}} \sigma_{\mathrm{bi}} = \mathrm{Vol} \cdot \eta$$

where η is the backscattering cross section per unit volume.

The scattering volume angular dimension for circularly symmetric and Gaussian shape antenna patterns (Figure A-1, inset) is given by:

Equivalent Angle

$$(\theta_e, \phi_e) = \frac{\pi\theta_{3dB}^2}{8\ln 2}$$

The sample volume depth is given by the depth of the equivalent rectangular pulse containing the same energy as the actual transmitter pulse (Figure A-1, inset) that, for the pulse shape used in the WSR-88D, is very close to the pulse half-power width.

A.1.1 Radar Cross Section of Raindrops. The radar cross section of a spheroid exhibits the resonance property illustrated in Figure A-2. For incident wavelengths, λ, large, compared to the radius, a, the cross section is given by Rayleigh's law. In the opposite case, for λ small compared to the radius, the cross section approaches the geometric cross section. Between these limits are the resonance maxima or Mie region. For the WSR-88D wavelength of 10 cm and liquid drops of diameter less than about 10 mm, the backscattering is well described by the Rayleigh law. However, large hail and graupel could have dimensions that carry the scattering over to the Mie region.

In the case of Rayleigh scattering, the sphere becomes an electric dipole with a radar cross section that can be shown to be:

$$\sigma_b = 4\pi\left(\frac{2\pi}{\lambda}\right)a^6\left|\frac{\varepsilon - 1}{\varepsilon + 2}\right|^2$$

where ε is the dielectric constant. For a water drop, | ε | >>1, the above reduces to:

$$\sigma_b = 4\left(\frac{2\pi a}{\lambda}\right)^4 \pi a^2$$

For a conducting metal sphere with ε = ∞:

$$\sigma_b = 9\left(\frac{2\pi a}{\lambda}\right)^4 \pi a^2$$

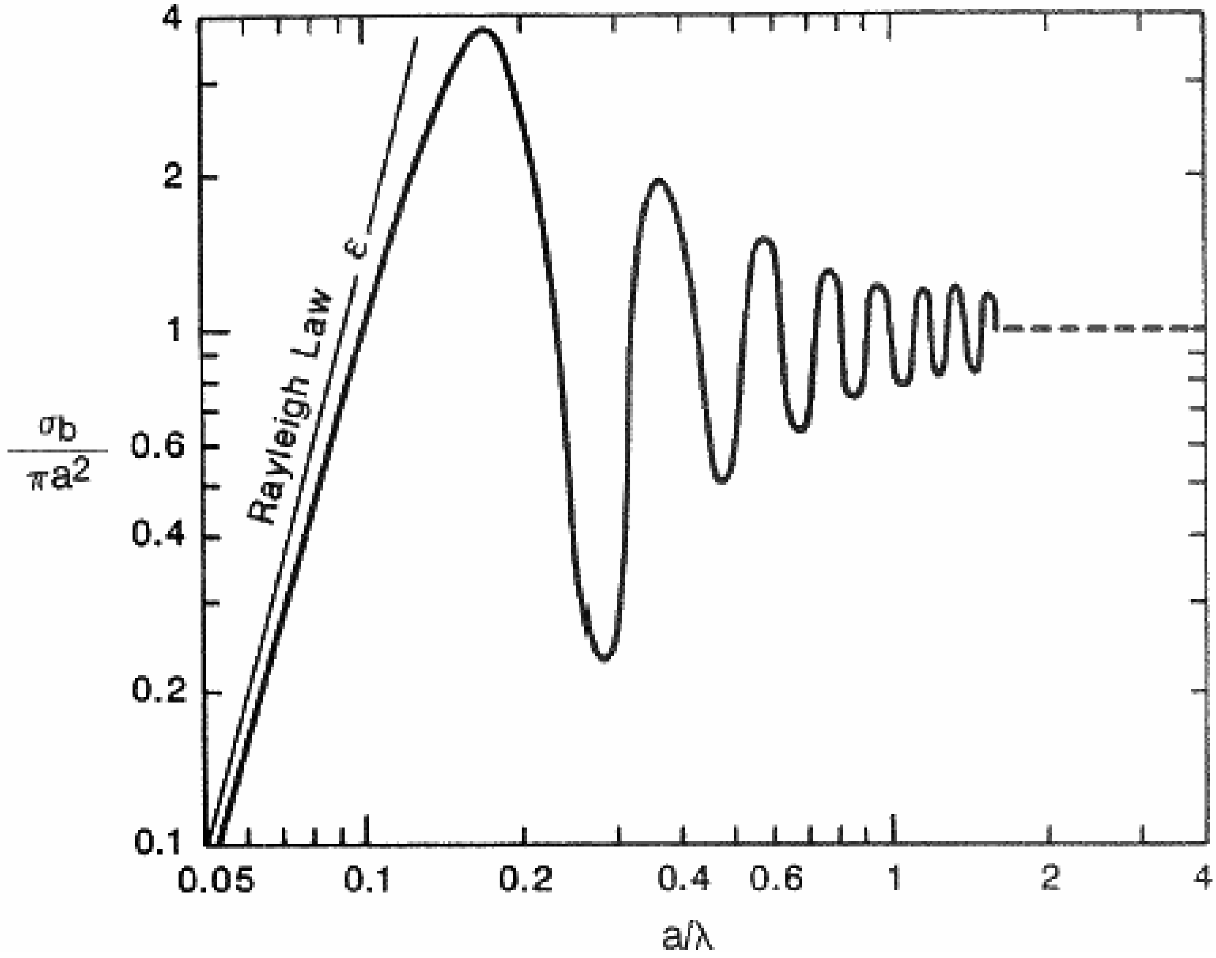

Figure A-2
Radar Cross Section of a Metallic Sphere

Radar cross section, σ_b, normalized to geometric cross section, πa^2. The straight line is the cross section predicted by the Rayleigh Law.

From the above, it is seen that σ_b is strongly dependent on the drop size ($\sigma_b \propto a^6$). The backscattering cross section per unit volume, η, is thus dependent on drop size distribution, i.e., the number of drops of radius a, $\eta(a)$. Since η is the summation of individual cross sections:

$$\eta = 4\pi \int_0^\infty a^2 \left(\frac{2\pi a}{\lambda} \right)^4 \eta(a)\, da$$

$$\eta = \frac{2^6 \pi^5}{\lambda^4} \int_0^\infty a^6 \eta(a)\, da$$

The integral in the above expression is, under suitable restriction, proportional to the total volume liquid water per unit volume, which is the quantity of interest with meteorological radars.

A.1.2 Equivalent Radar Reflectivity Factor. Total liquid water per unit volume is a more meaningful quantity to radar meteorologists than radar cross sections per unit volume and, by convention, radar meteorologists describe the meteorological target by the "equivalent radar reflectivity factor," Z_e, which is related to η by:

$$\eta = \frac{\pi^5}{\lambda^4} |K|^2 Z_e$$

where $|K|^2$ is the complex index of refraction ($K = 0.93$ for water and 0.2 for ice).

For example, if all drops have diameter D_e and radar cross section σ_b, Z_e reduces to:

$$Z_e = \frac{6\lambda^4 \sigma_b M}{\pi^6 |K|^2 \rho D_e^3}$$

where M is the mass liquid water content and ρ is the density of water.

Z_e is usually expressed in $mm^6\, m^{-3}$ requiring a units conversion factor of 10^{-18} to be consistent with the units of η, which is area per unit volume in m^{-1} in the standard equation.

A.1.3 Meteorological Radar Equation. Substituting the composite radar cross section:

$$\sum_i \sigma_{bi} = Vol \bullet \eta = \frac{c\tau}{2} \frac{\pi\theta^2 r^2}{8\ln 2} \bullet \frac{\pi^5}{\lambda^4} |K|^2 Z_e$$

into the general radar equation we have:

$$\overline{P}_r = \frac{(\pi)^3 P_t G^2 \theta_{3dB}^2 \; c\tau |K|^2 Z_e}{2^{10} \lambda^2 r^2 \ln 2} L$$

where:

$\overline{P}_r$ = average return power, watts
P_t = peak transmitted power, watts
G = antenna gain, dimensionless
λ = radar wavelength, meter
θ_{3dB} = antenna half-power beamwidth, radian
τ = pulse duration, second
c = electromagnetic propagation constant $\simeq 3(10^8)$ m s^{-1}
r = range to pulse volume, meter
K = complex index of refraction; $|K|^2$ is conventionally taken to be 0.93 for water and 0.2 for ice.
Z_e = equivalent radar reflectivity factor, m^3 (often expressed in $mm^6\ m^{-3}$ for use in empirical rainfall rate equations such as $Z = 200R^{1.6}$ with rate, R, in mm hr^{-1}).
L = loss factors associated with propagation and receiver detection.

Typical detection capability of the WSR-88D is shown in Figure A-3. The ability to provide a quantitative measurement is not so dependent on return absolute power as it is on the signal to noise ratio.

A.2 Doppler Effect. Consider again the radar signal return as a function of time, t, from a single target at range r. At the receiver input this voltage, V, is given by:

$$V(t,\ r) = A \exp\left[j f\, 2\pi\left(t - 2\frac{r}{c} \right) + j\,\psi \right] U\left(t - 2\frac{r}{c} \right)$$

where A is the composite signal amplitude, f is the radar frequency, ψ is the initial phase and U is the gating function, U = 1, for $0<(t-2r/c)<\tau$, U = 0, otherwise.

After the first mixer:

$$V(t,\ r) = b\ A \exp\left[-\ j\left(\frac{4\pi r}{\lambda} - \psi \right) \exp(j\ 2\pi\ f\ \Delta t) \right] U\left(t - 2\frac{r}{c} \right)$$

where b is gain constant, the first exponential is the target modulation signal, and the second is the subcarrier.

Doppler radars capable of velocity sign detection, such as the WSR-88D, typically generate the signal phasor by homodyning down to zero frequency carrier both the return signal and the return signal phase shifted by $\pi/2$. The outputs are an Inphase, I, and Quadrature, Q, signal.

$$I\left(t,r\right) = A_I \cos\left(\frac{4\pi r}{\lambda} - \psi \right) U(t,\ r)$$

$$Q\left(t,r\right) = A_Q \sin\left(\frac{4\pi r}{\lambda} - \psi \right) U(t,\ r)$$

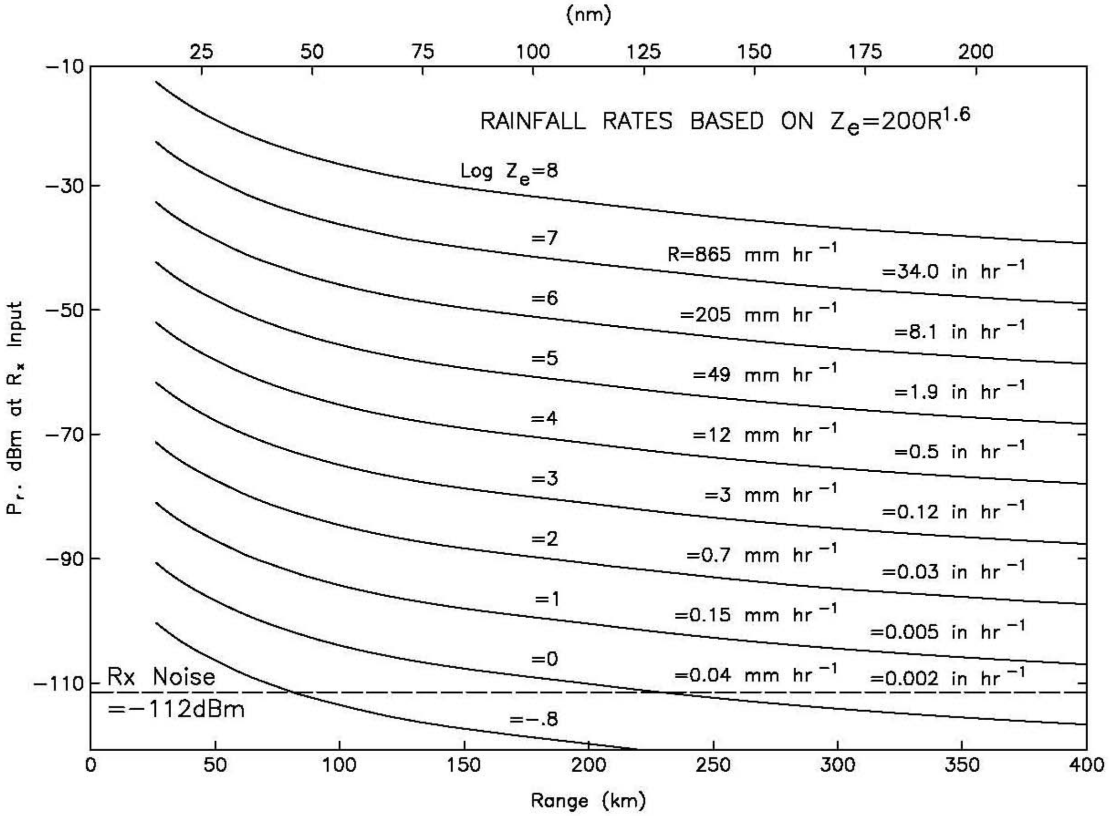

Figure A-3
Reflectivity Detection Capability of the WSR-88D

The equivalent reflectivity, Z_e, rainfall rate relationship of $Z_e = 200R^{1.6}$ is a good general relationship, but is not optimum for all types of liquid precipitation and is not valid for snow.

If the range, r, changes with time (target moving relative to radar with a velocity, v_r) the signal argument (phase) becomes a function of time.

Time rate of phase change is the angular velocity ω. Angular velocity is related to frequency, f, by $\omega = 2\pi f$, thus:

$$\frac{d}{dt}\left(\frac{4r\pi}{\lambda} - \psi\right) = \frac{4\pi}{\lambda}\frac{dr}{dt} = \frac{4\pi}{\lambda}v_r = 2f_d\pi$$

where f_d is the Doppler frequency and:

$$f_d = \frac{2v_r}{\lambda}$$

is the Doppler equation.

The frequency shift of interest in meteorological radars corresponds to radial velocities of tens of meters per second down to a fraction of a meter per second, resulting in very small phase shift during the radar pulse period.

For example, at λ =10 cm the phase shift during a typical pulse width:

$$\tau \simeq 1.4\ (10^{-6})\ \text{s}$$

for a radial velocity, v_r, of 1 m s^{-1}, is:

$$\Delta\ \text{angle} = \left(\frac{4\pi}{\lambda}v_r\right)\Delta t \approx 10^{-2}\,\text{deg}$$

Such small phase shifts cannot be measured with existing techniques. Consequently most radars are configured to measure phase shift from pulse to pulse (PRT ~ 10^{-3} s), which is a much larger angle; about 1 degree for the above example.

However, this results in a sample data system subject to the Nyquist sampling criteria:

$$f_n = \frac{f_s}{2}$$

where f_n is the maximum unambiguous frequency (Nyquist frequency) and f_s is the sampling frequency (radar pulse repetition frequency).

Since the radar unambiguous range is also dictated by the pulse repetition frequency, there is a coupling between maximum unambiguous frequency, f_n (or velocity, v_a), and unambiguous range, r_a, given by:

$$f = \frac{f_s}{2} = \frac{2v_a}{\lambda} = \frac{1}{2r_a}\frac{c}{2}$$

and:

$$v_a r_a = \frac{c\lambda}{8}$$

This relationship, shown in Figure A-4, is one of the more important constraints on pulse Doppler radar, and gives rise to the operational problems of range folding and velocity aliasing.

A.3 <u>Statistics of the Raindrop Array</u>. As previously noted, the weather echo is not produced by a single target but is made up of signals from a dense array of point scatterers and the instantaneous signal is a vector sum of amplitude and phase of weighted returns:

$$V(t,\ r) = \sum_i A_i \exp\left(j \frac{4\pi r_i}{\lambda} \right)$$

Instantaneous echo sample power is proportional to the product of voltage and its complex conjugate:

$$P \propto \frac{1}{2}[VV^*] = \frac{1}{2} \sum_{i,\,k} A_i A_k^* \exp\left(j\, 4\, \pi \frac{(r_i - r_k)}{\lambda} \right)$$

therefore,

$$P \propto \frac{1}{2} \sum_i A_i^2 + \frac{1}{2} \sum_{i \neq k} A_i A_k^* \exp\left(j\, 4\, \pi \frac{(r_i - r_k)}{\lambda} \right)$$

Under constraints of long-term averaging, uniform distribution of targets, and random shuffling of targets within the radar sample volume, the second term tends to zero. Return power can then be related to the sum of the scatterers, $\sum_i A_i^2$, and interactive effects of the raindrop array ignored.

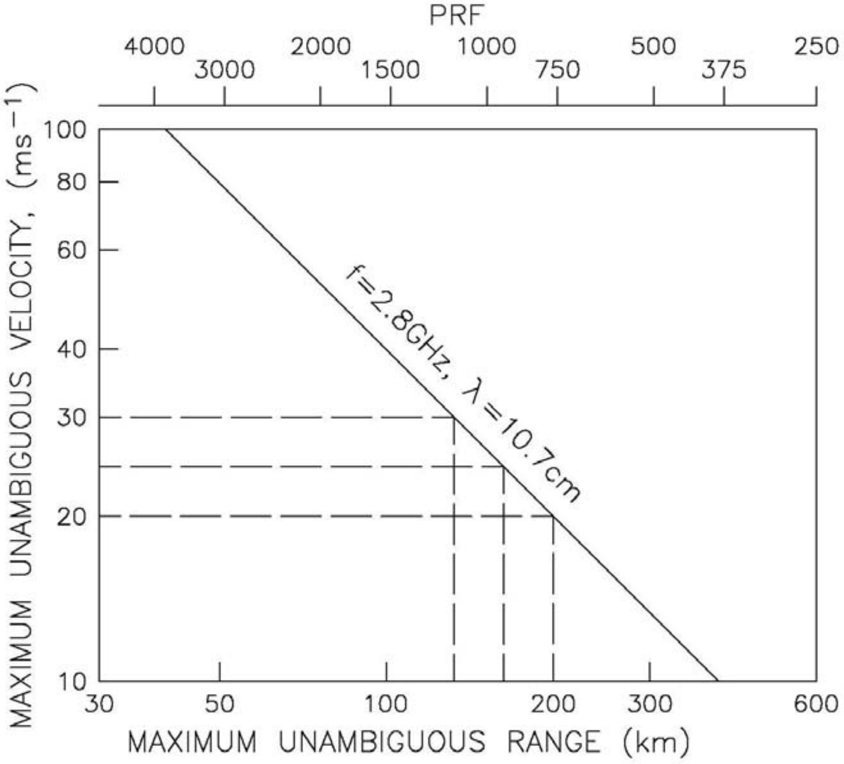

Figure A-4
Unambiguous Range-Velocity Relationship for the WSR-88D

Dashed lines are for unambiguous velocities of 30, 25, and 20 ms^{-1} with associated unambiguous ranges of 134, 160, and 200 km.

An important statistical parameter can be inferred from the statistical independence of the individual signal contributions. If the I, Q signals are composed of a large number of statistically independent contributions, the amplitude probability densities approach a Gaussian function by the Central Limit Theorem and (σ is standard deviation):

$$\text{Prob } A_I = \frac{1}{2\,\pi\,\sigma^2}\exp\left(- \frac{I^2}{2\,\sigma^2} \right)$$

$$\text{Prob } A_Q = \frac{1}{2\,\pi\,\sigma^2}\exp\left(- \frac{Q^2}{2\,\sigma^2} \right)$$

The probability of any function of these signals such as signal return power, $P_r = A_I + A_Q$, signal envelope amplitude, $A = [A_I + A_Q]^{1/2}$, or the logarithm of the return power $\text{Log } P_r = \text{Log } [A_I + A_Q]$ can then be derived by probability density transformation. However, in WSR-88D signal processing, the return power estimates are made directly from averages of return power rather than indirectly from signal amplitude or log power; thus, the statistics of these functions of power are of little interest.

Whereas the signal amplitude and power statistics describe the meteorological target backscattering cross section, the frequency or velocity statistics describe target motion, weighted by the target reflectivity. The function of velocity, most easily interpreted in terms of the meteorology, is the power spectral density. The spectral density used here is the velocity spectral density, i.e., the return power as a function of velocity (velocity being related to frequency by the Doppler equation). Parameters of interest are the first moment about zero or mean velocity and first moment about the mean or spectrum width.

The mean velocity thus represents a radar return, power-weighted mean of all scatterers in the "radar sample volume." Spectrum width is a measure of the dispersion of scatterer velocity about this mean.

Spectrum width is a function of radar system characteristics such as beamwidth, pulse width, wavelength and antenna rotation rate, as well as meteorological parameters describing the velocity dispersion within the radar sample volume. Some of the more significant contributions to velocity variance, σ_v^2, are:

$$\sigma_v^2 = \sigma_d^2 + \sigma_r^2 + \sigma_s^2 + \sigma_t^2$$

Where:

σ_d^2 = variance due to drop size distribution

σ_r^2 = variance due to antenna motion

σ_s^2 = variance due to wind shear
σ_t^2 = variance due to turbulence

If none of the mechanisms are dominant, we would expect the spectral density to be Gaussian by the Central Limit Theorem. With rare but important exception (mesocyclone and tornadic vortex), this is the case.

An estimate of the contribution due to individual effects can be made as follows:

Drop Size Distribution

$\sigma_d^2 = (\sigma_{do} \sin \phi_e)^2$

σ_{do} = standard deviation of drop terminal velocities ($\simeq$ 1 m s^{-1})

ϕ_e = antenna elevation angle

Antenna Rotation

$$\sigma_r^2 \sim \left(\frac{\alpha \lambda}{10.7\, \theta_2} \right)$$

where:

α = antenna rotation rate, deg s^{-1}
λ = wavelength, m
θ_2 = two-way antenna 3 dB beamwidth, deg
($\theta_2 \simeq 0.7\, \theta_{3dB}$ for Gaussian beams)

Wind Shear

$$\sigma_s^2 = \sigma_{s\theta}^2 + \sigma_{s\phi}^2 + \sigma_{sr}^2$$

for constant gradients, k, in azimuth, elevation, and range and a Gaussian antenna pattern

$$\sigma_{s\theta}^2 + \sigma_{s\phi}^2 = (r\, \sigma_\theta\, \kappa_\theta)^2 + (r\, \sigma_\phi\, \kappa_\theta)^2$$

$$\sigma_{sr}^2 = [\beta\, k_r\, (c\, \tau/2)]^2$$

where:

1) κ is a shear constant (meters per second per meter)

2) $\sqrt{s\theta}^{2}$ is variance due to wind gradient in the azmuthal direction

3) $\sqrt{s\phi}^{2}$ is variance due to wind gradient in elevation

4) $\sqrt{s\,r}^{2}$ is variance due to wind gradient in range

$\beta \simeq 0.29$ for rectangular pulse and wideband receiver

$\beta \simeq 0.34$ for rectangular pulse and matched receiver

Turbulence – Median Values:

$$2m^2s^{-2} \leq \sigma_t^2 \leq 16m^2s^{-2}$$

Stratiform rain snow	convective storms

Typical composite values are shown in Figure A-5 for:

λ = 10 cm
θ = 1°
α = 18° s^{-1}
κ = 4 (10^{-3}) s^{-1}
ϕ_t^2 = 1.4 m s^{-1}

Note the range dependency of σ_V predicted if the shear is sustained over the radar sample volume at all ranges. In practice, this is usually not found to be the case. Small scale turbulence is the more significant contribution, especially in convective storms.

A.4 <u>Return Power, Velocity, and Spectrum Width Estimation</u>. The uncertainty associated with a single sample of return power, amplitude, or spectrum width is very large. Consequently, the estimate consist of averages where the standard deviation is reduced to an acceptable value, typically 1 dBZ_e for return power and 1 m s^{-1} for the mean velocity and spectrum width.

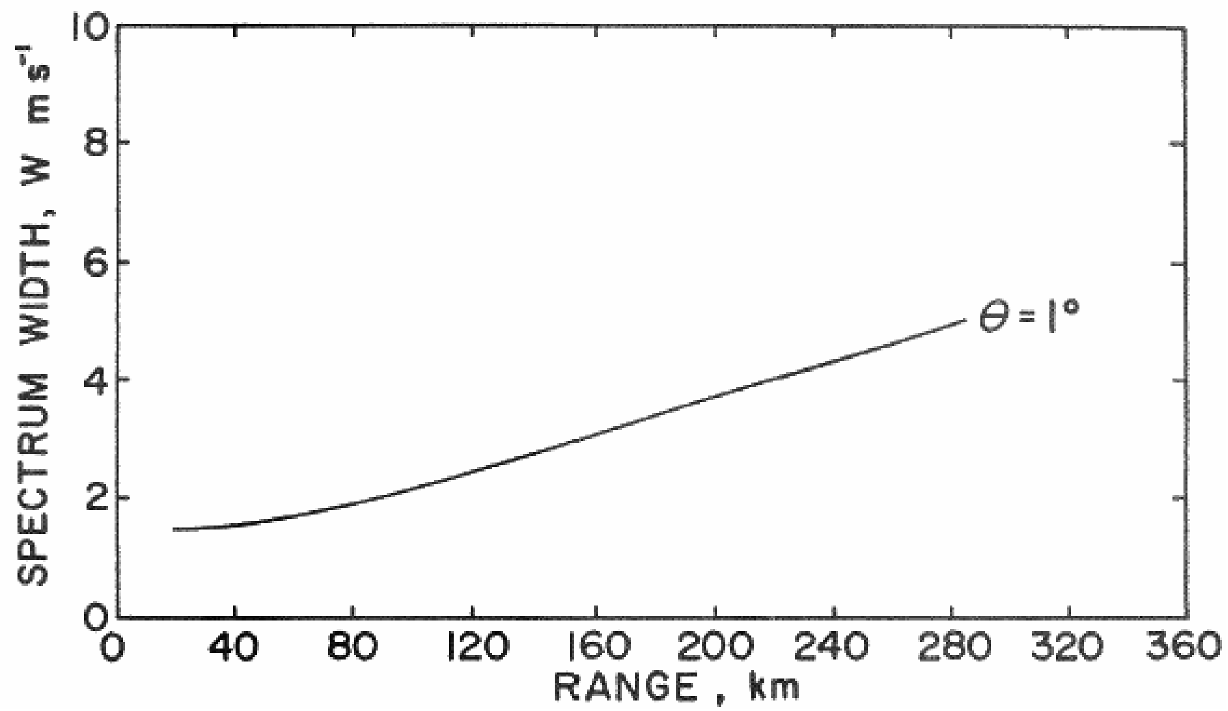

Figure A-5
Theoretical Spectrum Width Versus Range for the WSR-88D

Spectrum width at an antenna speed of 3 rpm assuming a vertical wind shear of $4(10^{-3})$ s^{-1} and a small turbulence of 1.4 ms^{-1}.

A.4.1 Estimation of Return Power (Z_e). Return power is estimated from the signal envelope by a combination of time (pulse to pulse) and range (adjacent sample volume) averaging.

A mean estimate, $\overline{X}$, by a linear average of N independent samples drawn from a population with variance σ_i^2:

$$\overline{X} = \frac{1}{N}\sum_{i=1}^{N} X_i$$

has variance,

$$\sigma\overline{X}^2 = \frac{1}{N}\sigma_i^2$$

However, if the samples are correlated, the variance of a Ns sample average becomes:

$$\sigma\overline{X}^2 = \sigma_i^2 \sum_{m=-(Ns-1)}^{Ns-1} \frac{Ns - |m|}{Ns^2} R(mTs) \quad = \frac{1}{N_I}\sigma_i^2$$

where R(mTs) is the correlation between samples and Ts is the sampling interval. The mean estimate variance ratio for N_I independent samples to Ns correlated samples is:

$$\frac{\sigma I^2}{\sigma s^2} = \frac{Ns}{N_I} = \sum_{m=-(Ns-1)}^{Ns-1} \left(1 - \frac{|m|}{Ns}\right) R(mTs)$$

where:

$$N \sim \frac{4\sqrt{\pi}\,\sigma v \; Ns \; Ts}{\lambda}$$

The correlation of the samples is related to the PRT and the velocity spectrum width by the following. In general the spectral density functional form is Gaussian:

$$W(f) = W_o \exp\left[-\frac{(f - \bar{f})^2}{2\sigma_f^2}\right]$$

where σ_f is the frequency standard deviation.

The normalized autocorrelation is given by the inverse Fourier transform:

$$r(t) = \exp\left[-\frac{t^2}{2\sigma_t^2} \right]$$

where σ_t is the time standard deviation.

Parameters σ_f and σ_t are related to each other by:

$$\sigma_t = \frac{1}{2\pi\sigma_f}$$

and to the velocity spectrum by:

$$\sigma_f = \frac{2\sigma_v}{\lambda}$$

where σ_v is the standard deviation of the velocity spectrum, i.e.:

$$W(v) = W \exp\left[-\frac{(v - \overline{v})^2}{2\sigma_v^2} \right]$$

and:

$$r(t) = \exp\left[-t^2 \frac{2\pi\,\sigma_v^2}{\lambda} \right]$$

For a receiver having an output directly proportional to input power (square law receiver) used in the WSR-88D, the amplitude variance is twice the frequency prior to amplitude detection and the correlation becomes:

$$r(t) = \exp\left[-t^2 \frac{2\pi\,\sigma_v^2}{\lambda} \right]$$

Estimate variance can also be reduced by averaging in range. The averaging interval is chosen so as to preserve the small-scale features of the meteorology and range sample spacing is selected by consideration of signal redundancy from correlation by transmitter pulse and receiver band width, and reduction of noise variance at low signal to noise ratio.

As the discrete average approaches a continuous integration, the number of independent samples in range approaches:

$$N_{Ir} = \frac{3m}{2} + \frac{3}{8},$$

where m is the number of pulse depths averaged.

The overall estimate variance reduction factor is the product of the number of independent samples in range and the number of independent samples in time with the product usually being about fifty.

A.4.2 Estimation of Mean Velocity. Mean velocity estimates in the WSR-88D system are made by a technique that circumvents the spectral density calculation and estimates the first moment of the spectral density from the argument of the complex covariance. The technique is commonly referred to as “pulse-pair processing.”

The rigor of this estimator lies in the Moment Theorem. The moments of a random variable, w:

$$E\,(w^{n}) = M_{n}$$

are related to the derivatives of its characteristic function, Φ , by:

$$jM = \frac{d^{n\Phi}\,(o)}{dx^{n}}$$

In particular this implies that, since the complex covariance and the spectral density constitute a Fourier transform pair, the spectral density moments correspond to the complex covariance evaluated at zero lag.

Expressing the covariance in polar form:

$$r(\tau) = A(\tau)\,\exp[\,j\,2\pi\,\delta(\tau)]$$

Where $A(\tau)$ is a real even function of τ and $\delta\,(\tau)$ is a real odd function of:

$$f = \frac{1}{j2\,\pi}\,\frac{\frac{d}{d\,\tau}[r(\,\tau\,)]}{r(\,\tau\,)}\bigg|_{\tau=0} = \frac{d}{d\,\tau}[\,\delta\,(\,\tau\,)]\bigg|_{\tau=0}$$

that for small $\tau_s = 0$:

$$\frac{d}{d\,\tau}[\,\delta\,(\,\tau\,)]\;\frac{\delta\,(\tau_{s}) - \delta\,(0)}{\tau_{s}} = \frac{\delta\,(\tau_{s})}{\tau_{s}}$$

and:

$$\hat{f} = \frac{1}{2\pi\,\tau_{s}}\,\mathrm{Arg}\big[r(\tau_{s})\big]$$

A maximum likelihood unbiased estimator of r(τ):

$$r(\tau_s) = \frac{1}{N} \sum_{n=1}^{N} Z_{n+1} Z_n^*$$

where:

Z = I + jQ
Z* = complex conjugate of Z

forms the basis for an estimator of spectral density mean given by:

$$f_{ppp} = \frac{1}{\pi} \arctan \frac{\sum_n \operatorname{Im}\left(Z_{n+1} Z_n^*\right)}{\sum_n \operatorname{Re}\left(Z_{n+1} Z_n^*\right)}$$

The restrictions imposed on A(t) and w(t) require the spectral to be unimodal and symmetric about its mean, This is generally true for meteorological signals but there are important exceptions such as the mesocyclone and the tornadic vortex. Performance of this estimator is shown in Figure A-6.

A.4.3 Estimation of Spectrum Width. Spectrum width estimates in the WSR-88D unit are also calculated in the time domain. The estimate is by signal autocorrelation and the rigor is derived from the fact that signal correlation and spectral density constitute a Fourier Transform Pair. The particular algorithm used, however, is valid only for weather signals having Gaussian spectra.

Fundamentally, the width frequency estimate is the standard deviation of the input spectral density (assumed to be Gaussian) given by the autocorrelation of input signal, i.e.:

$$W = \frac{1}{\sqrt{2}\,\pi \tau_s} \left| \ln \left(\frac{\hat{S}}{\left|\hat{r}(\tau_s)\right|} \right) \right|^{1/2} \text{Hz}$$

where τ_s is the sampling interval (PRT), S is the signal power estimate after removal of noise power from total power, and $r(\tau_s)$ is the complex covariance at lag τ_s.

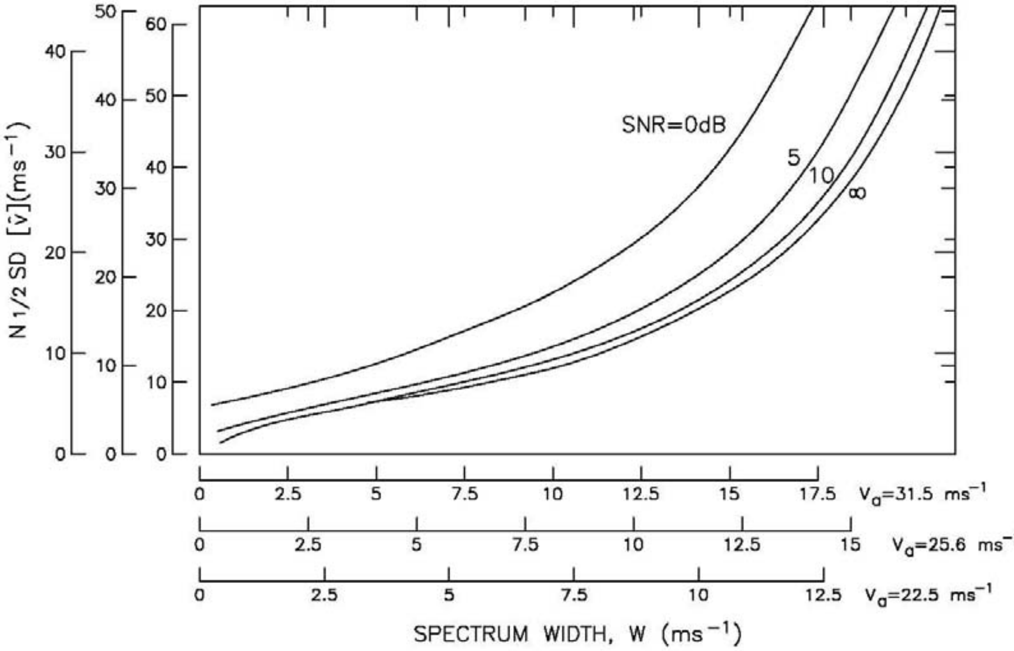

Figure A-6
Standard Deviation of the Mean Velocity Estimate

This figure depicts the normalized standard deviation of the mean velocity estimate as a function of spectrum width for three unambiguous velocities and four levels of signal-to-noise ratio (SNR). Note the ordinate value must be divided by $N^{1/2}$, the square root of the number of samples in the estimate.

The algorithm used delivers the width velocity and uses intermediate terms of the covariance as well as logarithmic algebra to be expressed as

$$\hat{W} = \frac{v_a}{\pi}\left[\left|\ln\left(\frac{\frac{R_e^2 + Im^2}{(m-1)^2}}{\left(\frac{Pn}{m} - n\right)^2}\right)\right|\right]^{1/2} \quad m\ s^{-1}$$

where:

v_a = Unambiguous velocity
R_e = real part of $R(\tau_s)$
Im = imaginary part of $R(\tau_s)$
Pn = signal plus noise power
n = noise power
m = number of samples in the estimate

The performance estimator is shown in Figure A-7.

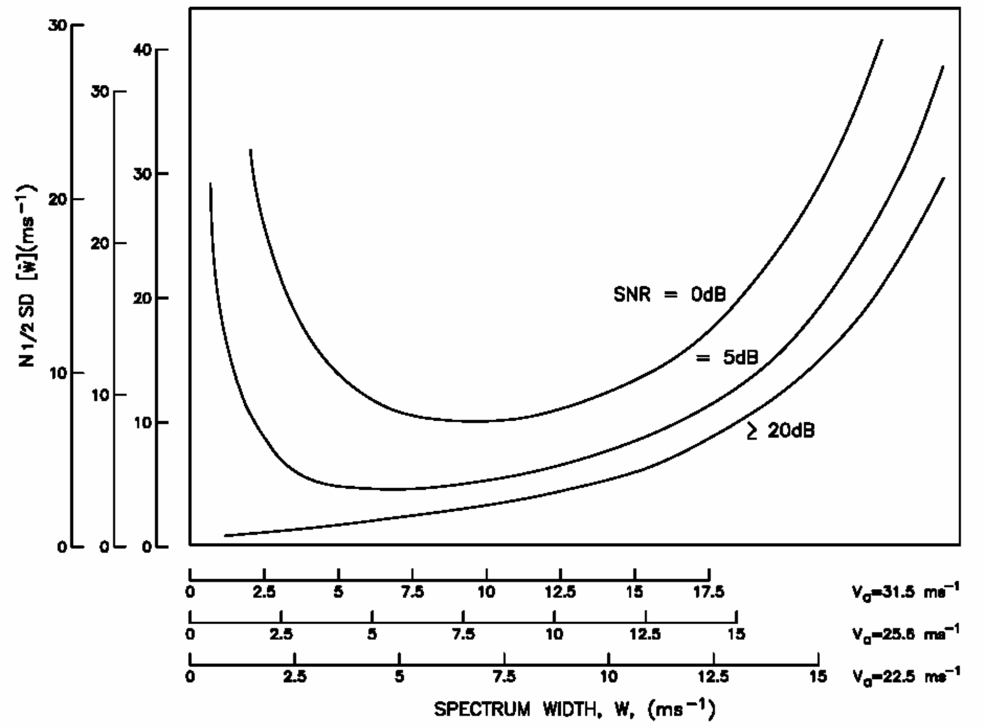

Figure A-7
Standard Deviation of the Spectrum Width Estimate

This figure depicts the normalized standard deviation of the spectrum width estimate as a function of spectrum width for three unambiguous velocities and three levels of signal-to-noise ratio (SNR). Note the ordinate value must be divided by $N^{1/2}$, the square root of the number of samples in the estimate.

BIBLIOGRAPHY

Battan, L. J., 1973: *Radar Observation of the Atmosphere*, Univ. of Chicago Press, Chicago, IL, 324 pp.

Berger, T., and H. L. Groginsky, 1973: Estimation of the spectral moments of pulse trains, Presented at *International Conference on Information Theory*, Tel-Aviv, Israel.

Marshall, J. S., and H. Hitschfeld, 1953: Interpretation of the fluctuating echo from randomly distributed scatterers, *Canadian Journal of Physics*, **31,** 962-94.

Miller, K. S., and M. M. Rochwarger, 1972: A covariance approach to spectral moment estimation. IEEE Transactions on Information Theory, IT-18 no. 5, pp. 588-596.

Probert-Jones, J. R., 1962: The radar equation in meteorology, *Quart. J. Roy. Meteor. Soc.,* **88,** 485-95.

Rummler, W. D., 1968: *Introduction of a new estimator for velocity spectral parameters.* Bell Telephone Labs., Whippany, New Jersey, Technical Memorandum MM68-4121-5, 24 pp.

Sirmans, D. and R. J. Doviak, 1973: *Meteorological radar signal intensity estimation*, NOAA Technical Memoranda, ERL NSSL-64, 80 pp.

Sirmans, D., and B. Bumgarner, 1975a: Numerical comparison of five mean frequency estimations. *Journ. of Appl. Meteor.,* **14,** 991-1003.

APPENDIX B

POINT TARGETS AND CLEAR AIR RETURNS

The detection capability of the WSR-88D is such as to enable detection of very small targets (targets having a radar and geometric cross-sectional area of a few hundredths of a square meter) to ranges of tens of kilometers. While “point targets” span a large range of radar cross sections, from tens of meters square for a large aircraft to the undetectable, all share some common features of scale. All have an apparent extent (both azimuth and elevation) equal to the two-way antenna pattern.

Since these targets do not fill the radar beam, the basic radar equation for point targets is different than that for distributed targets. For monostatic radars, an expression for return power is given by:

$$P_r = \frac{P_t G^2 \lambda^2}{(4\pi)^3 r^4} \sigma_b L$$

where σ_b is the radar cross section in units of area, and all other symbols are the same as previous. Comparing the above with the radar equation for precipitation, we note that point target detection is not dependent on transmitter pulse width or antenna beam width and has a range dependency of r^{-4} rather than r^{-2}.

Typical detection capability of the WSR-88D for point targets is given in Figure B-1. Scattering from small point targets ($\sigma_b \simeq 10^{-5}$ m^2) or conglomerates of small targets is one type of “clear air return.”

True clear air return, though, is radar backscattering due to variation in refractive index of the atmosphere on a scale comparable to the radar wavelength. A quantitative description of the actual scattering mechanism is somewhat complicated; however, the process can be visualized as a reflection due to a mismatch in the transmission medium (the atmosphere) caused by a change in refractive index of the medium.

Clear air return is a volumetric scattering filling the radar beam and the basic radar equation for backscattering, due to refractive index variance, is the same as that for precipitation except that volume reflectivity, η, is expressed in terms of the refractive index structure constant, C_n^2, rather than Z_e. The structure constant is a measure of the mean-square fluctuation of refractive index with distance. Although a measure of different quantities (Z_e a liquid water, C_n^2 is proportional to the refractive index variance) the backscattering can be related through volume reflectivity.

$$\eta = \frac{\pi^5}{\lambda^4} |K|^2 Z_e = 0.39\ \lambda^{-1/3} C_n^2$$

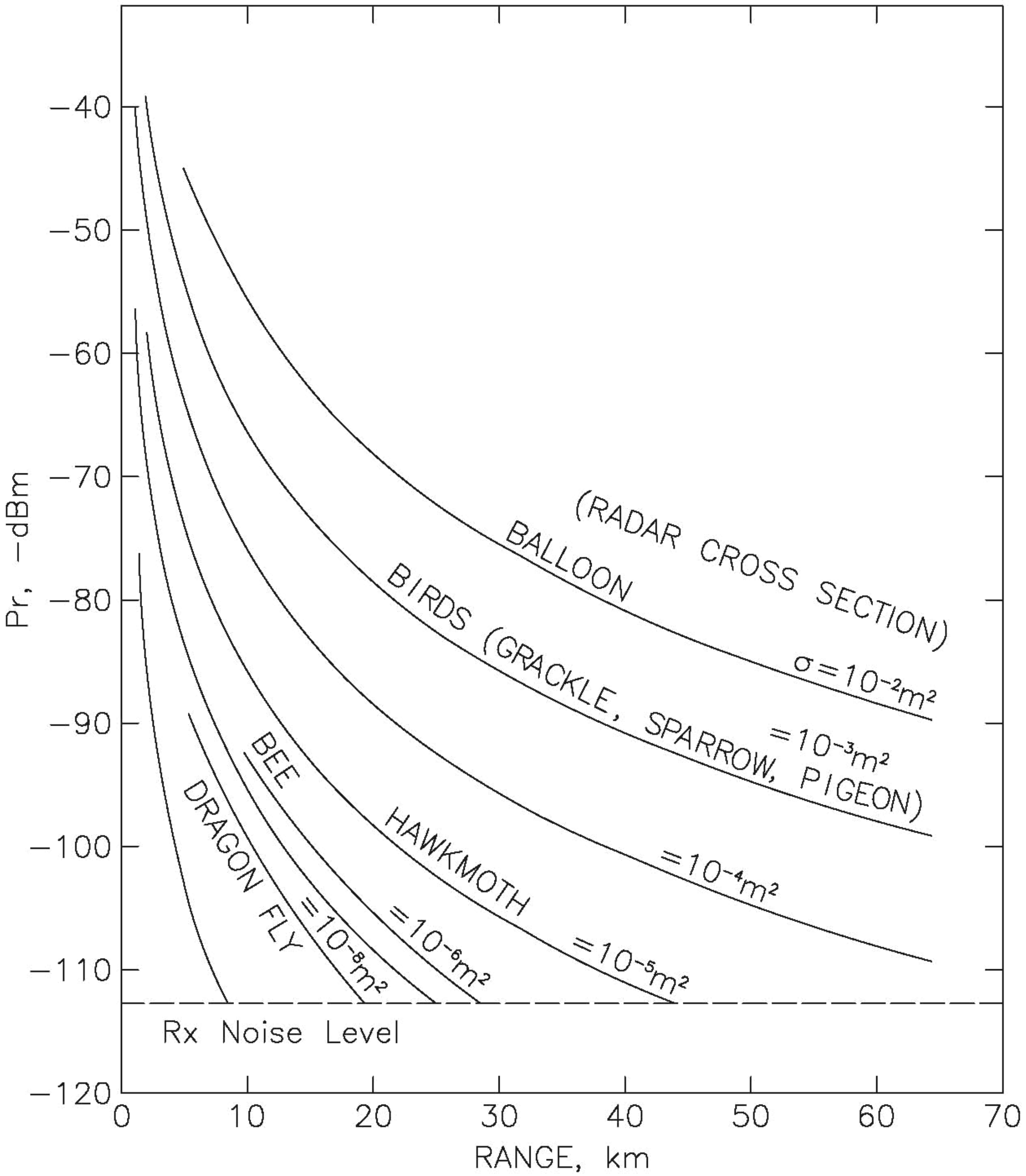

Figure B-1
Typical Point Target Detection Capability of the WSR-88D

and the radar equation for scattering by refractive index fluctuations becomes:

$$P_r = \frac{P_t G^2 \theta^2 c_\tau \lambda^{5/3} (0.39) C_n^2}{2^{10} \pi^2 \ln 2} L$$

The structure constant, C_n^2, varies widely with meteorological condition with a mean value of about 10^{-14} $m^{-2/3}$. Note that η has units of m^{-1} while C_n^2 has units of $m^{-2/3}$. Typical detection capability of the WSR-88D for log C_n^2 can be derived from Figure A-2 by adding 2.52 to log Z_e, i.e., log C_n^2 = 2.52 + log Z_e. Detection to ranges corresponding to the top of the planetary boundary layer is not unusual.

The clear air characteristics and utility in the velocity domain depend on the type of target. Targets capable of independent flight, such as aircraft and birds that are not tracers of the wind, provide little useful information to the meteorologist. The WSR-88D system has the capability to remove these types of returns from the data field by logic based on the target radar cross section and range extent (Point Clutter Rejection).

Small targets, on the other hand ($\sigma_b < 10^{-4}$ m^2), are usually good tracers of the environmental wind and these measurements provide valid wind field information.

Measurements based on refractive index fluctuations are, of course, a direct measure of the air motion.

BIBLIOGRAPHY

Hennington, L., R. J. Doviak, D. Sirmans, D. Zrnic', and R. Strauch, 1975: Measurements of winds in the optically clear air with microwave pulse-Doppler radar. Preprints, *17th Conference on Radar Meteorology*, Seattle, WA, Amer. Meteor. Soc., 342-348.

APPENDIX C

ACRONYMS AND ABBREVIATIONS

AGC - Automatic Gain Control
AGL - Above Ground Level
AP - Anomalous Propagation
AWIPS - Advanced Weather Interactive Processing System

BAMEX - Bow Echo and MCV (Mesoscale Convective Vortices) Experiment
BWER - Bounded Weak Echo Region

CAPE - Conditional Available Potential Energy
CL - Classic Supercell (storm)
COMET - Cooperative Program for Operational Meteorology, Education and Training
CRPL - Central Radio Propagation Laboratory

dB - Decibel
dBZ - Radar Reflectivity Factor
DCAPE - Downdraft Conditional Available Potential Energy
DCZ - Deep Convergence Zone
DoC - Department of Commerce
DoD - Department of Defense
DoT - Department of Transportation

ERL - Environmental Research Laboratories
ETC - Extratropical Cyclone

FAA - Federal Aviation Administration
FAR - False Alarm Ratio
FO - Forward Overhang

GARP - Global Atmospheric Research Program
GATE - GARP Atlantic Tropical Experiment
G/R - Gage/Radar

HP - High Precipitation supercell (storm)

I - Analog In Phase
ICAO - International Civil Aviation Organization
ICMSSR - Interdepartmental Committee for Meteorological Services and Supporting Research
IEEE - Institute of Electrical and Electronic Engineers
IR - Infrared (satellite data)

JDOP - Joint Doppler Operational Project
JSPO - Joint System Program Office

LEWP - Line Echo Wave Pattern
LP - Low Precipitation Supercell (storm)

M - Mesocyclone Product
MARC - Mid Altitude Radial Convergence
MCC - Mesoscale Convective Complex
MCS - Mesoscale Convective System
MPDA - Multiple Pulse Repetition Frequency (PRF) Dealiasing Algorithm
MSCF - Master System Control Function

NEXRAD - Next Generation Weather Radar
NOAA - National Oceanic and Atmospheric Administration
NPC - NEXRAD Program Council
NSSFC - National Severe Storms Forecast Center
NSSL - National Severe Storms Laboratory
NTIS - National Technical Information Service
NWS - National Weather Service

OFCM - Office of the Federal Coordinator for Meteorological Services and Supporting Research

PPI - Plan Position Indicator
PRF - Pulse Repetition Frequency
PRT - Pulse Repetition Time

Q - Quadrature
QLCS - Quasi Linear Convective Systems

R - Rainfall Rate in Z-R relationship
RDA - Radar Data Acquisition
rf - Radio Frequency
RFD - Rear Flank Downdraft
RIJ - Rear Inflow Jet
RPG - Radar Product Generator
ROC - Radar Operations Center
RPM, rpm - Revolutions Per Minute

S/C - Ratio of Signal Power to Clutter Power
SL - Severe Left-Moving Supercell
SNR - Signal-to-Noise Ratio
SR - Severe Right-Moving Supercell
SRR - Storm Relative Mean Radial Velocity Region Product

TVS - Tornadic Vortex Signature (in velocity data) and in the WSR -88D Product

UTC - Coordinated Universal Time

v - Velocity data
VAD - Velocity Azimuth Display, VAD Wind Profile product.
VCP - Volume Coverage Pattern
VIL - Vertically Integrated Liquid Product
VWP - Velocity Azimuth Display Wind Profile Product

W - Spectrum Width Data
WER - Weak Echo Region
WSR-88D - Weather Surveillance Radar - 1988 Doppler

Z - Radar Reflectivity Data
Z_e - Equivalent Radar Reflectivity

APPENDIX D

GLOSSARY

Aliasing: The process by which frequencies too high to be analyzed with the given sampling interval appear at a frequency less than the Nyquist frequency.

Ambiguous Velocity: See Velocity Aliasing.

Amplitude: The maximum magnitude of a quantity.

Analog: Class of devices in which the output varies continuously as a function of the input.

Anomalous Propagation (AP): When non-standard index-of-refraction distributions prevail, “abnormal” or “anomalous” propagation occurs. When abnormal downward bending occurs, it is called “superrefraction.” The term “subrefraction” is applied when there is abnormal upward bending.

Antenna Gain: The measure of effectiveness of a directional antenna as compared to an isotropic radiator; maximum value is called antenna gain by convection.

Antenna pattern: (Also called radiation pattern, beam pattern, lobe pattern.) A graphical representation of the radiating properties of an antenna as a function of space coordinates.

Attenuation: Any process in which the flux density (power) of a beam of energy is dissipated.

Autocorrelation: A measure of similarity between displaced and undisplaced (in time, space, etc.) versions of the same function.

Automatic Gain Control: Any method of automatically controlling the gain of a receiver, particularly one that holds the output level constant regardless of the input level.

Azimuth: A direction in terms of the 360 degree compass.

Backing Wind: A change in wind direction in a counterclockwise sense representing cold air advection.

Backscatter: That portion of power scattered back in the incident direction.

Bandpass Filter: A filter whose frequencies are between given upper and lower cutoff values, while substantially attenuating all frequencies outside these values (this band).

Band Width: The number of cycles per second between the limits of a frequency band.

Band reject filter: (or notch filters) are used to pass a large operating band of frequencies, while rejecting a narrow band of frequencies.

Baroclinic: The variation with depth of motions associated with variation of density with depth.

Baroclinity: (Or baroclinicity.) The state of stratification in a fluid in which surfaces of constant pressure (isobaric) intersect surfaces of constant density (isosteric).

Base Data: Those digital fields of reflectivity, mean radial velocity, and spectrum width data in spherical coordinates provided at the finest resolution available from the radar.

Base Products: Those products that present some representation of the base data. This representation may not necessarily be either in full resolution or depict the full area of coverage. Base products can be used to generate a graphic display or further processing.

Batch Mode: A radar transmission technique that uses alternating low and high PRFs on each radial of a scanning radar for one full rotation at each elevation angle.

Beam Filling: The measure of variation of hydrometer density throughout the radar sampling volume. If there is no variation in density, the beam is considered to be filled.

Beam Width: Angular width of the antenna pattern. Usually the width where the power density is one-half that of the axis of the beam.

Bias: A systematic difference between an estimate of and the true value of the parameter.

Boundary Layer: The layer of a fluid adjacent to a physical boundary in which the fluid motion is affected by the boundary and has a mean velocity less than the free-stream value.

Bounded Weak Echo Region (BWER): A core of weak equivalent reflectivity in a thunderstorm that identifies the location of an intense updraft. The updraft is so strong that large precipitation particles do not have time to form in the lower and mid-levels of the storm and are prevented from falling back into the updraft core from above. The Weak Echo Region is bounded when, in a horizontal section, the weak echo is completely surrounded or bounded by higher reflectivity values. See also Weak Echo Region.

Bow Echo: Rapidly moving crescent shaped echo that is convex in the direction of motion. Typically associated with strong straight-line winds. See also Line Echo Wave Pattern.

Bright Band: The enhanced radar echo caused by the difference in radar reflectivity of ice and water particles. This echo is interpreted as the delineation on a radar display between frozen and liquid precipitation.

Convective Available Potential Energy: (Abbreviated CAPE.) The maximum energy available to an ascending parcel, according to parcel theory. On a thermodynamic diagram this is called positive area, and can be seen as the region between the lifted parcel process curve and the environmental sounding, from the parcel's level of free convection to its level of neutral buoyancy.

Cell: A compact region of relatively strong vertical air motion (at least 10 ms^{-1}; 19 knots).

Central Limit Theorem: Statistical theorem showing that averages approach a Gaussian distribution independent of the input distribution.

Centroid: The center of mass of a storm.

Clutter: Echoes that interfere with observations of desired signals on a radar display. Usually applied to ground targets.

Clutter Suppression or rejection: Any of a variety of processes or techniques to eliminate the effects of unwanted signals (clutter) in radar measurements.

Coherence: The property of two or more waves that are in phase both temporally and spatially. Waves are coherent if they have the same wavelength and a fixed phase relationship with each other.

Coherent Radar: A radar that utilizes both signal phase and amplitude to determine target characteristics.

Cokriging: A technique for estimating values of a spatial process (e.g., a precipitation field) given point observations of the process (e.g., rain gage observations) and possibly auxiliary observations (e.g., radar and satellite observations).

Complex Signal: A signal containing both amplitude and phase information.

Conditional Instability: The state of a layer of unsaturated air when its lapse rate of temperature is less than the dry-adiabatic lapse rate but greater than the moist-adiabatic lapse rate.

Convergence: A measure of the contraction of a vector field.

Correlation: A measure of similarity between variables or functions.

Couplet: Adjacent maxima of radial velocities of opposite signs.

Covariance: A measure of the degree of association between two variables. In Doppler radars, the argument (or angle) of the covariance of the complex signal is a measure of the Doppler frequency.

Covariance: A measure of the degree of association between two variables. In Doppler radars, the argument (or angle) of the covariance of the complex signal is a measure of the Doppler frequency.

Dealiasing: Process of correcting for aliases in the velocity measurement. See also Velocity Aliasing.

Deep Convergence Zone (DCZ): A linear region of apparent convergence detected by Doppler weather radar that is occurring over a long, narrow, and deep region of opposing Doppler velocities within some convective storms. The linear region can be up to 100 km or more in length, up to 13 km in depth, and the interface may be as narrow as ~ 250 m. Similar to the Mid-Altitude Radial Convergence Signature but substantially deeper.

Decibel (dB): A logarithmic expression for ratio of two quantities. dBm is a decibel with respect to 1 milliwatt.

Mathematically:

$$\mathrm{dB} = 10 \text{ Log } (P_1/P_2)$$

$$\mathrm{dBm} = 10 \text{ Log } (P/10^{-3})$$

$$\mathrm{dBZ} = 10 \text{ Log } (Z_e)$$

Deformation: The change in shape of a fluid mass by spatial variations in the velocity field, specifically by stretching or shearing.

Derecho: A widespread convectively induced straight-line windstorm. Specifically, the term is defined as any family of downburst clusters produced by an extratropical mesoscale convective system.

Dielectric Material: A substance that contains no or few free charges and that can support electromagnetic stress.

Dielectric Constant: For a given substance, the ratio of the capacity of a condenser with that substance as dielectric to the capacity of that condenser with a vacuum as dielectric.

Disdrometer: Equipment that measures and records the size distribution of raindrops.

Distortion: Change in a signal resulting in gross non-linearities in signal processing or handling.

Divergence: A measure of the expansion or spreading out in a vector field.

Doppler Shift: The change in frequency at a receiver due to the relative motion of the receiver and the energy source.

Doppler Spectral Moments: Statistical moments of Doppler frequency or Doppler velocity, regarding these quantities as continuously distributed random variables with a probability density function equal to the normalized Doppler spectrum.

Downburst: A strong downdraft that induces an outburst of damaging winds on or near the ground.

Downdraft: Current(s) of air with marked vertical downward motion.

Drop-Size Distribution: The frequency distribution of drop sizes (diameters, volumes) that is characteristic of a given cloud or of a given fall of rain.

Dryline: A mesoscale feature with its own associated vertical circulation. It is a narrow, almost vertical zone, across which a sharp moisture gradient, but little temperature gradient, occurs at the Earth's surface.

Dual-Polarization Radar: A radar capable of transmitting and receiving two orthogonal polarizations.

Ducting: The phenomenon by which the radar signal propagates along the boundary of two dissimilar air masses. The radar ranges with ducted propagation are greatly extended; holes can also appear in the coverage. Ducting occurs when the upper air is exceptionally warm and dry in comparison with the air at the surface. See also Anomalous Propagation.

Dwell Time: Time over which a signal estimate is made. Usually, the time required for the antenna to transverse one degree.

Dynamic Range: The ratio, usually expressed in decibels, or the maximum to the minimum signal that a system can handle. Used to describe limits of receivers.

Echo: Energy backscattered from a target as seen on the radar display.

Elevation Angle: The vertical pointing angle of the antenna (the WSR-88D antenna can vary from -1° to + 60°).

Equivalent Radar Reflectivity (Z_e): The concentration of uniformly distributed small (diameter one sixteenth wavelength or less) water particles that would return the amount of power received. Typically expressed as: $dBZ = 10 \text{ Log } Z_e$.

Estimate: A statement of the value of a quantity or function based on a finite number of samples.

Exclusion Zone: A region created to prevent known areas of persistent clutter residue from contaminating the Hybrid Scan Reflectivity.

Feeder Cloud: The flanking lines of developing cumulus congestus clouds that sometimes merge with and appear to intensify supercells.

Folding: See Range Folding.

Frequency: The number of recurrences of a periodic phenomenon per unit time. Electromagnetic energy is usually specified in Hertz (Hz), which is a unit of frequency equal to one cycle per second.

Frequency Carrier: For the WSR-88D, the fundamental transmitted microwave frequency between 2,700 and 3,000 megahertz. It is modulated so that it exists for a few microseconds each pulse repetition time. This limit is called the transmitted pulse.

Gating (Range Gating): The use of electronic circuits in radar to eliminate or discard the target signals from all targets falling outside certain desired range limits.

Gaussian: Refers to the Normal distribution; phenomena whose events are normally distributed are Gaussian distributed. This is the most common distribution encountered in physical processes.

Gravity Wave: (Also called gravitational wave.) A wave disturbance in which buoyancy (or reduced gravity) acts as the restoring force on parcels displaced from hydrostatic equilibrium.

Ground Clutter: The pattern of radar echoes from fixed ground targets.

Gust Front: The boundary between the horizontally propagating cold air outflow from a thunderstorm and the surrounding environmental air.

Helicity: One-half the scalar product of the velocity and vorticity vectors. It is a conserved quantity if the flow is inviscid and homogeneous in density, but is not conserved in more general viscous flows with buoyancy effects. The concept is useful in understanding severe convective storms and tornadoes, since in strong updrafts the velocity and vorticity vectors tend to be aligned, yielding high helicity.

Homodyning: The transfer of signal intelligence from one carrier to another by mixing of signals at different frequencies.

Hook Echo: A pendant of hook on the right side of an echo that often identifies mesocyclones on the radar display. The hook is caused by precipitation drawn into a cyclonic spiral by he winds, and the associated notch in the echo is caused by precipitation-free, warm, moist air flowing into the storm.

Hybrid Scan: An approach in which different elevation angles (normally the lowest four) are used to minimize the effects of ground clutter and data voids on radar based observations such as precipitation estimates.

Incident Power Density: Energy per unit area incident on the radar target.

Inphase: The component of a complex signal along the real axis in the complex plane.

Isodop: Contour of constant Doppler velocity values.

Isolated Storm: An individual cell or group of cells that are identifiable and separate from other cells in a given geographic area.

Instability: A property of the steady state of a system such that certain disturbances or perturbations introduced into the steady state will increase in magnitude, the maximum perturbation amplitude always remaining larger than the initial amplitude.

Klystron: An electron tube used as a low-power oscillator or a high-power amplifier at ultrahigh frequencies. Noted for exceptional stability over long periods of transmission.

Line Echo Wave Pattern (LEWP): A radar echo pattern formed when a segment of a line of thunderstorms surges forward at an accelerated rate. A mesohigh pressure area is usually present behind the accelerating thunderstorms. A mesolow pressure area is usually present at the crest of the wave.

Macroburst: Large downburst with 4 km (2.2 nmi) or larger outflow size with damaging wind lasting 5 to 20 minutes.

Mainlobe: The envelope of electromagnetic energy along the main axis of the beam.

Master System Control Function (MSCF): A graphical user interface used to set all adjustable parameters that determine pulse repetition frequency, antenna motion, and all processing thresholds and limits, including the setting of adjustable parameters that affect the seasonal and geographical performance of the hydrometerological algorithms.

Maximum Unambiguous Range: The maximum range to which transmitted pulse wave can travel and return to the radar before the next pulse is transmitted.

Maximum Unambiguous Velocity: The maximum range of radial velocity that can be observed without ambiguity by a Doppler radar. Velocities outside this interval are folded into the interval. *See* Velocity aliasing and Nyquist Frequency.

Mean Doppler Velocity: Reflectivity-weighted average velocity of targets in a given volume sample. Usually determined from a large number of successive pulses. Also called mean radial velocity. Doppler velocity usually refers to spectral density first moment; radial velocity to base data.

Mesocyclone: A 3-dimensional region in a storm that rotates cyclonically and is closely correlated with severe weather.

Mesoscale: Pertaining to atmospheric phenomena having horizontal scales ranging from a few to several hundred kilometers, including thunderstorms, squall lines, fronts, precipitation bands in tropical and extratropical cyclones, and topographically generated weather systems such as mountain waves and sea and land breezes.

Mesoscale Convective Complex (MCC): A quasi-circular conglomeration of thunderstorms having a cloud-top area larger than 100,000 km^2 (29,000 n mi^2) and persisting for more than 6 hours.

Mesoscale Convective System (MCS): Precipitation systems 20 to 500 km (11 to 270 n mi) wide that contain deep convection. Examples in mid-latitudes are large isolated thunderstorms, squall lines, Mesoscale Convective Complexes, and rainbands.

Microburst: Small downburst, 1 to 4 km (0.54 to 2.2 nmi) in outflow size, with peak winds lasting 2 to 15 minutes.

Microwave: Electromagnetic radiation having wavelengths between approximately 1 mm and 1 m (corresponding to 0.3- and 300-GHz frequency). Active systems operating at these wavelengths are called radar, although the definition of radar requires a capability to measure distance that is not always included in active microwave systems.

Mid-Altitude Radial Convergence Signature (MARC): Persistent areas of radial convergence within mid-levels (~ 3 to 7 km AGL)and within the larger zone of convergence along the forward flank of the convective line or storm and appears to be linked to the greatest degree of wind damage. Similar to the Deep Convergence Zone but generally confined to the mid-levels.

Mie Scattering or Region: Radar backscattering by targets having dimensions somewhat greater than 1/10 the wavelength of the radar but less than several radar wavelengths.

Modulation: Variation of the amplitude, frequency, or phase of a wave due to the mixing of two signals.

Monostatic Radar: A radar that uses a common antenna for both transmitting and receiving.

Notch Width: The 3 dB band width of a rejection filter.

Nyquist interval: (Also Nyquist velocity). The maximum time interval between equally spaced samples of a signal that will enable the signal waveform to be completely determined. Also known as the (absolute value) of the maximum unambiguous velocity that can be measured by a Doppler radar, e.g., 50 kts.

Nyquist Co-Interval: The full range of the Nyquist interval, e.g., +/- 50 kts.

Nyquist Frequency: The highest frequency that can by determined in data that have been discretely sampled. For data sampled at frequency f_S, this frequency is $f_S/2$.

Nyquist Sampling Theorem: In order to unambiguously measure a frequency, a sampling rate of at least two times this frequency is required. Doppler radar sampling rate is equal to the pulse repetition frequency (PRF).

Oscillator: The general term for an electric device that generates alternating currents or voltage. The oscillator is classified according to frequency of the generated signal.

Phase: A particular angular stage or point of advancement in a cycle; the fractional part of the angular period through which the wave had advanced, measured from the phase reference.

Phase Shift: The angular difference of two periodic functions.

Polarization: With respect to a transverse electromagnetic wave, the correlation between two orthogonal components of its electric (or, equivalently, magnetic) field.

Propagation: Transmission of electromagnetic energy as waves through or along a medium.

Pulse: A single short duration transmission of electromagnetic energy.

Pulse Duration: Time occupied by a burst of transmitted radio energy. This may also be expressed in units of range (pulse length). Also called pulse width.

Pulse Pair Processing: Name for the technique of mean velocity estimation by calculation of the signal complex covariance argument. The calculation requires two consecutive pulses.

Pulse Radar (or Pulsed Radar): A type of radar, designed to facilitate range measurement, in which the transmitted energy is emitted in periodic brief transmissions.

Pulse Repetition Frequency (PRF): The number of pulses transmitted per second.

Pulse Repetition Rate: See Pulse Repetition Frequency.

Pulse Repetition Time (PRT): The pulse interval from the beginning of one pulse to the beginning of the next succeeding pulse.

Pulse Width: The time occupied by an individual broadcast from a radar.

Quadrature: The component of the complex signal that is 90 degrees out of phase with the inphase component. This component lies along the imaginary axis in the complex plane.

Radar Cross Section: The area of a fictitious perfect reflector of electromagnetic waves that would reflect the same amount of energy back to the radar as the actual target.

Radar Reflectivity Factor: A quantity determined by the drop-size distribution of precipitation, which is proportional to the radar reflectivity if the precipitation particles are spheres small compared with the radar wavelength.

Radar Velocity (v): The component of motion of the target toward or away from the radar.

Random Variable (Variate): A variable characterized by random behavior in assuming its different possible values. Mathematically, it is described by its probability distribution, which specifies the possible values of a random variable together with the probability associated (in an appropriate sense) with each value. A random variable is said to be "continuous" if its possible values extend over a continuum, "discrete" if its possible values are separated by finite intervals.

Range Folding: Apparent range placement of a multiple trip return. A multiple return appears at the difference of the true range and a multiple of the unambiguous range.

Range Gate: A selectable interval of range (or of time delay from transmission) within which returning radar signals are measured. Gating is used to isolate the echoes from different regions of distributed targets.

Range Unfolding: Process of removing range ambiguity in apparent range of a multitrip target.

Rankine Vortex: Velocity profile for a symmetric circulation in which the inner core is in solid rotation, and tangential winds outside the core vary inversely with radial distance from the center.

Rayleigh Scattering: Scattering by spherical particles whose radii are smaller than about one-tenth the radar wavelength.

Receiver: An instrument used to detect the presence of and to determine the information carried by electromagnetic radiation. A receiver includes circuits designed to detect, amplify, rectify, and shape the incoming radio-frequency signals received at the antenna.

Reflectivity (Z): A measure of the fraction of radiation reflected by a given surface; defined as a ratio of the radiant energy reflected to the total that is incident upon that surface.

Refraction: Changes in the direction of energy propagation (due to changes in speed) as a result of density changes within the propagating medium.

Refractive Index: A measure of the amount of refraction. Numerically equal to the ratio of wave velocity in a vacuum to wave speed in the medium.

Scatterer: Any object capable of reflecting the radar signal.

Sectorized Hybrid Scan: A single reflectivity scan composed of data from the lowest four elevation scans. Close to the radar, higher tilts are used to reduce clutter. At further ranges, either the maximum values from the lowest two scans are sued or the second scan values are used alone.

Severe Storm: A storm producing a tornado, surface hail $\geq$3/4 inch, or wind gusts $\geq$50 knots, or all three.

Shear: The rate of change of the vector wind in a specified direction normal to the wind direction. Vertical shear is the variation of the horizontal wind in the vertical direction.

Shelf Cloud: A type of arcus (or roll) cloud. It is a low-level horizontal accessory cloud that appears to be a wedge shape as it approaches as seen along the leading edge of approaching thunderstorms. It is accompanied by gusty straight-line winds and is followed by precipitation.

Sidelobe: Secondary radiated energy maximum other than the radar main beam. Typically contains a small percentage of energy compared to the mainlobe.

Signal Processor: A computer processor used to apply a series of algorithms to the output of the receiver in order to estimate the spectral moments contained in the received backscattered signal.

Signal to Noise Ratio: A ratio that measures the comprehensibility of data, usually expressed as the signal power divided by the noise power.

Slant Range: The line-of-sight distance between two objects.

Slantwise Convection: A form of convection driven by a combination of gravitational and centrifugal forces.

Spearhead Echo: A radar echo associated with a downburst with a pointed appendage extending toward the direction of the echo motion. The appendage moves much faster than the parent echo, which is drawn into the appendage. During the mature stage, the appendage turns into a major echo and the parent echo loses its identity.

Specific Humidity: In a system of moist air, the ratio of the mass of water vapor to the total mass of the system.

Spectral Density: The distribution of power by frequency.

Spectrum Width: A measure of dispersion of velocities within the radar sample volume. Standard deviation of the mean radial velocity spectrum.

Squall Line: A line of active thunderstorms, either continuous or with breaks, including contiguous precipitation areas resulting from the existence of the thunderstorms. The squall line is a type of mesoscale convective system distinguished from other types by a larger length-to-width ratio.

Standard Atmosphere: A hypothetical vertical distribution of atmospheric temperature, pressure, and density that, by international agreement, is taken to be representative of the atmosphere for purposes of pressure altimeter calibrations, aircraft performance calculations, aircraft and missile design, ballistic tables, etc. The air is assumed to obey the perfect gas law and the hydrostatic equation.

Standard Deviation: The positive square root of the signal variance. In the WSR-88D, the velocity standard deviation is called spectrum width.

Storm: Any disturbed state of the atmosphere, especially as affecting the Earth's surface, and strongly implying destructive and otherwise unpleasant weather. Storms range in scale from tornadoes and thunderstorms, through tropical cyclones, to widespread extratropical cyclones.

Storm Motion: The velocity at which a storm travels.

Stratiform: Descriptive of clouds of extensive horizontal development, as contrasted to the vertically developed cumuliform types.

Supercell: An often dangerous convective storm which persists in a quasi-steady state for a period of time longer than it takes an air parcel to rise from the base of the updraft to its summit. It distinguishes itself from ordinary convection in that it contains a mesocyclone and is generally capable of producing the most severe weather (tornadoes, high winds, and giant hail).

Synchronous Detection: Processing that retains the received amplitude and phase but that removes the intermediate frequency carrier.

Target: Precipitation or other phenomena that produce echoes.

Temperature Inversion: A departure from the usual decrease with altitude of the air temperature.

Thin Line Echo: A narrow, elongated non-precipitating echo usually associated with thunderstorm outflow, fronts, or other density discontinuities, also known as a fine line.

Transmitter: The equipment used for generating and amplifying a radio frequency (rf) carrier signal, modulating the carrier signal with intelligence, and feeding the modulated carrier to an antenna for radiation into space as electromagnetic waves.

Unambiguous Range: The range to which a transmitted pulse wave can travel and return to the radar before the next pulse is transmitted.

Updraft: Current(s) of air with marked vertical upward motion.

Unimodal: A distribution having only one localized maximum, i.e., only one peak.

Variance: A measure of variability.

Veering Wind: A change in wind direction in a clockwise sense representing warm air advection.

Velocity Aliasing: Ambiguous detection of radial velocities outside the Nyquist co-interval.

Volume Coverage Pattern: Automatic radar scanning sequence control as it scans the atmospheric volume (from the surface to 70,000 ft and from the radar to 248 nm radius) surrounding the radar providing the data used for meteorological.

Vortex: In its most general use, any flow possessing vorticity. More often the term refers to a flow with closed streamlines.

Vorticity: A vector measure of local rotation in a fluid flow.

Wall Cloud: A local, abrupt lowering of a rain-free cumulonimbus base into a low-hanging accessory cloud, from 1.6 to 6.4 km (1 to 4 n mi) in diameter. The wall cloud is usually located in the southwestern part of a severe thunderstorm in the main updraft to the southwest of the main precipitation region. Rapid upward motion and visible rotation may be seen in wall clouds from several km away. Almost all strong tornadoes develop from wall clouds.

Watershed: The total area drained by a river and its tributaries.

Watt: The unit of power in the meter-kilogram-second (mks) system of units; equal to one joule per second.

Wavelength: The distance a wave will travel in the time required to generate one cycle.

Weak Echo Region (WER): (Abbreviated WER.) A region of weak radar echo that is bounded on one side and above by strong echo. It is located on the low-altitude inflow side of the storm. The WER is produced by strong updraft that carries precipitation particles to midlevels in a convective storm before they grow to radar-detectable sizes. The WER is also, in part, created when strong mid and upper-level echo is carried horizontally and outward aloft from due to strong divergence from an intense updraft. (e.g., the spreading cumuliform anvil on the updraft flank). *See also* bounded weak echo region (BWER).

Wind Shear: The local variation of the wind vector or any of its components in a given direction.

WSR-88D System: The summation of all hardware, software, facilities, communications, logistics, staffing, training, operations, and procedures specifically associated with the collection, processing, analysis, dissemination, and application of data from the WSR-88D unit.

WSR-88D Unit: The combination of one RDA, one RPG, and all associated OPUPs and interconnecting communications.